

Oxidation Catalysis Using Transition Metals and Rare Earth Oxides

A Thesis

Submitted to the School of Chemistry

of

Cardiff University

by

Soon Wen Hoh

In Partial Fulfilment of the

Requirements for the Degree

Of

Doctor of Philosophy

September 2014

Cardiff University

DECLARATION

This work has not been submitted in substance for any other degree or award at this university or any other university or place of learning, nor is being submitted concurrently in candidature for any degree or other award.

Signed _____ Date _____

STATEMENT 1

This thesis is being submitted in partial fulfilment of the requirements for the degree of Doctor of Philosophy.

Signed _____ Date _____

STATEMENT 2

This thesis is the result of my own independent work/investigation, except where otherwise stated. Other sources are acknowledged by explicit references. The views expressed are my own.

Signed _____ Date _____

STATEMENT 3

I hereby give consent for my thesis, if accepted, to be available online in the University's Open Access repository and for inter-library loan, and for the title and summary to be made available to outside organisations.

Signed _____ Date _____

STATEMENT 4: PREVIOUSLY APPROVED BAR ON ACCESS

I hereby give consent for my thesis, if accepted, to be available online in the University's Open Access repository and for inter-library loans **after expiry of a bar on access previously approved by the Academic Standards & Quality Committee.**

Signed _____ Date _____

Dedicated to
Mum and Dad

Acknowledgements

My experience in Cardiff University never would have been better without the people who have been there with me throughout those four years. Firstly, I would like to express my gratitude to my Ph.D. project supervisor, Dr David J. Willock, for his superb supervision and fruitful discussions, may it be work or non-work related. I appreciate the time taken by him to attend to my work, especially the writing up of this work. I would like to thank my current mentor, Dr James A. Platts, for helping out in various ways throughout my Ph.D. studies. Never would I have met another supervisor and mentor who are as enthusiastic and friendly as Dave and Jamie. I would also like to thank our industrial contact/project manager from Johnson Matthey, Dr Glenn Jones. He has been providing helpful feedbacks in a view of a surface scientist and made the project more interesting.

Besides, I am grateful to other past and present staff members of the Theoretical and Computational group (Prof. Peter Knowles, Dr Massimo Mella, and Dr Stefano Leoni) for showing interest in my talks and fruitful discussions on various chemistry problems during our weekly group meetings. I also appreciate all those who were in room 1.95 and room 56/1.04 (Adam Thetford, Niamh Hickey, Shaun Mutter, Christopher Lee, Filippo Marozzelli, Liam Thomas, Carlo Buono, Christian Reece, and Constantinos Zeinalipour-Yazdi). It would have been a dull three years without those occasional bowling night outs and random “interesting” conversations with you guys. I would like to thank the MChem and MSc students whom I have worked with throughout the years for they have helped me practice my mentoring skills on them.

I am also blessed to have wonderful housemates who have accompanied my throughout my stay in Cardiff. I have also been blessed with great friends from church and cell-group who have shared my great and not so great times. With their presence I have put on a few extra kilos. My free times were always filled with joy and adventure in their company.

I am also grateful to have teachers who have educated and instilled good moral values in me (too many names to mention). Most importantly, I am very thankful to have wonderful parents who have supported me in many ways. I am greatly indebted by their positive upbringing that has made me the person I am today. Without their support, I wouldn't have gone this far.

I gratefully acknowledge the funding support by Johnson Matthey and Cardiff University. All computational resources were provided by three different providers:

- 1) Cardiff University's ARCCA supercomputer, Raven,
- 2) Wales' national supercomputing service provider, High Performance Computing (HPC) Wales
- 3) UK's national high performance computing service, which is funded by the Office of Science and Technology through EPSRC's High End Computing Programme, HECToR and ARCHER.

Special thanks to the ARCCA and HPC Wales committee and support staff who have provided their support throughout the use of the service.

"I shall be with Christ, and that is enough."

-Michael Faraday (1791 – 1867)

Summary

Oxygen abstraction together with CO adsorption and oxidation over palladium/platinum-doped cerium (IV) oxide and gold catalyst supported on iron (III) oxide were studied employing density functional theory with the inclusion of on-site Coulomb interaction (DFT+U). Hybrid functionals employing DFT method are able to re-produce structural properties for CeO₂ that agrees well with experimental data. The localisation of two excess electrons upon the removal of an oxygen atom from the CeO₂ lattice is well described by DFT+U and is found to be most favourable on two next nearest neighbour cerium sites from the vacancy site. This defective bulk structure gave an oxygen vacancy formation energy (E_{vac}) of 2.45 eV using PW91+U (2.43 eV using PBE+U). The surface defect formation energies are calculated to be lower than that of the bulk structure. Other structures with different pair of Ce³⁺ sites at higher E_{vac} are also present. At higher temperature, it is predicted that the energy gained from thermal heating will allow the defect structure to end up at one of the higher energy defective structures obtained. Both the CeO₂ and α -Fe₂O₃ support are reduced more easily in the presence of transition metal atoms or clusters. Supported gold nanoparticle is found to affect the E_{vac} on the α -Fe₂O₃(0001) surface only to a certain limited influential area around the nanoparticle. The E_{vac} is reduced further when the Au atoms at the periphery sites are oxidised to give Au₁₀O₆ cluster. CO has weak interaction with the CeO₂(111) surface. However, by doping the surface with Pd²⁺ and Pt²⁺ ions, CO is found to adsorb strongly at the three coordinated metal dopant that has a vacancy coordination site exposed on the surface. Weak adsorptions are also observed at the perimeter sites of Au₁₀O₆/ α -Fe₂O₃(0001). Overall, it is predicted that CO oxidation, which follows the Mars-van Krevelen type mechanism can be enhanced by the presence of transition metal dopants or clusters. The continuous effort of researchers to reduce CO emission and the curiosity on where the excess electrons from the removed oxygen localised in the CeO₂ system have been the motivation of this project. This work will provide insight on catalyst design and the understanding of the electronic structure of the systems studied.

List of papers

Chapter 3: Structural and electronic properties of stoichiometric and defective bulk ceria

- Defective structure of ceria. *In preparation.*
- Pd/Pt dopant effects on the reduction of bulk ceria. *In preparation.*

Chapter 4: CeO₂ (111) and (110) surfaces

- Effects of PGM dopants on the reduction of CeO₂ surfaces. *In preparation.*

Chapter 5: Gold nanoparticles supported on α -Fe₂O₃(0001) surface

- S.W. Hoh, L. Thomas, G. Jones, D.J. Willock, “A density functional study of oxygen vacancy formation on α -Fe₂O₃(0001) surface and the effect of supported Au nanoparticles”, *Research Chemical Intermediates*, Accepted in November 2014.
- CO adsorption and oxidation at the interface of oxidised Au₁₀O₆/ α -Fe₂O₃(0001) surface. *In preparation.*

Contents

Declaration	i
Acknowledgements	iii
Summary	v
List of papers	vi
Contents	vii
1 Introduction	1
1.1 General overview	1
1.2 Abatement of noxious emissions in automotive exhaust gases	2
1.3 Metal oxide support for transition metal catalysts.....	4
1.3.1 Ceria as support for noble metal catalysts	4
A. Oxygen deficient ceria.....	5
B. Metal-support interaction	13
1.3.2 Gold catalysts	20
1.4 Computational approach to modelling α -Fe ₂ O ₃ , and CeO ₂	23
1.4.1 Strongly correlated <i>d</i> -electrons and spin frustration of Fe ³⁺ centres in α -Fe ₂ O ₃	23
1.4.2 Tackling the strongly correlated <i>f</i> -electrons of cerium in CeO ₂	25
1.5 Project goals	30
2 Theory and methods	32
2.1 Schrödinger Equation	32
2.2 Density Functional Theory	33
2.2.1 The Hohenberg-Kohn theorems	34
2.2.2 Kohn-Sham Self-consistent Equations	35
2.2.3 Generalised Gradient Approximation.....	36
2.2.4 Hubbard model and on-site corrected DFT (GGA+U).....	37
2.2.5 Hybrid functionals	39
2.3 DFT code – VASP	41

2.3.1	Projector augmented wave method.....	41
2.3.2	Optimisers.....	43
2.3.3	Using planewave basis set	45
2.3.4	Bulk and surface optimisations.....	48
2.3.5	Generation of different spin permutations on Ce sites	50
2.4	DFT code – CRYSTAL09	51
2.4.1	Basis sets.....	51
2.4.2	Effective core potentials	53
2.5	Nudged elastic band method.....	54
2.6	Vibrational frequency analysis	55
2.7	Density of states (DOS).....	56
2.8	Bader charge analysis	58
3	Structural and electronic properties of stoichiometric and defective bulk CeO₂	61
3.1	Introduction	61
3.2	Computational details	63
3.3	Stoichiometric bulk structure of ceria	68
3.4	Structural and electronic properties of defective bulk ceria	73
3.5	Doping bulk ceria with platinum group metals (PGM)	80
3.6	Effects of platinum group metal (PGM) dopants on oxygen vacancy formation in bulk ceria	90
3.7	Conclusion	95
4	CeO₂ (111) and (110) surfaces	98
4.1	Introduction	98
4.2	Computational details	101
4.3	Surface energy and oxygen vacancy formation on low index and 110-type step surfaces of CeO ₂	105
4.4	Doping CeO ₂ (111) surface with platinum group metals (PGM).....	116

4.5	Doping CeO ₂ $\langle 110 \rangle$ -type step surfaces with platinum group metals (PGM).....	121
4.6	CO adsorption and oxidation on CeO ₂ surfaces	123
4.7	Conclusion	132
5	Gold nanoparticles supported on α-Fe₂O₃ surface	135
5.1	Introduction	135
5.2	Computational details	138
5.3	Effects of Au ₁₀ nanoparticle on oxygen vacancy formation on α -Fe ₂ O ₃ (0001) surface	141
5.4	CO adsorption on Au ₁₀ O ₆ /Fe ₂ O ₃	155
5.5	CO oxidation.....	158
5.6	Conclusion	163
6	General conclusions.....	165
6.1	Future work.....	170
	Appendix	171
A1.	Basis sets and ECPs for CeO ₂ in CRYSTAL09	171
A2.	Structural and electronic properties of defective bulk ceria	176
A3.	Effects of platinum group metal (PGM) dopants on oxygen vacancy formation in bulk ceria	177
A4.	Effects of platinum group metal (PGM) dopants on oxygen vacancy formation in bulk ceria	178

Chapter 1

Introduction

1.1 General overview

This chapter gives an overview of the aims and scope of the research work presented in this thesis. In addition, it will discuss the literature available for noble metal catalysts (Pd, Pt, Au), role of cerium (IV) dioxide (ceria or CeO_2) as support, and computational approaches in modelling ceria and alpha phase iron (III) oxide (hematite or $\alpha\text{-Fe}_2\text{O}_3$). This thesis aims to present the application of computational chemistry to study oxidation catalysis using transition metals and rare earth oxides. There is a huge interest in the use of catalysts which contains both metal and metal oxides that applies in heterogeneous catalysis. Metal oxides and oxide supported metals are involved in reactions such as oxidation of hydrocarbons (HC)¹⁻⁶ and carbon monoxide (CO), as well as the reduction of nitrogen oxides (NO_x)^{1, 3-5, 7-9}. The focus is mainly on ceria and hematite as the support. Metal oxides and oxide supported metal systems were modelled to study the metal-support interactions and its effect on oxidation reactions at the atomic level using density functional theory (DFT) with the inclusion of the on-site Coulomb interaction correction term (DFT + Hubbard U). The systems that are presented in this thesis consist mainly of Pd/Pt doped bulk and (111) surface of ceria, and hematite supported Au_{10} nanoparticle.

Chapter 2 will discuss the necessary theory and methods applied in our research work. This will include some basics on DFT and its implementations in two different codes used, which are Vienna Ab-initio Simulation Package (VASP)¹⁰⁻¹³ and CRYSTAL09^{14, 15}. Details of methods used for optimisation of structures and their lattice parameters, determination of bulk modulus, and transition state search will also be presented.

Chapter 3 will show the calculation results obtained for stoichiometric and platinum group metal (PGM) doped bulk. The structural and electronic properties of defective ceria and the effects of dopant on oxygen vacancy formation in these systems will be discussed. Activation barriers for oxygen diffusion in these defective structures are also presented.

Results on calculations on the (111) and (110) surfaces of ceria will be discussed in Chapter 4. The defective structure of the surfaces has been investigated and it is found that dopants can lower the vacancy formation energy of the CeO₂ support. CO adsorption on this oxide support will also be discussed.

Chapter 5 will shift the focus to Au₁₀ nanoparticle supported on (0001) surface of hematite. Similarly, vacancy formation energy will be discussed. CO adsorption and oxidation at the interface between the α -Fe₂O₃ surface and the supported Au nanoparticles will also be presented.

The final chapter consists of the general conclusions and findings from this research. An abstract of the thesis and related publications in preparation are presented at the start of this thesis. Relevant appendices are included at the end of this thesis.

1.2 Abatement of noxious emissions in automotive exhaust gases

Ambient air pollution has been a serious issue for centuries. The Great Smog of 1952 is one of the examples that occurred in London where the use of coal to keep warm during the winter caused the forming of thick layer of smog over the city.^{16, 17} About 4000 people and cattle were killed by the smog.¹⁷ A similar tragedy occurred in the industrial town of Donora, Pennsylvania in October 1948 where the thick cloud of pollution which lingered in the air for 5 days killed 20 people and caused sickness in 6,000 of the town's 14,000 people.¹⁸ Even till now air pollution is still a problem as a result from industrial revolution and also the increase in motor vehicles. Authorities in the United States have passed the initial Clean Air Act of 1963, which established the funding for the study and clean-up of air pollution.¹⁹ Subsequent amendments to the Clean Air Act introduced more stringent requirements to tackle the air pollution issue such as the amendment of 1970, part of which required a 90% reduction in emissions from new automobiles by 1975.²⁰ There are six common air pollutants that require emission standards to be set, which are ground-level ozone, particulate matter, sulfur oxides (SO_x), CO, HC, and NO_x.²¹ In the same year, the first European Economic Community (EEC) directive has been implemented to establish standards of emissions from positive-ignition engines of motor vehicles such as CO, HC, NO_x, and particulates.²² There on, more stringent amendments have

been made to the emission standards which the current one is referred to as Euro 5²³ and Euro 6²³ for passenger cars and Euro VI²⁴ for heavy duty vehicles.

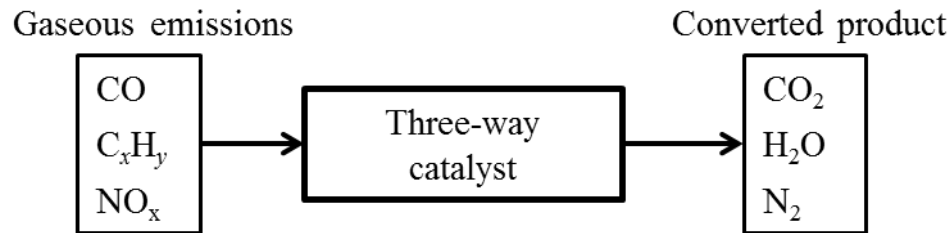
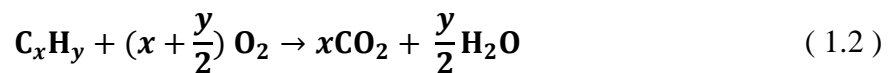


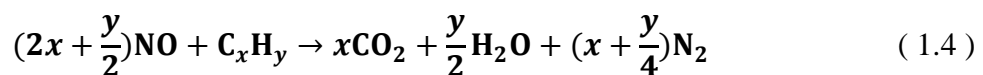
Figure 1.1 A schematic diagram of process in three-way catalytic converter. The exhaust emissions pass through the TWC will flow through the channels in the ceramic monolith. Catalytic reactions occur as CO, HC, and NO_x encounter the metal particles supported on the washcoat.

Johnson Matthey has been involved in the emissions control industry for over 40 years²⁵⁻²⁸ and in 1972, positive benefits of platinum based catalysts to clean up car exhaust were successfully developed and demonstrated by the company.²⁹ Thus, the catalytic converter (containing the autocatalysts) became the preferred technology in controlling exhaust emissions.²⁹ The first production line of autocatalysts was then manufactured in Johnson Matthey's plant in Royston, UK in late 1973.²⁹ These were just the oxidation or two-way catalytic converters as they only oxidise CO and unburnt HC to produce carbon dioxide (CO₂) and water (H₂O). Later on, tighter emission standard were required for NO_x, too. Thus, a platinum/rhodium based three-way catalyst that is able to control all three pollutants mentioned earlier simultaneously was developed and then fitted on most American cars by 1982. In simple terms the reactions that occur in:- a) a two-way and b) a three-way catalyst are:

- a) oxidation of CO and HC in a two-way catalyst to produce CO₂ and H₂O.



- b) oxidation reactions in a three-way catalyst shown in Equations (1.1) and (1.2), and reduction of NO_x with CO and HC to produce nitrogen (N₂).



1.3 Metal oxide support for transition metal catalysts

In a three-way catalytic converter (TWC), the catalyst is usually supported on ceramic monolith which has a honeycomb structure. A coating also termed as washcoat is applied to the channels or cells within the honeycomb structure to increase the surface area so that an adequate amount of active catalytic metals can be dispersed on it. Figure 1.2 shows the cross section of a ceramic monolith. Usually, aluminium oxide (alumina), titanium dioxide (titania), cerium (IV) dioxide (ceria) or a mixture of silicon dioxide (silica) and alumina are used as washcoat. Reducible metal oxides are a major component here as the surface oxygen can be a source of oxidation reactions. The oxygen storage capability is defined as the ability of the metal to change its oxidation state during reversible storage and release of oxygen for catalytic reactions. As a catalysts support, the oxygen storage capability provides a balance of air-to-fuel ratio at the optimum under “rich” and “lean” mixture conditions, respectively.³⁰

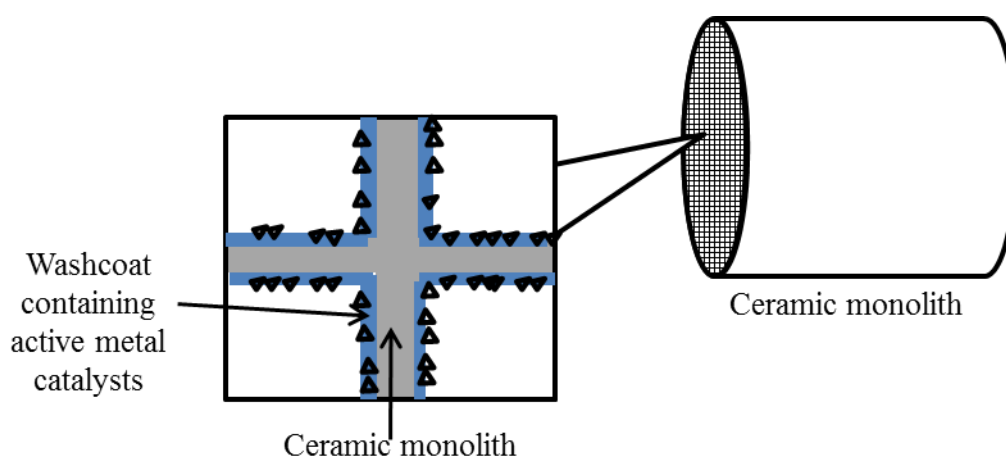


Figure 1.2 Cross section of a ceramic monolith. Enlarged picture shows the walls of the channels inside a monolith which are coated with washcoat containing active metal catalysts.

As mentioned, our main metal oxide support systems are ceria and hematite. Thus, the literature review here is mainly focused on palladium and platinum metal catalysts supported on ceria and then gold catalyst supported on hematite.

1.3.1 Ceria as support for noble metal catalysts

Ceria (CeO_2) takes on the fluorite lattice structure of space group $\text{Fm}\bar{3}\text{m}$ over the whole temperature range from room temperature to melting point. A single unit cell contains four cerium and eight oxygen atoms, with each cerium ion co-ordinated to

eight oxygen ions in a cubic arrangement. The experimental lattice parameter reported for ceria is 5.411 \AA .³¹⁻³³ A variety of experimental bulk modulus values have been obtained using different methods ranging from 204 to 236 GPa.^{31, 32, 34, 35}

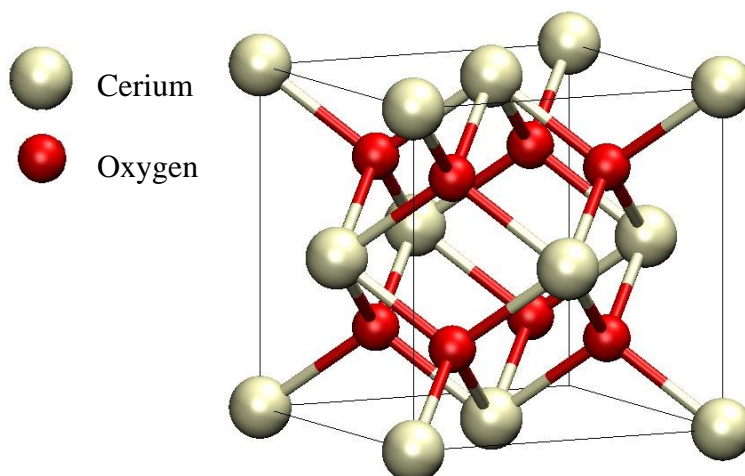


Figure 1.3 Single unit face centred cubic cell of ceria with 4 cerium atoms (white) and 8 oxygen atoms (red).

Over the years, ceria has been utilised in various areas of catalysis. Using “ceria” as a search keyword in Web of Science results in approximately 11,670 publications to date. This approximate number has increased by 3,725 since 2011 (Accessed 14 January, 2014). Ceria has been one of the major components used in the washcoat of TWC for the treatment of noxious exhaust emissions from automobiles.^{36, 37} Ceria also acts as promoter for metal catalyst and enhanced water-gas shift reactions.³⁰ Besides, ceria is also involved in biomedicine,^{38, 39} in removal of soot from diesel engine exhaust,^{40, 41} for the removal of organics in wastewater,⁴² as an additive for combustion catalysts,^{43, 44} and in redox and electrochemical reactions.^{45, 46} Such widespread applications is mainly due to the unique oxygen storage capability of ceria.

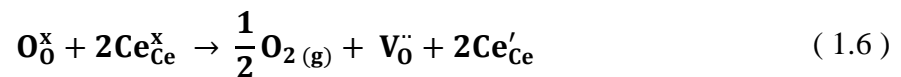
A. Oxygen deficient ceria

The oxygen deficient, non-stoichiometric CeO_{2-x} (where $0 < x \leq 0.5$) is known to be formed under reducing environment at elevated temperatures. Touret and co-workers reported that ceria still preserves its fluorite structure at a reduction temperature of 900 K even after losing a large amount of oxygen from its lattice and with the formation of oxygen vacancies.^{47, 48} These structures are readily re-oxidised to CeO_2 under oxidising environment.⁴⁷⁻⁴⁹ This also means that the ceria lattice is likely to be stable against degradation due to repeated reduction/oxidation cycles used in catalysis. For instance, in the automobile exhaust environment, the relative

partial pressures of oxygen and reductants such as CO and un-burnt HC shift the equilibrium of the redox reaction:



This depends on the ability of the oxide cation to switch between the two stable valence states Ce^{4+} and Ce^{3+} . The reduction of Ce^{4+} to Ce^{3+} proceeds by the release of a lattice oxygen anion as an oxygen atom in $\frac{1}{2}\text{O}_2$ with the two electrons left behind in the $4f$ states of two cerium atoms.^{50, 51} This can be shown using the Kröger-Vink notation;



where O_O^x and Ce_{Ce}^x are O and Ce ions on their respective lattice sites with the expected formal charges, $\text{V}_\text{O}^{\cdot\cdot}$ is the vacancy of an oxygen site with an effective charge of +2, and Ce'_{Ce} denotes Ce on a Ce site with an effective charge of -1, corresponding to Ce^{3+} ion. This notation emphasises the importance of lattice oxygen vacancies in the reduction process.

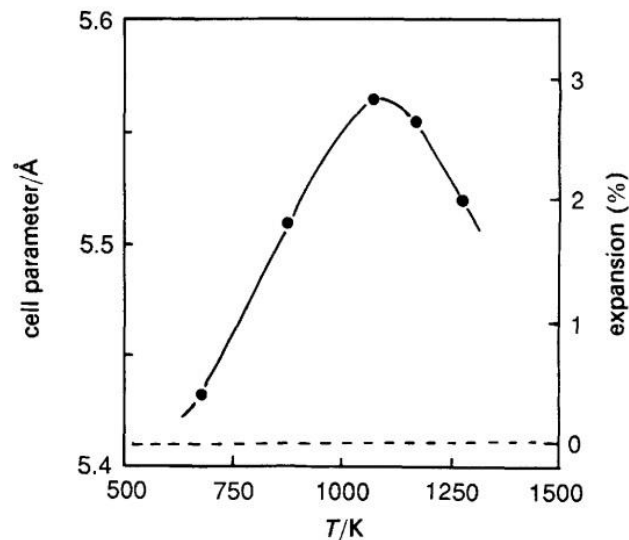


Figure 1.4 Variation of unit cell parameter of the cubic phase CeO_2 vs. reduction temperature. At temperature between 1070 K and 1170 K an intermediate cubic phase Ce_2O_3 was observed. For higher reduction temperatures, the lattice expansion decreases and the hexagonal Ce_2O_3 phase was observed.⁴⁸

A noticeable lattice expansion by 1.8% with respect to the stoichiometric ceria (5.411 Å) was observed by Perrichon *et al.*⁴⁸ at reduction temperature of 873 K as shown in Figure 1.4. They have reported that the increase in lattice parameter is due to the presence of Ce^{3+} as a result of reducing Ce^{4+} ions as deduced using the Shannon's ionic radii.^{48, 52, 53} At higher temperature (>1070 K), initial phase change

occurs starting with an intermediate cubic phase Ce_2O_3 until CeO_2 is fully reduced to the hexagonal phase Ce_2O_3 structure. This oxygen releasing reaction can be written as



The heat of reaction of equation (1.7) is related to the oxygen vacancy formation and most likely represents the upper limit as suggested by Paier *et al.*⁵⁴ in their recent review on oxygen defects and surface chemistry of ceria. Using the data of observed heats of formation (ΔH_f°) of CeO_2 (-1088.7 kJ/mol) and Ce_2O_3 (-1796.2 kJ/mol),⁵⁵ the reduction enthalpies (ΔH_r°) are calculated following equation (1.7) at a temperature of 298 K to be 381.2 kJ/mol (3.95 eV). The observed ΔH_f° of CeO_2 and Ce_2O_3 from various sources were tabulated by Paier *et al.*⁵⁴ together with the calculated ΔH_r° (Table 1.1).

Table 1.1 Observed heats of formation (ΔH_f°) of CeO_2 and Ce_2O_3 , and reduction enthalpies (ΔH_r°) following equation (1.7), at 298.15 K.⁵⁴

ΔH_f° (kJ/mol)		ΔH_r°		T (K)	Reference
CeO_2	Ce_2O_3	kJ/mol	eV		
-1088.7	-1796.2	381.2*	3.95	298.15	CRC ⁵⁵
-1088.6 ± 1.4 ⁵⁶	-1796.2 ± 2.8	381.0 ± 0.7	3.95	298.15	Baker <i>et al.</i> ⁵⁷
-1090.4	-1792.4	388.4*	4.03	298.15	Zinkevich <i>et al.</i> ⁵⁸

*Calculated from heats of formation.

From the review by Paier *et al.*⁵⁴, the experimental oxygen vacancy formation energy ($\Delta H_d \left(\frac{1}{2}\text{O}_2 \right)$) are mostly derived from conductivity data and is dependent on both formation of defects and their migration. The conductivity model applied suggests the following temperature coefficient

$$\frac{2}{5}\Delta H_d \left(\frac{1}{2}\text{O}_2 \right) + \Delta H_{\text{ion}}^\ddagger \quad (1.8)$$

The $\Delta H_d \left(\frac{1}{2}\text{O}_2 \right)$ is the defect formation energy according to equation (1.6) and $\Delta H_{\text{ion}}^\ddagger$ is the activation energy for migration of the defect.^{54, 59} Paier *et al.* have applied a prefactor of $\frac{2}{5}$ since they have used $\frac{1}{2}\text{O}_2$ as reference. They also mentioned that the prefactor is twice the factor given by Steele and Floyd.⁵⁹

Table 1.2 Heats of oxygen vacancy formation ($\Delta H_d(\frac{1}{2}O_2)$) and oxygen vacancy activation enthalpy (E_a) collected from different sources. PAW is projector augmented wave.

Method	$\Delta H_d(\frac{1}{2}O_2)$		Reference
	kJ/mol	eV	
Experiments			
Oxygen diffusion (1150 – 1400 K)	321 ^a	3.33 ^a	Steele <i>et al.</i> ⁵⁹
Electronic conductivity (1100 K)			Panhans <i>et al.</i> ⁶⁰
CeO _{1-x} (x<0.25)	419±32 ^b	4.34±0.33 ^b	
CeO _{1.75}	397±32 ^c	4.12±0.33 ^c	
Coulometric titration (873 – 973 K)	387±13	4.01±0.14	Gorte ⁶¹
Method	E_a		Reference
	kJ/mol	eV	
Theoretical calculations			
Interatomic potential	61	0.63	Balducci <i>et al.</i> ⁶²
DFT (PAW & all electron methods)			Frayret <i>et al.</i> ⁶³
CeO _{1.75} (a=5.411 Å)	106±2	1.10±0.02	
CeO _{1.75} (a=5.458 Å)	91±2	0.94±0.02	
CeO _{1.875} (a=5.411 Å)	77±2	0.80±0.02	
CeO _{1.875} (a=5.458 Å)	69±2	0.72±0.02	
DFT+U (PAW method)			
CeO _{1.96}	51	0.53	Nolan <i>et al.</i> ⁶⁴
Molecular dynamics (800 – 2200 K)			
CeO _{1.8778}	56	0.58	Gotte <i>et al.</i> ⁶⁵

^acf. Paier *et al.*⁵⁴, ^busing $\Delta H_{\text{polaron}}^{\ddagger} = 39$ kJ/mol from Tuller and Nowick⁶⁶, ^cusing $\Delta H_{\text{polaron}}^{\ddagger} = 50$ kJ/mol for CeO_{1.75} from Tuller and Nowick⁶⁶.

The few literature cited in their review are obtained through oxygen diffusion,⁵⁹ electronic conduction,⁶⁰ and coulometric titration.⁶¹ The oxygen diffusion migration barrier for temperatures between 1150 and 1450 K obtained by Steele and Floyd (cf. Paier *et al.*⁵⁴) is 50 ± 16 kJ/mol for CeO_{1.92} and values between 73 ± 8 and 104 ± 15 kJ/mol for defect concentrations below 0.02%.⁵⁹ Paier obtained the E_{vac} of 321 kJ/mol by using the reported activation energy (E_a) for conductivity (212 kJ/mol)⁵⁹ and the average value of 83.7 kJ/mol for the activation enthalpy for the motion of oxygen ions.⁵⁴ In 2006, Nolan *et al.*⁶⁴ has reported that it is more favourable to create an oxygen vacancy at the surfaces than in the bulk ceria, which also confirms the results obtained in interatomic potential (IP) calculations.^{67, 68} In the same report, they also reported an E_a for the oxygen vacancy migration to be 51 kJ/mol which is in good agreement with the experimental value of 50 ± 16 kJ/mol obtained by Steele

and Floyd for $\text{CeO}_{1.92}$.⁵⁹ This value is lower than that reported by Balducci *et al.* (about 61 kJ/mol) in an earlier work using interatomic potentials.⁶² Previous DFT calculations also showed that E_a for the oxygen vacancy migration is dependent on vacancy concentration.⁶³ The E_a for oxygen vacancy migration increases with oxygen vacancy concentration. A year later, Gotte *et al.*⁶⁵ reported an E_a of 56 kJ/mol at temperatures 800–2200 K using molecular dynamics simulations (MD). This agrees well with experimental values⁵⁹ and other theoretical values^{62, 64, 67, 68} reported.

For the electronic conduction, Panhans and Blumenthal⁶⁰ obtained a temperature coefficient of 248 ± 32 kJ/mol. Using this temperature coefficient and the experimental barrier obtained for polaron hopping, $\Delta H_{\text{polaron}}^{\ddagger} = 39$ kJ/mol at small x of CeO_{2-x} , by Tuller and Nowick^{66, 69}, an oxygen vacancy formation energy $\Delta H_d \left(\frac{1}{2} \text{O}_2 \right) = 419$ kJ/mol is calculated following the model by Panhans and Blumenthal⁶⁰

$$\frac{1}{2} \Delta H_d \left(\frac{1}{2} \text{O}_2 \right) + \Delta H_{\text{polaron}}^{\ddagger} \quad (1.9)$$

At $x = 0.25$, the $\Delta H_{\text{polaron}}^{\ddagger}$ increases to 50 kJ/mol⁶⁶ which then give a $\Delta H_d \left(\frac{1}{2} \text{O}_2 \right) = 397$ kJ/mol. Recently, Plata *et al.*⁷⁰ calculated a value of $\Delta H_{\text{polaron}}^{\ddagger} = 39$ kJ/mol using DFT, which agrees well to the experimental produced by Tuller and Nowick.⁶⁶ In the coulometric titration method, Gorte⁶¹ reported a $\Delta H_d \left(\frac{1}{2} \text{O}_2 \right)$ between 375 and 400 kJ/mol (387 ± 13 kJ/mol) at temperatures from 873 K to 973 K. All these values are summarised in Table 1.2 as this will ease the comparison with calculated theoretical values for oxygen vacancy formation energies in Chapter 2 and 3.

As mentioned earlier, the reduction of ceria will form two Ce^{3+} cations with every oxygen ion vacancy created. One of our research aims is to investigate various Ce localisation sites. Experiments by x-ray photoelectron spectroscopy (XPS),^{71, 72} ultraviolet photoelectron spectroscopy (UPS),⁷² high resolution electron energy-loss spectroscopy (HREELS),⁷² diffuse reflectance spectroscopy (DRS),⁷³ and Fourier transform infrared (FTIR)⁷³ has shown the presence of Ce^{3+} species in both reduced bulk and surface of CeO_2 . Skorodumova *et al.*⁵⁰ has shown that the two excess electrons left by the removal of a neutral oxygen are localised on the empty f states two cerium atoms, which therefore change their valence from +4 to +3 using first-

principle calculations and Monte Carlo simulation with no adjustable parameters. Scanning tunnelling microscopy (STM),⁷⁴⁻⁷⁶ noncontact atomic force microscopy (NC-AFM),⁷⁷⁻⁷⁹ and dynamic force microscopy (DFM)⁸⁰ were also used to investigate the single oxygen vacancy mostly on the (111) facet of ceria.

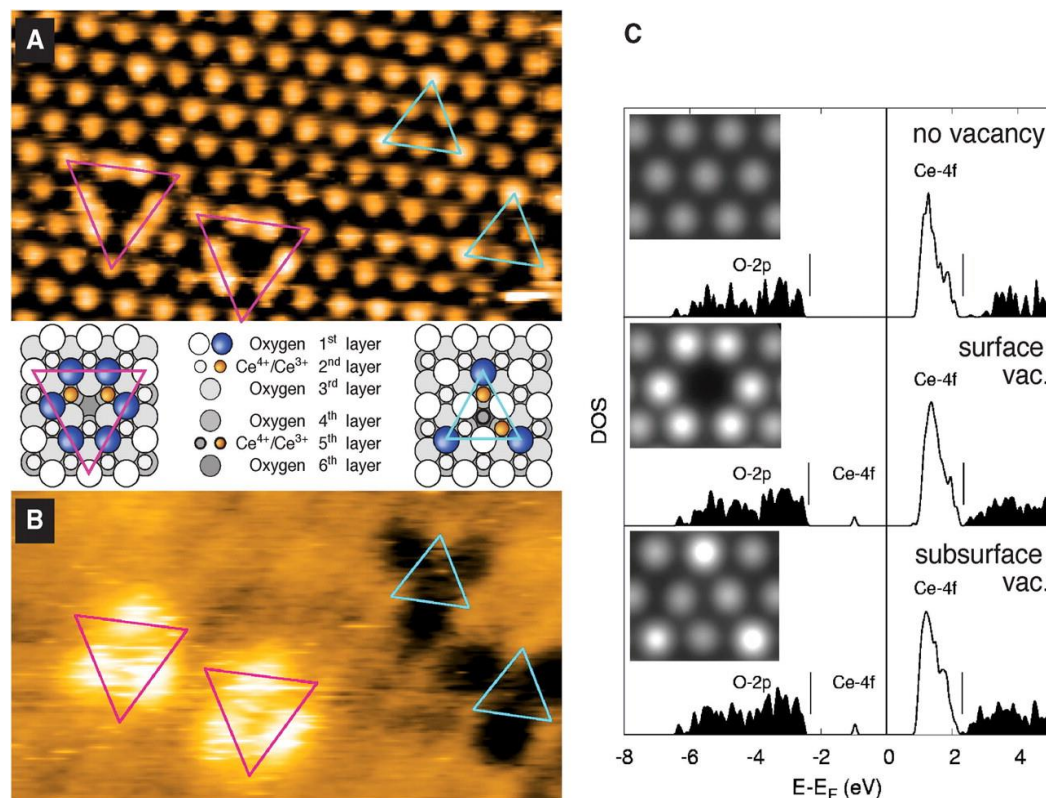


Figure 1.5 A) Filled-state and B) empty-state STM images of single vacancies and related structure model (left, surface vacancy; right, subsurface vacancy; characteristics O rim atoms in blue).⁷⁵

Esch *et al.*⁷⁵ reported that there is significant lattice distortion complementing the oxygen vacancy formation. They have used DFT calculations to explain the features observed in the STM images as shown in Figure 1.5. Surface oxygen vacancies are surrounded by three paired lobes (marked with magenta triangles in Figure 1.5 A). According to the calculations, these paired lobes are the six oxygen atoms surrounding the vacancy which relaxed outwards (0.08 to 0.09 Å) and laterally (0.11 to 0.16 Å away from the closest Ce ions). As for the sub-surface oxygen vacancy, triple protrusions (marked with cyan triangles in Figure 1.5 A) are observed. These are the three surrounding oxygen atoms, which relaxed outwards (0.19 Å). These surface structure relaxations around the single vacancies are mainly controlled by the positive electrostatic field centred on the vacancy that repels the nearest neighbour Ce cations and attracts, to a lesser extent, the second nearest neighbour O anions.⁷⁵ They also stated that the Ce^{3+} ions are always at the nearest neighbours to the defect

site due to the same positive electrostatic field that attracts the two excess electrons near the vacancy. The increase in the ionic radius of Ce then pushes the neighbouring O atoms away.

A few years later, the groups of Hu and Sauer have both independently reported findings on the electron localisation on (111) surface of ceria using DFT+U.^{81, 82} Both groups showed that the formation of a single sub-surface oxygen vacancy is favourable compared to that of a surface oxygen vacancy. Li *et al.* reported both the surface and sub-surface oxygen vacancy with the excess electrons localised on two next nearest Ce neighbours (hereon denoted as $2_1 - 2_1$; where 2 is the next nearest neighbour, and the subscript being the n^{th} atomic layer the Ce is at, 1 being the surface) to be the lowest energy structure for each case, respectively.⁸¹ However, Paier *et al.*'s work was performed on $p(2 \times 2)$ surface. Therefore, in the case of the surface oxygen vacancy, their lowest energy structure corresponded to two Ce^{3+} cations at the nearest and next nearest Ce neighbours ($1_1 - 2_1$) to the defect site.⁸²

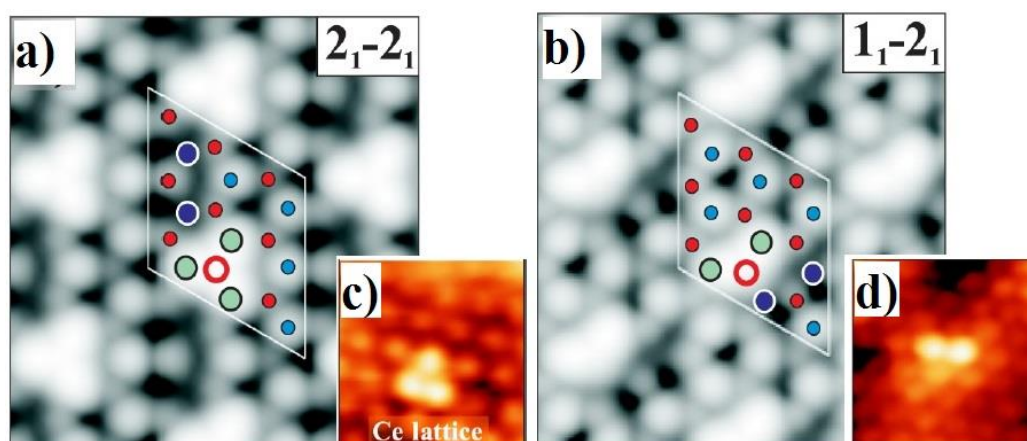


Figure 1.6 (a), (b) Experimental STM imaged with a tip configuration, that is sensitive to Ce lattice (1.2 V , $2.4 \times 2.4 \text{ nm}^2$), and (c), (d) DFT simulated empty-state STM images ($0 - 2 \text{ eV}$) of O defects with (a),(c) three, and (b),(d) two Ce^{4+} (bright spots; large green dots) next to the O vacancy (red circle). Small blue dots denote other Ce^{4+} ions on the surface, red dots the O^{2-} , and large blue circles the Ce^{3+} ions.⁷⁶

Recently, Jerratsch *et al.*⁷⁶ have applied STM and DFT+U to study electron localisation in defective ceria films. Their highly resolved STM measurements have shown that the Ce^{3+} ion pairs are at different positions on an oxygen defective CeO_2 (111) surface as shown in Figure 1.6. The most frequently seen arrangement is when one Ce^{3+} ion is next to the oxygen vacancy site while the second Ce^{3+} ion is at the next nearest neighbour ($1_1 - 2_1$). Other occurrences include:

- 1) both Ce^{3+} cations are positioned away from the vacancy site;

- 2) one Ce^{3+} cation at nearest neighbour and the other is nowhere to be seen in the image;
- 3) both the Ce^{3+} are at the nearest neighbour position.

However, the third occurrence is not detected in their STM experiment while 1) and 2) are relatively less abundant compared to the $2_1 - 2_1$ configuration.

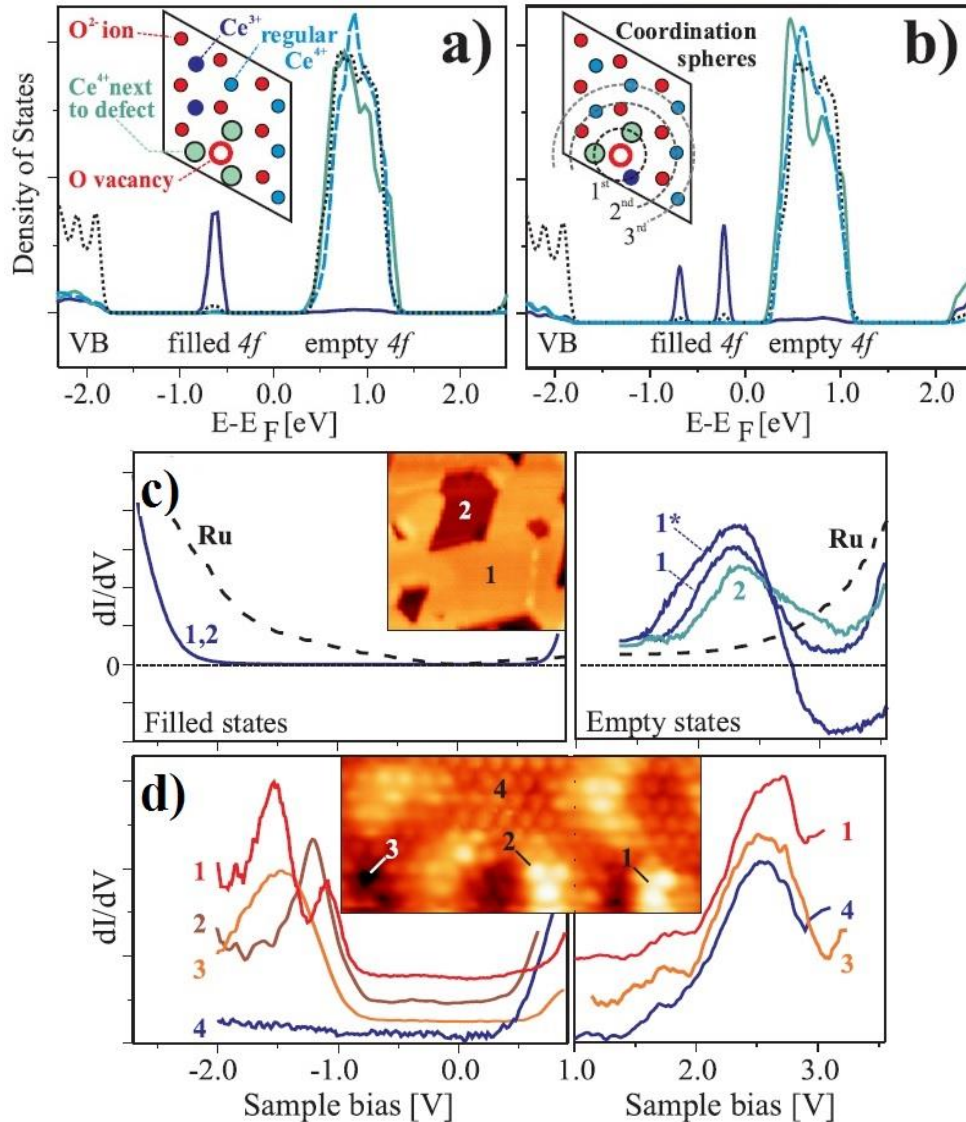


Figure 1.7 Total and atom-projected density of states for (a) the energetically favoured $2_1 - 2_1$ and (b) the $1_1 - 4_2$ Ce^{3+} ion pair. Dark solid line: Ce^{3+} ; bright solid line: Ce^{4+} next to an O vacancy; dashed line: other surface Ce^{4+} ; and dotted line: total density of states. All spectra are normalised with respect to the number of Ce ions. The respective unit cells and defect coordination spheres are shown in the insets. Conductance spectra of (c) stoichiometric and (d) reduced CeO_2 (111) taken at negative (left) and positive bias (right). The spectral positions are marked in the insets (c) 2.0 V, $15 \times 15 \text{ nm}^2$; (d) 1.2 V, $8 \times 4 \text{ nm}^2$. All curves have been taken with 5 pA current, apart from 1* (50 pA). While the dI/dV maximum at 2.3 V reflects the empty Ce 4f band, the peaks around -1.5 V are assigned to filled f states.⁷⁶

Jerratsch *et al.* have also explained that the splitting of f orbitals is due to the different distances of Ce^{3+} with different coordination number (CN) from the vacancy as shown in Figure 1.7. A splitting of 0.5 V for the f orbital is observed in conductance spectra when a pair of Ce^{3+} ion with the configuration $1_1 - 4_2$ consisting of six- and eight-coordinated Ce^{3+} ions in the surface and subsurface layer.⁷⁶ This explains the results obtained from experimental spectra showing the double peak structure where the two Ce^{3+} ions are apparently located in a rather different environment.⁷⁶ As for the single peak structure in the experimental spectra, it corresponds to the Ce^{3+} ions with similar CN.

B. Metal-support interaction

Although ceria has a wide commercial application in catalysis, pure ceria alone as the support is of little interest due to its drawbacks as an oxygen storage system. These drawbacks are related to thermal resistance and low-temperature activity of pure ceria.⁸³ When used alone, ceria has a low textural stability which is unable to meet the requirements of high-temperature gas-phase catalytic reactions.^{84, 85} Therefore, much research has been done in developing catalyst formulations which can enhance the thermal stability and at the same time maintain its special features. This can be done by:

- 1) doping ceria with other transition and rare earth metals or by metal dispersion on the surface^{37, 45, 86-99}
- 2) mixing ceria with other transition or rare earth oxides^{95, 100-106} which gives a mixed oxide support system.

The metal dopants can promote the reduction of ceria while mixed oxide systems improve the thermal stability of ceria as well as its redox properties. Thus, more efficient redox processes can occur at much lower temperature and an increase in catalytic activity will be observed. Other factors such as the extent of dispersion, relative amount or size of metal present, the surface morphology of the metal, and strength of interaction between support and the metal also affects the performance of catalysts in the oxides.¹⁰⁷⁻¹⁰⁹

The theoretical study on ceria presented in this thesis focuses mainly on PGM dopant effects on CO adsorption and oxidation, but not so on the mixed oxide systems. Experimentally, methods such as co-precipitation, deposition and impregnation, ion exchange, sol-gel, incipient wetness, and solution combustion

method are used to disperse the metal on the oxide support. Usually, the metals dispersed on the support are either as fine metal particles or as surface-oxidised metal. The surface-oxidised metal are formed following a high temperature calcination of the M/CeO₂ compound (M = Pd or Pt).^{110, 111} This has been widely discussed as the strong metal support interaction (SMSI) effects, where later on in 2010, Caballero *et al.* has also described how high temperature reducing conditions can lead to the oxide appearing to grow over the metal particle and effectively encapsulate it.¹¹²

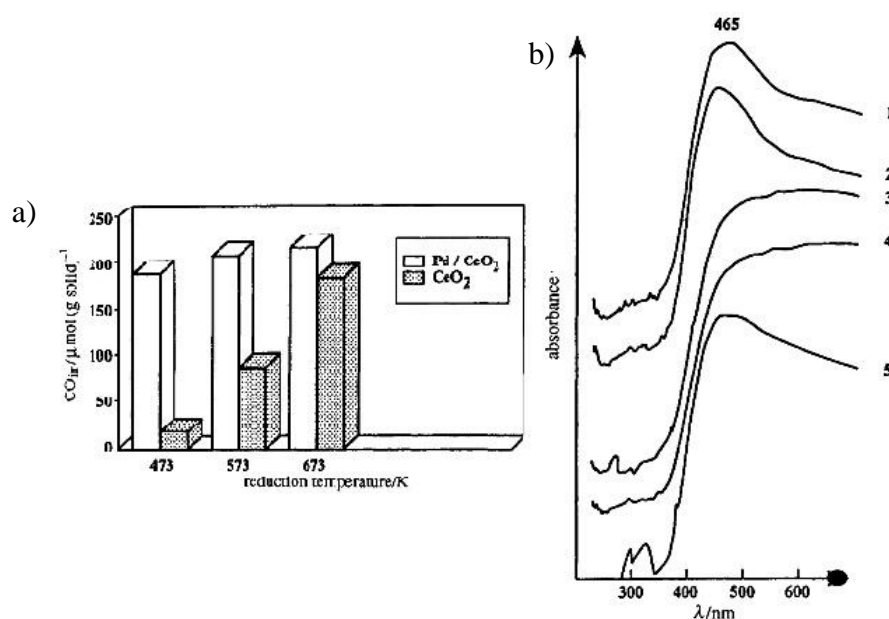


Figure 1.8 a) Influence of reduction temperature on the amount of CO adsorbed on ceria and 1.58% Pd/ceria catalysts. b) DRS of a 0.44% Pd/CeO₂ sample calcined at 673 K. 1) initial sample in air; 2) after outgassing at room temperature (RT) for 15 minutes (min.); 3) immediately after CO adsorption (100 Torr) at RT; 4) after outgassing at RT (15 min.) and oxygen adsorption (100 Torr) at RT for 1 hour; 5) after heating in oxygen (100 Torr) at 573 K for 1 hour.⁹⁶

CO is highly sensitive to site differences and its adsorption has been extensively used as a probe of active surface sites on both supported and non-supported platinum.¹¹³ It has been shown that CO adsorption occurs at both cationic Pt and fully reduced metal on the Pt/CeO₂ catalyst.¹¹³ The dissociation of CO has also been observed resulting in poisoning of active sites with the residual C but is removed following oxidation by the support at elevated temperature.¹¹³ Bensalem *et al.* did a spectroscopic study for CO adsorption on Pd/CeO₂ catalysts which concluded that CO adsorption on ceria is favoured by the presence of palladium.⁹⁶ They found samples containing small PdO particles are immediately reduced upon adsorption of CO at room temperature. Figure 1.8 shows the spectrum of the solid obtained from

UV-VIS DRS. The broad band centred near 450 nm is ascribed to the well dispersed PdO. As soon as the sample is in contact with CO (100 Torr) at room temperature, this band disappears. No changes to the spectrum are observed on subsequent sample outgassing at room temperature. Palladium oxide species is restored only by heating in oxygen (100 Torr) at 573 K for an hour.⁹⁶ In addition, Bensalem *et al.* reported that palladium enhances the concentration of donor levels (i.e. Ce³⁺ ions, oxygen vacancies) during pre-treatment of samples in hydrogen. Interaction of these basic sites with palladium reinforces the Pd – CO bond strength as indicated by the low value of CO stretching frequency (2025 – 2030 cm⁻¹) and the resistance of these species to evacuation at room temperature. They suggested that electron transfer occurs from ceria to palladium in a reducing atmosphere.

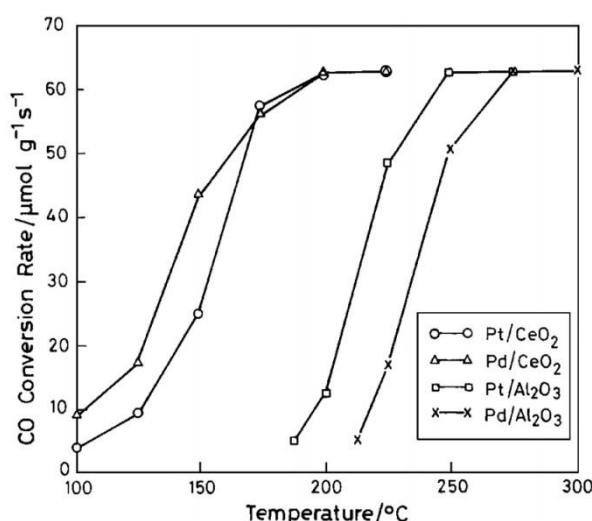


Figure 1.9 Rate of CO conversion over CeO₂- and Al₂O₃-supported Pd and Pt catalysts for CO + O₂ reactions. 0.1–0.2 g of the catalysts were used.¹

Recent experiments showed that ionically dispersed Pt, Pd, and Rh on ceria through solution combustion method have increased their catalytic activity.^{1, 4, 88-90, 114, 115} Bera *et al.*¹ found that the nearly 100% conversion temperatures of CO, HC and NO are lower on CeO₂ supported Pt and Pd catalysts compared to Al₂O₃ support. Figure 1.9 shows the rate of CO conversion over CeO₂- and Al₂O₃-supported Pd and Pt catalysts for CO + O₂ reactions. Higher rate for CO + O₂ reactions and turnover frequencies (TOF) are observed in Pd/CeO₂ compared to Pt/CeO₂ which is shown in Table 1.3. They have calculated the activation energy (E_a) from Arrhenius plots of ln(rate) vs 1/T for CO + O₂ reaction on Pt/CeO₂ and Pt/Al₂O₃ to be 31.2 kJ mol⁻¹ and 53.9 kJ mol⁻¹, respectively. They have also concluded that ionic dispersion of Pt and Pd metals in the form of a solid solution brings about metal ion incorporation in the CeO₂ matrix. Since only 1% of Ce⁴⁺ ions are substituted by Pt²⁺ and Pd²⁺ ions, O²⁻

ions associated with the metal ions are bonded to Ce^{4+} ions which contributes to the stability of Pt^{2+} and Pd^{2+} ions toward reduction. They suggest that the active adsorption sites for CO and other gases studied have to be Pt^{2+} and Pd^{2+} ions on CeO_2 surface since pure CeO_2 do not show any of the studied catalytic reactions at such low temperatures.

Table 1.3 Rate ($\mu\text{mol g}^{-1} \text{s}^{-1}$) and TOF (s^{-1}) data of NO + CO and CO + O₂ reactions over CeO_2 - and Al_2O_3 -supported Pt and Pd catalysts.¹

Catalysts	NO + CO		CO + O ₂	
	Rate	TOF	Rate	TOF
1% Pt/ CeO_2	27.10 (225 °C)	0.47 (225 °C)	25.00 (150 °C)	0.44 (150 °C)
	47.50 (250 °C)	0.83 (250 °C)	57.08 (175 °C)	0.99 (175 °C)
1% Pd/ CeO_2	11.88 (125 °C)	0.21 (125 °C)	43.75 (150 °C)	0.76 (150 °C)
	47.50 (150 °C)	0.82 (150 °C)	56.67 (175 °C)	0.98 (175 °C)
1% Pt/ Al_2O_3	40.42 (375 °C)	0.42 (375 °C)	12.92 (200 °C)	0.13 (200 °C)
	54.58 (400 °C)	0.57 (400 °C)	48.33 (225 °C)	0.50 (225 °C)
1% Pd/ Al_2O_3	23.31 (325 °C)	0.24 (325 °C)	17.10 (225 °C)	0.18 (225 °C)
	56.25 (350 °C)	0.58 (350 °C)	50.83 (250 °C)	0.52 (250 °C)

Recent studies by Chen *et al.*¹¹⁶ showed that as Pt loading decreases, Pt is better dispersed on CeO_2 than on Al_2O_3 or SiO_2 . Higher percentage of $\text{Pt}^{\delta+}$ is obtained at lower Pt loading due to the smaller Pt particles which are more easily oxidised. In addition, the Pt interface is located on the oxide surface bond with surface oxygen.¹¹⁷ The reaction rate at room temperature calculated from the total amount of Pt loaded on CeO_2 support is $2.2 \times 10^{-3} \text{s}^{-1}$ and generally as shown in Figure 1.10, the highly dispersed 0.25 wt% Pt/ CeO_2 showed good catalytic activity for low temperature CO oxidation with a lower light-off temperature compared to the rest of the catalyst compositions.¹¹⁶

This indicates that supported Pd and Pt catalysts are good for CO oxidation. However, we also need to know the structure of the catalysts in order to model them computationally. We find the following publications by Priolkar *et al.*⁸⁹ and Bera *et al.*⁸⁸ which we think are interesting and able to provide us some insight to the modelling of CeO_2 systems that involves the substitution of divalent cations into the CeO_2 matrix.

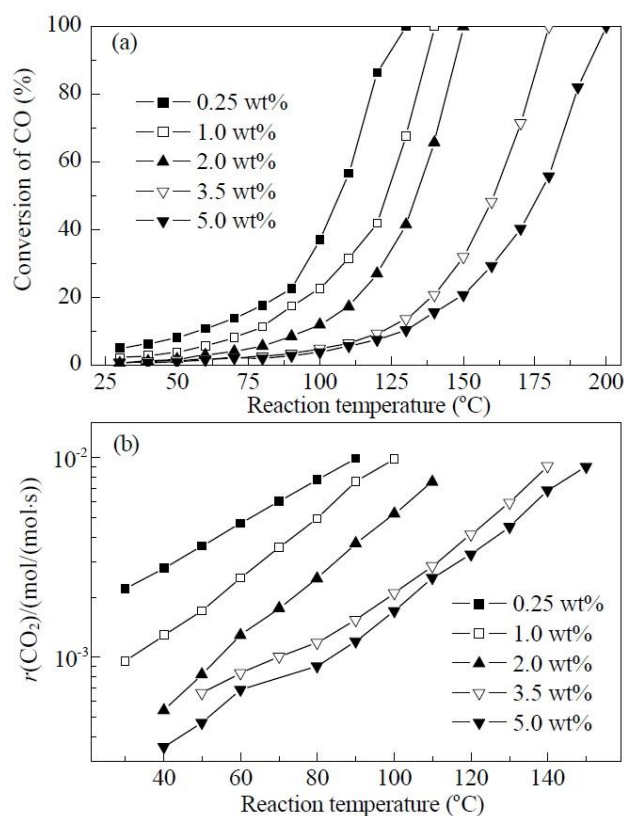


Figure 1.10 a) CO conversion rate and b) CO₂ production rate of various Pt/CeO₂ catalysts for CO oxidation at different temperatures. The reaction was carried out under atmospheric pressure at a CO:O₂:H₂ ratio of 1:1:98 and flow rate of 30 ml/min. The amount of catalyst was 400, 100, 50, 28, 6, and 20 mg for 0.25, 1.0, 2.0, 3.5, and 5.0 wt % Pt/CeO₂ catalysts(60 – 80 mesh), respectively.¹¹⁶

Priolkar *et al.*⁸⁹ investigated the structure of solution combustion synthesised Pd/CeO₂ catalysts using X-ray diffraction (XRD), X-ray photoelectron spectroscopy (XPS), and extended X-ray absorption fine structure (EXAFS) spectroscopy. In their XRD results, there is no presence of Pd metal particles or pure PdO phase for 1 atomic (at.) % Pd/CeO₂ but Pd metal particles are present in 5 at. % Pd/CeO₂. For the 1 at. % Pd/CeO₂ catalyst, the structure of Pd/CeO₂ catalysts could be refined to solid-solution phase of Ce_{1-x}Pd_xO_{2-δ} ($0 \leq x \leq 0.03$) with 3% oxide ion vacancy. XPS (Figure 1.11) and XANES data confirmed that Pd²⁺ species is present in the catalyst. The surface Pd²⁺ ions are observed to have a coordination number of 3 as indicated in EXAFS studies. This lower coordination of Pd²⁺ ions than in PdO or the surface Ce⁴⁺ ions that have a coordination number of 4 indicates that the oxide ion vacancies are around Pd²⁺ ions. Pd²⁺ is observed to interact strongly with the ceria support showing a Pd–O–Ce interaction. Structural distortion is also observed in the compound where Pd–O, Pd–Pd, and Pd–Ce distances obtained are 2.02, 2.72, and 3.31 Å. Finally, by comparing CO oxidation on 1 at. % Pd/CeO₂, Pd metal, PdO, and

1 at. % Pd dispersed on CeO₂ (1 at. % Pd/CeO₂ (dispersed)), they concluded that Pd²⁺ ions in CeO₂ matrix are the active sites for CO adsorption. This is because oxidation is found to occur at much lower temperature on 1 at. % Pd/CeO₂ which contains only Pd²⁺ ions. Furthermore, complete CO oxidation occurs below 448.15 K over 1 at. % Pd/CeO₂, which is lower when compared to oxidation over PdO, Pd metal particles and 1 at. % Pd/CeO₂ (dispersed), which require 523.15, 623.15, and 548.15 K.

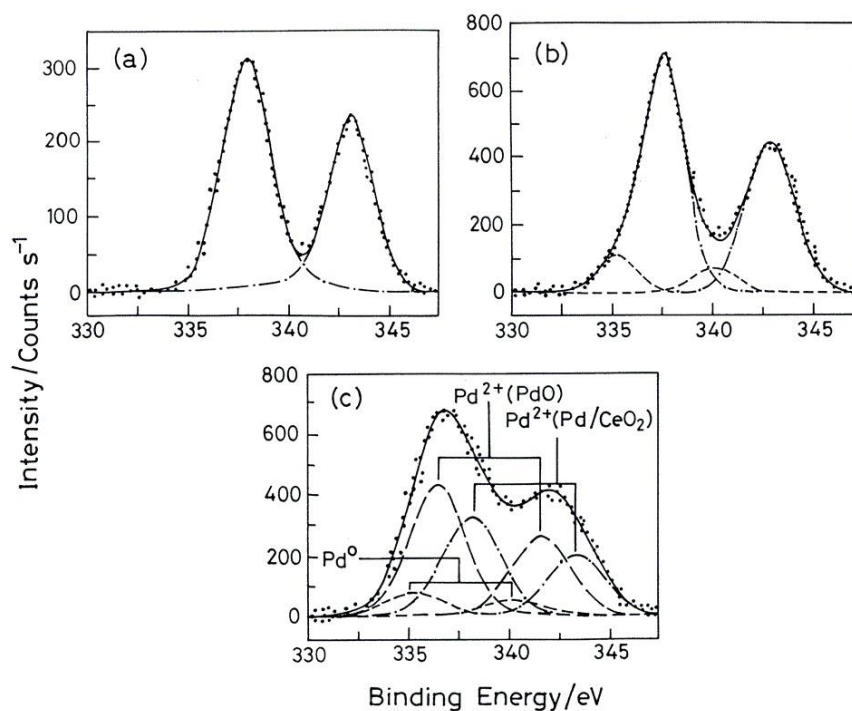


Figure 1.11 XPS of Pd(3d) core level region of a) 1 at. % Pd/CeO₂, b) 5 at. % Pd/CeO₂, and c) 1 at. % Pd/CeO₂ (dispersed).⁸⁹

Similarly, Bera *et al.*⁸⁸ have investigated the structure and chemical nature of Pt in combustion synthesised Pt/CeO₂ catalysts. They stated that the chemical environment of Pt in combustion synthesised Pt/CeO₂ is different from that of 2 at. % Pt dispersed over CeO₂ (2% Pt/CeO₂ (dispersed)), and of fine Pt metal particles. Further, they observed that CO oxidation occurs at much lower temperature over combustion synthesised 2% Pt/CeO₂ catalysts compared to 2% Pt/CeO₂ (dispersed) and fine Pt metal particles. The calculated activation energies (E_a) from Arrhenius plot of $\ln(\text{rate})$ vs $1/T$ of CO oxidation are 44, 52, and 106 kJ mol⁻¹ over combustion synthesised 2% Pt/CeO₂, 2% Pt/CeO₂ (dispersed), and fine metal Pt particles, respectively.

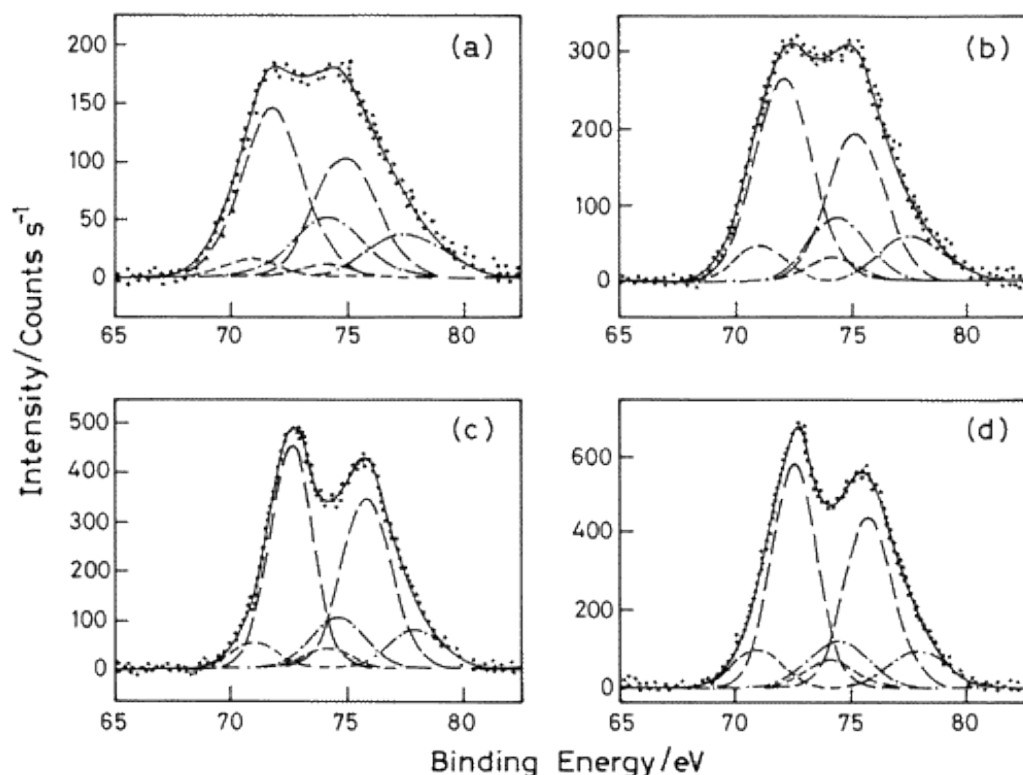


Figure 1.12 XPS of core level region of Pt in as-prepared a) 1% Pt/CeO₂ and b) 2% Pt/CeO₂ and heat-treated c) 1% Pt/CeO₂ and d) 2% Pt/CeO₂ at 1073 K for 100 hours. Pt(4f_{7/2, 5/2}) peaks at a) 71.0, 74.2; 71.9, 75.1; 74.3, 77.5 eV corresponds to Pt⁰; Pt²⁺; and Pt⁴⁺; respectively, b) 71.0, 72.1, 74.4 eV corresponds to Pt⁰, Pt²⁺, and Pt⁴⁺, respectively, c) 71.0, 72.9, 74.6 eV corresponds to Pt⁰, Pt²⁺, and Pt⁴⁺, respectively, d) 71.1, 72.8, 74.9 eV corresponds to Pt⁰, Pt²⁺, and Pt⁴⁺, respectively.⁸⁸

Bera *et al.*⁸⁸ also reported that PtO and PtO₂ phases are absent from 1% Pt/CeO₂ catalyst and XRD, TEM, and XPS (Figure 1.12) studies confirmed that the Pt is in +2 and +4 oxidation states along with a trace amount of metal. Upon treating the samples by heat at 1073 K for 100 hours, the Pt²⁺ ions increased at the cost of Pt⁴⁺ ions. Structural distortion is also observed with Pt²⁺–O–Ce⁴⁺ at a distance of 3.28 Å. Through the EXAFS analysis, they suggested the Pt–O–Ce to be slightly larger than 90° as they showed that, if the corresponding angle was 90° (under the assumption that the ionic radii of Pt²⁺ (0.80 Å), O²⁻ (1.40 Å), and Ce⁴⁺ (1.01 Å)), the Pt–Ce distance would be 3.21 Å. In addition, they reported the Pt–O, Pt–Pt, and Pt–Ce bond distances to be about 2.00 Å, 2.97 Å, and 3.28 Å, respectively. Thus, they suggested that there is a metal–ceria interaction, that leads to the formation of solid solution Ce_{1-x}Pt_xO_{2-δ} on the surface due to substitution of Pt²⁺ into Ce⁴⁺ sites.

1.3.2 Gold catalysts

Gold is widely used in jewellery and in electronics. However, a rapid growth is observed for gold catalysts in the last few decades. Bulk gold is chemically inert and has often been regarded to be poorly active as catalyst.^{118, 119} Bone and Andrew showed the use of Au catalyst for CO oxidation in 1925.¹²⁰ In 1973, Bond *et al.*¹²¹ reported that supported Au catalysts were able to catalyse the hydrogenation of mono-olefins, buta-1,3-diene, and but-2-yne. They suggested that preparing gold particles at 380 – 400 K either introduces a large number of defects, which are the active sites for hydrogen dissociation, or that the activity resides in some very small particles not sensed by electron microscopy. Then, both Haruta and Hutchings independently predicted and experimentally confirmed gold to be a good catalyst by investigating CO oxidation at temperature less than 0°C¹²² and hydrogenation of acetylene to vinyl chloride¹²³, respectively. These pioneering works have prompted others to study the origin of the exceptional catalytic properties of supported Au catalysts. At present, gold catalysts are also applied in de-NO_x,^{124, 125} catalytic combustion of volatile organic compounds (VOCs), water-gas shift reactions,^{126, 127} direct synthesis of H₂O₂ from H₂ and O₂¹²⁸ and other organic reactions.¹²⁹ CO oxidation over supported Au nanoparticles is one of the most studied and simplest reactions which cover a wide range of applications from gas masks, gas sensors, indoor air quality control, to hydrogen purification for polymer electrolyte fuel cells.¹³⁰

The reactivity of Au nanoparticle in CO oxidation relies on the use and choice of support, size and morphology of the nanoparticle, and the preparation method of the catalysts. These were also mentioned in reviews of gold catalysis done by various authors.^{119, 130-136} Throughout the years, research and published results show that supported Au nanoparticles are effective for CO oxidation at low temperature, even as low as -70°C.¹²² Schubert *et al.*¹³⁷ have shown that the choice of support material can influence the activity of gold catalyst for CO oxidation. They have grouped the support into two:

- 1) irreducible metal oxide and;
- 2) reducible transition metal oxide supports.

The irreducible metal oxides used were Al₂O₃ and MgO, which have a low ability to adsorb or store oxygen at low temperatures. Reducible transition metal

oxides were Fe_2O_3 , NiO_x , CoO_x , or TiO_2 , which exhibited superior activity up to one magnitude higher.¹³⁷ Schubert *et al.* also observed that the activity for CO oxidation on Au catalysts supported on irreducible metal oxides seems to depend very critically on the diameter of the gold particles. They have observed that Au/Mg(OH)₂ catalysts with a gold particle size of 0.6 – 1.2 nm has a turnover frequency (TOF) greater than 1.2 s^{-1} , whereas gold particle size less than 4 nm gave a TOF of $0.5 - 0.9 \text{ s}^{-1}$. Similarly, using the Au/Al₂O₃ with gold particle size of 2.4, 3.5, and 4.4, a TOF of 0.5 s^{-1} , 0.35 s^{-1} , and 0.35 s^{-1} were observed, respectively. This suggests the catalysts depend strongly on the metal particle size and rapidly lose their activity with increasing size of the gold particles. They also suggested that the oxygen adsorption to occur directly on the gold particles, either on defect sites or facilitated by variations in the electronic structure of small metal particles.¹³⁷

On the other hand, for support materials such as Fe_2O_3 and TiO_2 , the size of the gold particles only plays a secondary role. This is due to the oxide support's ability to provide reactive oxygen for the CO oxidation reaction. They have investigated this by measuring the TOF for CO oxidation at Au/Fe₂O₃.MgO mixed oxide catalysts as a function of the Mg content in the support material. Since oxygen dissociation is no longer rate-limiting and, as a consequence, the TOF is not governed by particle size effects. With this, Schubert *et al.* postulated that the independence of the TOF from Au particle size applies only to low metal loadings, where the metal particles are sufficiently distant from each other and the oxygen supply is not rate-limiting. This also suggests that the CO oxidation occurs at the metal-support interface as has been presented by Bond and Thompson¹³⁸ in their review on gold catalysed oxidation of carbon monoxide.

Fourier transform infrared method (FTIR) has identified several different kinds of gold species on chemisorbed carbon monoxide.^{139, 140} The gold species found include Au^0 , in high or low coordination, “positively polarized” (Au^{x+}) gold atoms at the periphery, and gold species on which both carbon monoxide and oxygen atoms are adsorbed.¹³⁹⁻¹⁴²

Small supported gold nanoparticles less than 5 nm showed high catalytic activities with the highest rate being shown at sizes of about 2 – 3 nm.¹⁴³ It has been suggested that decreasing gold particle size, which causes the increase in activity of gold catalysts is connected to the higher concentration of low coordinated gold atoms

at corner or edge positions in smallest nanoparticles.¹⁴⁴ Recent experiments showed that bilayer particles have greater activity than either thinner layer particles or larger multilayer particles.^{145, 146} Bond and Thompson¹⁴⁴ discussed that CO molecules are assumed to adsorb with sufficient stability on low coordinated atoms. In large multilayer particles, the low coordinated atoms are too distant from the first layer atoms to be useful.

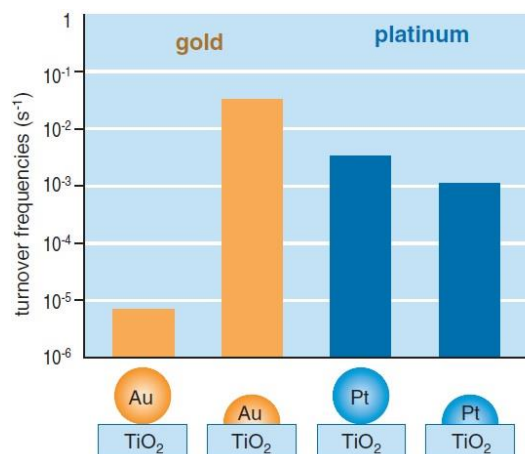


Figure 1.13 Turnover frequencies for CO oxidation over spherical and hemispherical particles of Au and Pt supported on TiO₂.¹¹⁹

It is also important to take note of the precise nature of the interaction between the metal nanoparticle and the oxide support. The contact of gold nanoparticles with the support can be controlled by the method of preparation as discussed by Haruta.¹¹⁹ In 1983, Haruta *et al.* found that once Au is deposited as hemispherical nanoparticles on selected metal oxides, it exhibits surprisingly high catalytic activity for CO oxidation, even at 200 K.^{147, 148} Bamwenda *et al.*¹⁴⁹ have shown that the TOF of CO oxidation at 300 K over Au/TiO₂ is ten times larger than the Pt/TiO₂ catalysts. The activity of CO oxidation on Au/TiO₂ is strongly dependent on the preparation method such as deposition-precipitation, photocatalytic deposition, and impregnation methods.¹⁴⁹ Hemispherical metal nanoparticles were produced using the deposition-precipitation. The flat planes of the nanoparticle are strongly attached to the TiO₂ support. On the other hand, much larger spherical particles were produced using impregnation methods. They observed that the TOF of Pt catalysts did not show any significant difference between the different preparation methods. This is due to the reaction of CO with O₂ can take place on the Pt surfaces and the metal oxide support is not directly involved in the reaction. However, the TOF of Au/TiO₂ clearly depends on the contact structure changing by four orders of magnitude.

1.4 Computational approach to modelling α -Fe₂O₃, and CeO₂

Our aim is to apply suitable computational methods for modelling the catalytic systems (CeO₂ and metal supported on α -Fe₂O₃). From the literature, we can find that various methods were used to model these systems. These references are discussed in two different sub-sections showing the methods used to tackle the strongly correlated *d*- and *f*-electrons of iron and cerium cations, respectively. Solids with incompletely filled *d*- or *f*-electron shells with narrow energy bands, which are not well described using classical DFT are usually termed as strongly correlated materials. The electrons are strongly localised (narrow bands) on the metal centres and so the electron-electron correlation becomes more important than in systems with delocalised electron states, i.e. broad bands.

1.4.1 Strongly correlated *d*-electrons and spin frustration of Fe³⁺ centres in α -Fe₂O₃

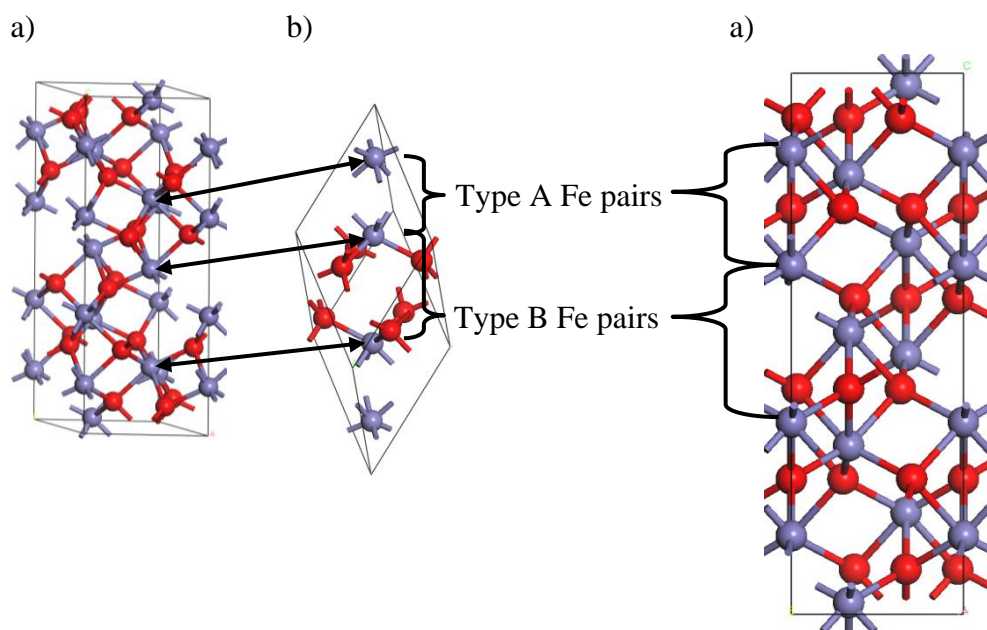


Figure 1.14 a) Hexagonal unit cell and the b) rhombohedral primitive cell of α -Fe₂O₃. Violet (iron) and red (oxygen).

The rhombohedral corundum type α -Fe₂O₃ (Figure 1.14 b) is most common on earth among the iron oxides. Spectroscopic experiments characterised the antiferromagnetic insulator, α -Fe₂O₃, as a charge transfer (CT) insulator.¹⁵⁰ The Fe *d* electrons in Fe₂O₃ are strongly correlated. DFT is known to have failed to correctly describe such strongly correlated material, so methods beyond ordinary DFT is essential to correctly describe such systems.

Catti *et al.*¹⁵¹ has studied the rhombohedral α -Fe₂O₃ using the *ab initio* periodic unrestricted Hartree-Fock (HF) approach. The energy difference between the antiferromagnetic and ferromagnetic configurations was overestimated by the use of pseudopotential to represent the Fe atoms. They have also found that the inclusion of correction for correlation energy enhances the stability of the antiferromagnetic structure significantly, with respect to Hartree-Fock results alone. The computed total spin magnetic moment is 4.74 μ_B , which agrees well with the experimental result¹⁵² of 4.90 μ_B .

Sandratskii *et al.*¹⁵³ studied α -Fe₂O₃ using local spin-density approximation (LSDA) applying the augmented spherical wave (ASW) method. They have reported that the lowest energy structure is obtained from the (+ + - -) (+/- indicates opposite Fe spin states) configuration (following the sequence of Fe atoms from top to bottom in Figure 1.14 b). Other two antiferromagnetic, (+ - + -) and (+ - - +), were separated in energy by about 0.20 eV per Fe atom with respect to the lowest energy structure. The ferromagnetic configuration is about 0.49 eV higher than the lowest energy structure. The computed total spin magnetic moment reported for the lowest energy system is 3.72 μ_B , which is smaller than the experimental value of 4.90 μ_B . The LSDA approach underestimates the band gap (0.75 eV) when compared to the optical gap of about 2.0 eV.¹⁵⁴

In another published work by Punkkinen *et al.*¹⁵⁵, the energy gap and spin magnetic moment were calculated to be 0.51 eV and 3.43 μ_B using LSDA, respectively. They have also performed calculations with the inclusion of the on-site Coulomb interaction correction, U (2.0 eV). The energy gap and spin magnetic moment obtained using this approach (LSDA+U) are 1.42 eV and 3.84 μ_B , respectively. A higher value of U (3.5 eV) was found to produce an energy gap ($E_{\text{gap}} = 2.04$ eV) which is very close to the experimental value¹⁵⁴ ($E_{\text{gap}} = 2.0$ eV). The spin magnetic moment was calculated to be 4.01 μ_B . However, they observed that the Fe 3d states were shifted strongly to the bottom of the valence band, which does not agree well with the spectroscopy data.^{150, 156} Punkkinen *et al.* showed in their work that correlation effects beyond the LSDA are important in hematite due to the localised nature of the 3d states.¹⁵⁵

Rollmann *et al.*¹⁵⁷ have performed calculations on a hexagonal unit cell of hematite under rhombohedral symmetry constraints using DFT and DFT+U

approaches by applying the PW91 functional. The antiferromagnetic (+ + - -) state is found to be the lowest energy configuration from a PW91 calculation. They have identified two types of pairs of Fe atoms, which are:

- 1) short Fe-Fe distance (type A) and
- 2) long Fe-Fe distance (type B) along the hexagonal axis.

In the lowest energy configuration, the type A pairs of Fe atoms have opposite magnetic moments, while the type B pairs have equal magnetic moments. The magnetic moments obtained are $3.44 \mu_B$, $3.38 \mu_B$, $3.45 \mu_B$, and $2.60 \mu_B$ for the magnetic states (+ + - -), (+ - + -), (+ - - +), and (+ + + +), respectively. The difference in energy, with respect to the lowest energy configuration, between the antiferromagnetic states are $0.21 \text{ eV}/(\text{Fe atom})$ and $0.22 \text{ eV}/(\text{Fe atom})$ for (+ - + -) and (+ - - +), respectively. The ferromagnetic solution is $0.39 \text{ eV}/(\text{Fe atom})$ higher than that of the lowest energy antiferromagnetic configuration. They have also reported that the energy gap and magnetic moments are found to increase (improve) with increasing U values. They have considered that $U = 4 \text{ eV}$ is the value for which best overall agreement (band gap, magnetic moment, structural properties, electronic properties) is achieved. When $U = 4.0 \text{ eV}$, a charge transfer type O $2p - \text{Fe } 3d$ gap of nearly 2.0 eV is produced, which is in agreement with the experiment¹⁵⁴ ($E_{\text{gap}} = 2.0 \text{ eV}$).

In another work by Rohrbach *et al.*¹⁵⁸, the group has obtained the gap energy (2.0 eV) and magnetic moment ($4.11 \mu_B$) for $\alpha\text{-Fe}_2\text{O}_3$ using PW91+ U ($U = 4.0 \text{ eV}$). They have studied the (0001) surface of $\alpha\text{-Fe}_2\text{O}_3$ with the Fe terminated surface, where half of the Fe atoms from the surface layer are eliminated. They have ensure that the Fe atoms in between the O_3 layers have the same spin by setting the magnetic ordering of Fe cations to $++\text{O}_3- -\text{O}_3++$. This same magnetic ordering is confirmed by Howard and Willock¹⁵⁹ to be lower in energy than the alternative ordering with the Fe atoms between layers having opposite spins, $+-\text{O}_3-+\text{O}_3+-$. They have also showed that the $++\text{O}_3- -\text{O}_3++$ arrangement gives good agreement with the available experimental cell volume, bulk modulus, and magnetic moment.^{154, 160}

1.4.2 Tackling the strongly correlated f -electrons of cerium in CeO_2

Similar to the Fe d electrons in $\alpha\text{-Fe}_2\text{O}_3$, the Ce f electrons in CeO_2 are strongly correlated. References in the literature^{75, 76} have demonstrated that experimental

techniques such as STM and AFM can be complemented with quantum mechanical calculations to provide explanation for arrangement of atoms and electronic properties of the surface. Throughout the years, the main challenge in theoretical and computational study of ceria is to accurately describe the electronic structure. Stoichiometric ceria is an insulator with an unoccupied Ce 4*f* band. When the material is reduced, this Ce 4*f* band becomes partially occupied and splits with localised electrons corresponding to the Ce³⁺ ions in a narrow filled band. These spatially localised Ce 4*f* filled states mean that ceria remains an insulator on reduction.

In the literature, various computational methods have been applied to attempt to reproduce this behaviour for bulk CeO₂ and its surfaces. In one of the earliest studies, Hill and Catlow¹⁶¹ used periodic HF calculations on bulk CeO₂ with a small basis set. They obtained a lattice parameter of 5.385 Å which is smaller than the experimental value³² of 5.411 Å. HF was also found to greatly overestimate the bulk modulus of the material giving 357 GPa compared to the experimental values ranging from 204 to 236 GPa.^{31, 32, 34, 35} Later on, the method was improved with the addition of a post-optimisation electron correlation correction bringing both the lattice parameter (5.419 Å) and bulk modulus (254 GPa) into closer agreement with experiment.¹⁶² However, both approaches overestimate the O 2*p* – Ce 5*d* band gap compared to experiment¹⁶³ (~6 eV) as expected for the HF approximation. An earlier work¹⁶¹ predicted a gap about 16 eV and 14 eV for the post-optimisation electrons correlation corrected calculation.¹⁶²

Since DFT is known to be unable to accurately describe strongly correlated systems, different approaches such as hybrid methods and the inclusion of on-site Coulomb interactions correction term, U, to DFT calculations (DFT+U) has been widely applied in theoretical studies of the bulk,^{51, 64, 164-168} surface of CeO₂,^{64, 165, 169-171} and some oxidation and reduction reactions on CeO₂ surface.¹⁷²⁻¹⁷⁵ Hybrid methods reduce the improper self-interaction by introducing a percentage of non-local HF exchange in the exchange-correlation functionals (details are discussed in Chapter 2). Reported literature¹⁷⁶⁻¹⁷⁸ show that the hybrid DFT calculations produce structural properties which agree with experimental values (**Table 1.4**). Proper description of the Ce 4*f* states are also accounted for but due to HF contribution, the O 2*p* – Ce 5*d* band gap is overestimated with reference to the experimental value of about 6 eV.¹⁶³ However, hybrid methods are still computationally expensive when it

comes to applying it to bigger systems or systems consisting of heavy atoms in solid state calculations.

Table 1.4 Experimental and theoretical calculated lattice parameter, O $2p$ – Ce $4f$, and O $2p$ – Ce $5d$ band gaps for CeO₂.

Methods	$a_0 / \text{Å}$	Band gaps / eV	
		O $2p$ – Ce $4f$	O $2p$ – Ce $5d$
Experimental			
- X-ray diffraction	5.411 ^a ,	-	-
- XPS & BIS spectra ^c	5.406 ^b	3.0	6.0
- Optical reflectivity measurements ^d	-	3.2	~6.0
Theoretical calculations		~4.5	7.93
- PBE0 (PAW) ^e	5.39	2.95 ^f , 4.30 ^g	8.45 ^f , 8.52 ^g
- PBE0 (basis set)	5.423 ^f , 5.40 ^g	2.39 ^f , 3.70 ^g	8.06 ^f , 8.16 ^g
- B3LYP (basis set)	5.503 ^f , 5.47 ^g	7.50	10.64
- HH ^g	5.34	7.18	10.75
- HHLYP ^g	5.42	3.18	7.48
- B1-WC ^g	5.38		

a Ref. ^{31,32}; *b* Ref. ³⁴; *c* Ref. ¹⁶³; *d* Ref. ¹⁷⁹; *e* Ref. ¹⁷⁸; *f* Ref. ¹⁷⁶; *g* Ref. ¹⁷⁷

The DFT+U approach has produced promising results such as good structural properties and accurate electronic band structure of bulk ceria. Nevertheless, the use of a proper U_{eff} value ($U_{eff} = U - J$, detailed explanation in Chapter 2) is subjective as it is parameterised to a specific property under study, which has also been suggested by Castleton *et al.*¹⁸⁰ Loschen *et al.*¹⁶⁶ showed that the U_{eff} values used modestly affects the structural properties, as well as the O $2p$ – Ce $4f$ and O $2p$ – Ce $5d$ band gaps for bulk CeO₂. Thus, they suggested that appropriate U_{eff} values from their self-consistent calculations are around 7.5 – 9.5 eV for LDA+U calculations and 3.5 – 5.0 eV for GGA+U calculations. Recently, studies have been performed on the effects of adding U term to oxygen $2p$ electrons.¹⁶⁷ Plata *et al.*¹⁶⁷ showed that by systematically increasing U_{eff} for oxygen $2p$ orbital ($U_{eff,p}$) with a given U value for Ce $4f$ decreases the lattice parameter and increases the band gap of CeO₂. This is the result that one would like to achieve since the inclusion of U_{eff} for Ce $4f$ orbitals alone produced a larger lattice parameter and still slightly smaller band gap when compared to experimental.^{166, 181} They have concluded that the combination pair of U_{eff} (5+5) and (5+6) applied to p and f orbitals, respectively produced reasonable CeO₂ formation energy and reduction energy in close agreement to experimental values.¹⁶⁷

When an oxygen defect is created in the CeO₂ lattice, there are two electrons to be accommodated. One of the investigations regarding the defective CeO₂ structure is the localisation site of the two excess electrons. In 2005, Fabris *et al.*¹⁶⁹ have reported that the excess electrons are always localised on two Ce atoms neighbouring the oxygen vacancy. They also reported that the sub-surface oxygen defect is more stable compared to surface oxygen defect when LDA+U method was applied, but GGA+U gave the opposite results. Few years after, Li *et al.*⁸¹ and Ganduglia-Pirovano *et al.*⁸² reported different results. Ganduglia-Pirovano investigated a $p(2\times 2)$ (111) surface unit and reported that the sub-surface oxygen defect is a more stable system using PBE+U, LDA+U, and HSE06. Excess electrons tend to localise on the next nearest neighbours of the sub-surface oxygen vacancy site. Li studied a bigger surface, $p(3\times 4)$, and showed that the excess electrons localised on the next nearest neighbours from the vacancy site for both sub-surface and surface defects. The sub-surface oxygen defect was reported to be more stable compared to surface oxygen defect system.⁸¹ In another work, Li *et al.*¹⁸² reported the oxygen diffusion mechanisms on the (111) surface of CeO₂. They have shown that a two-step exchange mechanism involves first the diffusion of sub-surface oxygen to the top surface vacancy site ($E_a = 0.44$ eV) and then the sub-surface vacancy created is filled with the nearest top surface oxygen ($E_a = 0.61$ eV). While the hopping mechanism, which involves the movement of oxygen across the surface from the nearest top surface oxygen to the vacancy site, resulted into a higher diffusion barrier ($E_a = 1.60$ eV). They have clearly explained that the high barrier from the hopping mechanism is caused by the breaking of two Ce–O bonds instead of one as in the exchange mechanism.

Li *et al.*¹⁸³ studied the growth behaviour of Pd and Rh particles on the CeO₂ (111) surface using DFT+U method. They showed that Pd and Rh 3D particles are energetically preferred compared to isolated atoms and 2D islands on the CeO₂ (111) surface due to strong cohesive energy. They have also performed molecular dynamics (MD) simulations in order to explain the growth behaviour of Rh particles on the surface. Rh agglomeration is inhibited by the strong Rh–O interactions under oxidative conditions. However, under reductive conditions, the cleavage in Rh–CeO₂ bonding is facilitated and caused the agglomeration of metallic Rh.

In another work, Scanlon *et al.*¹⁶⁸ investigated the origin of enhanced oxygen storage capacity (OSC) of Pd/Pt-doped CeO₂ using DFT+U ($U_{eff} = 5$ eV). They

showed that the increased OSC is due to the large displacement of the dopant ions from the Ce lattice sites. The Pd(II)/Pt(II) (in a d^8 configuration) adopt a square planar coordination with four neighbouring oxygen atoms due to crystal field effects. The source in increased OSC is due to availability of three-coordinated oxygen atoms, which can be easily removed.

Marrochelli *et al.*^{184, 185} reported, that the factors responsible for defect-induced chemical expansion observed in CeO_{2-x} using DFT+U and potential based MD simulations studies are the result of two competing processes:

- 1) the formation of a vacancy which leads to a lattice contraction primarily due to electrostatic interactions; and
- 2) the cation radius changes which leads to a lattice expansion primarily due to steric effects.

The chemical expansion coefficient, α_C , that they stated is modelled as the summation of two terms that are proportional to the cation, α_M , and oxygen, α_V , radius change.

$$\alpha_C = \alpha_M + \alpha_V \quad (1.10)$$

Henkelman and co-workers presented a number of studies related to CO oxidation at the interface between CeO_2 surfaces and supported Au nanoparticles. All were studied using DFT+U method. In one of their reports, they have shown that the doping of CeO_2 support opens the CO oxidation pathway by the Mars-van Krevelen mechanism.¹⁸⁶ The dopants are found to also significantly lower the vacancy formation energy of the CeO_2 support and the electron donation from the supported Au_{13} nanoparticle shifts the vacancy formation energy of doped CeO_2 .¹⁸⁶

1.5 Project goals

In this research project, the main goal is to study the effects of PGM dopants on catalytic activity of CeO₂ support. As discussed in previous sections, the ceria lattice is likely to be stable against degradation due to repeated reduction/oxidation cycles used in catalysis. Thus, it is also crucial to understand the ease of oxygen vacancy formation in the bulk and surfaces of CeO₂ with or without the presence of PGM dopant metals. This will lead to the understanding of oxygen storage capacity in CeO₂.

The first step is to describe the electronic structure of both the stoichiometric and defective structure of ceria. This can be done by using DFT+U or hybrid functional methods. These methods are proven to yield results in agreement to experimental data as discussed in earlier sections.

Oxygen vacancy formation energies determine the ease of oxygen extraction from the bulk and surface structures of CeO₂. There is much uncertainty on which cerium sites will the excess electron left by the extracted oxygen be localised on. Literature has reported that the excess electrons will localised on two next nearest neighbours cerium which reduced it to Ce³⁺. Our work will study the various pairs of cerium sites for excess electron localisation by generating a series of permutations.

The migration barrier of an oxygen vacancy across the bulk structure provides insight into the ease of oxygen diffusion. One of the challenges consists of determining whether the defect site or the electron migrate first. The activation energy for the migration of the defect site is proportional to the oxygen vacancy concentration. Plata *et al.* have shown that the electron transfer process in a stoichiometric bulk CeO₂ is mainly adiabatic, with an adiabatic barrier for polaron hopping of 0.40 eV (39 kJ/mol). A mixture of initial and final states with different Ce³⁺ sites will be used for the evaluation of oxygen defect migration activation energy. The aim of obtaining these activation energies is to show the ease with which the oxygen used at the surface can be replenished by transport of anions from the sub-surface or bulk.

It is also discussed that oxygen vacancy formation is easier on the surfaces of CeO₂ compared to bulk. The ease of the formation of oxygen vacancy on the surface will determine the catalytic activity on the system. PGM dopants have shown to increase the catalytic activity on CeO₂ systems and promote the reduction of ceria.

Thus, a hypothesis can be drawn that the oxygen vacancy formation will be easier on PGM doped ceria and result in the increased activity of CO oxidation reactions. Models of PGM doped CeO₂ surface will be built and investigated using DFT+U method to confirm the proposed hypothesis.

The same type of study was applied to Au₁₀ supported on α -Fe₂O₃ system. Literature reports have shown that CO oxidation activities are higher on supported Au catalysts. The effect of Au₁₀ nanoparticle on the formation of oxygen vacancy will be investigated. These results will show to determine a CO oxidation reaction mechanism.

Chapter 2

Theory and methods

In this chapter, I will present the theory and methods that have formed the basis for this thesis. Density functional theory (DFT) was used in all calculations presented in this thesis. The theory for each approach will be presented at the front of each section, followed by practical examples which we have performed as applications of the theory. The origins of DFT have been discussed thoroughly in a selection of computational chemistry textbooks¹⁸⁷⁻¹⁸⁹ and the book “*Introduction of Nanoscience*”¹⁹⁰.

2.1 Schrödinger Equation

The many body Schrödinger equation is used to determine the properties of atoms and molecules of a chemical system. The Hamiltonian operator, \hat{H} , corresponds to the total energy of a system, which is the sum of operators corresponding to the kinetic (T) and potential (V) energies of the system.

$$\hat{H}\Psi = (\hat{T} + \hat{V})\Psi = E\Psi \quad (2.1)$$

Ψ is the wave function of the system. The kinetic energy operator can be written as:

$$\hat{T} = \frac{\left(-i\hbar\left(\frac{\partial}{\partial x}\right)\right)^2}{2m} \quad (2.2)$$

$$\hat{T} = -\frac{\hbar^2}{2m}\left(\frac{\partial^2}{\partial x^2}\right) \quad (2.3)$$

The physical constant, \hbar , is Planck’s constant over 2π . Mass of an electron is written as m . The potential energy operator is written as:

$$\hat{V} = V(x) \quad (2.4)$$

Thus,

$$\hat{H} = \hat{T} + \hat{V} = -\frac{\hbar^2}{2m}\left(\frac{\partial^2}{\partial x^2}\right) + V(x) \quad (2.5)$$

In three dimensions, equation is written as:

$$\hat{H} = -\frac{\hbar^2}{2m}\nabla_{\mathbf{r}}^2 + V(\mathbf{r}) \quad (2.6)$$

Where

$$\nabla_{\mathbf{r}}^2 = \frac{\partial^2}{\partial x^2} + \frac{\partial^2}{\partial y^2} + \frac{\partial^2}{\partial z^2} \quad (2.7)$$

The potential energy of a charged system is

$$V(\mathbf{r}) = \sum_{i>j} \frac{Z_i Z_j e^2}{4\pi\epsilon_0} \left(\frac{1}{|\mathbf{r}_i - \mathbf{r}_j|} \right) \quad (2.8)$$

In a molecular system, the kinetic energy can be separated into summations over electrons and over nuclei. Similarly with the potential energy, it can be separated to terms representing the interactions between nuclei, between electrons, and between electrons and nuclei. The Hamiltonian operator for a molecular system is written as

$$\begin{aligned} \hat{H} = & \sum_A \frac{1}{2M_A} \nabla_A^2 + \sum_i \frac{1}{2} \nabla_i^2 + \sum_{A>B} \frac{Z_A Z_B}{|\mathbf{r}_A - \mathbf{r}_B|} - \sum_{A>B} \frac{Z_A}{|\mathbf{r}_A - \mathbf{r}_i|} \\ & + \sum_{i>j} \frac{1}{|\mathbf{r}_i - \mathbf{r}_j|} \end{aligned} \quad (2.9)$$

2.2 Density Functional Theory

Density functional theory (DFT) is based on the total electronic density distribution of a system rather than the wave function Ψ and its corresponding Schrödinger equation. This approach is computationally less expensive which made it the most promising approach to compute the electronic structure of matter. It has been widely applied in computational chemistry as it includes both electronic exchange and correlation. However, due to the ‘local’ approximation, its standard forms do not contain long range correlation such as van der Waals. DFT is not perfect as it also encounters multi-reference and self-interaction problems. These are all due to the deficiencies of the approximate exchange correlation functionals used. Functionals such as the local density approximation (LDA) are less reliable in prediction of hydrogen bondings when compared to generalised gradient approximations (GGA).¹⁹¹ However, with the advent of the GGA functionals, DFT became useful as a pragmatic, alternative to wavefunction based methods.

2.2.1 The Hohenberg-Kohn theorems

In 1927, Thomas and Fermi suggested a method to describe the distribution of the electrons in an atom.^{192, 193} They attempted to calculate the total energy of an atom with a nucleus of charge Z using:

$$E^{TF}\{\rho(\mathbf{r})\} = 2.871 \int \rho^{\frac{5}{3}}(\mathbf{r}) d\mathbf{r} - \sum_i Z_i \int \frac{\rho(\mathbf{r})}{|\mathbf{r} - \mathbf{R}_i|} d\mathbf{r} + \frac{1}{2} \iint \frac{\rho(\mathbf{r})\rho(\mathbf{r}')}{|\mathbf{r} - \mathbf{r}'|} d\mathbf{r}d\mathbf{r}' \quad (2.10)$$

where the first term is the kinetic energy while the second and third terms are the electron-nucleus and the electron-electron potential energies, respectively. However, there are flaws in this approach, such as the errors for the atomic total energies are relatively large especially for light atoms, and the inability to describe molecular bonding.

DFT is essentially based on the Hohenberg-Kohn theorems.¹⁹⁴

- 1) The ground state electron density can completely determine all properties of any system of interacting particles in an external potential $V_{\text{ext}}(\mathbf{r})$.
- 2) That there exists a universal functional of the density, $F^{HK}[\rho(\mathbf{r})]$, and the exact ground state density and energy of the system is the global minimum value of the total energy functional $E^{HK}[\rho(\mathbf{r})]$.

The total energy functional is the addition of the interaction of electrons with an external potential, $V_{\text{ext}}(\mathbf{r})$, and $F^{HK}[\rho(\mathbf{r})]$, which is the sum of the electron's kinetic energy and inter-electronic interactions.

$$E^{HK}[\rho(\mathbf{r})] = \int V_{\text{ext}}(\mathbf{r})\rho(\mathbf{r})d\mathbf{r} + F^{HK}[\rho(\mathbf{r})] \quad (2.11)$$

$$F^{HK}[\rho(\mathbf{r})] = T[\rho(\mathbf{r})] + E_{\text{int}}[\rho(\mathbf{r})] \quad (2.12)$$

The inter-electronic interaction term contains the contributions of a Coulomb part, $J[\rho(\mathbf{r})]$, and a term containing all the non-classical contributions to the electron-electron interaction, $E_{\text{ncl}}[\rho(\mathbf{r})]$.

$$E_{\text{int}}[\rho(\mathbf{r})] = J[\rho(\mathbf{r})] + E_{\text{ncl}}[\rho(\mathbf{r})] \quad (2.13)$$

The expressions for $T[\rho(\mathbf{r})]$ and $E_{\text{ncl}}[\rho(\mathbf{r})]$ are the major challenge of this ‘‘orbital-free’’ DFT approach. This is due to $T[\rho(\mathbf{r})]$ being a functional of the density, which causes it to yield a poor representation of the kinetic energy.[ref]

2.2.2 Kohn-Sham Self-consistent Equations

In order to solve the problem caused by the way the kinetic energy is described, Kohn and Sham¹⁹⁵ have proposed the idea of a fictitious system built from a set of orbitals where the electrons are non-interacting. The kinetic energy part is treated as accurately as possible by using orbitals and the exchange-correlation part is treated through approximation. The functional of the total energy is then written as:

$$E[\rho(\mathbf{r})] = T_s[\rho(\mathbf{r})] + \int V_{ext}(\mathbf{r})\rho(\mathbf{r})d\mathbf{r} + J[\rho(\mathbf{r})] + E_{XC}[\rho(\mathbf{r})] \quad (2.14)$$

and can be written in simplified form as:

$$E_{DFT}[\rho] = T_s[\rho] + E_{ne}[\rho] + J[\rho] + E_{XC}[\rho] \quad (2.15)$$

In equation (2.14), $T_s[\rho(\mathbf{r})]$ is the kinetic energy functional for non-interacting electrons. This term can be expressed in terms of one electron integrals:

$$T_s[\rho(\mathbf{r})] = -\frac{1}{2} \sum_{i=1}^N \langle \varphi_i | \nabla^2 | \varphi_i \rangle \quad (2.16)$$

Second term in equation (2.14) represents the electron-nucleus electrostatic energies, and V_{ext} is the potential arising from the nuclei:

$$V_{ext} = \sum_A \frac{Z_A}{|R_A - r|} \quad (2.17)$$

The term $J[\rho(\mathbf{r})]$ is the classical Coulomb interaction energy of the electron density $\rho(\mathbf{r})$ interacting with itself and is given by:

$$\hat{J}[\rho(\mathbf{r})] = \frac{1}{2} \int \frac{\rho(\mathbf{r})\rho(\mathbf{r}')}{|\mathbf{r} - \mathbf{r}'|} d\mathbf{r}d\mathbf{r}' \quad (2.18)$$

\mathbf{r} and \mathbf{r}' represent the coordinates of the 2 electrons.

E_{XC} consists of two parts, a pure exchange, E_X , and a correlation part, E_C . which can be expressed as:

$$E_{XC}[\rho(\mathbf{r})] = E_X[\rho(\mathbf{r})] + E_C[\rho(\mathbf{r})] \quad (2.19)$$

However, the actual form of E_{XC} is unknown. Thus, approximate functionals based upon the electron spin density $\rho_\alpha(\mathbf{r})$ and $\rho_\beta(\mathbf{r})$ have to be introduced to describe this term. The approximate functionals employed by current DFT methods are based on these Kohn-Sham self-consistent equations.

2.2.3 Generalised Gradient Approximation

One of the approximations to the exchange correlation energy, E_{XC} , functional is the local density approximation (LDA) or local spin density approximation (when α and β densities are not equal). However, this will not be discussed thoroughly as our work is based more on the generalised gradient approximation (GGA) functionals. LSDA describes the exchange correlation energy with an integral over all space with the exchange correlation energy density at each point, \mathbf{r} , assumed to be uniform in a homogenous electron gas with that density.

$$E_{XC}^{LSD}[\rho_\alpha(\mathbf{r}), \rho_\beta(\mathbf{r})] = \int \rho(\mathbf{r}) \varepsilon_{XC}(\rho_\alpha(\mathbf{r}), \rho_\beta(\mathbf{r})) d\mathbf{r} \quad (2.20)$$

The LSDA ignores corrections to the exchange correlation energy due to inhomogeneity in the electron density at \mathbf{r} . It has met with impressive practical success, although it underbinds the core electrons in an atom and overbinds the atoms in a molecule or solid.

In GGA, the non-uniform electron gas is considered with the inclusion of the magnitude of the gradient of the density, $|\nabla\rho|$, as well as the density itself at each point. The typical form for the GGA exchange correlation functional can be written as:

$$E_{XC}^{GGA}[\rho_\alpha(\mathbf{r}), \rho_\beta(\mathbf{r})] = \int \rho(\mathbf{r}) \varepsilon_{XC}[\rho_\alpha(\mathbf{r}), \rho_\beta(\mathbf{r}), \nabla\rho_\alpha(\mathbf{r}), \nabla\rho_\beta(\mathbf{r})] d\mathbf{r} \quad (2.21)$$

Examples of the available GGA density functionals used in our work here are PW91¹⁹⁶⁻¹⁹⁸ and PBE^{199, 200}.

In 1991, Perdew and Wang (PW91) presented a unified real-space-cutoff construction of a GGA for exchange and correlation.¹⁹⁶⁻¹⁹⁸ PW91 is purely *ab initio* and fulfils almost all scaling relations except high density limit of uniform scaling. The exact exchange energy of this functional is defined by:

$$E_X^{GGA}[\rho_\alpha(\mathbf{r}), \rho_\beta(\mathbf{r})] = \frac{1}{2} (E_X[\rho_\alpha(\mathbf{r})] + E_X[\rho_\beta(\mathbf{r})]) \quad (2.22)$$

where

$$E_X^{PW91}[\rho(\mathbf{r})] = \int \rho(\mathbf{r}) \varepsilon_X(\mathbf{r}_s, 0) F(s) d\mathbf{r} , \quad (2.23)$$

$$\varepsilon_X(\mathbf{r}_s, 0) = -\frac{3k_F}{4\pi} \quad (2.24)$$

with the local Fermi wave vector, $k_F = (3\pi^2 n)^{1/3} = 1.91916/r_s$ and the scaled density gradient, $s = |\nabla\rho(\mathbf{r})|/2k_F\rho(\mathbf{r})$. The function $F(s)$ is:

$$F(s) = \frac{1 + 0.19645s \sinh^{-1}(7.7956s) + (0.2743 - 0.1508e^{-100s^2})s^2}{1 + 0.19645s \sinh^{-1}(7.7956s) + 0.004s^4} \quad (2.25)$$

The correlation energy is

$$E_C^{PW91}[\rho_\alpha(\mathbf{r}), \rho_\beta(\mathbf{r})] = \int \rho[\varepsilon(\mathbf{r}_s, \zeta) + H(t, \mathbf{r}_s, \zeta)]d\mathbf{r} \quad (2.26)$$

where $t = |\nabla\rho(\mathbf{r})|/2\phi k_{s\rho}(\mathbf{r})$ is another scaled density gradient, with $\phi = [(1+\zeta)^{2/3} + (1-\zeta)^{2/3}]/2$ as the spin scaling factor. The local screening wave vector is $k_s = (4k_F/\pi)^{1/2}$.

The difference between PW91 and the functional developed by Perdew, Burke, and Ernzerhof (PBE) is minor since it is constructed based on the PW91 functional^{199, 200}. The changes made include an accurate description of the linear response of the uniform electron gas, correct behaviour under uniform scaling, and a smoother potential.^{199, 200} The exchange energy is defined by:

$$E_X^{PBE}[\rho(\mathbf{r})] = \int \rho(\mathbf{r})\varepsilon_X(\rho(\mathbf{r}))F_X(s)d\mathbf{r} , \quad (2.27)$$

$$\varepsilon_X = -\frac{3e^2 k_F}{4\pi} \quad (2.28)$$

where $s = |\nabla\rho(\mathbf{r})|/2k_F\rho(\mathbf{r})$, $F_X(s) = 1 + \kappa - \kappa/(1 + \mu s^2/\kappa)$, with $\kappa = 0.804$ and $\mu = 0.21951$.

Under uniform scaling to high density limit,

$$E_C^{PBE}[\rho_\alpha(\mathbf{r}), \rho_\beta(\mathbf{r})] = -\frac{e^2}{a_0} \int n\gamma\phi^3 \times \ln \left[1 + \frac{1}{\frac{\chi s^2}{\phi^2} + \left(\frac{\chi s^2}{\phi^2}\right)^2} \right] d\mathbf{r} \quad (2.29)$$

where the factor e^2/a_0 , with the Bohr radius $a_0 = \hbar^2/me^2$, is unity in atomic units. The spin scaling factor, $\phi = [(1+\zeta)^{2/3} + (1-\zeta)^{2/3}]/2$, $\chi \approx 0.72161$, and $\gamma = 0.025$.

2.2.4 Hubbard model and on-site corrected DFT (GGA+U)

Improvements are still being made in developing functionals for exchange and correlation. However, there are still no functionals which are able to describe the strongly correlated systems such transition metal oxides and rare earth elements and compounds with localised and strongly interacting d and f electrons. A method that involves LDA- or GGA-type calculation with the inclusion of an on-site Coulomb

interaction (hereby will be refer as LDA+U and GGA+U, respectively) based on the Hubbard model is able to address this problem. Through this added term, the localised orbitals are shifted in relative to the other orbitals, which attempts to correct errors known to be large in the usual LDA or GGA calculations. The U parameter is usually determined through fitting of known properties of the system or through self-consistent calculations.

We have applied the simplified (rotationally invariant) approach proposed by Dudarev *et al.*²⁰¹. The GGA+U takes the following form:

$$E_{GGA+U} = E_{GGA} + \frac{U-J}{2} \sum_{\sigma} \left[\left(\sum_i \rho_{ii}^{\sigma} \right) - \left(\sum_{i,j} \rho_{ij}^{\sigma} \rho_{ji}^{\sigma} \right) \right] \quad (2.30)$$

where U is a spherically averaged Hubbard parameter describing the energy increase for placing an extra electron on a particular site, J is a parameter representing the screened exchange and ρ_{ij}^{σ} is the on-site density matrix of the *d* or *f* electrons. In the Dudarev approach, the parameters U and J are not entered separately, only the difference ($U_{eff} = U - J$) is meaningful. A larger (U_{eff}) simply means a stronger observance of the on-site idempotency and is achieved by lowering the one-electron potential locally for a particular metal *d*- or *f*-orbital.

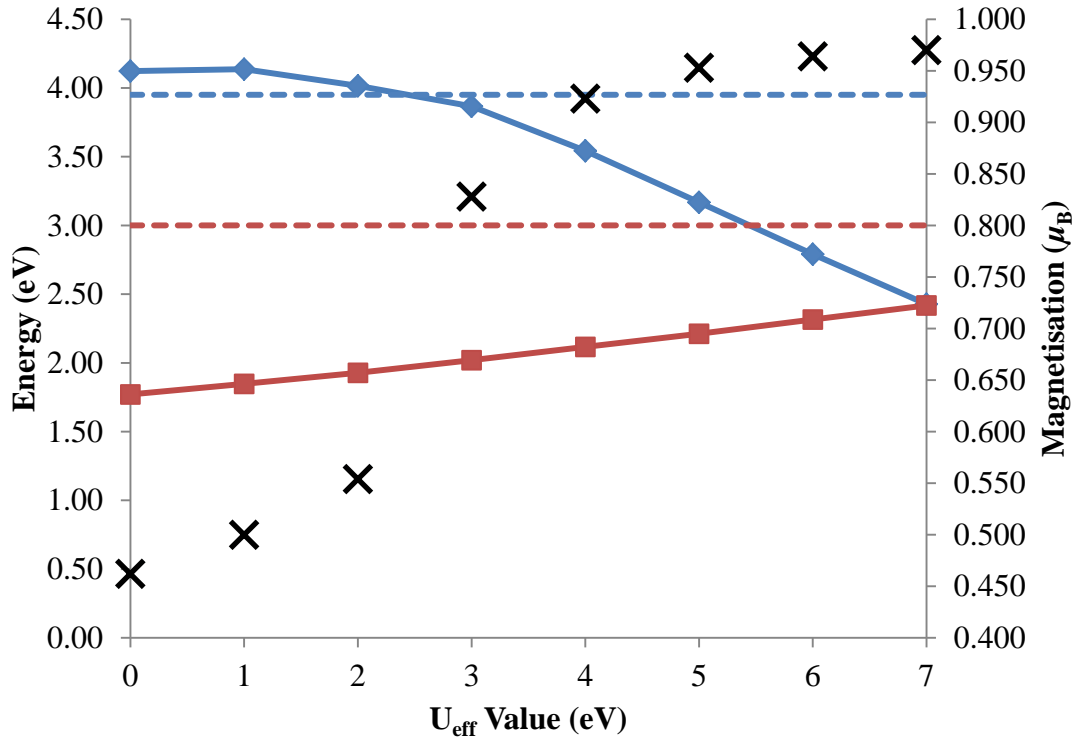


Figure 2.1 The O 2*p* – Ce 4*f* band gap values (filled red squares), oxygen vacancy formation energies (filled blue diamonds), and magnetisation of a reduced Ce atom

(black crosses) of a single unit cell CeO₂ bulk ($a_0 = 5.51 \text{ \AA}$) obtained from different U_{eff} values using PW91+U. Red and blue dashed lines are the experimental value^{163, 179} for O 2*p* – Ce 4*f* band gap ($\sim 3.00 \text{ eV}$) and oxygen vacancy formation energy obtained from heats of formation⁵⁵ ($E_{vac} = 3.99 \text{ eV}$).

For the case of Ce 4*f* orbital in CeO₂ systems, we have chosen $U_{eff} = 5.0 \text{ eV}$. We performed GGA+U calculations using PW91 functional on CeO₂ bulk structure with a series of U_{eff} values ranging from 0 – 7 eV. The change in band gap values, oxygen vacancy formation energies, and magnetisation of a reduced Ce ion (Ce³⁺) with different values of U_{eff} are shown in Figure 2.1. We can observe in Figure 2.1 that the $U_{eff} > 4 \text{ eV}$ is needed to properly describe the magnetisation of Ce³⁺ ions in a reduced CeO₂ bulk. At $U_{eff} = 5 \text{ eV}$, the Ce³⁺ ions have a magnetisation of $0.953 \mu_B$. The oxygen vacancy formation energy, E_{vac} , is found to decrease with increasing U_{eff} values and at $U_{eff} = 5 \text{ eV}$, the E_{vac} is 3.17 eV which is 0.82 eV lower than that obtained from the heats of formation⁵⁵. As for the O 2*p* – Ce 4*f* band gap, the gap increases with increasing U_{eff} values. At $U_{eff} = 5 \text{ eV}$, a band gap value of 2.21 eV is obtained which is about 0.79 eV smaller than the experimental value ($\sim 3.00 \text{ eV}$) observed by Wuilloud *et al.*¹⁶³ and Marabelli *et al.*¹⁷⁹. Our reason for choosing the mentioned U_{eff} value is that it is a compromise between the three properties that we have looked at and it has been used in a number of publications.^{82, 166, 170, 173, 186, 202, 203} Nolan *et al.* have shown that upon the creation of an oxygen vacancy, the two Ce ions are reduced from Ce⁴⁺ to Ce³⁺ with use of DFT+U ($U_{eff} = 5 \text{ eV}$).¹⁷⁰ Besides, the appearance of a gap state due to the Ce³⁺ cations in between the top of the valence band and the unoccupied 4*f* (Ce⁴⁺) states was also seen when DFT+U is applied. Loschen *et al.* showed the dependence of O 2*p* – Ce 4*f* and O 2*p* – Ce 5*d* band gaps on different U_{eff} values.¹⁶⁶ The O 2*p* – Ce 4*f* and O 2*p* – Ce 5*d* were observed to increase and decrease, respectively with increasing U_{eff} values.¹⁶⁶ Huang and Fabris found that CO adsorption energies were overestimated with $U_{eff} > 4 \text{ eV}$ but the energy for CO oxidation is effectively independent of the U parameter.¹⁷³

As for the Fe 3*d* orbitals in Fe₂O₃ systems, we have used $U_{eff} = 4.0 \text{ eV}$. This value has shown to give reasonable results regarding lattice, parameters, bulk moduli, density of states, band gap, and magnetic moment for the Fe₂O₃ system.^{158,}

159

2.2.5 Hybrid functionals

Usually the exchange contribution is significantly larger in absolute numbers than the corresponding correlation effects. A strategy has been adapted to use the Hartree-Fock exact exchange energy combined with the exchange and correlation density functionals.

$$E_{XC}^{hybrid} = \alpha(E_X^{HF} - E_X^{GGA}) + E_{XC}^{GGA} \quad (2.31)$$

The coefficient α determined by semi-empirical methods and E_X^{HF} is the Hartree Fock exchange.^{204, 205}

A number of hybrid functionals have been developed. We have used PBE0, HSE06, B3LYP, and B3PW. Here, we will briefly outline the definition of the exchange-correlation energy for each of the hybrid functionals mentioned. Becke has presented the parameterised form that is accurate for many molecules. In B3LYP, Becke's 3 parameter functional is combined with the non-local correlation LYP.²⁰⁶ In CRYSTAL09^{14, 15}, the B3LYP is based on the 'exact' form of the Vosko-Wilk-Nusair correlation potential (corresponds to a fit to the Ceperley-Alder data). In the original paper²⁰⁶ it is reported as functional V, which is used to extract the 'local' part of the LYP correlations potential. The E_{XC}^{B3LYP} can be written as:

$$E_{XC} = (1 - A)(E_X^{LDA} + B(E_X^{Becke}) + A(E_X^{HF}) + (1 - C)(E_C^{VWN}) + C(E_C^{LYP}) \quad (2.32)$$

The default values of A, B, and C used in CRYSTAL09 are 20, 0.9, and 0.81, which are the Fock exchange percentage, exchange weight of the non-local part of exchange, and weight of the non-local correlation, respectively.¹⁵ For the B3PW, the correlation part is replaced with the one from Perdew and Wang (PW91)^{196, 207, 208} and the whole exchange-correlation approximation can be written as:

$$E_{XC} = (1 - A)E_{XC}^{LSDA} + AE_X^{HF} + B\Delta E_X^{B88} + E_C^{LSDA} + C\Delta E_C^{PW91} \quad (2.33)$$

where the coefficients $a_0 = 0.2$, $a_X = 0.72$, and $a_C = 0.81$ based on fitting to heats of formation of small molecules.²⁰⁹

PBE0 hybrid functional is based on the PBE exchange-correlation functional and assumes the following for the exchange-correlation energy^{210, 211}:

$$E_{XC}^{PBE0} = \frac{1}{4}E_X^{HF} + \frac{3}{4}E_X^{PBE} + E_C^{PBE} \quad (2.34)$$

The HSE06 hybrid functional is based on the PBE0 exchange-correlation functional. However, its exchange energy term split into short range (SR) and long range (LR) components and the HF long range is neglected but compensated by the PBE long range.²¹²⁻²¹⁴ HSE06 takes the following form for exchange-correlation energy:

$$E_{XC}^{HSE} = \frac{1}{4} E_X^{HF,SR}(\omega) + \frac{3}{4} E_X^{\omega PBE,SR}(\omega) + E_X^{\omega PBE,LR}(\omega) + E_C^{PBE} \quad (2.35)$$

where $E_X^{HF,SR}$ is the SR HF exchange. $E_X^{\omega PBE,SR}$ and $E_X^{\omega PBE,LR}$ are the short and long range components of the PBE exchange functional. The splitting parameter, $\omega = 0.20 a_0^{-1}$, separates the range.

2.3 DFT code – VASP

There are quite a number of computational software packages that use methods of theoretical chemistry to calculate structures and properties of molecules and solids. The primary DFT codes used throughout the work presented in this thesis is the Vienna Ab-initio Simulation Package (VASP)¹⁰⁻¹³ which uses pseudopotentials or the projector- wave method (PAW)^{215, 216} and a plane wave basis set. This ab-initio code is used for atomic scale materials modelling such as electronic structure calculations and quantum-mechanical Born-Oppenheimer molecular dynamics.

VASP uses efficient matrix diagonalisation schemes and Pulay/Broyden charge density mixing in its self-consistency cycle for Kohn-Sham ground-state calculations.²¹⁷ These avoid all problems possibly occurring in the original Car-Parinello method, which is based on the simultaneous integration of electronic and ionic equations of motion. The forces and full stress tensor can be calculated with VASP and used to relax the geometry of the system. Implemented iterative mixing diagonalisation schemes (RMM-DISS and blocked Davidson) are among the fastest schemes implemented.

2.3.1 Projector augmented wave method

The projector augmented wave method is first introduced by Blöchl in 1994.²¹⁵ This method generalises both the pseudopotential method and linear augmented-plane-wave (LAPW) method in a natural way. Similar to the LAPW method, this approach can be used to treat first-row and transition metal elements with affordable effort and provides access to the full wave function.

Using PAW, the core electrons are kept frozen in the calculation. The linear transformation to the all-electron valence functional, ψ^v , from that in the PAW representation $\tilde{\psi}^v$ is achieved using an operator \mathcal{T} .

$$\psi^v = \mathcal{T}\tilde{\psi}^v \quad (2.36)$$

The operator \mathcal{T} is assumed to be a sum of non-overlapping atom-centered contributions,

$$\mathcal{T} = 1 + \sum_{\mathbf{R}} \mathcal{T}_{\mathbf{R}} \quad (2.37)$$

with \mathbf{R} the nuclear position. Each $\mathcal{T}_{\mathbf{R}}$ is localised to a sphere denoted Ω_{vecr} . When the smooth function $|\tilde{\psi}\rangle$ is expanded in partial waves m within each sphere, the expansion can be written as:

$$|\tilde{\psi}\rangle = \sum_m c_m |\tilde{\psi}_m\rangle \quad (2.38)$$

with the corresponding all electron function,

$$|\psi\rangle = \mathcal{T}|\tilde{\psi}\rangle = \sum_m c_m |\psi_m\rangle \quad (2.39)$$

Hence, the full wavefunction in all space can be written as:

$$|\psi\rangle = |\tilde{\psi}\rangle + \sum_{\mathbf{R}m} c_{\mathbf{R}m} [|\psi_{\mathbf{R}m}\rangle - |\tilde{\psi}_{\mathbf{R}m}\rangle] \quad (2.40)$$

where the coefficients $c_{\mathbf{R}m}$ are given by the projection in each sphere,

$$c_{\mathbf{R}m} = \langle \tilde{p}_{\mathbf{R}m} | \tilde{\psi} \rangle \quad (2.41)$$

for some set of projection operators $\tilde{p}_{\mathbf{R}m}$. Thus, the total energy can be written as a sum of three terms,

$$E = \tilde{E} + E^1 - \tilde{E}^1 \quad (2.42)$$

where \tilde{E} is the energy due to smooth functions evaluated in Fourier space or a grid that extends throughout space, \tilde{E}^1 is the same terms evaluated only in the spheres on radial grids, and E^1 is the energy in the spheres with the full functions.

For the CeO₂ systems, the cerium $5s$, $5p$, $5d$, $4f$, $6s$ and oxygen $2s$, $2p$ electrons were treated explicitly as valence electrons in both PW91 and PBE calculations. For Fe₂O₃ systems, the Fe $3d$ $4s$, and oxygen $2s$, $2p$ electrons were treated explicitly as

valence electrons in PBE calculations. The palladium $5s$, $4d$, platinum $6s$, $5d$, and gold $6s$, $5d$ electrons were treated as valence electrons in all calculations. These PAW functionals are provided by VASP database for which the pseudopotential radii are shown in Table 2.1.

Table 2.1 VASP's PW91 and PBE PAW pseudopotential for Ce, O, Pd, Pt, Au, and Fe with their corresponding radii cutoff value for each state.

Element	states	Radii cutoff (\AA)	
		PW91	PBE
Ce	s	1.65	1.50
	p	1.80	2.00
	d	2.30	2.50
	f	2.57	2.70
O	s	1.20	1.20
	p	1.52	1.52
Pd	s	2.40	2.40
	d	2.40	2.60
Pt	s	2.50	2.50
	d	2.50	2.60
Au	s	-	2.50
	d	-	2.50
Fe	s	-	2.30
	d	-	2.30

2.3.2 Optimisers

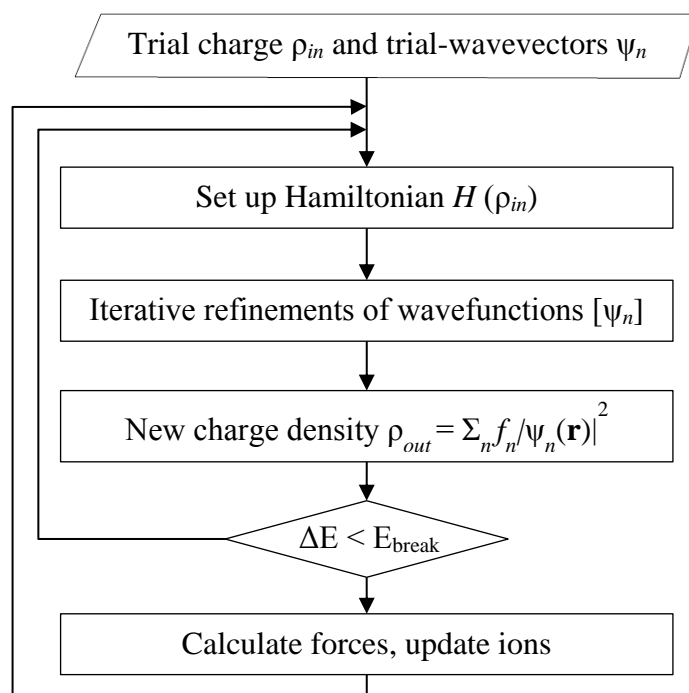


Figure 2.2 Self-consistent optimisation scheme.

Generally, there is one outer loop and one inner loop for the minimization algorithm in VASP.²¹⁷ The outer loop optimises the charge density, and the wavefunctions are optimised in the inner loop. Figure 2.2 shows the self-consistent density functional calculation in a flow chart. Within each self-consistent optimisation loop, the charge density is used to set up the Hamiltonian, and then the wavefunctions are optimised iteratively so that they get closer to the exact wavefunctions of this Hamiltonian. A new charge density is calculated from the optimised wavefunctions, which is then mixed with the old input-charge density using an efficient Pulay/Broyden mixing scheme. The algorithm used for the refinement of wavefunctions are determined by the ALGO-tag. The wavefunctions are optimised using either the blocked algorithm (ALGO=Normal), residual minimisation scheme – direct inversion in the iterative subspace (RMM-DISS) (ALGO=Very fast), or the mixture of blocked Davidson with RMM-DISS algorithm (ALGO=Fast). For all the calculations we performed in VASP, we have set ALGO=Fast.

In order to determine the way ions are updated and moved, the IBRION-tag is specified in the input file for VASP. Generally, we have used the conjugate gradient algorithm (IBRION=2) which is also recommended in the VASP manual for difficult relaxation problems. This method required a line minimisation, which is performed

in several steps. Firstly, a trial step into the search direction is done. Then, the energy and forces are recalculated. Secondly, a trial or predictor step is performed. The approximate minimum of the total energy is calculated from a cubic (or quadratic) interpolation taking into account the change of the total energy and the change of the forces. After that, a corrector step to the approximate minimum is performed. The forces and energy are recalculated after the corrector step and is checked whether the forces contain a significant component parallel to the previous search direction. If the line minimisation is sufficiently accurate, the cycle starts again.

2.3.3 Using planewave basis set

The systems studied are replicated periodically throughout space. However, this causes a problem with infinite number of electrons and requires one to solve the wavefunction over infinite space. Using the Bloch's theorem²¹⁵, the wavefunction of the electrons can be expressed as a wave like part and a cell periodic part. The wavefunction, $\psi(\mathbf{r})$, is written as:

$$\psi(\mathbf{r}) = \exp(i\mathbf{k} \cdot \mathbf{r}) u(\mathbf{r}) \quad (2.43)$$

with \mathbf{r} as the position in the lattice. The cell-periodic function, $u(\mathbf{r})$, can be expressed as a Fourier series, \mathbf{k} is the vector describing a point the reciprocal cell.

$$u(\mathbf{r}) = \sum_{\mathbf{G}} \tilde{u}_{\mathbf{G}} \exp(i\mathbf{G} \cdot \mathbf{r}) \quad (2.44)$$

\mathbf{G} is the reciprocal lattice vector $\mathbf{G} = m_1\mathbf{g}_1 + m_2\mathbf{g}_2 + m_3\mathbf{g}_3$ and the m_i are integers. The state $|\psi_{nk}\rangle$ can now be expressed as a linear combination of plane-waves:

$$\psi_{nk}(\mathbf{r}) = \exp(i\mathbf{k} \cdot \mathbf{r}) u_{nk}(\mathbf{r}) \quad (2.45)$$

$$\psi_{nk}(\mathbf{r}) = \sum_{\mathbf{G}} c_{nk}(\mathbf{G}) \exp[i(\mathbf{k} + \mathbf{G}) \cdot \mathbf{r}] \quad (2.46)$$

One now only has to solve the wavefunction within a single cell even with an infinite number of possible values for \mathbf{k} .

First thing to determine in our calculations is the energy cut-off value to be used for planewave basis. An infinite number of plane waves are needed to obtain the exact wave function. As more plane waves are added together, the Fourier transform becomes a closer representation of the periodic Gaussian function. The energy cut-off of a plane wave basis set is defined as:

$$E_{cut} = \frac{\hbar^2}{2m} \mathbf{G}_{cut}^2 \quad (2.47)$$

Increasing the cut-off energy causes the magnitude of the \mathbf{G} vector to increase as well and so increases the accuracy of the Fourier transform. The lowest energy waves contribute most to the Fourier transform, thus it is possible to exclude the higher energy wavelength from the calculation. By increasing the cut-off energy of the plane wave basis set, we can check the convergence of the energy of a system.

For CeO_2 bulk, we have performed calculation using plane wave basis set cut-off energies from 200 to 600 eV with a 50 eV step in between. Figure 2.3 shows the energy convergence for bulk CeO_2 , with an initial lattice parameter of $a_0 = 5.411 \text{ \AA}$, with respect of energy cut-off. The graph shows that the energy is converging at 500 eV. The difference in energy between the cut-off energy of 450 and 500 eV is 0.037 eV, while between 500 and 550 eV is 0.001 eV. Thus, we have selected 500 eV as the cut-off energy for VASP calculation with CeO_2 system.

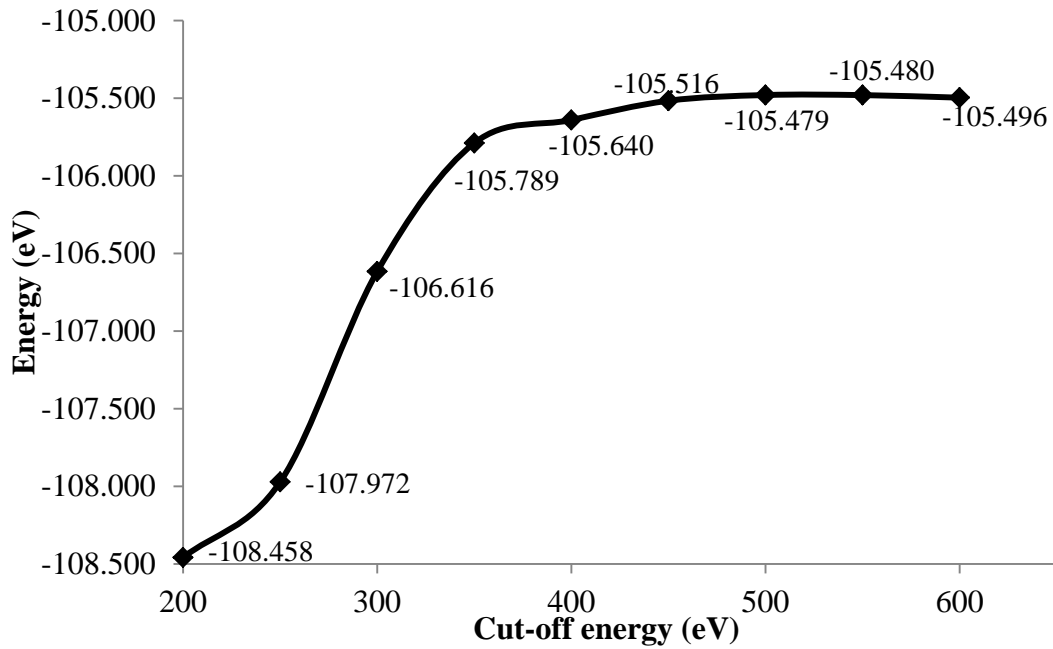


Figure 2.3 Convergence of the bulk energy of CeO_2 ($a_0 = 5.411 \text{ \AA}$) with respect to the plane wave cut-off energy using PW91.

A converged number of k -points is necessary for a calculation. In general, metallic systems required an order of magnitude more k -points than semiconducting and insulation systems.²¹⁷ Partial occupancies help to decrease the number of k -points necessary to calculate accurate band structure energy. There are several methods to set the partial occupancies for each orbital by setting the ISMEAR tag in

the input file. It was recommended to use tetrahedron method with Blöchl corrections (ISMEAR=-5) for smearing in semiconductors and insulators. However, if the cell is too large to use tetrahedron method, the Gaussian smearing is used instead (ISMEAR=0) accompanied by a small σ value (width of smearing) of 0.05 eV. The tetrahedron method is not variational with respect to the partial occupancies so calculated forces and stress tensor can be wrong by up to 5 to 10 % for metals. Thus, it was recommended to use the Methfessel-Paxton scheme for relaxation in metals with an appropriate σ value which is usually 0.2 eV in default. As for the density of states calculation, the tetrahedron method is recommended. We have used the Gaussian smearing method for all the surface calculations and the tetrahedron method with Blöchl corrections for the bulk calculations.

The k -point mesh is optimised for the bulk structure and is used for the surface model. In the surface model, there is one long lattice vector along the z -direction, and the other two are short lattice vectors. Along the z -direction, there is a vacuum space of at least 15 Å. The band dispersion is zero due to the vacuum so one division for the k -point mesh along this direction is sufficient. As for the short directions, the number of divisions used is approximately the same as the ones used in bulk calculations. The CeO₂ bulk energy convergence is checked with different k -point grid (Figure 2.4). A k -point grid of $7 \times 7 \times 7$ is enough as increasing the grid to $9 \times 9 \times 9$ did not yield significant difference in the energy of the CeO₂ bulk. Thus, we have chosen $7 \times 7 \times 7$ as the k -point grid applied to bulk calculations using the Monkhorst-Pack scheme^{218, 219} while surface slab of a single cell unit used a $7 \times 7 \times 1$ k -point grid. Surface slabs are expanded to supercell ($a=15.58$ Å, $b=13.50$ Å, $c=22.95$ Å) in calculations involving defects and reactions. Calculations are done using the Γ -point for these systems as they are large enough for the reciprocal space to be very small and only a few k -points need to be considered to describe the variation across the Brillouin zone accurately.

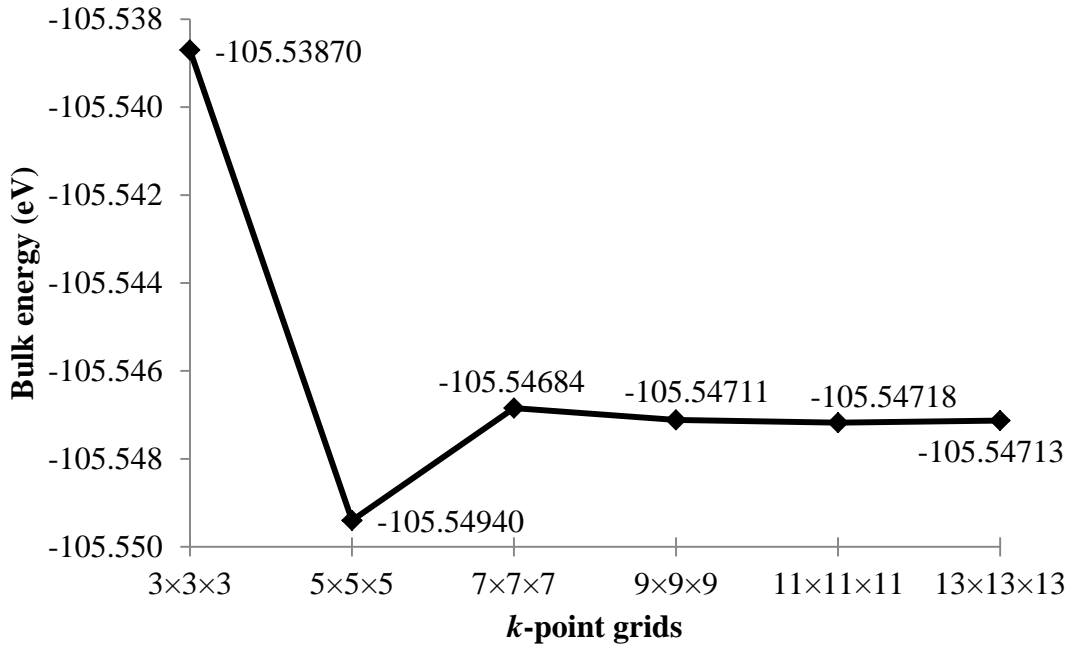


Figure 2.4 Convergence of bulk energy for CeO₂, with respect to the k -point grid using PW91. Energies shown are calculated with optimised bulk lattice parameter at each k -point grid.

2.3.4 Bulk and surface optimisations

The initial bulk lattice parameter for a single unit cell of CeO₂ taken from experiment³¹, (consisting of eight oxygen atoms, and 4 cerium atoms) is 5.411 Å. The bulk modulus of a material measures the resistance of a material with volume, V , to uniform pressure, p . Given that:

$$B_0 = -\frac{V\partial p}{\partial V} \quad (2.48)$$

where $p=F/A$. When a uniform force, F , applied to all faces of area, A , the face moves a small distance, δx , in response to this force. Thus, the force will be related to the change in potential energy by:

$$F = -\frac{\delta E}{\delta x} \quad (2.49)$$

so

$$p = -\frac{1}{A} \left(\frac{\delta E}{\delta x} \right) = -\frac{\delta E}{\delta V} \quad (2.50)$$

so that

$$B_0 = V \left(\frac{\delta^2 E}{\delta V^2} \right) \quad (2.51)$$

The second derivative of energy with respect to volume can be estimated from the quadratic fit using equation (2.54). Thus,

$$\frac{\partial E}{\partial V} = 2aV + b \quad (2.52)$$

and

$$\frac{\partial^2 E}{\partial V^2} = 2a \quad (2.53)$$

We have performed a series of calculations at different volumes with the same cut-off energy for each k -point grid mentioned earlier. The energies obtained from each calculation are fitted to two equations: 1) the quadratic equation; 2) the Murnaghan equation of state.²²⁰ The quadratic equation is fitted to the energy vs volume plot obtained from VASP calculations.

$$E = aV^2 + bV + c \quad (2.54)$$

where a , b , and c are coefficients obtained from the fitting. For the Murnaghan equation of state, there are several parameters which are used in fitting to energy vs volume data obtained from VASP calculations. The equation is written as:

$$E = E_0 + \frac{B_0 V}{B'_0} \left[\frac{\left(\frac{V_0}{V} \right)^{B'_0}}{B'_0 - 1} + 1 \right] - \frac{V_0 B_0}{B'_0 - 1} \quad (2.55)$$

where V is the volume, B_0 and B'_0 are the bulk modulus and its pressure derivative at the minimum volume V_0 , and E_0 is the energy at volume V_0 . All these parameters are initial guesses which can be obtained from the quadratic fitting. A value of 2 – 4 for B'_0 is a good starting guess when fitting data to the Murnaghan equation of state. Through these fitting methods, we can calculate the volume at minimum bulk energy, and the bulk modulus, B_0 , of the structure. Since, CeO_2 is a cubic cell, the lattice parameter is the cube root of the volume. The optimised bulk lattice parameter for PW91 calculation is found to be 5.479 Å which expanded about 1.3% from the experimental lattice parameter of 5.411 Å.

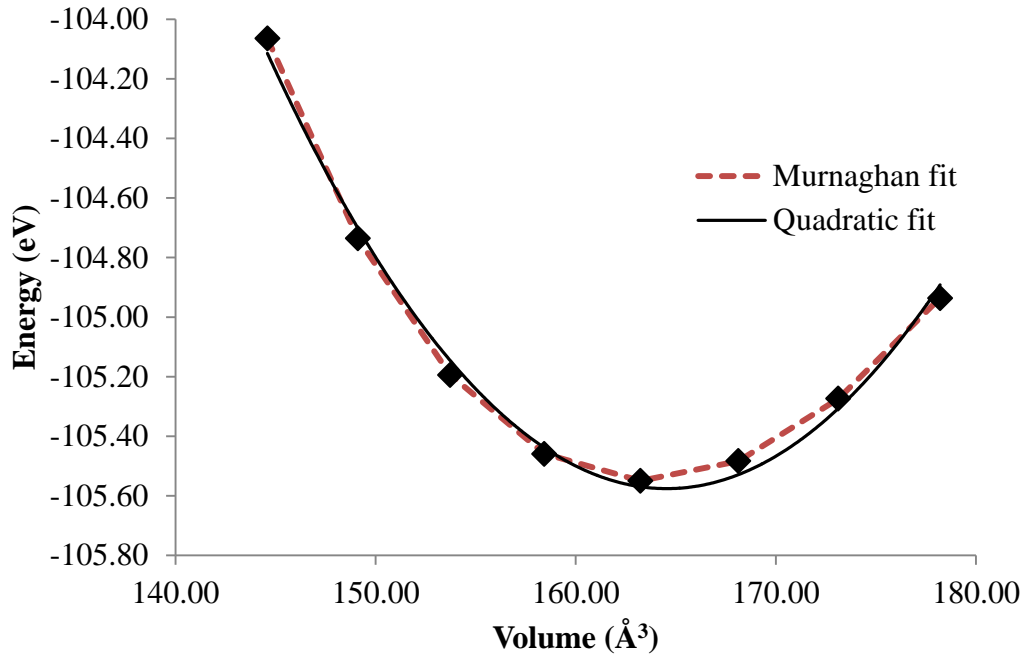


Figure 2.5 Energy of bulk CeO₂ with respect to volume.

The coefficient for x^2 from the fit (equation (2.54)) gives the required second derivative and the bulk modulus can be obtained using equation (2.51). The bulk modulus, B_0 , obtained with this method for CeO₂ using k -point grid $7 \times 7 \times 7$ is 210 GPa, which falls within the range of experimental values reported in literature^{31, 32, 34, 35} ($B_0 = 204$ to 236 GPa). However, using the Murnaghan equation of state, the B_0 calculated is 173 GPa.

2.3.5 Generation of different spin permutations on Ce sites

When we have study oxygen defects in ceria in Chapter 3 and 4, we consider the different localisation sites for the excess electron left by the removal of an oxygen atom in both the bulk and surface of ceria (CeO₂). The Ce³⁺ ions (1.283 Å), which have larger radius compared to Ce⁴⁺ ions (1.11 Å)^{52, 53, 221}, cause a polaron distortion to the immediate neighbouring oxygen atoms. Thus, in order to ensure the electron localised on the sites that they are designated to, we have replaced the designated sites with lanthanum and optimisation was performed. Lanthanum has an oxidation state of +3 and a radius similar to Ce³⁺, so it is enough to provide a reasonable distortion to the immediate neighbouring atoms and give us a starting structure with the designated localisation sites. Then, a final optimisation is performed after replacing the lanthanum with cerium atoms.

The number of pairs of localisation sites is huge depending on the size of the system or the number of cerium atoms available. In order to ease the generation of these structures, an in-house routine was implemented in C language for pre- and post- processing of VASP calculations. The concept is to acquire the total number of sites which can be considered for electron localisation and loop through the various sites to create pairs of localisation sites.

A threshold for maximum distance of the cerium atom from the oxygen vacancy site is set to ensure only the atoms in the range of interest are taken into consideration when generating the structures. The localisation sites to vacancy sites distances are calculated using the co-ordinates of the cerium atom and the oxygen atom prior to removal. Cerium to cerium distances are also calculated for each pair of localisation sites. These distances will be compared between different generated pairs of localisation sites to ensure only unique pairs are used in calculations. Pairs that have matching distances from the oxygen vacancy and from each other are counted as equivalent pairs.

2.4 DFT code – CRYSTAL09

CRYSTAL is a general-purpose program for the study of crystalline solids.¹⁵ The code performs *ab initio* calculations of the ground state energy, energy gradient, electronic wave function and properties of periodic systems within Hartree Fock, density functional or various hybrid approximations. Restricted and unrestricted calculations can be performed with all electron and valence-only basis sets with effective core pseudo-potentials (ECP). The single particle wave functions are expanded as a linear combination of Blochl functions defined in terms of local functions, which are linear combinations of Gaussian type functions (GTF) whose exponents and coefficients are defined by the input in basis sets used. DFT calculations involving all electron basis sets and ECP were performed using the CRYSTAL09^{14, 15} package.

2.4.1 Basis sets

Basis sets are sets of functions usually based on atomic orbitals in CRYSTAL09 used to create the molecular orbitals, which are expanded as a linear combination of basis functions.

$$\psi_i = \sum_{\mu=1}^n c_{\mu i} \phi_{\mu} \quad (2.56)$$

where ψ_i is the i -th molecular orbital, $c_{\mu i}$ are the coefficients of linear combination, ϕ_{μ} is the μ -th basis function, and n is the number of basis function. The two types of basis functions are Slater type orbitals²²² (STO) and Gaussian type orbitals²²³ (GTO) which are defined in their functional form shown in equation (2.57) and (2.58), respectively.

$$\phi_{\zeta,n,l,m}(r, \theta, \varphi) = N Y_{l,m}(\theta, \varphi) r^{n-1} e^{-\zeta r} \quad (2.57)$$

$$\phi_{\zeta,n,l,m}(r, \theta, \varphi) = N Y_{l,m}(\theta, \varphi) r^{(2n-2-l)} e^{-\zeta r^2} \quad (2.58)$$

N is a normalisation constant and $Y_{l,m}$ are the usual spherical harmonic functions. Gaussian functions are preferred mostly in electronic structure calculations because they allow for efficient computation of overlap integrals. The number of functions used governs the quality of the basis set.

The $1s$ electrons account for a large part of the total energy, and minimising the energy will tend to make the basis set optimum for the core electrons, and less than optimum for the valence electrons.¹⁸⁷ The core electrons are energetically important but the valence electrons are chemically important. An energy optimised basis set which gives a good description of the outer part of the wave function therefore needs to be very large, with the majority of the functions being used to describe $1s$ electrons with accuracy comparable to that for the outer electrons in an energetic sense. The computational cost increases as the fourth power (or higher) of the number of basis functions, which makes it computationally inefficient since the majority of the computational effort is spent describing the chemically uninteresting part of the wave function. However, by contracting the basis set, the number of basis functions to be handled by the variational procedure can be reduced. This can be done by combining the full set of basis functions, known as the primitive GTOs (PGTOs), into a smaller set of functions by forming fixed linear combinations which then gives us functions called contracted GTOs (CGTO).

$$\phi(\text{CGTO}) = \sum_i^k a_i \phi_i(\text{PGTO}) \quad (2.59)$$

In our calculations using CRYSTAL09, we have applied the CGTO valence-only basis set with effective core potentials (ECP) for cerium atoms, and Pople's split

valence basis set for oxygen atoms. The 8-411G* basis set is used with its most diffuse functions re-optimised by Désaunay *et al.*¹⁷⁶ based on the total energy per unit cell of CeO₂. For the Ce atoms, we have applied two different valence basis sets according to the type of effective core potentials that we have used. More about the effective core potentials will be explained in Section 2.3.2.

We have used the double zeta basis set which is developed by Dolg and co-workers to work with the large core potential.²²⁴ For a small core potential, we have applied a double zeta basis set (mRSC) for the Ce atoms, which is adapted from Désaunay *et al.*¹⁷⁶ This modified version of the double zeta basis set (RSC1997-AVDZ) was taken from the EMSL basis set exchange website.²²⁵ Désaunay has reconstructed the basis set by removing the $8s$, $7p$, and $7d$, diffuse functions and reoptimising the $7s$, $6p$, $5d$, and $5f$ polarization functions. The original $4s$, $4p$, $4d$, and $4f$ contractions were taken from the RSC1997 basis set^{225, 226} to explicitly treat the electrons with principal quantum number of 4. The resulting contraction scheme is (16s13p10d7f)/[4s3p3d2f]. The basis sets are available in Appendix A1.

2.4.2 Effective core potentials

As we have mentioned that the core electrons are generally unimportant in chemical sense and with the increase in number of electrons per atom, a large number of basis functions would be needed to expand the corresponding orbitals. Otherwise, the valence orbitals will not be properly described due to a poor description of the electron-electron repulsion. A way to tackle this problem is by introducing an effective core potential (ECP) to represent the core electrons.^{227, 228} The core electrons are described by a potential which effectively accounts for the relativistic and electrostatic effects. The valence orbitals are described by a set of nodeless pseudo-orbitals. The computation time used can be reduced with the use of ECP. It is most beneficial when ECP is applied in calculations involving atoms at the lower part of the periodic table.

CRYSTAL has implemented the pseudopotential, W_{ps} , as a sum of three terms, which are the Coulomb term (C), a local term (W0), and a semi-local term (SL):

$$W_{ps} = C + W0 + SL \quad (2.60)$$

where:

$$C = -Z_N/r \quad (2.61)$$

$$W0 = \sum_{k=1}^M r^{n_k} C_k e^{-\alpha_k r^2} \quad (2.62)$$

$$SL = \sum_{\ell=0}^4 \left[\sum_{k=1}^{M_\ell} r^{n_{k\ell}} C_{k\ell} e^{-\alpha_{k\ell} r^2} \right] P_\ell \quad (2.63)$$

with Z_N as the effective nuclear charge, which is equal to the total of nuclear charge minus the number of electrons represented by the ECP, P_ℓ is the projection operator related to ℓ angular quantum number and M , n_k , α_k , M_ℓ , $n_{k\ell}$, $C_{k\ell}$, $\alpha_{k\ell}$ are the atomic pseudopotential parameters.

There are two different types of ECP that we have used for cerium atoms in our CRYSTAL09 calculations. They are the small core ECP and the large core ECP. Both of which were developed by the Stuttgart-Dresden group.^{224, 229} In the small core ECP, only 28 electrons are described as the core while the remaining 30 electrons are attributed to the valence space.²²⁹ The total electron configuration of cerium is $[\text{Kr}]4d^{10}5s^25p^64f^45d^16s^2$. These 30 electrons are from the $4s$, $4p$, $4d$, $5s$, $5d$, $4f$, $5d$, and $6s$ shells. We have used this small core ECP with the mRSC basis set which was adapted from Désaunay *et al.*¹⁷⁶ as mentioned in Section 2.3.1. For the large core ECP, only the $5s$, $5d$, $4f$, $5d$, and $6s$ electrons are treated explicitly as valence electrons while the core is represented by 46 electrons.²²⁴ The ECPs used are available in Appendix A1.

2.5 Nudged elastic band method

The nudged elastic band (NEB) method^{230, 231} has been applied for transition state (TS) search along a minimum energy path (MEP) between a pair of stable states. This will allow one to obtain the energy barrier of a reaction path. A string of images in between the initial optimised start and end points is used to describe a reaction pathway in this method. A force projection scheme, where the potential forces act perpendicularly to the tangent and spring forces act along the tangent, is used to relax the images along the NEB to the MEP. The total force acting on image i is the sum of true force perpendicular to the tangent and the spring force along the tangent:

$$\vec{F}_i = -\vec{\nabla}V(\vec{R}_i)|_{\perp} + \vec{F}_i^s \quad (2.64)$$

where the true force is described as:

$$\vec{\nabla}V(\vec{R}_i)|_{\perp} = \vec{\nabla}(\vec{R}_i) - \vec{\nabla}(\vec{R}_i) \cdot \hat{t}_i \quad (2.65)$$

and the spring force as:

$$\vec{F}_i^s = k[(\vec{R}_{i+1} - \vec{R}_i) - (\vec{R}_i - \vec{R}_{i-1})] \cdot \hat{t}_i \hat{t}_i \quad (2.66)$$

where k is the spring constant, \vec{R}_i is the vector of all atoms positions in the i th image, and \hat{t}_i is the normalised tangent at image i .

In VASP, the nudge elastic band method is used when SPRING tag is present in the input file (SPRING<=0). We have used SPRING=-5 for all the NEB calculations that we have performed. The images are kept equidistant with additional tangential springs which are introduced when the SPRING tag holds a negative value.

2.6 Vibrational frequency analysis

The principle idea in calculating vibrational frequency is that each vibration is treated as though it corresponds to a spring. In the harmonic approximation, the spring obeys Hooke's law, where the force is proportional to the displacement. The vibrational frequency is defined as:

$$v = \frac{1}{2\pi} \sqrt{\frac{k}{\mu}} \quad (2.67)$$

where k is the force constant and μ is the reduced mass. In VASP, the vibrational frequencies and the Hessian matrix of a system are determined when the IBRION tags are set to IBRION=5 or IBRION=6 in the input file. Each ion is displaced in the direction of each Cartesian coordinate, and from the forces the Hessian matrix is determined. The Hessian matrix is defined as:

$$H_{i,j} = \frac{\delta^2 E}{\delta x_i \delta x_j} \quad (2.68)$$

By finite displacements, the gradients are calculated at a small increment, Δx , and then recalculated after decrement of each atomic coordinate x_i . The second derivative is obtained from the difference of the two derivatives and the step size.

$$H_{i,j} = \frac{\left(\left(\frac{\delta E}{\delta x_i} \right)_{+0.5\Delta x_j} - \left(\frac{\delta E}{\delta x_i} \right)_{-0.5\Delta x_j} \right)}{\Delta x_j} \quad (2.69)$$

The Hessian is symmetric, so it can be redefined to reduce the random errors that occur in the gradient calculations.

$$H_{i,j} = \frac{1}{2} \left(\frac{\left(\frac{\delta E}{\delta x_i} \right)_{+0.5\Delta x_j} - \left(\frac{\delta E}{\delta x_i} \right)_{-0.5\Delta x_j}}{\Delta x_j} + \frac{\left(\frac{\delta E}{\delta x_j} \right)_{+0.5\Delta x_i} - \left(\frac{\delta E}{\delta x_j} \right)_{-0.5\Delta x_i}}{\Delta x_i} \right) \quad (2.70)$$

In order to calculate the vibrational frequencies, the Hessian matrix is first mass-weighted:

$$H_{i,j}^m = \frac{H_{i,j}}{\sqrt{M_i \times M_j}} \quad (2.71)$$

Diagonalisation of this matrix yields the eigenvalues, ε , which represents the quantities $(k/\mu)^{1/2}$, from which the vibrational frequencies can be calculated.

$$\bar{\nu}_i = \frac{1}{2\pi c} \sqrt{\varepsilon_i} \quad (2.72)$$

We have only used IBRION=5 tag for our vibrational frequency calculations. When it is used with the “*Selective dynamics*” line present in the structure input file, the components of the Hessian matrix are calculated only for the atoms which are selected. We have used central difference for the displacement of ions, where each ion is displaced in each direction by a small positive and negative displacement (NFREE=2). We have used vibrational frequency analysis to classify the transition state of a reaction, which can be identified as a structure having only a single imaginary frequency.

2.7 Density of states (DOS)

An important quantity for many purposes is the density of states (DOS). First, the available states in \mathbf{k} -space are calculated and then the energy-momentum relation is used in a parabolic band to give the density of states in terms of energy. Explicitly, the volume of \mathbf{k} -space would be:

$$V_{3D} = \left(\frac{2\pi}{L} \right)^3 \quad (2.73)$$

with L the length of the box. The number of allowed states is determined between spheres of radius \mathbf{k} and $\mathbf{k}+d\mathbf{k}$. The volume between two shells in 3-dimension is given by

$$V_{s3D}d\mathbf{k} = 4\pi|\mathbf{k}|^2d\mathbf{k} \quad (2.74)$$

Therefore, by dividing this volume by the volume of a single energy state, we can determine the number of states. The fact that any state can contain two electrons, spin up and spin down, a factor of two is included.

$$g(\mathbf{k})_{3D}d\mathbf{k} = 2 \times \frac{V_{s3D}d\mathbf{k}}{V_{3D}} = \frac{|\mathbf{k}|^2d\mathbf{k}L^3}{\pi^2} \quad (2.75)$$

In order to obtain the density of states per unit volume in terms of the energy, the relation between E and \mathbf{k} must be determined.

$$E = \frac{\hbar^2|\mathbf{k}|^2}{2m} \quad (2.76)$$

with m the mass of the particle and $\hbar = \frac{h}{2\pi}$. After rearranging, we obtain:

$$|\mathbf{k}| = \sqrt{\frac{2mE}{\hbar^2}} \quad (2.77)$$

Differentiating equation (2.77) with respect to energy gives:

$$d\mathbf{k} = \left(\frac{2mE}{\hbar^2}\right)^{-\frac{1}{2}} \left(\frac{m}{\hbar^2}\right) dE \quad (2.78)$$

Thus, in the case of a bulk system, the density of states per unit volume at an energy E is given by:

$$g(E)_{3D} = \frac{\mathbf{k}^2d\mathbf{k}}{\pi^2dE} = \frac{1}{2\pi^2} \left(\frac{2m}{\hbar^2}\right)^{\frac{3}{2}} E^{\frac{1}{2}} \quad (2.79)$$

We have used a denser k -point grid for DOS calculations. For example, in a single unit cell of bulk CeO₂, we have used 9×9×9 k -point grid for the DOS calculation rather than 7×7×7. This is because $g(E)$ requires a derivative of E with respect to \mathbf{k} . We set the number of grid points on which the electron density is requested to 600 for DOS calculations. The calculation is set to read a charge density (from CHGCAR file) obtained from a previous self-consistent run.

Figure 2.6 shows the DOS plot for CeO₂ obtained using PW91+U with different levels of smearing. States shown below Fermi level are all occupied and the ones above Fermi level are unoccupied states. A Gaussian smearing is applied to obtain a smooth plot. We need to take note that when too large a value of smearing is used, features within the DOS plots are lost, for example here, the splitting in energy of the f -orbitals due to the crystal field at between 2 – 3 eV (Figure 2.6).

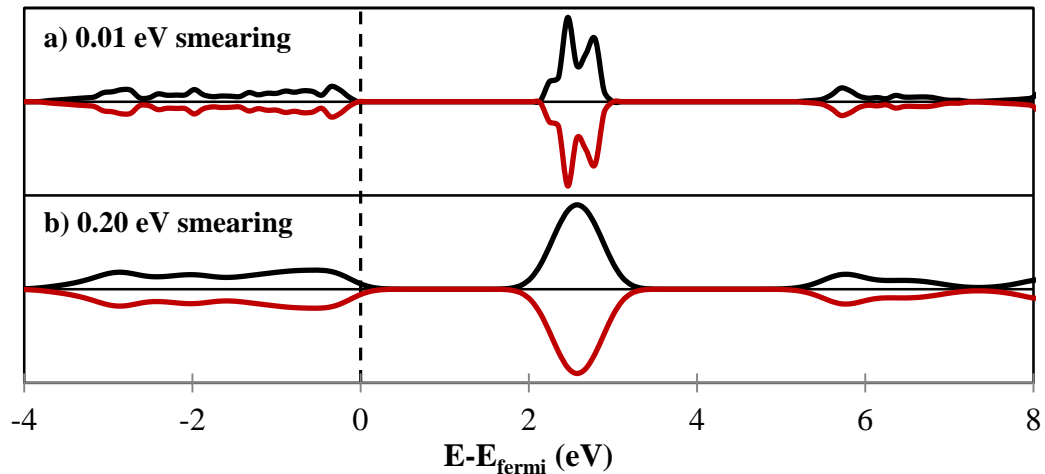


Figure 2.6 Total DOS for bulk CeO_2 calculated by VASP using spin polarised PW91+U method with a Gaussian smearing width of a) 0.01 and b) 0.2 eV. Up and down spins are black and red solid lines, respectively. The vertical dashed line indicates the Fermi energy corrected to 0 eV.

2.8 Bader charge analysis

The output in quantum mechanical calculations is a continuous electronic charge density. There is a problem as to how the electrons should be partitioned between atoms or molecules of a system. One of the solutions is through a topological analysis of the charge density proposed by Bader.²³² Via this approach, it is possible to analyse the electron density, $\rho(x, y, z)$, of the system generated by planewave calculations (e.g from VASP). The nuclei act as point attractors immersed in a cloud of negative charge, the electron density, $\rho(\mathbf{r})$. The local maxima in the electron density can be found at the position of the nuclei and rapidly decay away from these points. The boundaries of each individual atoms are determined by the minimum in the electron density perpendicular to the 2-D surface. This is called the surface of normal flux.

We have used the code developed by Henkelman *et al.*²³³⁻²³⁵ to acquire the Bader charges through the Bader decomposition of charge density. The recent developed near-grid method²³⁵ corrects the lattice bias using the on-grid method²³³ which causes the trajectory between attractors to deviate and the dividing surface to follow the lattice direction instead of the true dividing surface. In the near-grid method, the trajectory of steepest ascent is followed up the charge density from an initial grid point (i, j, k) . Each step is made to one of the 26 neighbouring grid points. The charge density gradient, $\nabla\rho$, is calculated from the charge density of six nearest

neighbours using a central finite difference scheme. This is done in order to make a step. The components of the charge density in the x , y , and z directions are:

$$\Delta\rho_x = \frac{\rho(i+1, j, k) - \rho(i-1, j, k)}{|\vec{r}(i+1, j, k) - \vec{r}(i-1, j, k)|} \quad (2.80)$$

$$\Delta\rho_y = \frac{\rho(i, j+1, k) - \rho(i, j-1, k)}{|\vec{r}(i, j+1, k) - \vec{r}(i, j-1, k)|} \quad (2.81)$$

$$\Delta\rho_z = \frac{\rho(i, j, k+1) - \rho(i, j, k-1)}{|\vec{r}(i, j, k+1) - \vec{r}(i, j, k-1)|} \quad (2.82)$$

In order to advance the trajectory by one grid point along the gradient, a step is taken along the gradient vector:

$$\vec{r}_{grad} = c(\nabla\rho_x, \nabla\rho_y, \nabla\rho_z) \quad (2.83)$$

where the constant, c , has been chosen as:

$$c = \min\left(\frac{dx}{|\nabla\rho_x|}, \frac{dy}{|\nabla\rho_y|}, \frac{dz}{|\nabla\rho_z|}\right) \quad (2.84)$$

with dx , dy , and dz as the grid spacings along the x , y , and z Cartesian directions. In general, the step \vec{r}_{grad} takes the trajectory off the grid. A hopping process between grid points is needed to retain the efficiency of the on-grid method. This step between grid points is labelled as \vec{r}_{grid} . Then, a correction vector (initially zero) from the final grid point to the location of the true trajectory is described as:

$$\Delta\vec{r} = \Delta\vec{r} + (\vec{r}_{grad} - \vec{r}_{grid}) \quad (2.85)$$

With the correction vector, the true trajectory is never more than half a grid point from the current grid point in any direction. The ascent trajectory is terminated when it reaches a charge density maximum or a point for which the point itself and all of its neighbours are assigned to the same Bader region. All the grid points along the ascent trajectory are assigned to the same Bader region as the end points of the trajectory.

An ascent trajectory is calculated from each grid point until all are assigned to a Bader volume. From each new trajectory, the correction vector $\Delta\vec{r}$ is reset to (0,0,0). A final refinement of the grid points adjacent to the Bader surfaces is required when all the points are assigned unless smooth charge density grids were used.

Table 2.2 Bader charges with respect to grid points used obtained for a single unit cell of bulk CeO₂ calculated using PW91.

Grid points (Å)	Grid spacing (Å)	Bader charges (<i>e</i>)	
		O	Ce
280	0.020	-1.14	2.28
182	0.030	-1.14	2.28
136	0.040	-1.13	2.25
109	0.050	-1.15	2.30
91	0.060	-1.11,-1.12	2.23
78	0.070	-1.15,-1.16	2.30
64	0.086	-1.09	2.18

In VASP calculations using the PAW pseudopotentials, the charge density (written in CHGCAR files) only contains the valence charge density. The use of LAECHG=.TRUE. tag in a VASP calculation input file is necessary to allow the core charge to be written from PAW calculations. Both the core and valence charge densities are summed up and are analysed using the Bader code developed by Henkelman *et al.*²³⁶ In order to reproduce the correct total core charge, a few calculations with different number of grid-points for the second finer FFT-mesh is performed. This is done by increasing NG(X,Y,Z)F values. Table 2.2 shows the values of grid spacing set by varying the NG(X,Y,Z)F values along with the resulting Bader charge calculated using the Bader code for a single unit cell of bulk CeO₂. The Bader charges have started to converge at a grid spacing of 0.03 Å. There are no significant difference in the Bader charges for the O and Ce species between grid spacing 0.03 Å and 0.02 Å. Thus, we have used a grid spacing of 0.02 Å for all Bader charge analysis.

Chapter 3

Structural and electronic properties of stoichiometric and defective bulk CeO₂.

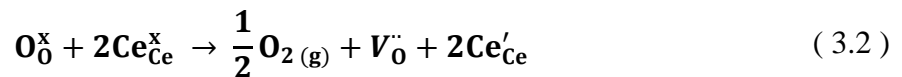
This chapter deals with the structural and electronic properties of bulk cerium (IV) oxide (CeO₂ or ceria). The chapter will begin with a brief introduction and computational details, followed by results that will be discussed in three different sections: stoichiometric bulk, defective bulk and electron localisation, and finally effects of PGM dopant on bulk CeO₂.

3.1 Introduction

An important factor in heterogeneous catalysis involving metal oxides is the oxygen storage capability of the oxide. This is defined by the ability of the metal to change its oxidation state during the reversible storage and release of oxygen for catalytic reactions. In a catalytic converter, the oxygen storage capability provides a balance of air-to-fuel ratio at the optimum stoichiometric value by easily releasing or removing the oxygen under “rich” and “lean” mixture conditions, respectively.³⁰ Among various metal oxides, ceria is one of the preferred materials for its oxygen storage capacity (OSC) in three way catalysts (TWCs). The relative partial pressures of oxygen and reductants such as CO and un-burnt hydrocarbon in the exhaust environment shift the equilibrium between the fully oxidised and partially reduced forms of the oxide:



This depends on the ability of the oxide cation to switch between the two stable valence states Ce⁴⁺ and Ce³⁺. The reduction of Ce⁴⁺ to Ce³⁺ proceeds by the release of a lattice oxygen anion as an oxygen atom in ½O₂ with the two electrons left behind localized in the 4*f* states of two cerium cations.^{50, 169} This can be shown using the Kröger-Vink notation:



where O_O^x and Ce_{Ce}^x are O and Ce ions on their respective lattice sites with the expected formal charges, $V_O^{\cdot\cdot}$ is the vacancy on an oxygen site with an effective charge of +2, and Ce_{Ce}' denotes Ce on a Ce site with an effective charge of -1, corresponding to Ce^{3+} ion. This notation emphasises the importance of lattice oxygen vacancies in the reduction process.

Ceria is a wide gap insulator and adopts the fluorite structure, which has a face centred cubic unit cell with $Fm\bar{3}m$ space group. Figure 3.1a shows a single unit cell which contains four Ce atoms. The cubic cell has six faces with six cerium atoms from the centre of each face shared with neighbouring cells giving a total of three Ce atoms per unit cell. The eight corners of the cube make up one whole Ce atom. Each Ce atom is coordinated by 8 nearest neighbour O atoms. The O atoms are tetrahedrally coordinated by 4 Ce.

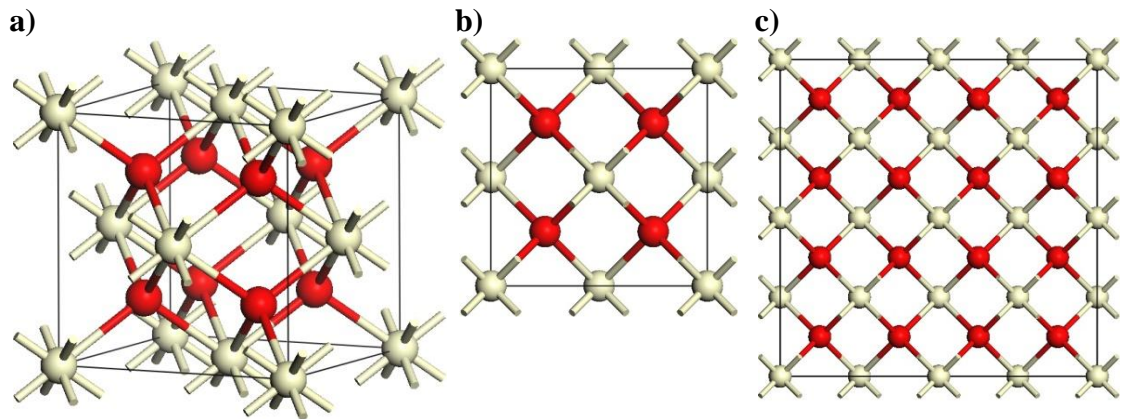


Figure 3.1 a) Single unit cell of bulk CeO₂. Side view of b) single unit cell and c) 2×2×2 expanded bulk supercell. Ce atom (white), O atom (red).

As mentioned earlier in Section 1.4.2, one of the challenges in theoretical and computational studies of ceria is to accurately describe the f states. The localization of electrons in f states accompanies the $Ce^{4+} \rightarrow Ce^{3+}$ reduction. Stoichiometric ceria is an insulator with an unoccupied Ce $4f$ band. When the material is reduced, this Ce $4f$ band becomes partially occupied and splits, with localised electrons corresponding to the Ce^{3+} ions in the narrow filled band.^{50, 169} These spatially localised Ce $4f$ filled states mean that ceria remains an insulator upon reduction. Studies have been done to investigate which two Ce atoms are reduced with the removal of an oxygen anion.^{50, 81, 82} All four Ce atoms in a single unit cell are sharing equivalent nearest neighbours of the oxygen anions in the cell. Thus, removing any of the oxygen will not change the fact that the Ce atoms are nearest neighbours and have equivalent symmetry

environment initially. The ionic radius of Ce³⁺ (1.283 Å) is larger than Ce⁴⁺ (1.11 Å).^{52, 53, 221} Thus, we would expect lattice strain to play a role in the choice of Ce sites to be reduced. In order to address this matter, a bulk supercell with a 2×2×2 expansion (Figure 3.1c) is required. Further details of this are presented in Section 3.2.

The overall aim of this chapter is to present and discuss the results from the application of different computational methods in describing stoichiometric and defective bulk ceria. Followed from that, we have continued using density functional theory with the on-site Coulomb interaction correction (DFT+U) method for the investigation of oxygen storage capacity in ceria. The ease of oxygen extraction from the lattice structure is determined from oxygen defect formation energies. These defect formation energies are dependent on the localisation of excess electrons on undoped and PGM doped ceria. The evaluation of energy barriers for oxygen diffusion to a nearby vacancy site will indicate the ease with which the O used at the surface can be replenished by transport of anions from the sub-surface or bulk.

3.2 Computational details

Periodic calculations were performed using Vienna *ab initio* simulation package (VASP)¹⁰⁻¹³ and CRYSTAL09^{14, 15}. In VASP, the core states were represented using the projected augmented wave (PAW) method.^{215, 216} The cerium atom's 5*s*, 5*p*, 5*d*, 4*f*, 6*s* and oxygen atom's 2*s*, 2*p* electrons were treated as valence electrons. The exchange-correlation interaction is treated using the generalised gradient approximation (GGA) applying the Perdew and Wang (PW91)^{197, 198} and Perdew-Burke-Ernzerhof (PBE)^{199, 200} functionals. Some of the calculations were performed using the hybrid functional method, Heyd-Scuseria-Ernzerhof (HSE06).²¹²⁻²¹⁴ HSE06 is implemented here with the mixing of 25% of non-local Fock exchange and 75% of PBE exchange, while the correlation functional corresponds to that of the PBE functional. A range separation parameter of 0.20 Å⁻¹ is used in HSE06 functional which splits the exchange energy term into short range and long range components. A plane wave cut-off of 500 eV was used throughout the calculations performed for this system. This cut-off value was determined through a test for the convergence of bulk lattice energy. The difference in energy calculated, using PW91 functional, between the cut-off energy of 450 and 500 eV is 0.037 eV, while between 500 and 550 eV is 0.001 eV.

Calculations within the DFT+U methodology (Section 2.1.4) were performed by applying the GGA functionals mentioned earlier with the supplement of Dudarev +U term²⁰¹ which will be the method focused on in this chapter. These calculations apply to models involving oxygen vacancies in the bulk. The U_{eff} value for Ce *f* orbital was set to 5.0 eV ($U=5.0$ eV, $J=0.0$ eV). U_{eff} is the combination of two parameters, $U_{eff}=U - J$, where U reflects the strength of the on-site Coulomb interaction, and J is the strength of exchange interaction, only the difference enters the Dudarev equations for the Hubbard term. Spin polarised calculations are applied throughout since unpaired electrons are involved when studying the defective bulk ceria. For the PW91 calculations, the interpolation for the correlation part of the exchange correlation functional is done according to Vosko, Wilk and Nusair.²⁰⁶ This usually enhances the magnetic moments and the magnetic energies and is usually applied in the context of gradient corrected functionals.

Through a series of calculations with different k -point grids ($3\times 3\times 3$, $5\times 5\times 5$, $7\times 7\times 7$, $9\times 9\times 9$, $11\times 11\times 11$, $13\times 13\times 13$), we have obtained convergence in bulk lattice energies and bulk modulus using the $7\times 7\times 7$ Monkhorst-Pack grid for single unit cell. The energies obtained are calculated with optimised bulk lattice parameter from each k -point grid. The energy difference from the optimised structures between $7\times 7\times 7$ and $13\times 13\times 13$ k -point grid is significant to three decimal places, where the minimum energy obtained are -105.54684 eV and -105.54713 eV, respectively.

The bulk moduli of bulk CeO₂ can be obtained from the calculations in VASP based on a set of structures with expansion factors of $\pm 3\%$ from the original experimental lattice parameter of 5.411 Å. An example of the quadratic fit and from the Murnaghan equation of state is shown in Figure 2.5 at Section 2.2.3. Through the same calculations, the optimal lattice parameters for the single unit cell are determined. A reduced k -point grid of $3\times 3\times 3$ is used for the larger real space unit cell of a bulk $2\times 2\times 2$ supercell. The bulk $2\times 2\times 2$ supercell is used for oxygen vacancy calculations because this larger cell provides 32 cerium atoms as localisation sites for the excess electrons instead of just 4 cerium atoms in the single unit cell. It also allows the lattice relaxation around a defect to be calculated with less defect–defect interaction than would be found for a single unit cell. Bulk calculations were set to converge when the forces on all atoms are less than 0.01 eV Å⁻¹ but 0.03 eV Å⁻¹ was used for calculations on supercells.

For the calculations of the defective bulk supercell of ceria, we have applied a method to generate different permutations of a pair of Ce³⁺ sites among the 32 Ce atoms using an in-house code written for pre- and post- processing of VASP calculations. Full details of this method have been explained thoroughly in Section 2.2.5. Results in reported theoretical work done by others, state that the energy difference between the ferromagnetic (FM) and anti-ferromagnetic (AFM) solutions is small.^{82, 169, 180, 181, 237, 238} Ganduglia-Pirovano *et al.* states that the difference between these two states is less than 5 meV.⁸² Therefore, we have decided to set the system to the ferromagnetic solution (or triplet state). This is done by setting the difference between α and β spins to 2 (NUPDOWN=2, in VASP INCAR file). The magnetic moment of the pair of Ce³⁺ sites are both set to +1.0 using the MAGMOM tag in the input file to aid the convergence of the system in a way that it will ensure that the calculations will arrive at the given magnetic ordering.

The conjugate gradient algorithm is used in the optimisation calculations to relax the ions into their instantaneous ground state. This self-consistent calculation will then generate the charge density using the k -point grid defined earlier. This charge density will be used for density of states (DOS) calculations. Density of state calculations requires finer k -meshes, so a non-self-consistent calculation is performed for density of states by reading the previous charge density generated and by increasing the k -point grid. The charge density is regenerated through a single point calculation for the optimised defective bulk without the NUPDOWN tag since it was used during the optimisation process. The usage of the tag during optimisation causes the shifting of the Fermi energy.

We have carried out atoms in molecules type Bader analysis²³² on the charge density generated by VASP to obtain atomic charges in the structure. This was done using a code developed by Henkelman's research group.^{12, 233-235} The Bader analysis assumes that charge density maxima are located at atomic centres so we need to include the LAECHG tag to reintroduce the core charges into the calculated density.

The ease of oxygen diffusion to a neighbouring vacancy site is studied in this chapter. Oxygen diffusion is modelled using a chain of 10 images interpolated between two end points of the optimised bulk supercells with one oxygen vacancy. In order to save time from optimising a whole set of end points for the structures with different Ce³⁺ localisation sites, we have constructed mirror images of

optimised structures from selected starting points to be the end point structures. These end point structures are re-optimised. Linear interpolation was done to produce the images using an in-house code for pre- and post-processing of VASP calculations which has also been applied by Willock and co-workers for the deprotonation of H₂O₂.²³⁹ We have applied the nudged elastic band method (NEB) to obtain the energy barrier for the diffusion of an oxygen anion to a neighbouring vacancy site. The transition state is determined with a frequency calculation and when only one imaginary mode is present. The same method is also used to obtain energy barriers for the migration of dopant metals (only 5 images were used) and charge compensation vacancy in doped CeO₂ systems.

Calculations performed using CRYSTAL09 are based on the expansion of the single particle wave functions as a linear combination of atomic orbitals (LCAO). These are described by a contraction of Gaussian type functions (GTF). We have also used the effective core pseudopotential (ECP) to represent fully occupied inner core orbitals for Ce. DFT calculations were performed using several different functionals based on the GGA functional. Hybrid functionals such as B3LYP^{240, 241}, B3PW^{196, 207, 208, 240} and PBE0²¹¹ were also used. B3LYP combines Becke's three parameter exchange and the non-local Lee-Yang-Parr correlation while in the B3PW the PW91 functional is used for the correlation. A mixing of 20% Fock exchange is introduced in both the B3LYP and B3PW hybrid functional. In PBE0, a mixing of 25% Fock exchange is introduced with the PBE exchange-correlation functional.

We have applied the reconfigured 8-411G* basis set with its most diffuse functions re-optimised by Désaunay *et al.*¹⁷⁶ The inner core electrons for Ce atoms can be replaced by two different types of ECPs. The first one being defined as large core where the shells *1s-4d* are occupied with 46 electrons in total leaving 12 valence electrons. This approach is similar to the PAW pseudopotentials of Ce implemented in VASP which has the same number of valence electrons. The second type of ECP is the small core in which shells *1s-3d* are occupied with 28 electrons in total leaving 30 explicit valence electrons. These two types of ECP lead to several different approaches in tailoring the relevant basis set for the Ce atoms. Also mentioned in the report by Désaunay *et al.*,¹⁷⁶ the large core pseudopotentials neglecting the *4f* electrons completely has been tested by Gennard *et al.*¹⁶² Secondly, the *4f* electrons can be described implicitly in a large core pseudopotential similar to the core state model (CSM)²⁴² reported by Skorodumova *et al.* where more than 46 electrons are

taken into the core. In a third approach, the $4f$ electrons can be described explicitly, using either small core or large core pseudopotentials. We have performed calculations using the small core and large core pseudopotential with and without the $4f$ contraction functions, respectively.

The small core and large core pseudopotentials used were both constructed by the Stuttgart/Cologne group.^{224, 229} These are quasi-relativistic pseudopotentials generated using the neutral atom as reference system. The large core and small core pseudopotentials used are termed ECP46MWB²²⁴ and ECP28MWB²²⁹, respectively. A modified double zeta (mRSC) basis set²²⁹ for the Ce atom has been used with the ECP28MWB. This is adapted from Désaunay *et al.* where they have reconstructed the basis set by removing the $8s$, $7p$, and $7d$ diffuse functions and reoptimising the $7s$, $6p$, $5d$, and $5f$ polarization functions.¹⁷⁶ The original $4s$, $4p$, $4d$, and $4f$ contractions were taken from the RSC1997-AVDZ basis set^{225, 226} to explicitly treat the electrons with principal quantum number of 4. As for the ECP46WB, the double zeta basis set developed by Dolg and co-workers²²⁹ was used. The parameters of the basis sets and ECP used can be found in Appendix A1.

Full optimization has been performed on bulk calculations allowing the atom coordinates and cell parameters to be fully relaxed. The threshold on energy change between optimization steps was set to less than 10^{-8} hartree. Convergence criterion on the root mean square (RMS) of the gradient and displacement were set to 0.00006 hartree bohr⁻¹ and 0.00012 bohr, respectively. A check is done by setting FINALRUN=4 which performs a single point energy and gradient calculation on the final structure from a geometry optimisation. Optimization is restarted if the convergence criteria on gradients are not satisfied and will iterate to ensure a full stable optimization of the structure. Eigenvalue level shifting of 0.4 hartree is applied in the calculation. This adds a negative energy shift to the diagonal Fock/KS matrix elements of the occupied orbitals, thus reducing their coupling to the unoccupied set. The shift is maintained after diagonalization. A 40% of Fock/KS matrices mixing is used throughout the bulk calculations. The truncation criteria for bielectronic integrals for the Coulomb and HF exchange series are reconfigured. The overlap and penetration threshold for Coulomb integrals, and the overlap threshold and pseudo-overlap for HF exchange integrals were set to 10^{-7} . The final parameter in the truncation criteria is set to 10^{-14} for the pseudo-overlap. The bulk ceria is sampled

using a 9×9×9 Monkhorst-Pack k -point mesh. A second shrinking factor of 9 is used, which defines the sampling of k -points also termed “Gilat net”.^{243, 244}

In CRYSTAL09, the energy against volume curves were computed automatically with the built in function. This performs a constant volume geometry optimization for each point and the results were fitted to the Murnaghan equation of state.

Atomic charges of the structures optimised using CRYSTAL09 are obtained through Mulliken population analysis.²⁴⁵ Since we have used level shifter in the previous optimization calculation, a new set of Hartree-Fock/KS eigenvectors and eigenvalues have to be computed before running a calculation to obtain the density of states so that the correct Fermi energy and eigenvalues spectra are obtained. Band structure calculations are calculated by specifying the high symmetry k -points of a given path in the Brillouin zone.

3.3 Stoichiometric bulk structure of ceria

The experimental lattice parameter reported for ceria is 5.411 Å.³¹ For the experimental bulk modulus, a variety of values from 204 to 236 GPa have been reported in literature using different methods.^{31, 32, 34, 35} The Brillouin scattering technique has given a bulk modulus of 204 GPa³⁵ which is the lowest among the rest that were obtained using X-ray diffraction technique. These are tabulated in Table 3.1 together with the computed values of lattice parameters, bulk moduli, and band gaps calculated using various GGA and hybrid functionals applying the plane waves and all electron basis set approach.

Overall all computed values for the lattice parameters of ceria are higher than the reported experimental lattice constant (5.411 Å) by between 0.35% and 2.14%. This trend is also shown in other theoretical work referenced in Table 3.1. From the computed results using the plane waves approach, nearest agreement is obtained using the HSE06 hybrid functional. This yielded a lattice parameter of 5.472 Å which is greater by about 1% from the experimental value. While in standard DFT calculations using GGA functionals, the lattice parameter values produced are 0.01 Å larger (< 0.02%) than HSE06 results for both PW91 and PBE. Partly due to the method of calculation, where we have restarted the HSE06 calculation from the wavefunctions and structures obtained from the initial PBE calculations for lattice expansions. There are reasons for doing so, as suggested in the VASP manual that it

reduces the computation time and partly due to the correlation part of HSE06 is described using PBE functional.

Table 3.1 Experimental and computed values for lattice parameter (a_0), bulk modulus (B_0), and Ce–O bond length of bulk ceria using various methods. Bulk modulus in bracket are values from quadratic fitting. (self-interaction corrected local spin density (SIC-LSD) approximation)

Methods	$a_0 / \text{Å}$	B_0 / GPa	Ce–O bond length / Å
VASP			
- PW91	5.480	173 (210)	2.37
- PBE	5.479	173 (208)	2.37
- PW91+U ($U_{\text{eff}}=5 \text{ eV}$)	5.509	182 (194)	2.39
- PBE+U ($U_{\text{eff}}=5 \text{ eV}$)	5.504	181 (207)	2.38
- HSE06	5.472	188 (185)	2.37
CRYSTAL09			
LC			
- PW91	5.523	193	2.39
- PBE	5.527	191	2.39
SC mRSC basis set			
- PW91	5.514	152	2.39
- PBE	5.518	150	2.39
- PBE0	5.430	188	2.35
- B3PW	5.453	179	2.36
- B3LYP	5.506	168	2.38
Experimental			
- Brillouin scattering	-	204 ^a	-
- X-ray diffraction	5.411 ^{b,c} , 5.406 ^d	236±4 ^b , 220±9 ^c , 230±10 ^d	-
Other theoretical studies			
- SIC-LSDA ^d	5.384	176.9	-
- PW91 ^e	5.48	187.7	-
- PW91+U ($U_{\text{eff}} = 3 \text{ eV}$) ^{f,g}	5.48	187.0 ^f	-
- PW91+U ($U_{\text{eff}} = 5 \text{ eV}$) ^g	5.49	-	-
- PBE+U ($U_{\text{eff}} = 5^h, 4.5^i \text{ eV}$)	5.49	180 ⁱ	-
- PBE0 (PAW) ⁱ	5.39	-	-
- PBE0_mRSC ^j	5.423	-	-
- B3LYP_mRSC ^j	5.503	-	-
- PBE_mRSC ^j	5.515	-	-

a Ref.³⁵; *b* Ref.³¹; *c* Ref.³²; *d* Ref.³⁴; *e* Ref.²⁴²; *f* Ref.¹⁶⁶; *g* Ref.¹⁶⁷; *h* Ref.¹⁶⁸; *i* Ref.¹⁷⁸; *j* Ref.¹⁷⁶

The inclusion of an on-site Coulomb interaction correction term (DFT+U) has somehow caused a larger expansion of the bulk cell of ceria compared to the other

computed, experimental, and reported theoretical values. However, this agrees with the observation reported by Andersson *et al.* where the expansion in lattice of the system occurs with an increasing U value applied to the Ce 4*f* states.¹⁸¹ Energies and volume computed from lattice expansion are fitted to two equations: 1) the quadratic equation, where values are reported in brackets in Table 3.1; 2) the Murnaghan equation of state. The bulk moduli obtained through the quadratic fit are within 5% of the Brillouin scattering data reported.³⁵ Whereas, the values obtained through the Murnaghan equation of state fit are much lower compared to all the experimental values shown in Table 3.1.

As for the basis set approach, the best agreement with respect to experimental lattice parameter is from using PBE0 hybrid functional. Our results also agree well with the theoretical work reported by Desautay *et al.*, showing that the PBE0 calculation gives the nearest lattice parameter to experimental value.¹⁷⁶ The values obtained from these two approaches differ even by using the same functional is very likely due to the cut-off value and basis sets used. Bulk moduli calculated in the basis set approach are smaller than the values obtained from VASP calculations and experimental values reported in literature.^{31, 32, 34, 35}

Next, we have calculated the density of states for bulk ceria using the two approaches applying different functionals. Figure 3.2 shows the total density of states plots from plane waves and all electron basis sets calculations.

For DOS plots generated from VASP calculations, plots above the y axis are the spin up states and below are the spin down states. The calculated density of states for PW91+U and PBE+U using VASP (in Figure 3.2a), and for PBE0, B3LYP, and B3PW using CRYSTAL09 (in Figure 3.2b) yield similar results, in terms of band gaps which are reported in Table 3.2, as the electronic structure reported in experiment^{163, 179}. The band gap values are measured from edge to edge of the bands involved. As expected, the standard DFT has its shortcomings of underestimating band gaps which may be caused by the self-interaction problem. While DFT+U and hybrid methods give good agreement with experimental results for O 2*p* – Ce 4*f* band gap of 3.0 eV¹⁶³ and 3.2 eV¹⁷⁹. Table 3.2 shows the computed and experimental O 2*p* – Ce 4*f*, and O 2*p* – Ce 5*d* band gaps using various methods. When referring to band gaps, the conduction band is usually the *d*-band for the *d*-block metals of the periodic table. In our case, when the cerium atom receives an electron it will fill the

4*f* orbitals first rather than the 5*d* orbitals. So, the O 2*p* – 4*f* band gap is also measured here as the 4*f* band will shift along the energy level compared to the 5*d* band.

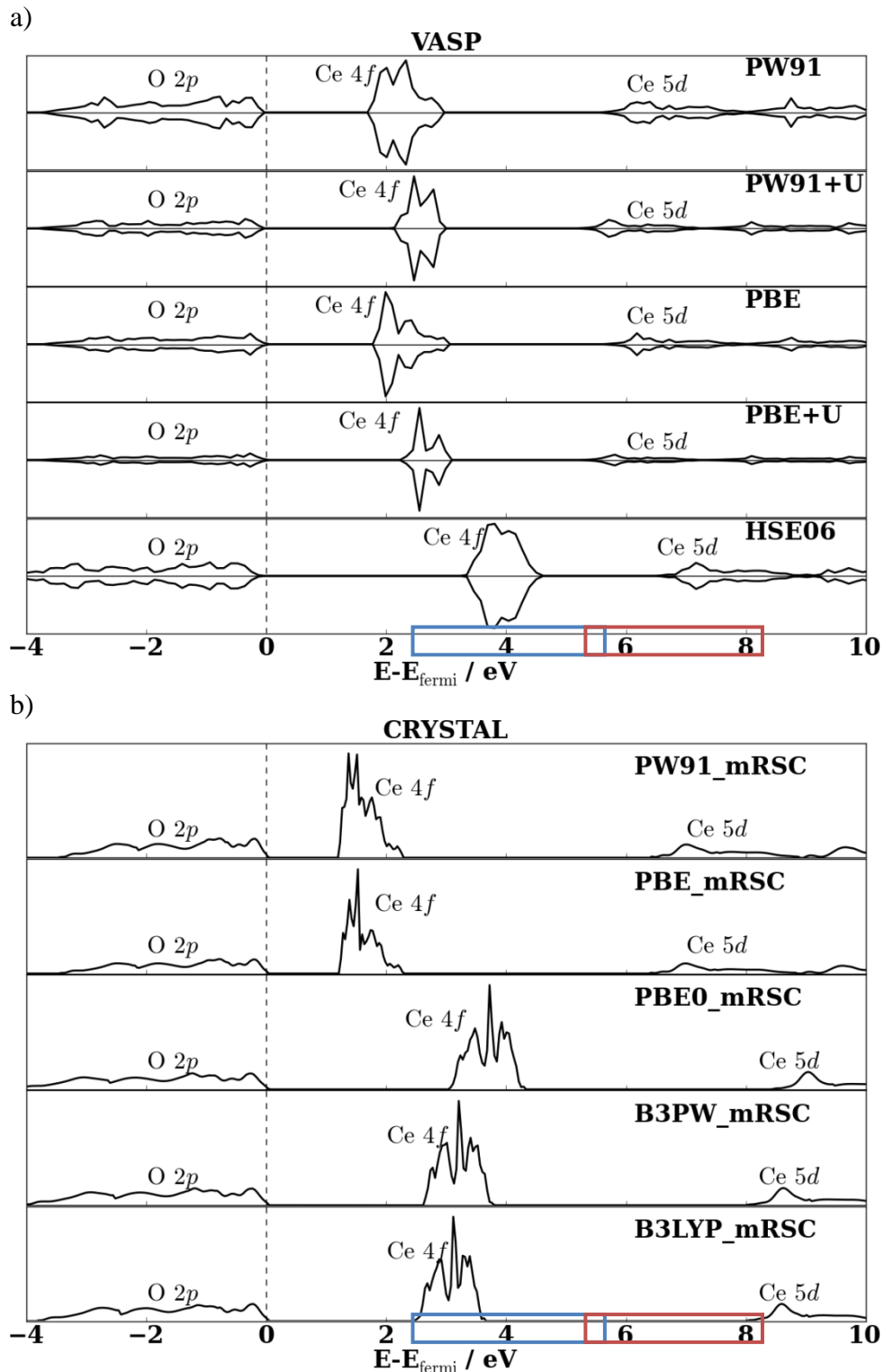


Figure 3.2 Total density of states plot of bulk CeO₂ computed using a) VASP and b) CRYSTAL09. The vertical dashed lines indicate the Fermi energy corrected to 0 eV. Rectangular boxes on *x*-axis indicate the common experimental values for O2*p* – Ce4*f* (blue box) and O2*p* – Ce5*d* (red box) band gap obtained using various methods

including X-ray photoelectron spectroscopy (XPS)^{72, 163}, bremsstrahlung isochromat spectroscopy (BIS)¹⁶³, photoluminescence analysis²⁴⁶, optical reflectivity¹⁷⁹, and high resolution electron energy-loss spectroscopy (HREELS)⁷².

Table 3.2 Experimental and computed values for O 2*p* – Ce 4*f* and O 2*p* – Ce 5*d* band gaps of bulk ceria using various methods.

Methods	Band gaps / eV	
	O 2 <i>p</i> – Ce 4 <i>f</i>	O 2 <i>p</i> – Ce 5 <i>d</i>
VASP		
- PW91	1.7	5.5
- PBE	1.7	5.5
- PW91+U (U _{eff} =5 eV)	2.2	5.2
- PBE+U (U _{eff} =5 eV)	2.3	5.1
- HSE06	3.2	6.6
CRYSTAL09		
Small core with mRSC basis set		
- PW91	1.2	6.8
- PBE	1.2	6.8
- PBE0	3.1	8.8
- B3PW	2.7	8.4
- B3LYP	2.6	8.4
Experimental		
- XPS and BIS spectra ^a	3.0	6.0
- Optical reflectivity measurements ^b	3.2	~6.0
Other theoretical studies		
- PW91+U (U _{eff} = 3 eV) ^{c,d}	~2.0 – 2.1 ^e	~5.4 – 5.5
- PW91+U (U _{eff} = 5 eV) ^d	~2.2 – 2.3	~5.3
- PBE+U (U _{eff} = 5 eV) ^e	~2.4	~5.3
- PBE0 (PAW) ^e	~4.5	7.93
- PBE0_mRSC ^f	2.95	8.45
- B3LYP_mRSC ^f	2.39	8.06
- PBE_mRSC ^f	1.26	6.46

^a Ref.¹⁶³; ^b Ref.¹⁷⁹; ^c Ref.¹⁶⁶; ^d Ref.¹⁶⁷; ^e Ref.¹⁷⁸; ^f Ref.¹⁷⁶

Standard DFT calculations in VASP underestimated the O 2*p* – Ce 4*f* band gaps by almost half the experimental value of 3.0 eV reported by Wuilloud *et al.*,¹⁶³ which are giving 1.7 eV for both PW91 and PBE. The on-site Coulomb interaction correction applied on Ce 4*f* orbitals has produced slightly improved results for the O2*p* – Ce 4*f* band gaps. The calculations from PW91+U and PBE+U yield a band gap of 2.2 and 2.3 eV, respectively. However, the O 2*p* – Ce 5*d* band gap decreases from 5.5 eV (both PW91 and PBE) to 5.2 eV and 5.1 eV for PW91+U and PBE+U. Such occurrence of decreasing O 2*p* – Ce 5*d* band gap has also been observed and reported in literature.¹⁶⁶

Using CRYSTAL09, PW91 and PBE calculations both yield a value of 1.2 eV and 6.8 eV for the O 2*p* – Ce 4*f* and O 2*p* – Ce 5*d* band gaps, respectively. Hybrid methods such as PBE0, B3LYP, and B3PW have produced O 2*p* – Ce 4*f* band gap of about 3 eV, 2.5 eV, and 2.8 eV, respectively. PBE0 has improved the O 2*p* – Ce 4*f* band gap and agrees excellently with the experimental value. However the O2*p* – Ce 5*d* band gap is overestimated in the hybrid calculations. Three of the functionals yield a gap from 8 – 9 eV, which is overestimated about 2 eV in comparison to the experimental value of 6 eV.¹⁶³ The inclusion of 20% HF exchange to both the B3LYP and B3PW hybrid functionals has increased the O2*p* – Ce 5*d* band gap by 1.6 eV when compared to PW91 and PBE results. A bigger increment (by 2 eV) is seen with PBE0 as a 25% exact HF exchange is applied in this functional. This overestimation is expected from the HF approximation.^{161, 162}

Overall our band gap values calculated from DFT+U and hybrid methods are reasonable when comparing to a range of experimental values we have obtained from literature.^{167, 176, 178} Due to some uncertainties in the determination of the precise value of band gaps in various reported experimental works, as mentioned by Castleton *et al.*¹⁸⁰, we have chosen the O 2*p* – Ce 4*f* band gap value in the range of 2.6 to 3.4 eV referring to the reported data from XPS^{72, 163}, BIS¹⁶³ and photoluminescence analysis²⁴⁶. As for the O 2*p* – Ce 5*d* band gap, we have chosen the range 5.4 to 6.6 eV following the measurements reported by optical reflectivity¹⁷⁹ and HREELS⁷².

3.4 Structural and electronic properties of defective bulk ceria

We have investigated the oxygen deficient bulk ceria. The defect structure requires 2 Ce sites to be reduced. Using the 2×2×2 supercell, a number of permutations were generated to check the localisation sites of the excess electrons which can occur at nearest neighbour (N), and next nearest neighbour (NN) with respect to the oxygen vacancy site. Details regarding the generation of these structures have been explained in Chapter 2.2.5. There are 4 N, 12 NN (4.57 Å away from vacancy site), and 12 NN* (6.01 Å from vacancy site) sites so a total of 378 reasonable permutations were generated. Since there are pairs of Ce³⁺ sites that have similar symmetry environments, only 17 unique permutations were chosen to be investigated among the 378 permutations generated. Calculations were performed on these 17 structures and oxygen vacancy formation energies are computed using

$$E_{vac} = E(CeO_{2-x}) - E(CeO_2) + \frac{1}{2}E(O_2) \quad (3.3)$$

where (CeO_{2-x}) is the system with an oxygen defect, CeO₂ and O₂ are the stoichiometric CeO₂ system and gas phase oxygen, respectively. From Equation (3.3), more positive vacancy formation energy signifies an endothermic process.

Table 3.3 Oxygen vacancy formation energy, E_{vac} , calculated using PW91+U and PBE+U together with the total number of structures generated with similar symmetry environment. Nearest neighbour (N) and next nearest neighbour (NN). NN and NN* corresponds to 4.57 Å and 6.01 Å away from vacancy site, respectively.

Structures	Localisation sites	E_{vac} / eV		Total number of structures with similar symmetry
		PW91+U	PBE+U	
A	NN_NN	2.45	2.43	12
B	NN_NN	2.46	2.44	24
C	NN_NN	2.46	2.43	30
D	NN_N	2.50	2.43	12
E	N_N	2.51	2.49	6
F	NN_N	2.53	2.51	24
G	NN_N	2.56	2.53	12
H	NN_NN*	2.60	2.58	60
I	NN*_NN	2.64	2.56	12
J	NN*_N	2.65	2.58	24
K	NN*_NN	2.66	2.63	48
L	NN*_N	2.70	2.63	12
M	NN*_NN*	2.72	2.70	12
N	NN*_NN*	2.73	2.71	24
O	NN*_NN*	2.79	2.77	30
P	NN_NN*	2.57	2.56	12
Q	NN*_NN	2.85	2.67	24

Table 3.3 shows the oxygen vacancy formation energy (E_{vac}) calculated using PW91+U and PBE+U for each structure generated and the total number of structures with Ce³⁺ pairs of similar symmetry environment. We found that the spins localized on two next nearest neighbours Ce atoms with respect to the oxygen vacancy site gave the lowest oxygen formation vacancy energy, with E_{vac} of 2.45 eV and 2.43 eV, using PW91+U and PBE+U, respectively. The isosurface of spin density for this lowest E_{vac} structure calculated using PW91+U is shown in Figure 3.3.

The structure with both Ce³⁺ sites at nearest neighbour gave an E_{vac} of 2.51 eV. This is just 0.06 eV higher compared to the lowest E_{vac} obtained. Thus, explaining

the possibility of getting localised electrons on nearest neighbour Ce atoms and the results reported in other theoretical work as this can be one of the local minimum with an energy that is not much different from the global minimum obtained here. Nolan *et al.*⁶⁴, Keating *et al.*²³⁸, and Scanlon *et al.*¹⁶⁸ have each reported the oxygen vacancy formation energy to be 3.39 eV, 2.11 eV, and 2.62 eV, respectively. Keating *et al.* also showed that the increase in CeO₂ bulk cell size (from 1×1×1 to 2×2×2) reduces the E_{vac} . The energy difference between the lowest and second lowest computed E_{vac} are 0.01 eV apart, which is not significantly large. Generally structures with Ce³⁺ at NN_NN sites are energetically most stable among the entire defect structures (refer Table 3.3).

In this PW91+U optimised structure (Figure 3.3a), the Ce³⁺ sites are 7.78 Å apart after optimization. The distances of the Ce³⁺ sites from the vacancy site (using the coordinates of the oxygen prior to removal) are both 4.56 Å. By checking the atom coordinates of this optimised structure, we can observe that the neighbouring oxygen atoms of the vacancy site have relaxed inwards to the site with O--O distance ranging from 2.48 Å to 2.58 Å, which are shorter than the distance (2.76 Å) obtained from an optimised stoichiometric bulk. However, the four neighbouring Ce⁴⁺ ions are pushed further away from the site with the increase of the Ce–O bond length from 2.39 Å to 2.55 Å.

The data are also presented as a histogram (Figure 3.4a) with a bin size of 0.05 eV. From the histogram, a large number of structures (84) fall in the E_{vac} range of 2.625 – 2.675 eV. Followed by the E_{vac} range of 2.425 – 2.475 eV with 66 structures. Similar trend is observed from PBE+U results, except that the E_{vac} ranges 2.575 – 2.625 eV and 2.625 – 2.675 eV have the same number of structures. All these shows that the possibility of getting structures with the lowest E_{vac} configuration is not low. Furthermore, these DFT calculations are performed with temperature at 0 K.

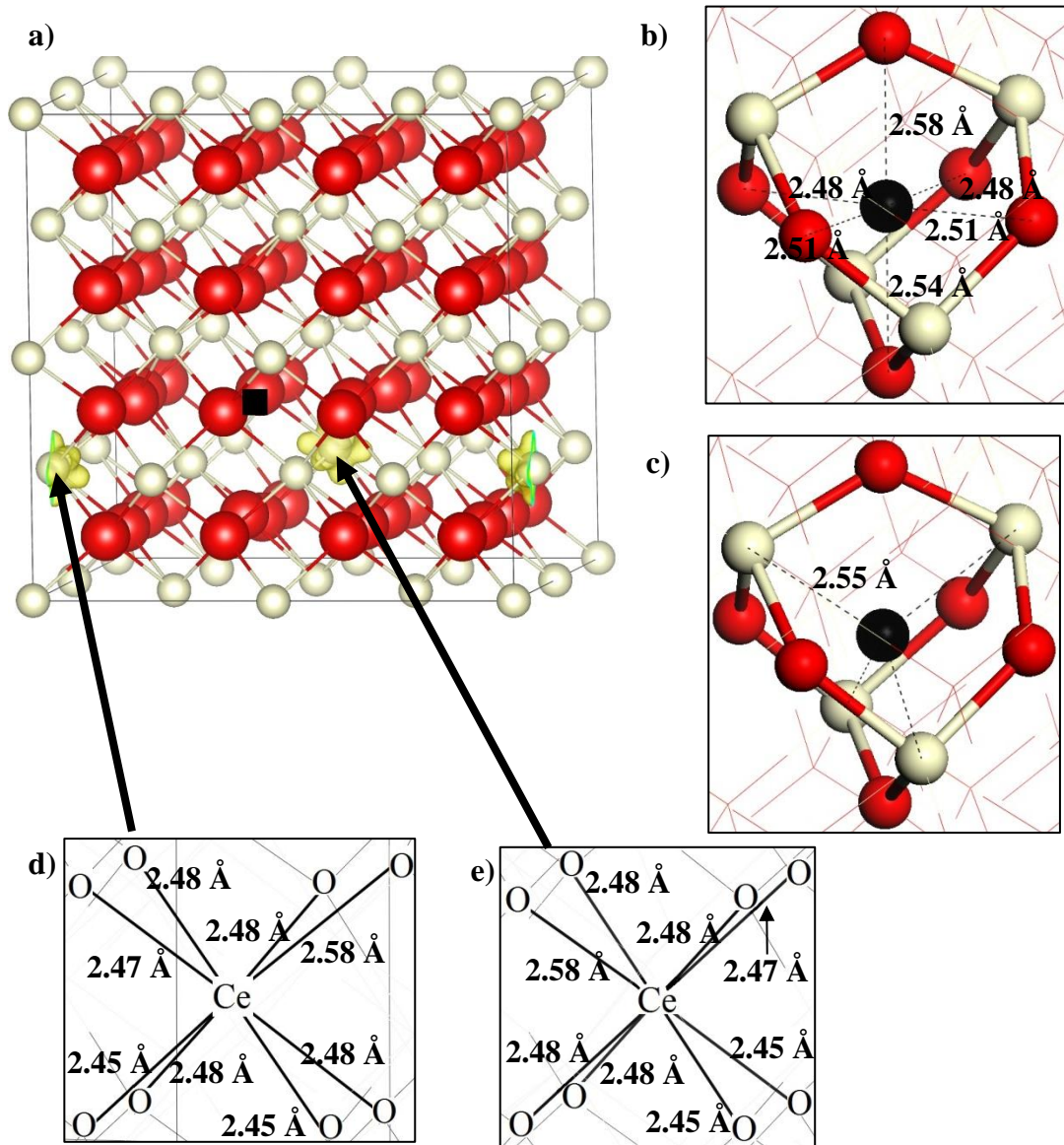


Figure 3.3 a) Isosurface of spin density for defective bulk ceria with the lowest E_{vac} produced from PW91+U calculation. Isosurface level is 0.04 electrons \AA^{-3} . O is red, Ce is white. Black box/atom is the vacancy site. Distances of immediate b) oxygen and c) cerium neighbours from the vacancy site. d) & e) Ce – O bond lengths at the Ce^{3+} sites.

At higher temperature, the energy gained from thermal heating will allow higher energy structures to be populated. In this case where the energy levels of the system are degenerate, the canonical partition function in terms of the contribution from the different energy levels can be written as

$$Z = \sum_j g_j e^{-\beta E_j} \quad (3.4)$$

where g_j is number of structures with energy E_j from different energy levels. Figure 3.5 shows the distribution of defect structure with different localisation sites at 300 K

and 700 K. We can clearly see that there is some increase in the population of defect structures with higher E_{vac} when the temperature is increased from 300 K to 700 K.

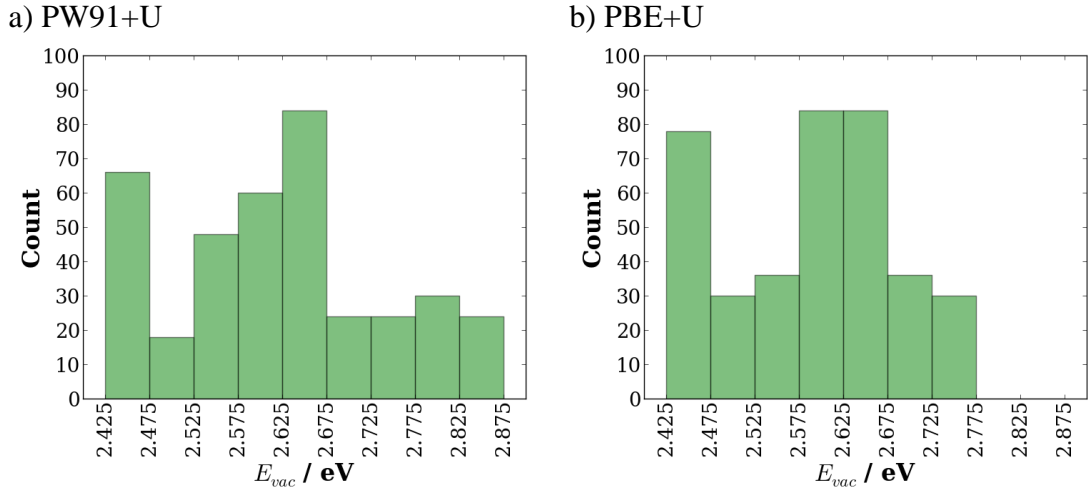


Figure 3.4 Histogram showing the number of structures in different ranges of E_{vac} obtained from a) PW91+U and b) PBE+U calculations.

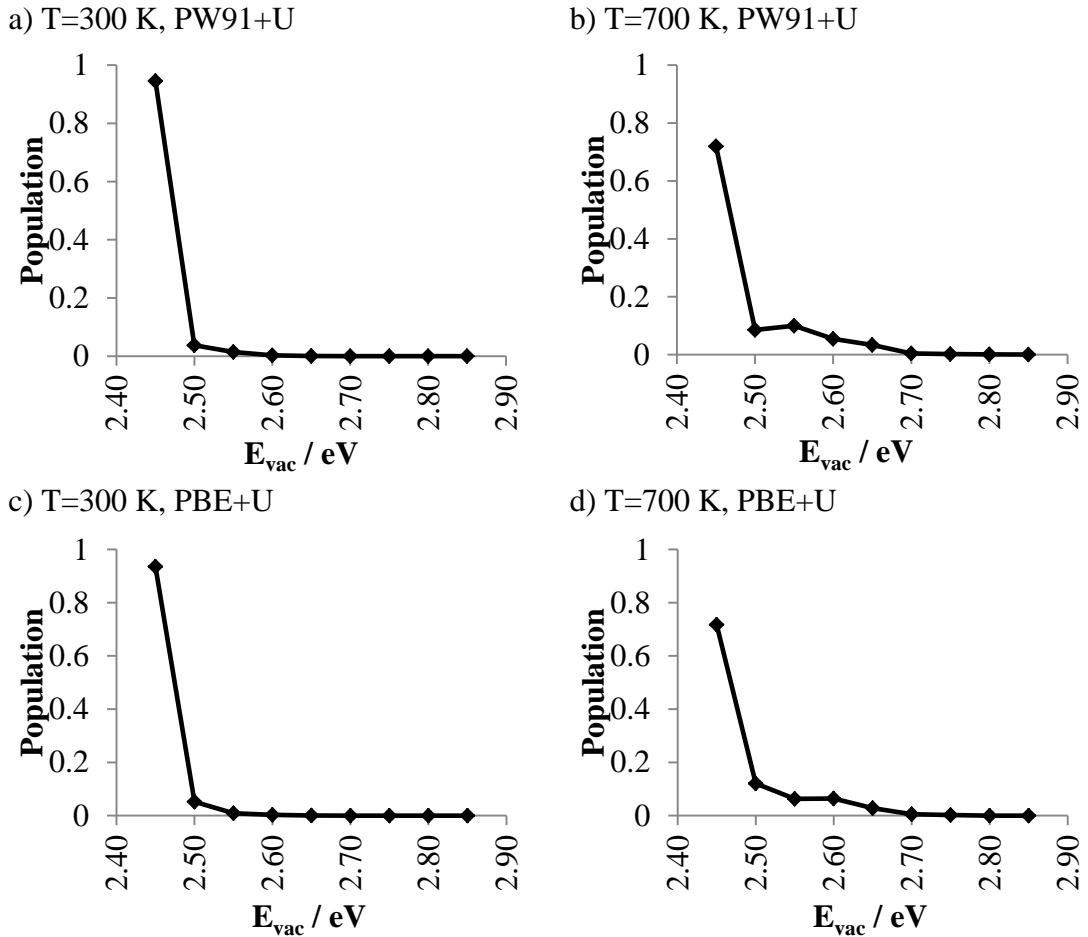


Figure 3.5 Distribution of defect structure with different localisation sites at a, c) 300 K and b, d) 700 K following Equation (3.4) using vacancy formation energies, E_{vac} , calculated with PW91+U and PBE+U, respectively.

The density of states for the lowest energy structure is shown in Figure 3.6. Figure 3.6 shows that there are gap states (indicated by arrow in Figure 3.6a), which lies about 1.2 eV above the valence band. This gap state reflects the presence of the reduced Ce³⁺ ions due to the splitting of the Ce 4*f* band split upon the occupation of one electron each for the two Ce³⁺ ions. The single peak indicates that the two Ce³⁺ cations are in a similar chemical environment. Two peaks were observed for structure P's DOS (Figure 3.6b) with a gap of about 0.16 eV apart. These two peaks correspond to two non-equivalent Ce³⁺ cations. As for structure Q's DOS (Figure 3.6c), it is observed that the two 4*f* peaks for Ce³⁺ cations are further apart. This is due to electrons being localised on two non-equivalent Ce³⁺ cations and also in different *f*-orbitals (refer to Figure A1 in Appendix A2 for spin density plot). This solution has also caused the E_{vac} for this structure to increase ($E_{vac} = 2.85$ eV).

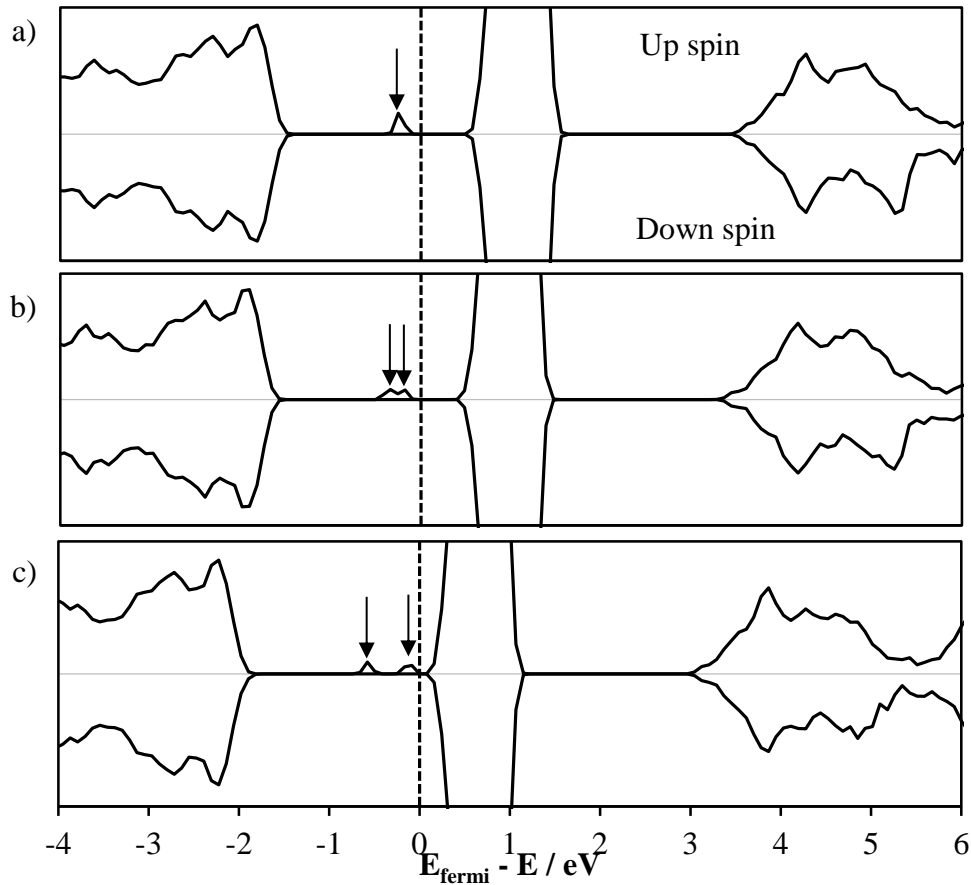


Figure 3.6 Total density of states (DOS) for defective ceria from structures a) **A**, b) **P**, and c) **Q** (refer Table 3.3) using PW91+U. The vertical dashed line indicates the Fermi energy corrected to 0 eV. The y-axis for total DOS and partial Ce³⁺ 4*f* are of different scale. Gaussian smearing width of 0.01 eV is applied.

After gaining some insight of the localisation of excess electrons in a defective bulk ceria, we have moved on to study the oxygen migration in the system. This will

provide information on the ease of oxygen diffusion to the vacancy site. For this, we have presented the oxygen migration energy barrier calculated using the NEB method in Figure 3.7.

Our results show that the energy barrier (E_a) for neighbouring oxygen to migrate to the vacancy site is about the same ($\Delta E_a = 0.02$ eV) regardless of whether the Ce³⁺ sites have shifted or not, providing that the end structure is the most stable arrangement with Ce³⁺ at NN_NN sites. This can be observed from the plots with black and red markers (Figure 3.7). The plot with black markers in Figure 3.7 shows the E_a (0.48 eV) for the oxygen to migrate to a vacancy site in a system with the lowest energy structure (structure A from Table 3.3). In this situation, the end structure is the mirror image of structure A (A*) which also gives an E_{vac} of 2.45 eV. The Ce³⁺ sites remained unchanged throughout the migration process as the sites are equidistant from the vacancy site on both the initial and end structures. An E_a of 0.46 eV is obtained (red markers in Figure 3.7) when the oxygen migration starts from structure A and ended up with the configuration of the mirror image of structure B (B*). In this process, the Ce³⁺ sites have moved along with the oxygen migration.

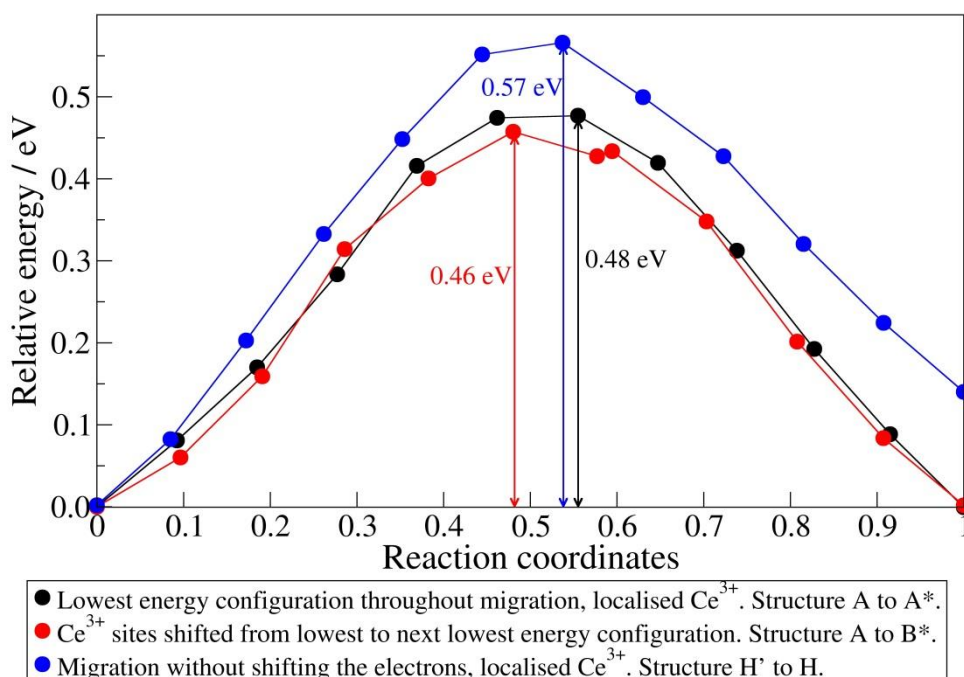


Figure 3.7 Oxygen migration energy barriers obtained from three different NEB calculations using PW91+U. Energies presented are relative to lowest energy configuration. Refer to Figure A2 in Appendix A3 for images of start and end structures used.

In the third NEB calculation (blue markers in Figure 3.7), we have used structure H, which has the NN_NN* localisation sites and the most structures with similar symmetry environment, as the end point (refer Table 3.3). For its starting point, we have used arrangement of structure H but with the vacancy site at an opposite position (H^o). This is done to model the migration of oxygen to the vacancy site without shifting the electron (i.e. the Ce³⁺ sites) starting from a more stable structure. The reason for the starting structure to be at lower energy is that it has a structure of any of the NN_NN localisation sites (refer Table 3.3), which generally are at lower energy range of the entire defect structures, rather than the NN_NN* or NN*_NN localisation sites. Oxygen migration in this system yields an E_a of 0.57 eV which is higher than the other two oxygen migration studied. This also explains that when the system is at 700 K (refer to Fig. 3.5b), the distribution of defect structures at localisation sites with higher energy increased with the decrease of the lower energy structures as the energy barrier of 0.57 eV can be overcome by the increase in temperature.

3.5 Doping bulk ceria with platinum group metals (PGM)

In this section, work on PGM doped ceria will be presented. Bulk ceria has been doped with platinum or palladium. The model structures for doping with a tetravalent Pd or Pt cation are created by replacing one of the Ce atoms with a dopant atom. As for divalently doped system, a pair of Ce and O atoms is replaced with one dopant atom. The process of the formation of a divalently doped system can be described as



while the tetravalently doped system can be described as



The doped systems are modelled by placing the dopants at two different starting points in the lattice: 1) at the Ce site (CS) and 2) at a square planar position (SPP) with four neighbouring oxygen atoms. The optimised structures of Pd and Pt doped bulk ceria are shown in Figure 3.8 and Figure 3.9, respectively.

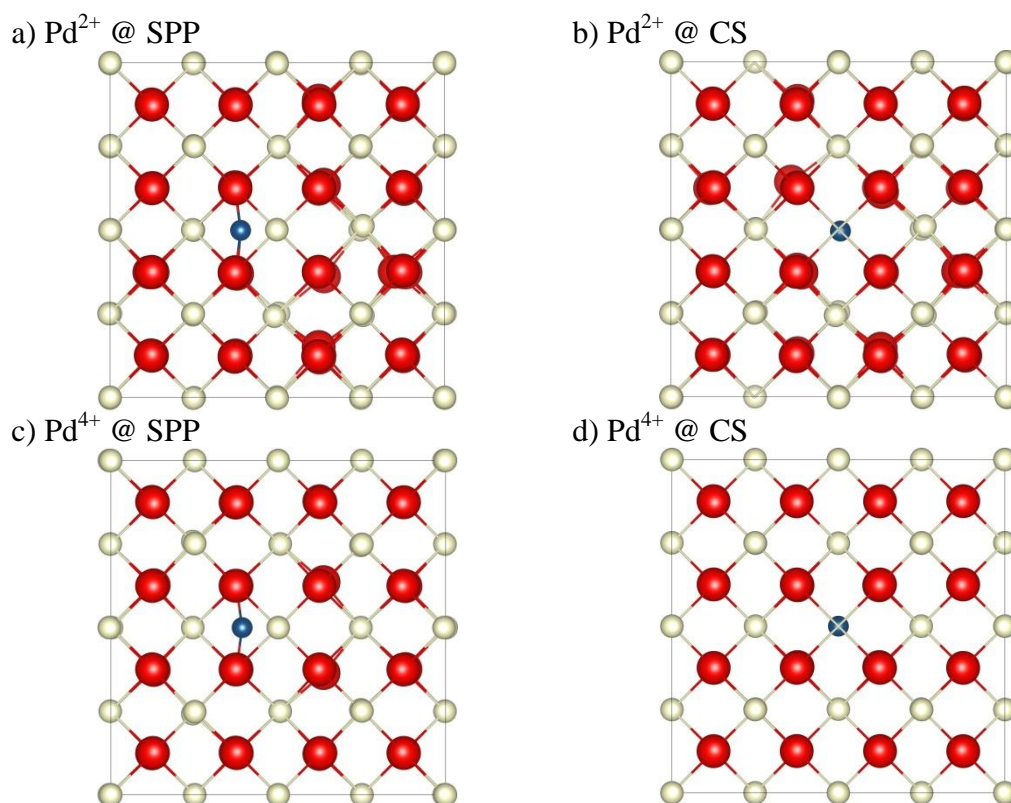


Figure 3.8 Side views of optimised structures of Pd²⁺ and Pd⁴⁺ doped ceria at a) & c) square planar position (SPP), respectively, and b) & d) cerium site (CS), respectively using PW91+U. Cerium (white), oxygen (red), and palladium (blue).

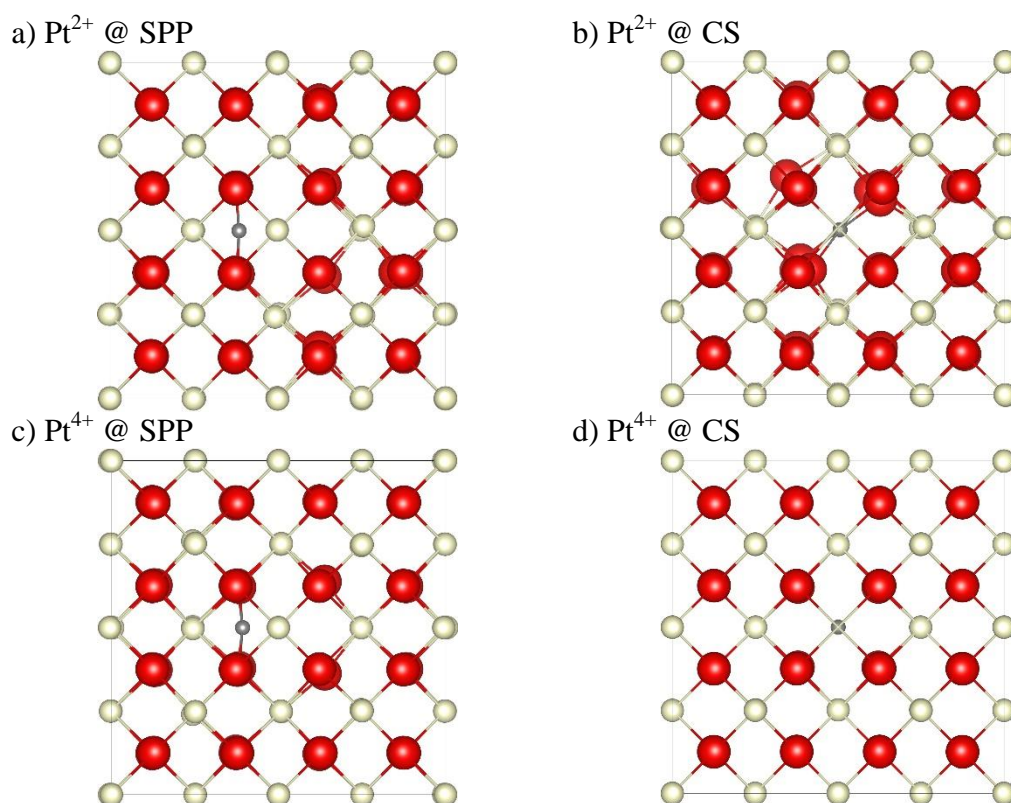


Figure 3.9 Side views of optimised structures of Pt²⁺ and Pt⁴⁺ doped ceria at a) & c) square planar position (SPP), respectively, and b) and d) cerium site (CS), respectively using PW91+U. Cerium (white), oxygen (red), and platinum (grey).

After optimizing the doped system, slight relaxation of the atoms is observed for both positions but more significant relaxation is seen in Pt²⁺ doped ceria at CS (refer to Table 3.4 for Pd/Pt–O distances). Pd⁴⁺ and Pt⁴⁺ at CS did not move much as the neighbouring Pd/Pt–O distances are not significantly different from the optimised Ce–O bond length of 2.39 Å (refer to Table 3.1). Similarly for Pd²⁺ cation at CS, only one of its neighbouring oxygen atoms moved further from the dopant giving a Pt–O distance of 2.81 Å. On the other hand, six of the neighbouring oxygen atoms have relaxed towards the Pt²⁺ cation at CS causing the Pt–O distances to be shorter than the optimised bond length of Ce–O of 2.39 Å. This may be due to the smaller ionic radius of a 6-coordinated platinum (0.94 Å) compared to the 6-coordinated palladium (1.00 Å) for the +2 oxidation state.^{52, 53, 221}

Table 3.4 Calculated Pd/Pt–O distances for Pd/Pt doped ceria using PW91+U together with the distances reported from literature.

Pd/Pt–O distances / Å							
SPP	O1	O2	O3	O4	O5	O6	O7
Pd ²⁺	2.01	2.02	2.01	2.01			
Pt ²⁺	2.01	2.01	2.01	2.01			
Pd ⁴⁺	1.96	1.96	1.96	1.96			
Pt ⁴⁺	1.89	1.98	1.89	1.98			
CS	O1	O2	O3	O4	O5	O6	O7
Pd ²⁺	2.39	2.81	2.38	2.32	2.32	2.39	2.32
Pt ²⁺	2.09	3.04	2.10	2.10	2.10	2.10	2.11
Pd ⁴⁺				all 2.34			
Pt ⁴⁺				all 2.31			
Experimental Pd/Pt – O distances / Å							
Pd ^a				2.02			
Pt ^b				~2.0			

^ataken from Ref. ⁸⁹; ^btaken from Ref. ⁸⁸

Substitution energies of the divalent and tetravalent dopants in bulk ceria were calculated using Equation (3.7) and (3.8), respectively.

$$E_{sub_di} = E((CeO_2)_{n-1}MO) - (n - 1)E(CeO_2) - E(MO) \quad (3.7)$$

$$E_{sub_tetra} = E(Ce_{n-1}O_{2n}MO) - (n - 1)E(CeO_2) - E(MO) - \frac{1}{2}E(O_2) \quad (3.8)$$

where $E((CeO_2)_{n-1}MO)$ is the total energy of the doped system, $(n - 1)$ being the number of CeO₂ pair remained in the doped system, $E(CeO_2)$ is the energy of 1 formula unit of cerium dioxide and $E(MO)$ is the energy of 1 formula unit of the

particular dopant's metal oxide (i.e. PdO or PtO). Oxygen reference energy is denoted as $\frac{1}{2} E(\text{O}_2)$ as only one oxygen atom is removed. $E(\text{O}_2)$ is obtained by spin polarised DFT calculation of an O₂ molecule (triplet state) in a cubic box of 15 Å in length.

Table 3.5 Calculated metal dopant substitution energies and neighbouring M--O distances of Pd/Pt doped ceria systems.

	Substitution energy / eV							
	Pd ²⁺		Pt ²⁺		Pd ⁴⁺		Pt ⁴⁺	
	SPP	CS	SPP	CS	SPP	CS	SPP	CS
PW91+U	2.32	3.44	2.05	2.56	3.10	3.11	2.15	2.84
PBE+U	2.27	3.40	1.99	2.89	3.01	3.14	2.05	2.85

Calculated substitution energies for both Pd and Pt in bulk ceria are tabulated in Table 3.5. From the calculated substitution energies of dopants, the more favourable structure of a Pd/Pt doped bulk ceria corresponds to a square planar coordination with 4 neighbouring oxygen atoms, with divalent dopants being more easily substituted into the bulk than tetravalent dopants. Not to our surprise, as this clearly shows the +2 oxidation states characteristics for both palladium and platinum as d⁸ metal ions. Our findings here agrees well with similar reported work by Scanlon *et al.*¹⁶⁸ which discussed the improved OSC of Pd/Pt-doped CeO₂ by the crystal field stabilisation of the d⁸ dopant ions in a square planar coordination environment.

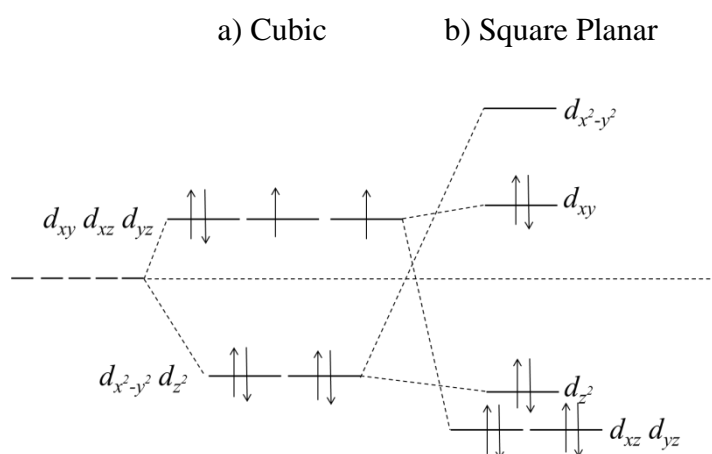
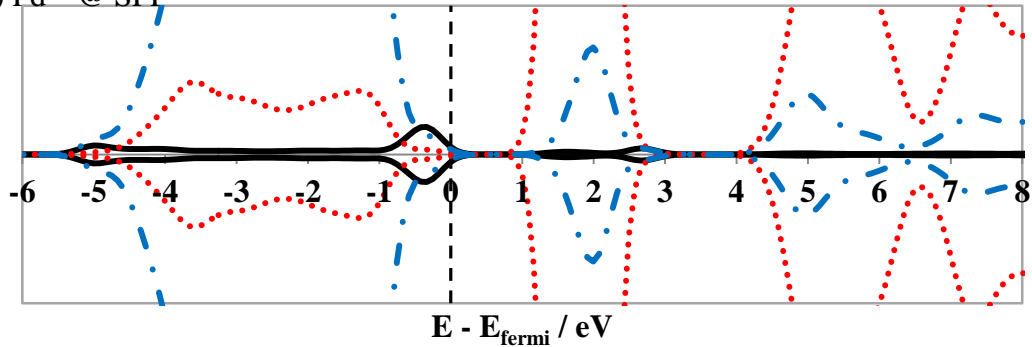
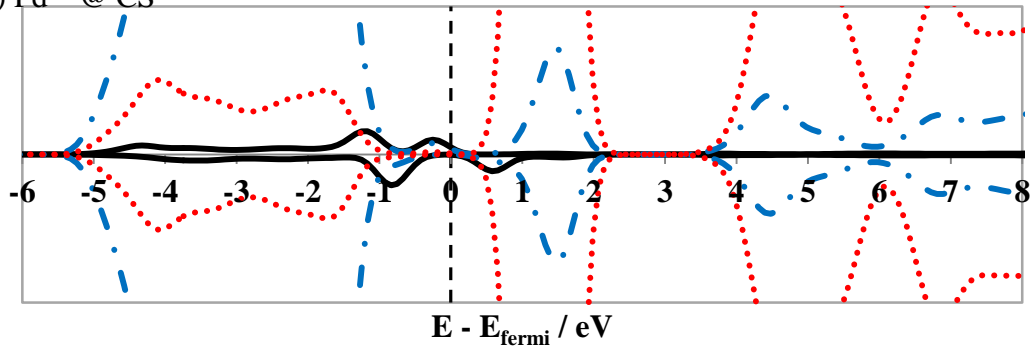
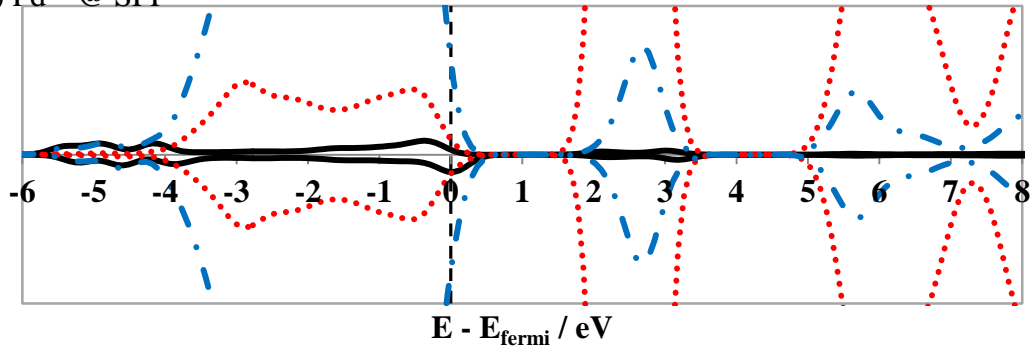


Figure 3.10 Crystal field splitting of a d⁸ metal ion in a a) cubic and b) square planar complex.

The Pd and Pt d⁸ ion prefers the square planar coordination over cubic, which can be explained in crystal field theory. By referring to Figure 3.10, we can see the splitting of the degenerate *d*-orbitals in a cubic and square planar complex. In the

cubic coordination (Figure 3.10a), the three energetically higher t_{2g} orbitals consist of d_{xy} , d_{xz} , and d_{yz} orbitals, while the e_g orbitals are d_{z^2} and $d_{x^2-y^2}$. For a d^8 ion in a square planar environment, there are no atoms coordinated along the z -axis. Therefore, the d -orbitals with a z component (d_{xz} , d_{yz} , and d_{z^2}) will fall in energy and the d_{xy} and $d_{x^2-y^2}$ orbitals will increase in energy. Thus, we can see the splitting of the orbitals for a square planar coordination shown in Figure 3.10b.

With the DOS analysis, we can further observe that expectation for Pd^{2+} @SPP shows the crystal field splitting of a square planar coordination, is correct. The atoms projected DOS (PDOS) plots for palladium substituted ceria are shown in Figure 3.11. The bands below the Fermi level (0 eV) are occupied states while the ones above the Fermi level are unoccupied states.

a) Pd^{2+} @ SPPb) Pd^{2+} @ CSc) Pd^{4+} @ SPP

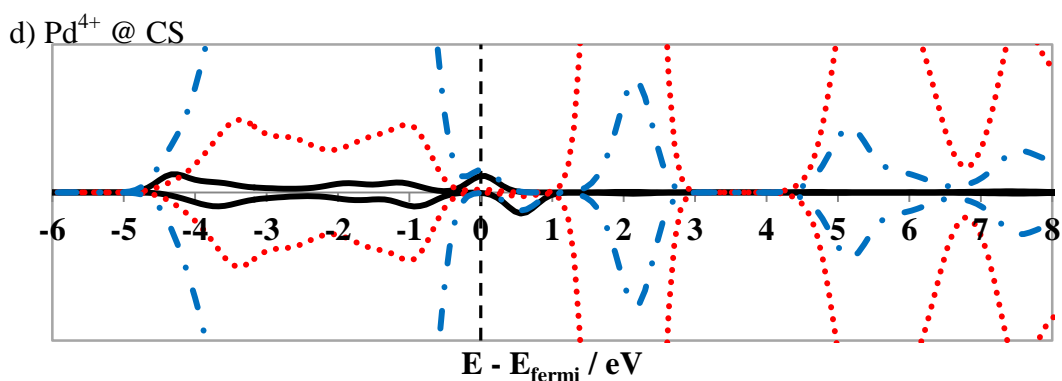


Figure 3.11 Atoms projected DOS of Pd²⁺ substituted CeO₂ at a) SPP and b) CS, and Pd⁴⁺ substituted CeO₂ at c) SPP and d) CS. Pd (black solid), Ce (red dots), and O (blue dash dot) calculated using PW91+U. Energies are corrected to Fermi level and Gaussian smearing width of 0.2 eV is applied.

The PDOS plots for Pd²⁺@ SPP are shown in Figure 3.11a. In this case, the Pd *d*-states have identical density of states for up and down spins which is consistent with the occupation of the energy levels for square planar coordination seen in Figure 3.10b. Three distinct peaks can be observed in the Pd *d*-states plot, where the maxima of the peak are located at about -5.0 eV, -0.5 eV, and 2.8 eV. The *d*-band peak around 2.8 eV above the Fermi level can be attributed to the $d_{x^2-y^2}$ orbital since it is the unoccupied orbital for the square planar coordination.

In Figure 3.11c, where we have substituted the Ce⁴⁺ with a Pd⁴⁺ and optimised it at the square planar position, it is observed that the up and down spins are asymmetrical. We can also observe charge donation to Pd centre to reduce its oxidation state. This is shown by the Ce 4*f* and O 2*p* states in the PDOS which cross the Fermi level. This suggests that not all spins are paired. In this case, there will not be a pair of electrons in the highest occupied state seen in Figure 3.10b.

In the Pd²⁺ and Pd⁴⁺ substituted ceria at cerium site, both the Pd ions are in a cubic coordination with neighbouring oxygen atoms, except that for Pd²⁺ which shows a slightly distorted cubic coordination due to lack of one oxygen neighbour. From the PDOS plot (Figure 3.11b and d), we observed a down spin peak at 0.8 eV and 0.7 eV for Pd²⁺ and Pd⁴⁺ systems, respectively, showing the unoccupied orbitals. Using the crystal field splitting theory, the cubic crystal field stabilisation energy for cubic coordination, Δ_c , is comparatively smaller than the pairing energy of the electrons, causing it to be a high spin complex and leaving none completely empty orbitals but rather mixture of filled and half-filled *d*-orbitals as shown in Figure 3.10a.

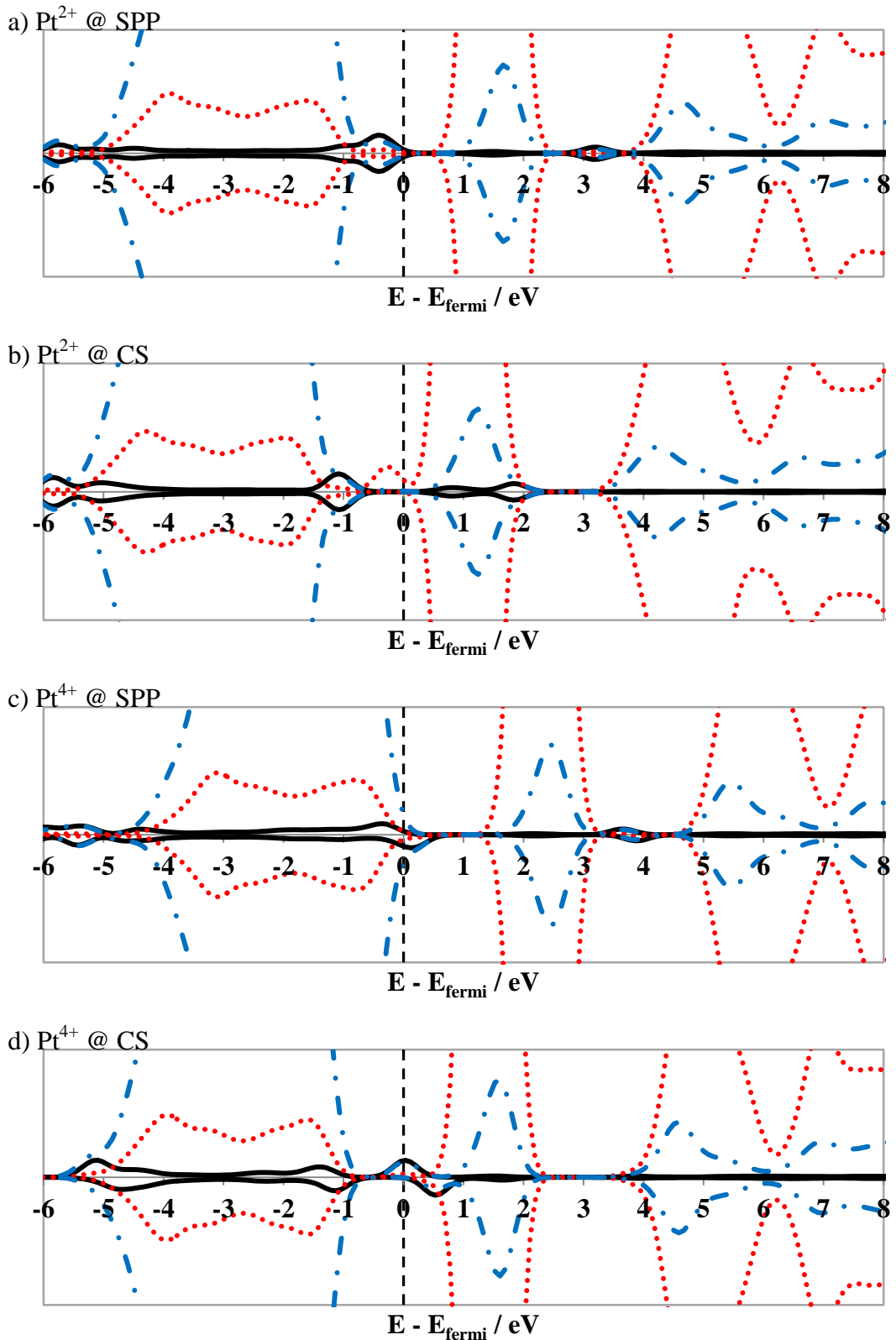


Figure 3.12 Atoms projected DOS of Pt²⁺ substituted CeO₂ at a) SPP and b) CS, and Pt⁴⁺ substituted CeO₂ at c) SPP and d) CS. Pd (black solid), Ce (red dots), and O (blue dash dot) calculated using PW91+U. Energies are corrected to Fermi level and Gaussian smearing width of 0.2 eV is applied.

The PDOS plots for Pt²⁺ @ SPP are shown in Figure 3.12a. Similar to Pd²⁺ @ SPP, the Pt *d*-states for the up and down spins are identical, showing that the

occupation of the energy levels are consistent with the square planar coordination seen in Figure 3.10b. We can observe 4 peaks in the Pt *d*-states plot, where the peaks are located at about -5.8 eV, -4.5 eV, -0.5 eV, and 3.2 eV. The *d*-band peak around 3.2 eV above the Fermi level can be attributed to the $d_{x^2-y^2}$ orbital since it is the unoccupied orbital for the square planar coordination. The rest of the peaks below the Fermi level should be d_{xz} , d_{yz} , d_{z^2} , and d_{xy} as they are all the occupied orbitals.

The PDOS plots for Pt⁴⁺ @ SPP are shown in Figure 3.12c. The Pt⁴⁺ is optimised at the square planar position and the Pt *d*-states up and down spins are observed to be asymmetrical. Similar to Pd⁴⁺ @ SPP system, the Ce 4*f* and O 2*p* states in the PDOS cross the Fermi level and so this suggests that there is charge donation to the Pt centre to lower its oxidation state. The PDOS plots for Pt⁴⁺ @ CS in Figure 3.12d shows a mixture of filled and half-filled *d*-orbitals for Pt⁴⁺ cation. The down spin peak at 0.6 eV indicates a partially filled *d*-orbital for the Pt⁴⁺ cation. This corresponds to Figure 3.10a, showing a cubic coordination for Pt⁴⁺ @ CS with the neighbouring oxygen atoms.

Slightly different results were obtained for the PDOS of Pt²⁺ @ SPP system. As shown in Figure 3.12b, there is a small peak at about 0.2 eV right below the Fermi level. This is an occupied Ce 4*f* peak that belongs to the Ce³⁺ cations, which can also be seen in a defective bulk ceria shown in Figure 3.6. These two next nearest Ce³⁺ cations neighbours have been reduced from their +4 oxidation state by the removal of an oxygen atom to create a Pt²⁺-doped system. This oxygen vacancy is termed charged compensating vacancy which will be discussed further later in this section. The reduction of two Ce atoms is unexpected as we thought the system will maintain a neutral charge with the removal of an oxygen atom and the substitution of a Ce⁴⁺ cation with a Pt²⁺ cation. This occurrence shows that Pt substitution at the cerium site somehow aids the reduction of bulk ceria which is similar to the one reported by Yang *et al.*,²⁴⁷ who has applied the DFT+U method with PBE functional to model the Pt and Rh-doped systems.

Table 3.6 Average Bader charges for the atoms in each of the stated Pd/Pt doped systems. Value in bracket shows the average Bader atomic charge for Ce³⁺ cations.

	Average Bader atomic charge / <i>e</i>							
	Pd doped Ceria				Pt doped Ceria			
	Pd	Ce	O	O _{Pd}	Pt	Ce	O	O _{Pt}
PW91+U								
M²⁺ @ SPP	0.81	2.40	-1.20	-1.09	0.81	2.40	-1.20	-1.09
M²⁺ @ CS	0.93	2.40	-1.20	-1.13	1.40	2.39 (2.13)	-1.20	-1.07
M⁴⁺ @ SPP	1.08	2.40	-1.19	-1.00	1.23	2.40	-1.19	-0.99
M⁴⁺ @ CS	1.22	2.39	-1.20	-1.05	1.32	2.39	-1.20	-1.06
MO*	0.81	-	-	-0.81	0.80	-	-	-0.80
MO₂*	1.40	-	-	-0.70	1.50	-	-	-0.75
CeO₂	-	2.41	-1.21	-	-	2.41	-1.21	-
PBE+U								
M²⁺ @ SPP	0.81	2.41	-1.21	-1.10	0.81	2.41	-1.19	-1.09
M²⁺ @ CS	0.94	2.41	-1.21	-1.14	1.40	2.41 (2.14)	-1.21	-1.08
M⁴⁺ @ SPP	1.11	2.41	-1.20	-1.00	1.24	2.42	-1.20	-1.00
M⁴⁺ @ CS	1.23	2.42	-1.21	-1.06	1.32	2.41	-1.21	-1.06
MO*	0.81	-	-	-0.81	0.82	-	-	-0.82
MO₂*	1.41	-	-	-0.70	1.50	-	-	-0.75
CeO₂	-	2.42	-1.21	-	-	2.42	-1.21	-

*calculations are performed using standard PW91/PBE functional without on-site Coulomb interaction correction.

A further analysis of the electronic structure was carried out via Bader analysis. Through the Bader analysis, we can roughly tell the oxidation states of each species in the system. Table 3.6 shows the average Bader charges for the atoms in each of the Pd doped ceria systems. Bader charges of the atoms Ce, O, and Pd from stoichiometric ceria and palladium (II) oxide, PdO, are used as reference of each atom type. We can further confirm that the Pd ion dopant substituted at SPP in ceria is in +2 oxidation state as there is no difference between the Bader charge for the Pd ion in Pd²⁺ @ SPP system and the Pd²⁺ reference charge in PdO. There is a slight loss of electrons in Pd²⁺ @ CS system when compared to Pd²⁺ @ SPP. This can be due to the cubic coordination which in this case has an extra 3 oxygen neighbours when compared to square planar coordination. The lower charge also suggests that there is more covalency in the Pd-O interaction in the SPP configuration. As for the Ce and O ions, there is not much change seen. For the Pt doped ceria systems, PW91+U calculations showed similar trends to that of Pd doped ceria and again

except for Pt²⁺ @ CS system. Yang *et al.* have reported a net charge of +1.48 for the Pt ions and found that two next nearest neighbours Ce⁴⁺ cations of the oxygen vacancy have been reduced to Ce³⁺.²⁴⁷ Our analysis yielded a net charge of +1.40 for the Pt ion using the PW91+U and PBE+U approach which is near to the Bader charge value for Pt⁴⁺ (1.50 *e*) in bulk PtO₂. Besides, two Ce ions are found to have lower Bader charge compared to the rest of the Ce ions which further confirms that these two Ce ions are probably reduced to +3 oxidation states as observed in PDOS plots (Figure 3.12b). Similar trends were also produced using PBE+U approach on Pd/Pt doped ceria.

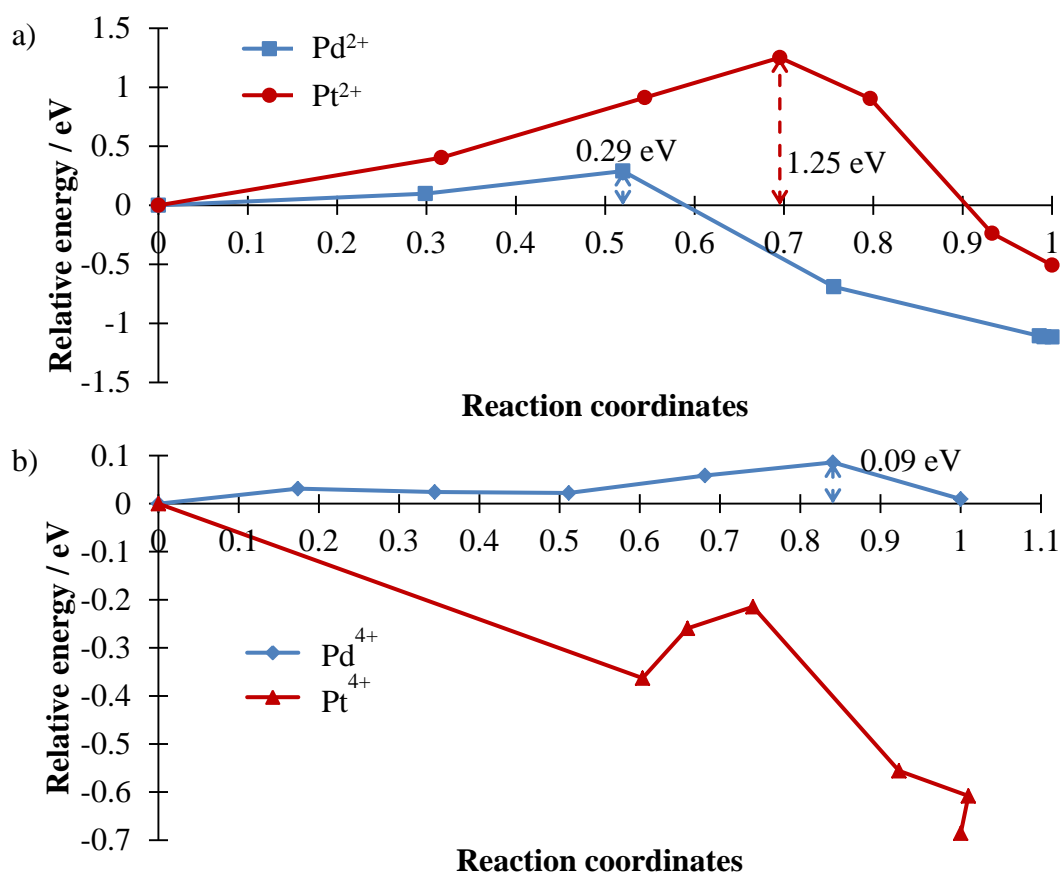


Figure 3.13 Calculated energy barriers for the migration of dopant metals from CS to SPP in a) Pd²⁺ (blue squares) and Pt²⁺ (red circles); b) Pd⁴⁺ (blue diamonds) and Pt⁴⁺ (red triangles) doped CeO₂ bulk systems using PW91+U. Energies presented are relative to energy of respective starting structures.

The migrations of dopant metals from cerium site to square planar position have also been studied using NEB method. From the PW91+U calculations, energy barriers for the migration of Pd²⁺ ($E_a = 0.29$ eV) and Pt²⁺ ($E_a = 1.25$ eV) from CS to SPP are obtained (refer Figure 3.13a). An energy barrier of 0.09 eV is required for the migration of Pd⁴⁺ (Figure 3.13b blue diamonds). However, no energy barrier is obtained for the migration of Pt⁴⁺ (Figure 3.13b red triangles).

The effect of dopant to the supercell bulk lattice parameter is also studied. An expansion within $\pm 2\%$ at the step of 0.5% is applied to the optimised doped CeO₂ structures. Using the Murnaghan equation of state, it is found that both the doped CeO₂ bulk structures have contracted by a little. The Pd²⁺@SPP system has contracted by about 0.15% and the Pt²⁺@SPP system has contracted by about 0.37%. The contraction occurs can be due to the defect-induced chemical expansion (in this case contraction) reported by Marrochelli *et al.*^{184, 185} The lattice contraction occurs primarily due to electrostatic interactions from the formation of a CCV and the steric effects caused by the substitution of a dopant which causes a change in cation radius, 1.11 Å to 0.78 Å for Pd²⁺@SPP and 1.11 Å to 0.74 Å for Pt²⁺@SPP. Thus, both processes have an effect in the contraction of the lattice of the doped bulk structures.

3.6 Effects of platinum group metal (PGM) dopants on oxygen vacancy formation in bulk ceria

From Equation (3.5), the divalently doped systems have an oxygen vacancy. This vacancy is termed the charge compensating vacancy (CCV) as it is required to ensure the correct oxidation state of the dopant in the lattice of the higher valency metal oxide. We have used Equation (3.9) to calculate the energy required to form a CCV (E_{CCV}) for each system. The summary of calculated E_{CCV} for each system is presented in Table 3.7.

$$E_{CCV} = E((CeO_2)_{n-1}MO) - E(Ce_{n-1}O_{2n}MO) + \frac{1}{2}E(O_2) \quad (3.9)$$

Yang *et al.* has first reported this CCV as reduction energy.^{247, 248} They have applied the DFT+U method using PBE functional to model the doping of ceria with Pd, Pt and Rh.^{247, 248} However, they only investigated structures in which the dopant is positioned at the Ce site (CS in our reference) and found that the E_{CCV} to be 0.59 eV and 0.96 eV for Pd-doped and Pt-doped ceria, respectively. Applying the same approach, the E_{CCV} reported by Scanlon *et al.* in Pd/Pt doped ceria are 0.66 eV and 1.19 eV, respectively.¹⁶⁸ They also reported the E_{CCV} for the metal dopant positioned at square planar coordination to be -0.72 eV and -0.75 eV for Pd-doped and Pt-doped ceria. This showed that the Pd²⁺ and Pt²⁺ cations are more favoured to be at a square planar position. In this work, we have similar findings for Pd-doped ceria systems. At the square planar position, the E_{CCV} are -0.78 eV and -0.75 eV using PW91+U and PBE+U. This agrees well with the values reported by Scanlon¹⁶⁸ using PBE+U.

As for the Ce site we found the energy to form a CCV to be lower than those reported in literature.^{168, 248} Using PW91+U and PBE+U we calculated the E_{CCV} to be 0.33 eV and 0.26 eV, respectively.

In the Pt-doped ceria system at square planar position, we have obtained a value of -0.10 eV and -0.06 eV for the E_{CCV} using PW91+U and PBE+U, respectively. These values are very different and in fact higher than those reported by Scanlon.¹⁶⁸ For the Pt dopant at Ce site, mixed results were found with the PW91+U and PBE+U approach. PW91+U calculations yield a negative value for E_{CCV} which is -0.28 eV whereas the PBE+U calculated E_{CCV} is 0.32 eV higher, which gives a value of 0.04 eV. These values are more than 0.90 eV lower than those reported in literature. One point which can be used to understand the origin of this difference is that as mentioned earlier, for the Pt²⁺ @ CS structure, the Pt cation is not actually in a +2 oxidation state or may be it is just less covalent in bonding. In addition, two Ce⁴⁺ ions have been reduced to Ce³⁺. However, this is not valid when comparing to results reported by Yang which also observed that the Pt is actually in its +4 oxidation state with two next nearest cerium neighbours being reduced to Ce³⁺ cations yet still yield a E_{CCV} of 0.96 eV.²⁴⁸

Table 3.7 Calculated charge compensating energy, E_{CCV} , for Pd/Pt doped CeO₂ systems.

	E_{CCV} / eV			
	Pd ²⁺		Pt ²⁺	
	SPP	CS	SPP	CS
PW91+U	-0.78	0.33	-0.10	-0.28
PBE+U	-0.75	0.26	-0.06	0.04

Using the E_{CCV} and energy barriers from the migration of dopant metals, a minimal energy pathway can be predicted for the formation of divalently doped CeO₂ systems. Initially, the tetravalent Pd/Pt cation at cerium site will migrate to the square planar position. Subsequently, a CCV is formed to obtain a divalently doped CeO₂ system.

$$E_{red} = E((\text{CeO}_2)_{n-2}\text{MO}) - E((\text{CeO}_2)_{n-1}\text{MO}) + \frac{1}{2}E(\text{O}_2) \quad (3.10)$$

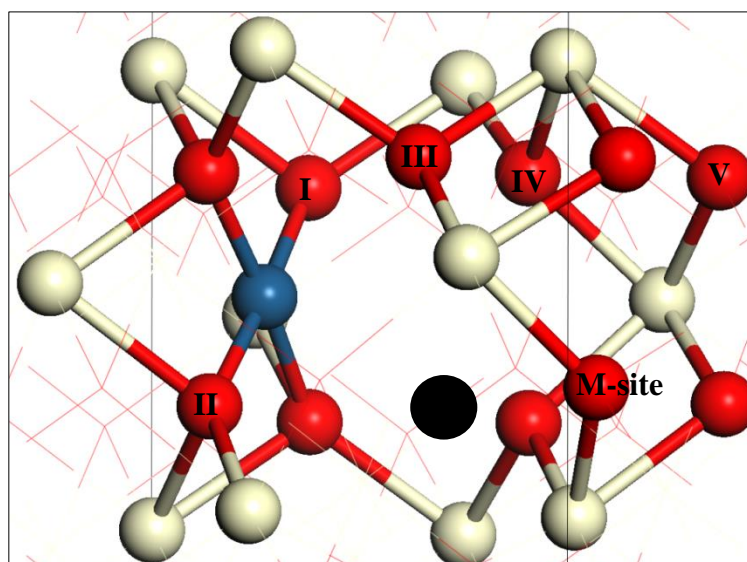


Figure 3.14 Pd/Pt doped CeO₂ bulk supercell at square planar position with second oxygen vacancy sites labelled in Roman numerals. Black circle indicates charge compensation vacancy site. M-site is the CCV migration site.

Subsequent oxygen vacancy is created near the metal dopant in order to obtain the reduction energy (following Equation (3.10)) for the divalently doped systems at square planar position. Figure 3.14 shows the vacancy sites studied on the M²⁺@SPP system (M=Pd or Pt) and Table 3.8 shows the reduction energy at each vacancy site. The two Ce³⁺ sites in these reduced systems are assumed to be at next nearest neighbours following the results obtained from the reduction of a clean stoichiometric bulk CeO₂.

Table 3.8 Reduction energy, E_{red} , for the divalently doped systems at square planar position. Refer to Figure 3.14 for the labels of different vacancy sites.

Vacancy site	E_{red} / eV	
	Pd ²⁺ @SPP	Pt ²⁺ @SPP
I	1.55	1.54
II	3.38	3.81
III	2.57	2.13
IV	1.52	1.68
V	2.38	2.22

Overall, the reduction energies for the divalently doped systems at square planar position are lower than that of an undoped bulk CeO₂ except for vacancy created at sites III for Pd²⁺@SPP, and II at both systems. The E_{red} for Pd²⁺@SPP (3.38 eV) and Pt²⁺@SPP (3.81 eV) at site II have both exceeded 3 eV. This shows that removing an oxygen atom bonded to the dopant metal is highly unfavourable. However, this is not

true for the case of vacancy created at site I. In fact, site I has the second lowest and lowest E_{red} for Pd²⁺@SPP (1.55 eV) and Pt²⁺@SPP (1.54 eV), respectively. The difference in the E_{red} at these two sites is due to the availability of neighbouring non-dopant bonded oxygen atom (O(IV) in Figure 3.14) to replenish the one extracted from site I. It is more favourable for the dopant metal to retain its square planar coordination with four neighbouring oxygen atoms rather than having a coordination number of three.

Figure 3.15 shows the optimised structure of reduced Pd²⁺@SPP when vacancy is formed at site I. The oxygen atom labelled at site IV has migrated to the vacancy site during the optimisation process. Thus, giving a lower E_{red} when compared to vacancy formed at site II as there are no non-dopant bonded oxygen atoms to replenish the vacancy site.

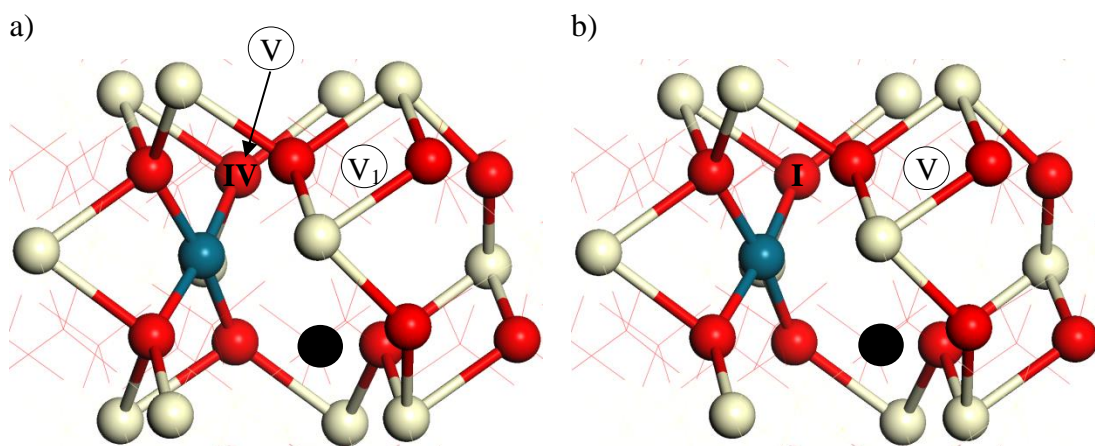


Figure 3.15 Optimised structures of reduced Pd²⁺@SPP when vacancy site is formed at site a) I, and b) site IV. Oxygen at site IV migrated to the vacancy site at site I during optimisation resulting in similar end structure to b). Black circle indicates CCV site, V in a circle indicates intended vacancy site, and V₁ in a circle indicates vacancy site after optimisation.

In order to further study the effects of dopants on the localisation of electrons on Ce sites, permutations of different pairs of Ce³⁺ cations positions are performed. This procedure was only carried out using the two optimised Pd²⁺@SPP structures (Vacancy site I and IV) with the lowest E_{red} because the computational time and resources required are quite expensive. A total number of 182 and 200 unique permutations of different Ce³⁺ pairs were generated for structures with vacancy at site I and IV, respectively. The lowest E_{red} obtained from the optimised structures is 1.42 eV. There are two permutations which yield this E_{red} (1.42 eV) and both of them have Ce³⁺ cations as next nearest neighbours with respect to the oxygen

vacancy site. In terms of Ce³⁺ to Pd²⁺ distance, one of the permutations has Ce³⁺ cations at next nearest neighbour and fifth nearest neighbour while the other has the cations both at fourth nearest neighbour.

The next lowest E_{red} is 1.43 eV which was obtained from three of the optimised structures. Two of these three structures have both the Ce³⁺ cations as next nearest neighbours with respect to oxygen vacancy site. The highest E_{red} obtained from the list of permuted structures for vacancy site IV is 2.08 eV where both the Ce³⁺ cations are third nearest neighbour with respect to oxygen vacancy site. These Ce³⁺ cations are also furthest (fifth nearest neighbour) from the Pd²⁺ cation. Figure A3 (Appendix A4) shows histograms of various distances of Ce³⁺ from Pd²⁺ with population of structures with different Ce³⁺ pairs with respect to oxygen vacancy site IV at different E_{red} range. There are no distinct trends which can be seen from these results regarding the localisation site of excess electrons from the removal of an oxygen atom and E_{red} .

From the permuted structures for vacancy site I, only 36 permutations were chosen to be optimised from a total of 182. This selection was made based on the list of E_{red} obtained from the structures with vacancy at site IV. The lowest E_{red} (1.42 eV) is also obtained from two different permutations. One of the permutations has both its Ce³⁺ cations at next nearest neighbour with respect to oxygen vacancy site (V₁ from Figure 3.15a) and they are at next nearest and fifth nearest neighbour from Pd²⁺. The other structure has both the Ce³⁺ cations at next nearest and third nearest neighbour with respect to oxygen vacancy site. These Ce³⁺ cations are both at fourth nearest neighbour from Pd²⁺. The next lowest E_{red} obtained is 1.43 eV and the highest E_{red} from the 36 structures is 3.09 eV.

Finally, the migration of CCV to a site further away from the dopant has been investigated. NEB method was used to model the migration of a neighbouring oxygen atom to the CCV site (labelled M-site in Figure 3.14). The energy barrier obtained for Pd²⁺@SPP (0.61 eV) and Pt²⁺@SPP (0.60 eV) is shown in Figure 3.16. This shows that the CCV site is more likely to stay at the next nearest position to the dopant rather than further away. Besides, the end structure where the CCV site is third nearest neighbour to the dopant is energetically less stable compared to the initial structure which has the CCV site at the next nearest neighbour position with respect to the dopant position.

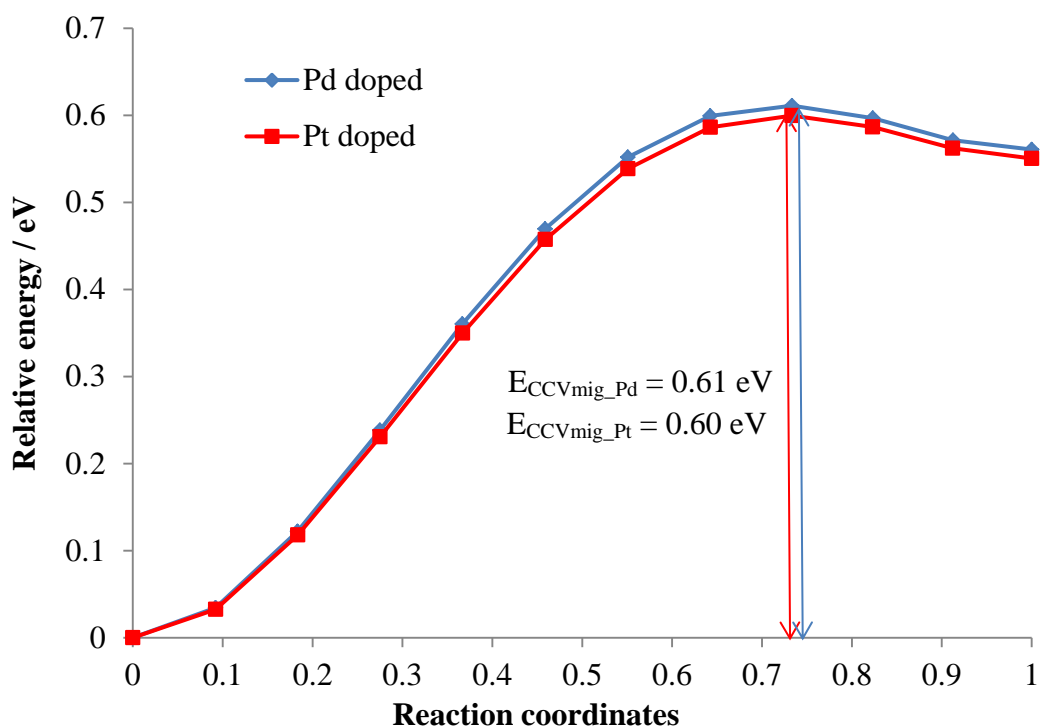


Figure 3.16 Charge compensation vacancy migration barrier ($E_{CCV_{mig}}$) at Pd²⁺@SPP (blue line) and Pt²⁺@SPP systems (red line).

3.7 Conclusion

In this chapter, it has been shown that the spins localized on two next nearest neighbours Ce atoms with respect to the oxygen vacancy site gave the lowest oxygen formation vacancy energy, with E_{vac} of 2.45 eV and 2.43 eV, using PW91+U and PBE+U, respectively. These values are in between those reported by Keating *et al.*²³⁸ ($E_{vac} = 2.11$ eV) and Scanlon *et al.*¹⁶⁸ ($E_{vac} = 2.62$ eV) but is about 0.94 eV lower than that reported by Nolan *et al.*⁶⁴ ($E_{vac} = 3.39$ eV). However, the reported results were based on excess electrons localised on two Ce³⁺ neighbouring the vacancy site.^{64, 238} There are other structures with different pairs of Ce³⁺ sites at higher E_{vac} . It is shown that reduced Ce at NN_NN sites yield lower E_{vac} . Practically, at 300 K the majority of the defective structures will have Ce³⁺ at NN_NN positions. The increase in temperature to 700 K causes a greater range of Ce³⁺ arrangements possible around a defect.

The energy barrier, E_a , for neighbouring oxygen to migrate to the vacancy site is about the same ($\Delta E_a = 0.02$ eV) regardless of whether the Ce³⁺ sites have shifted or not, providing that the end structure has Ce³⁺ cations positioned at NN_NN sites. The structures with Ce³⁺ cations localised at next nearest neighbours yield an E_a of

0.48 eV which is near to other reported theoretical calculated values of 0.53 – 1.10 eV depending on vacancy concentration.⁶²⁻⁶⁵ However, the barrier was reduced by 0.02 eV ($E_a = 0.46$ eV) when Ce³⁺ cations were shifted along with the migration of the oxygen. A higher energy barrier is needed ($E_a = 0.57$ eV) when the end structure resulting from the migration of an oxygen atom has Ce³⁺ cations at NN_NN* or NN*_NN positions with respect to the vacancy site.

For Pd/Pt doped ceria, we have found that the arrangement of atoms around the dopant metal was distorted in Pd²⁺/Pt²⁺@CS systems. It is suggested that the change in ionic radius upon the substitution of a dopant metal may induce steric effects that distorts the position of neighbouring atoms in the lattice structure.^{184, 185} Overall, the divalently doped systems yield more favourable substitution energies. The Pd²⁺/Pt²⁺@SPP are the most favourable doped CeO₂ structures with the substitution energy of 2.32 eV and 2.05 eV, respectively using PW91+U (2.27 eV and 1.99 eV using PBE+U).

When the Pt dopant metal is substituted at the Ce site, two Ce⁴⁺ cations were reduced. The atoms projected DOS in Figure 3.12b shows that there is a gap state similar to the one observed for a defective clean CeO₂ bulk (Figure 3.6). This shows that the Pt dopant metal aided the reduction of two Ce cations in the bulk.

The charge compensation vacancy is the removal of an oxygen atom in order to stabilise the reduction of the dopant metals and maintain an overall charge balance in the system. The formation of a charge compensation vacancy is spontaneous for the systems when metal dopant is positioned at square planar position which agrees to the X-ray photoelectron spectroscopy studies.^{89, 249} That study indicates that the Pd/Pt dopant prefer to present in the +2 oxidation state and is accompanied by spontaneously formed charge compensating vacancies.^{89, 249} An exception for the Pt²⁺@CS system due to the fact that the metal dopant was not reduced but two of the cerium cations were reduced to Ce³⁺. A deduction can be made for the process involved in doping the CeO₂ bulk structure using the energy barrier for the migration of metal dopant from CS to SPP and the energy needed to form a CCV. Initially, the tetravalent Pd/Pt cation at cerium site will migrate to the square planar position and a CCV is formed to obtain a divalently doped CeO₂ system.

Using DFT+U, the metal dopant has shown to lower the reduction energy for the CeO₂ bulk system which also agrees to results reported by Scanlon *et al.*¹⁶⁸ The

removal of an oxygen atom bonded to the metal dopant is less favourable compared to other vacancy sites studied. However, it can be made more favourable if there is an adjacent oxygen atom which can migrate to replenish the vacancy created next to the metal dopant. A large number of permutation sites for the localisation of excess electrons can be generated for each of the oxygen vacancy sites studied. This can lead to the finding of structures with lower E_{red} such as the ones found for structures with oxygen vacancy at site I and IV (Figure 3.14), respectively. For Pd²⁺@SP system, the formation of an oxygen vacancy at sites I and IV yield E_{red} of 1.42 eV which is slightly lower than that reported by Scanlon *et al.* for site IV ($E_{red} = 1.79$ eV).¹⁶⁸ Scanlon *et al.* has reported that the excess electrons left behind upon vacancy formation localised on two Ce ions neighbouring the vacancy which is different from our results.¹⁶⁸ The E_{red} of 1.42 eV was obtained from the structure where two next nearest neighbour Ce ions were reduced to Ce³⁺ rather than nearest neighbour Ce ions as reported by Scanlon *et al.* Once again, this shows that excess electrons that localised on next nearest neighbour Ce ions yield more stabilised defective structures which require lower oxygen vacancy formation energy.

Migration of a CCV to further away from the dopant metal is less favourable due to a high energy barrier ($E_{CCVmig_Pd}=0.61$ eV, $E_{CCVmig_Pt}=0.60$ eV). This suggests that the CCV tends to be formed at next nearest position to the dopant metal.

Chapter 4

CeO₂ (111) and (110) surface

This chapter consists of theoretical investigations on CeO₂ (111) and (110) surfaces. The chapter begins with a brief introduction followed by computational details and some results obtained which will discuss about the surface defects, platinum group metal (PGM) doped surfaces and their effects on vacancy formation energies, and CO adsorption and oxidation on the doped surfaces.

4.1 Introduction

Ceria serves as an important support for metal nanoparticles due to its great oxygen storage capacity (OSC). The low index CeO₂ surfaces with (111), (110), and (100) orientations are thermodynamically more stable than the alternative facets so a vast amount of studies has been performed on these surfaces.^{64, 74, 77, 79, 81, 82, 170, 172, 176, 182, 183, 203, 250-257} The reported surface energies and magnitude of surface relaxation increase in the order (111) < (110) < (100).^{170, 258, 259} Results from all the computational studies published also showed that oxygen vacancy formation on the (111) surface is energetically more difficult than that on (110) and (100) surfaces.^{64, 169, 170, 259, 260} These corresponds to the stability of the studied surface where the (111) surface is the most stable.

Step sites from (111) surface were also studied. Nilius *et al.* reported three different structures of CeO₂ (111) step sites: two types of <110> steps and one <211> step.²⁶¹ The three types of steps on CeO₂ (111) surface were reproduced by Kim *et al.*²⁵⁶ and studied using on-site Coulomb interaction corrected density function theory (DFT+U) approach. For easy reference, the <111> step surfaces are identified as they are named in the literature (CeO₂-U and CeO₂-D).²⁵⁶

It is necessary to apply the DFT+U method in order to properly describe the strongly localised electronic system of CeO₂ and to yield proper electronic structure of defective sites in CeO₂.^{51, 169, 170, 242, 259, 260} Huang and Fabris¹⁷³ reported that the use of the parameter $U = 4 - 5$ eV can lead to severe overestimation of molecular binding energy to ceria when surface reduction is involved. Thus, they suggested lower U values of $2 - 3$ eV when using DFT+U method to describe the surface

chemistry of ceria. In a recent work, Bennett and Jones²⁶² have studied the influence of Hubbard U parameter in simulating the catalytic behaviour of CeO₂. They have proposed a new method of finding the U value that uses the change in adsorption energy of a molecule with respect to U by keeping the relative changes in adsorption energies between molecules.²⁶² In that case, they have found that the average gradient of the adsorption energies are approaching zero between U = 5.5 eV and U = 6.5 eV.

There are reported theoretical studies of adsorption and doping of transition metals on CeO₂ surface.^{171, 202, 247, 253-255, 257, 263-268} In 2009, Mayernick and Janik²⁵³ have both studied Pd atom interaction with CeO₂ surfaces using DFT+U. They reported that the site residing overtop a sub-surface oxygen atom is the most favourable adsorption site for palladium with an adsorption energy of -1.78 eV. This is different from Lu *et al.*²⁶⁵ in which they have reported that the palladium and platinum adatoms are found to adsorb on the surface O-bridge sites. Mayernick and Janik also reported that Pd₄ cluster adsorbed most exothermic at a site which maximizes interaction of the tetrahedral Pd atoms in the cluster with surface oxygen atoms.²⁵³ In the same work, they have considered only the surface cerium site as substitution site for palladium. In our study on doping CeO₂ bulk with Pd/Pt metals, we have found that this is not the most favourable site. Nevertheless, in the previous²⁰² and recent²⁶⁶ work, they have shown that the catalytic activity can be improved by the substitution of a single Pd for a Ce atom on the CeO₂ (111) surface. The Pd-doped CeO₂ (111) surface is found to give lower reaction energy and barrier for the dissociation of methane into *CH₃ and *H radicals than the clean surface.²⁰² Lower methane activation barrier is also found over the Pd-doped CeO₂ (111) surface than that over CeO₂ (111), Pd (111), or PdO (100) surfaces; thus indicates unique methane oxidation activity.²⁶⁶

Krcha *et al.* have used DFT+U methods to examine the electronic and structural effect of transition metal dopants (groups IV–XII) in the CeO₂ (111) surface.²⁶⁷ They have reported that the reducibility of the surface is altered by dopants in groups IV and V while dopants in groups X–XII become the reduction centre. A volcano relationship with oxygen vacancy formation was observed for the conversion of methane to CO or CO₂. Pd, Co, Ni, and Mn metal dopants are found to be near the peak region of the volcano.

Recently, Ding *et al.* have investigated NO reduction with CO catalysed by a single Pd atom embedded in CeO₂ (111).²⁶⁸ They have shown that the system is active and selective towards N₂, which agrees with experimental literature.^{4, 90, 269} They have proposed that the Pd-O_v (O_v is oxygen vacancy) on the surface to be the active site, responsible for the formation of N₂O₂* by the reaction of two NO molecules and also the subsequent two deoxygenation steps to make N₂.²⁶⁸

Kim *et al.* have used DFT+U to investigate CO adsorption and oxidation mechanism on the interface of Au nanoclusters and CeO₂ (111) surface.^{186, 256} They have shown that doping the CeO₂ support with Au, Pt, Pd, Ti, Ru, or Zr metal accelerates CO oxidation by the Mars-van Krevelen (M-vK) mechanism at the Au-(M-Ce)O₂ interface.¹⁸⁶ The Au, Pd, Pt, and Ti dopants were found to significantly lower the vacancy formation energy of the CeO₂ support. This affected the vacancy formation energy of Au₁₃@(M-Ce)O₂ due to electron donation from the supported Au₁₃ nanocluster which shifts the vacancy formation energy of (M-Ce)O₂.¹⁸⁶ In the other work involving stepped CeO₂ (111) surface, Kim *et al.* suggested that the M-vK mechanism have significant effects to the CO oxidation activity at Au particles supported on the nano- or meso-structured CeO₂ found in industrial catalysts.²⁵⁶ They have shown that the lattice oxygen at the step edge of the surface oxidises CO bound to the Au₁₂ nanocluster through the M-vK mechanism. They have also suggested that the activity of oxidation catalysis by supported Au nanoclusters can be extensively modified by combining chemical and morphological optimisation of the oxide support.^{186, 256}

The overall aim of this chapter is to present and discuss the formation of an oxygen vacancy on the CeO₂ (111) and (110) surface. This includes using DFT+U to investigate the localisation of two excess electrons upon the removal of an oxygen atom on various cerium sites and the effects on vacancy formation energies. Following on from that, we have also investigated the effects of platinum group metal (PGM) dopants (Pd and Pt) on the vacancy formation energies. The ease of oxygen extraction from the lattice structure will provide insight for oxidation catalysis on the system. In this chapter, the doping of <110>-type step surfaces of CeO₂ is also studied. The evaluation of adsorption energies of carbon monoxide (CO) on these CeO₂ surfaces will allow us to identify various active sites available on these catalytic systems.

4.2 Computational details

Calculations were performed using the *ab initio* plane wave basis set code, VASP.¹⁰⁻¹³ The projector augmented wave method was used in representing the core states.^{215, 216} The cerium atom's *5s*, *5p*, *5d*, *4f*, *6s*, and oxygen atom's *2s*, *2p* electrons were treated explicitly as valence electrons with a plane wave cut-off of 500 eV. We have used generalized gradient approximation method applying the Perdew and Wang (PW91)^{197, 198} and Perdew-Burke-Ernzerhof (PBE)^{199, 200} functionals in this work. An on-site Coulomb interaction correction following Dudarev's approach ($U_{eff}=U - J$)²⁰¹ was applied to properly describe the strongly correlated *f*-states of cerium. A U_{eff} of 5.0 eV ($U=5.0$ eV, $J=0.0$ eV) was set for the Ce *f* orbital. For the PW91 calculations, the interpolation for the correlation part of the exchange correlation functional is done according to Vosko, Wilk, and Nusair.²⁰⁶

The (111) and (110) surfaces were cleaved from the final optimised bulk structure ($a = 5.51$ Å for PW91+U, $a = 5.50$ Å for PBE+U). Surfaces are modelled using slab technique where a vacuum gap of 15.0 Å is present perpendicular to the surface to ensure no interactions between subsequent slabs in the z-direction. Surface energies are calculated following:

$$\sigma = \frac{E_i^{slab} - nE^{bulk}}{2S} \quad (4.1)$$

where E_i^{slab} is the total energy of a i^{th} layer slab ($i = 3, 5, 7, 9, 11$), nE^{bulk} is the bulk energy multiplied with the correct stoichiometry of the slab to bulk ratio and $2S$ is the surface area of the top and bottom surface of the slab. Since the whole slab is symmetrical on both sides, σ is the energy required to cleave either side of the surface. Relaxing the whole slab will yield "relaxed" surface energies. However, only the top two trilayers and top four atomic layers for (111) and (110) surface, respectively, were allowed to relax during optimisation. The bottom layers of the slab are fixed to model the bulk like structure. Following on that, two different surface energies will be obtained. Thus, surface energies of the top relaxed layer are calculated following:

$$\sigma_{top_relax} = \frac{1}{S} (E_i^{slab} - nE^{bulk}) - \sigma_{unrelax} \quad (4.2)$$

with σ_{top_relax} and $\sigma_{unrelax}$ as the surface energy of the top relaxed layer and the bottom fixed layer, respectively. A single point energy calculation is performed for

the initial slab cleaved from the bulk structure. This will represent the fixed bulk like structure of bottom surface. Then, the total energy of the unrelaxed slab will be used in equation (4.1) to obtain σ_{unrelax} for equation (4.2). As a result, we are able to calculate the surface energies for the relaxed top layer and bulk like bottom layer of the surface slab.

Convergence of $p(1 \times 1)$ surface energy was checked with respect to the number of layers in the slab. The (111) surface converged with three trilayers of O-Ce-O (Figure 4.1a), while the (110) surface converged with seven atomic layers (Figure 4.1b). The calculations were performed using a $3 \times 3 \times 1$ k -point grid, with the third vector perpendicular to the surface. Other calculations regarding oxygen vacancy formation, transition metal substitution, and CO adsorption were performed on the $p(4 \times 4)$ and $p(3 \times 2)$ expansion of the CeO₂ (111) and (110) surfaces, respectively. All systems were sampled at the Γ -point using the Monkhorst-Pack scheme. A dipole correction along the z -direction of the slab is applied in all calculations.

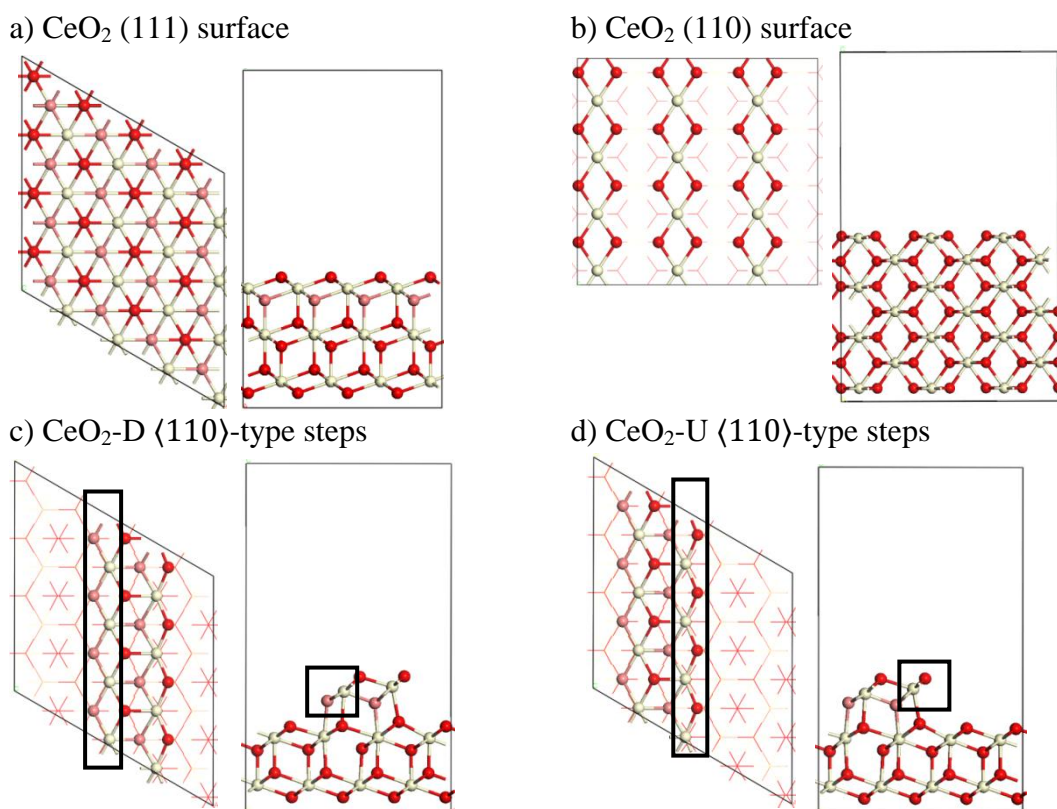


Figure 4.1 Top and side views of optimised structures for clean stoichiometric a) (111) and b) (110) surfaces of CeO₂. c) CeO₂-D and d) CeO₂-U describe the $\langle 110 \rangle$ -type steps with lower and upper rows of oxygen atoms, respectively. Pink coloured atoms in a), c), and d) represent sub-surface oxygen atoms in first layer. Oxygen (red), and cerium (cream). The rectangular and square boxes shows the upper and lower rows of oxygen at the step edge.

Only the $\langle 110 \rangle$ -type steps (CeO₂-U and CeO₂-D) of the CeO₂ (111) surfaces were investigated. These surfaces were constructed by adding a 1/2 ML of one O-Ce-O trilayer CeO₂ on the $p(4 \times 4)$ CeO₂ (111) slab with two trilayers (refer Figure 4.1) as has been done by Kim *et al.* on a $p(5 \times 5)$ CeO₂ (111) surface.²⁵⁶ The CeO₂-D (Figure 4.1c) has lower rows of oxygen at the step edge, while CeO₂-U (Figure 4.1d) has upper rows of oxygen at the step edge. The structures are identical with the ad-layer shifted along by one atomic row. The edge atoms along one side of the ad-layer as indicated by the suffix -U and -D, will be used for CO adsorption reaction.

The surfaces were also doped with a single divalent PGM (i.e. Pt, Pd). Two substitution sites were considered: i) four coordinated square planar site, and ii) three coordinated site (refer Figure 4.2). Substitution energies are calculated following:

$$\mathbf{E}_{\text{sub}} = \mathbf{E}((\text{CeO}_2)_{n-1}\text{MO}) - (\mathbf{n} - 1)\mathbf{E}(\text{CeO}_2) - \mathbf{E}(\text{MO}) \quad (4.3)$$

where $\mathbf{E}((\text{CeO}_2)_{n-1}\text{MO})$ is the total energy of the doped system, $(\mathbf{n} - 1)$ being the number of CeO₂ formula units remaining in the doped system, $\mathbf{E}(\text{CeO}_2)$ is the energy of 1 formula unit of cerium (IV) dioxide and $\mathbf{E}(\text{MO})$ is the energy of 1 formula unit of the particular dopant's metal oxide (i.e. PdO or PtO).

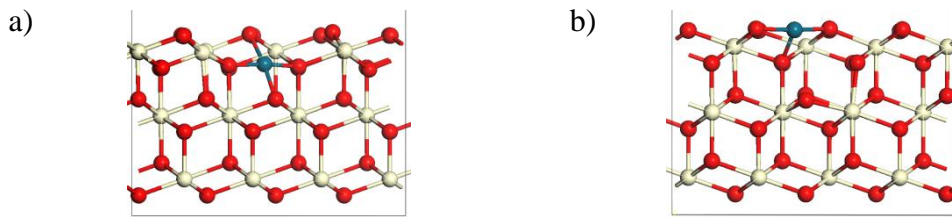


Figure 4.2 Side views for the two substitution sites of Pd and Pt on CeO₂ (111) surface: a) four coordinated square planar site, and b) three coordinated site. Oxygen (red), cerium (cream), and palladium/platinum (blue).

The formation of a single oxygen vacancy on the surfaces is investigated. The single oxygen vacancy formation energies on undoped (E_{vac}) and doped ($E_{\text{vac_doped}}$) surface were calculated as follows:

$$\mathbf{E}_{\text{vac}} = \mathbf{E}(\text{Ce}_{96}\text{O}_{47}) - \mathbf{E}(\text{Ce}_{96}\text{O}_{48}) + \frac{1}{2} \mathbf{E}(\text{O}_2) \quad (4.4)$$

$$\mathbf{E}_{\text{vac_doped}} = \mathbf{E}(\text{Ce}_{95}\text{PdO}_{46}) - \mathbf{E}(\text{Ce}_{95}\text{PdO}_{47}) + \frac{1}{2} \mathbf{E}(\text{O}_2) \quad (4.5)$$

where $(\text{Ce}_{96}\text{O}_{47})$ and $(\text{Ce}_{95}\text{PdO}_{46})$ are oxygen defective systems, $(\text{Ce}_{96}\text{O}_{48})$ and $(\text{Ce}_{95}\text{PdO}_{47})$ are the stoichiometric system, and (O_2) is the gas phase oxygen in the triplet ground state. From Equation (4.4), a more positive value signifies the process to be more endothermic.

A CO molecule was adsorbed on the (111) surface and the step sites. The adsorption energy is calculated following:

$$E_{\text{ads}} = E(\text{CO/CeO}_2) - E(\text{CO}) - E(\text{CeO}_2) \quad (4.6)$$

where $E(\text{CO/CeO}_2)$ is the energy of the adsorbed system, $E(\text{CO})$ and $E(\text{CeO}_2)$ are the energies of a CO molecule and CeO₂ slab, respectively. In the case of a defective CeO₂ surface, the $E(\text{CeO}_2)$ refers to the energy of the defective slab.

For the density of states calculation, the systems were sampled with $3 \times 3 \times 1$ k-points following the Monkhorst-Pack scheme. A smearing of 0.20 eV was used on the final density of states plots. The Bader analysis code developed by Henkelman's research group^{12, 233-235} was used to estimate the Bader charges of each ion species in the systems studied. The Bader charges, q , are computed following:

$$q_i = q_i(\text{valance}) - q_i(\text{Bader}) \quad (4.7)$$

where $q_i(\text{valance})$ is the valence charge obtained from POTCAR used and $q_i(\text{Bader})$ is the Bader charge obtained from Bader code for the i -th atom, respectively.

Energy barriers for the CO oxidation process were obtained using the nudged elastic band (NEB) method. The process was modelled using a chain of 5-10 images that were interpolated linearly between two end points of the optimised adsorbed and oxidised structures. The interpolation was performed using an in-house code for pre- and post-processing of VASP calculations which has also been applied by Willock and co-workers for the deprotonation of H₂O₂.²³⁹ The transition state is determined with a frequency calculation and when only one imaginary mode is present.

4.3 Surface energy and oxygen vacancy formation on low index and <110>-type step surfaces of CeO₂

Table 4.1 DFT and DFT+U (U_{eff}) calculated surface energies, σ , for (111) and (110) surfaces.

Method	σ / eV		
	Relaxed	Unrelaxed	Lower layer fixed
(111) surface			
PW91	0.70	0.71	0.70
PBE	0.68	0.70	0.68
PW91+U	0.76	0.77	0.76
PBE+U	0.73	0.74	0.74
(110) surface			
PW91+U	1.10	1.38	1.10

Investigation on the (111) and (110) surfaces were performed. From the calculated surface energies in Table 4.1, we can observe that the (111) surface is more stable than the (110) surface as reported in the literature.^{170, 258} The unrelaxed, relaxed, and lower layer fixed surface energies for the (111) surface are the same due to very little restructuring on relaxation from the bulk termination. The Ce and O ions at the top most trilayer of the (111) surface have relaxed towards the surface with the top surface oxygen being displaced the most (0.12 Å). For the (110) surface, the unrelaxed surface energy is much higher than the relaxed or lower layer fixed values. This suggests there is significant rearrangement of the structure where the top most Ce cations have relaxed towards the slab by about 0.20 Å. However, the oxygen anions at the same atomic layer have been displaced by only about 0.06 Å towards the slab. In contrast, the Ce cations on the second layer have relaxed upwards perpendicular to the surface by 0.08 Å while oxygen at the same layer moved to the opposite direction by about 0.03 Å. These structural relaxations caused the supposedly levelled Ce-O atomic layer to be disrupted.

Subsequent calculations are performed using PW91+U. In order to study the oxygen vacancy formation on these surfaces, we performed calculations on expanded surface slabs. The method for generating permutations for the localisation sites of the excess electrons in bulk ceria was used here to generate localisation sites on the CeO₂ (111) surface which can occur at nearest neighbour (N), next nearest neighbour (NN), third nearest neighbour (3N), fourth nearest neighbour (4N), or fifth

nearest neighbour (5N) with respect to the oxygen vacancy site. We will denote the two Ce³⁺ ion positions using the following format: N_N which indicates both Ce³⁺ cations at nearest neighbour positions or N_5N which indicates one Ce³⁺ at nearest neighbour position and the other at fifth nearest neighbour position. Only 163 of the 496 structures generated for the surface oxygen vacancy system are unique permutations since there are pairs of Ce³⁺ sites that have similar symmetry environments. As for the sub-surface oxygen defect system, only 159 permutations out of 465 permutations are unique. DFT+U calculations were performed on these 163 and 159 structures of surface and sub-surface oxygen defect systems, respectively. Equation (4.4) is used to calculate the oxygen vacancy formation energies and selected structures are shown in Figure 4.3.

For the surface oxygen vacancy system, the lowest energy structure ($E_{\text{vac}} = 1.56$ eV) is obtained when both the Ce³⁺ ions are located as next nearest neighbours to the oxygen vacancy site (Figure 4.3a). For this structure, neighbouring atoms to the Ce³⁺ ions have moved slightly. The six oxygen atoms around the two Ce³⁺ cations are pushed slightly away from the cations with an average Ce-O bond length of about 2.53 Å compared to 2.39 Å from the clean stoichiometric surface. This is due to the larger ionic radius of Ce³⁺ (1.283 Å) when compared to Ce⁴⁺ (1.11 Å) cation.^{52, 53, 221} This cation radius change leads to a lattice distortion around the cation due to steric effects which was also suggested by Marroccheli *et al.*^{184, 185} They also reported another process where the formation of the vacancy leads to a lattice contraction primarily due to electrostatic interactions. This might be the reason for our observation where the three sub-surface oxygen atoms neighbouring the vacancy site have relaxed towards the site and about 0.16 Å upwards away from the surface (0.25 Å for the two oxygen atoms neighbouring the Ce³⁺ cations). Similarly, Li *et al.* have also observed that the two oxygen atoms next to the vacancy site experience significant relaxation.⁸¹ The Ce³⁺-O bond lengths were reported to be 2.59 Å and 2.61 Å, which are longer than the average Ce-O bond length (~2.38 Å) in bulk ceria.⁸¹ In our lowest energy structure, the two Ce³⁺-O bond lengths are slightly longer (2.62 Å and 2.63 Å) than the rest bonded to the same cation and also the ones in the bulk (2.39 Å). The next lowest E_{vac} is 0.07 eV higher ($E_{\text{vac}}=1.63$ eV, Figure 4.3a). The structure with two nearest neighbour Ce³⁺ cations is 0.25 eV higher than the lowest energy structure.

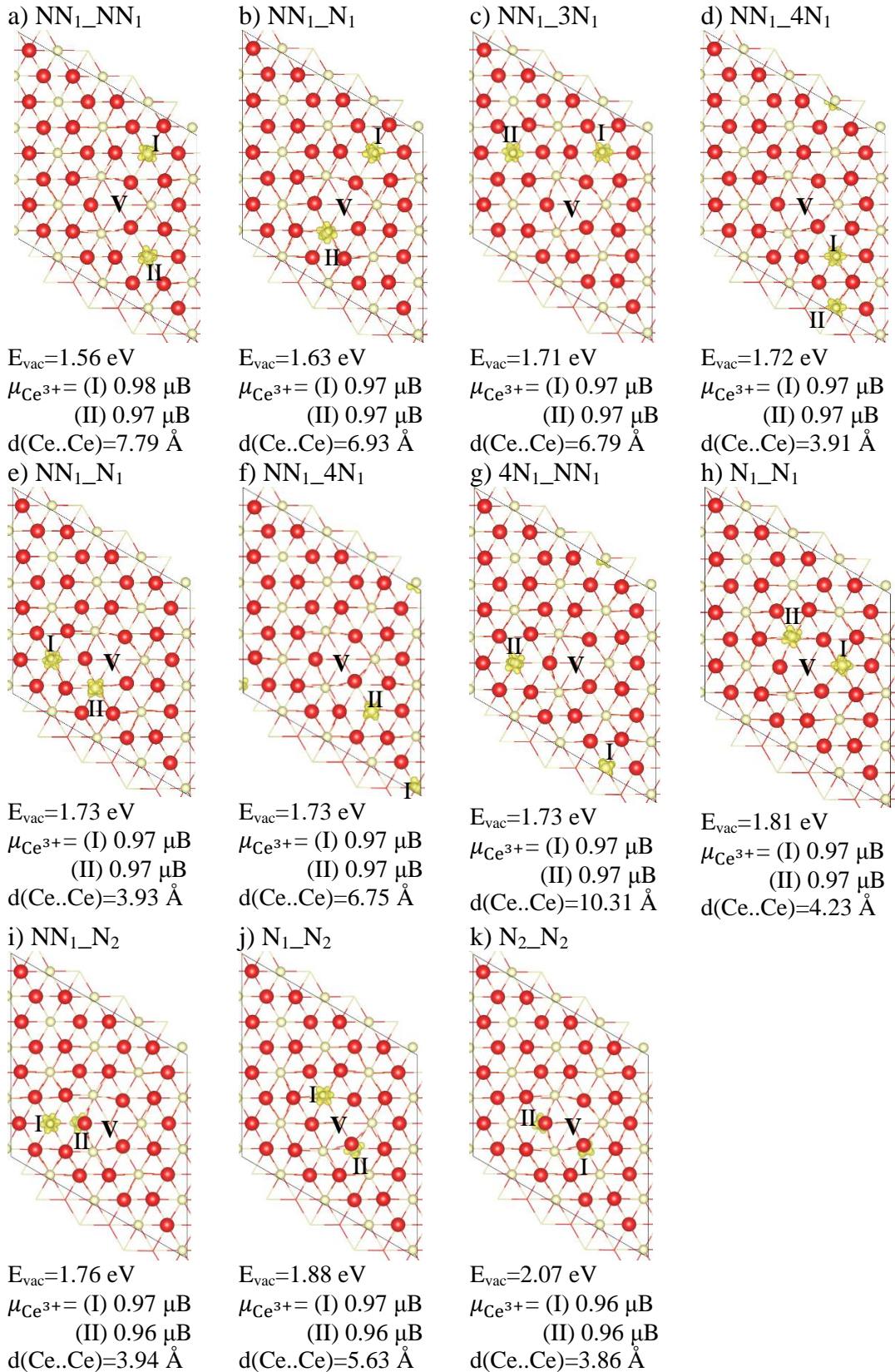


Figure 4.3 Spin density, magnetic moment, vacancy formation energy, and Ce³⁺...Ce³⁺ distance ($d(Ce..Ce)$) on CeO₂ (111) surface with a surface oxygen vacancy (V). N=nearest, NN=next nearest, 3N=third nearest, and 4N=fourth nearest neighbour. Subscript 1 denotes 1st layer, and 2 denotes 2nd layer. Oxygen (red) and cerium (cream). Isosurface level is 0.04 electrons Å⁻³.

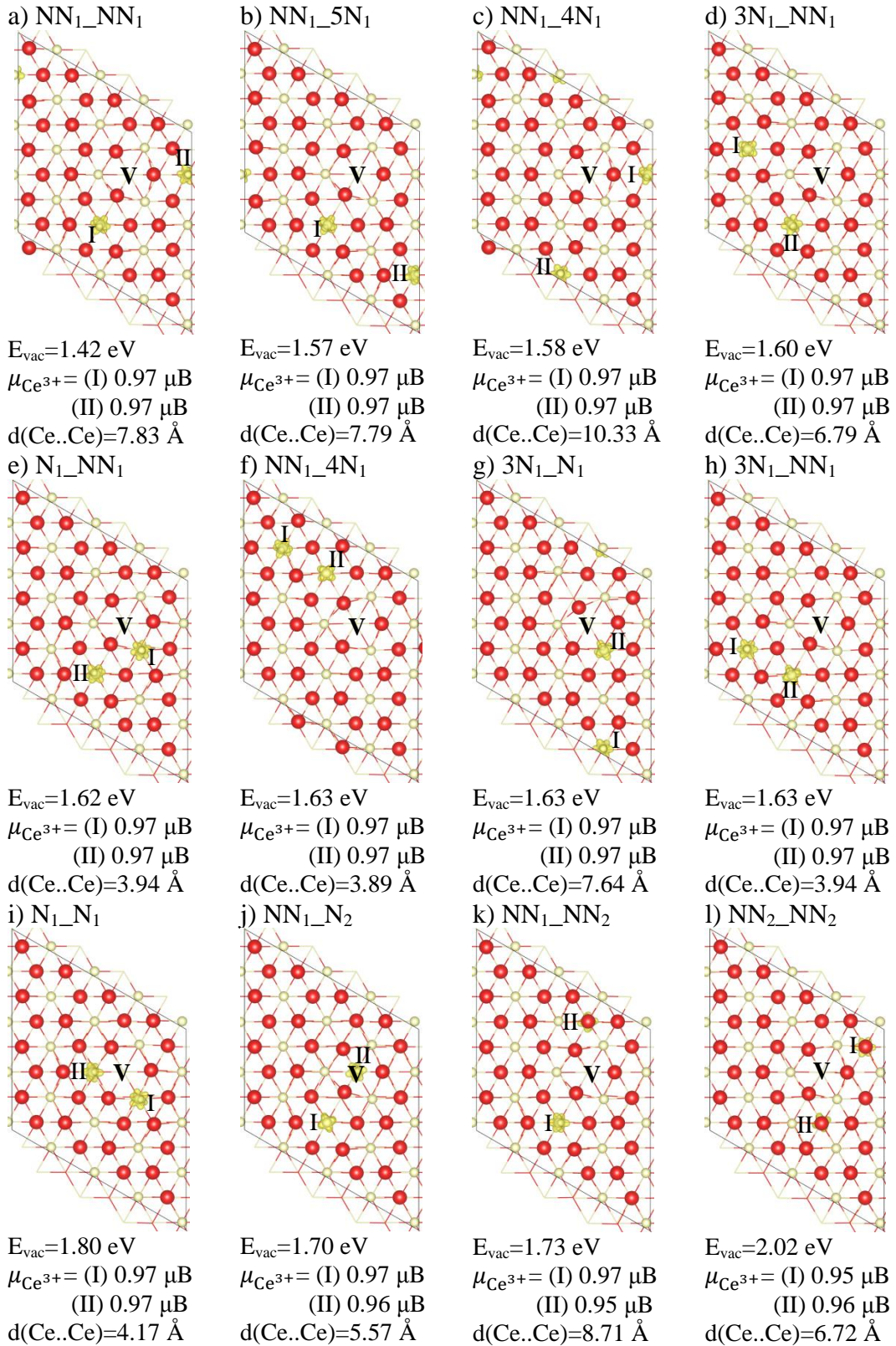


Figure 4.4 Spin density, magnetic moment, vacancy formation energy, and Ce³⁺...Ce³⁺ distance ($d(Ce..Ce)$) on CeO₂ (111) surface with a sub-surface oxygen vacancy (V). N=nearest, NN=next nearest, 3N=third nearest, 4N=fourth nearest neighbour, and 5N=fifth nearest neighbour. Subscript 1 denotes 1st layer, and 2 denotes 2nd layer. Oxygen (red) and cerium (cream). Isosurface level is 0.04 electrons Å⁻³.

The structure with Ce³⁺ cations at the NN₁_N₂ position (Figure 4.3i) is slightly more favourable ($\Delta E_{\text{vac}} = -0.05$ eV) than the structure with two surface Ce³⁺ at nearest neighbours positions. The structures with both Ce³⁺ cations at second layer yield E_{vac} of 2.0 eV and above. Ce³⁺ sites can also be determined through density of states (DOS) plots (Figure 4.5) whether they are at surface sites or bulk (second layer) sites. Figure 4.5d shows the DOS plot for the oxygen defective bulk CeO₂ where the Ce³⁺ sites are at nearest neighbours with respect to the vacancy site. The gap state (~ -0.2 eV) in between the O_{2p} – Ce_{4f} gap for this plot is attributed to the Ce³⁺ 4f band. The tail of the O 2p band ends at -1.5 eV while the unoccupied Ce 4f band span across 1.0 eV above the Fermi energy. From all the DOS plots for the oxygen defective CeO₂ (111) surface, the DOS where Ce³⁺ cations are at N₂_N₂ positions (Figure 4.5c) is most similar to the DOS for oxygen defective CeO₂ bulk (Figure 4.5d). This also shows that the Ce³⁺ cations are at the bulk Ce sites.

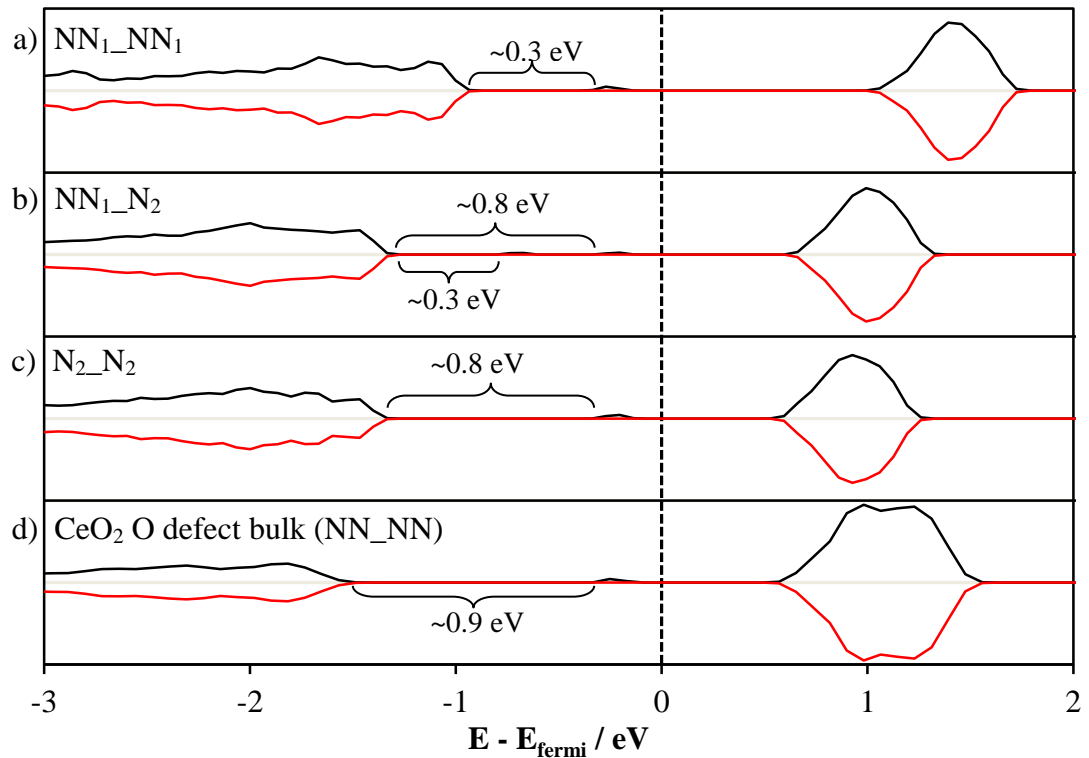


Figure 4.5 Total density of states (DOS) plot for the oxygen defective CeO₂ (111) surface with Ce³⁺ at a) NN₁_NN₁ (Figure 4.3a), b) NN₁_N₂ (Figure 4.1i), and c) N₂_N₂ (Figure 4.1k). d) DOS for oxygen defective bulk CeO₂ with Ce³⁺ at next nearest neighbour positions. Up and down spins are represented by black and red solid lines, respectively. The vertical dashed line indicates the Fermi energy corrected to 0 eV. Gaussian smearing width of 0.01 eV is applied.

From Figure 4.5b, there appear two gap states in between the O_{2p} – Ce_{4f} gap. These are the occupied 4f bands for the surface and bulk Ce³⁺. The gap state which is

about 0.3 eV and 0.8 eV from the O 2*p* band can be attribute to the surface and bulk Ce³⁺, respectively. This is confirmed by the DOS plot in Figure 4.5a and b. They show the DOS plots for two surface and two bulk Ce³⁺ sites with the gap value for O 2*p* – Ce³⁺ 4*f* of about 0.3 eV and 0.8 eV, respectively .

Figure 4.4 shows the selected structures for a sub-surface oxygen vacancy system. Similar to the surface oxygen vacancy system, the Ce³⁺ ions are found at next nearest neighbours from the oxygen vacancy site ($E_{\text{vac}}=1.42$ eV, Figure 4.4a). On optimisation, the three oxygen atoms neighbouring the vacancy site relaxed towards the vacancy site and about 0.21 Å downwards towards the surface. Similarly, six of the neighbouring oxygen atoms of the Ce³⁺ cations are pushed away from the cations. These observations are similar to the ones for a surface oxygen vacancy. Basically, the oxygen atoms are trying to contract into the vacancy site and the Ce³⁺ neighbouring oxygen atoms are pushed away from the reduced centre. Our findings also agree well with the theoretical results presented by Li *et al.*⁸¹ and Ganduglia-Pirovano *et al.*⁸² Similarly, the structure with two Ce³⁺ at nearest neighbour positions (Figure 4.4i) have higher E_{vac} (1.80 eV) than the structure with Ce cations at NN₁_N₂ positions (Figure 4.4j, $E_{\text{vac}}=1.70$ eV). Structures with two Ce³⁺ at sub-surface sites yield E_{vac} higher than 2.00 eV.

Table 4.2 Bader charges of Ce³⁺ cations from selected CeO₂ (111) surface and sub-surface oxygen vacancy structures. Values in brackets are Bader charges of respective Ce⁴⁺ cations in the stoichiometric CeO₂ (111) surface.

Structure	Bader charge / <i>e</i>	
	Ce ³⁺ (I)	Ce ³⁺ (II)
Surface Oxygen Vacancy (Figure 4.1)		
a	2.14 (2.38)	2.14 (2.37)
h	2.13 (2.38)	2.13 (2.40)
k	2.13 (2.40)	2.13 (2.40)
Sub-surface oxygen (Figure 4.2)		
a	2.13 (2.37)	2.13 (2.37)
j	2.13 (2.37)	2.11 (2.40)
l	2.14 (2.40)	2.14 (2.40)

Table 4.2 shows the Bader charges of Ce³⁺ cations on selected structures (Figure 4.3a, h, k, and Figure 4.4a, j, l) and their respective Ce⁴⁺ cations on stoichiometric CeO₂ (111) surface. The Bader charges further confirm that the cations are reduced

upon the removal of an oxygen atom and confirm the formation of Ce³⁺ cations on the defective CeO₂ (111) surfaces.

There are no distinct trends which can be observed for the E_{vac} with respect to the Ce³⁺ sites. Nevertheless, some observations can still be made from the results obtained. When the Ce³⁺ sites are both at the next nearest neighbours (Figure 4.3a and Figure 4.4a), the two oxygen atoms which are next to the vacancy site receive an extra “*push*” to relax towards the vacancy site from the steric effects of the Ce³⁺ cations. As mentioned earlier, the two Ce³⁺-O bond lengths are slightly longer than the others. This is a favourable process since the neighbouring oxygen atoms are relaxing towards the vacancy site. On the other hand, with two nearest neighbours Ce³⁺ cations (Figure 4.3h and Figure 4.4i), three of the neighbouring oxygen atoms to the vacancy site encounter steric effects from the Ce³⁺ cations while trying to relax towards the vacancy site. Besides, one of the three oxygen atoms is experiencing steric effects from both Ce³⁺ cations. This resulted to a less favourable process in relaxation of the atoms around the vacancy site. Hence, a higher E_{vac} should be expected from this configuration. These observations are also in agreement to the suggestion by Li *et al.* where the distribution of localised electrons and relative stabilities of top- and sub-surface O vacancies are determined by structural relaxations.⁸¹

Another observation which can be made is that the Ce³⁺..Ce³⁺ distance did not affect the E_{vac} as strongly as first thought. From Figure 4.3d, f, and g, where one Ce³⁺ is at NN site and one at 3N site with a distance of 3.91 Å, 6.75 Å, and 10.31 Å apart, respectively, it is observed that the difference in E_{vac} is just 0.01 eV. Similarly, the difference in E_{vac} is just 0.03 eV for the structures with one of the Ce³⁺ cations at NN site and the other at 4N site (Figure 4.4 c, f) and when each is at NN and 3N sites, respectively (Figure 4.4d,h). However, a slightly higher E_{vac} difference (0.10 eV) is observed with structures in Figure 4.3b, and e, where the Ce³⁺ cations are each at N and NN sites, respectively. This might be due to the favourable and less favourable processes discussed earlier regarding the oxygen atoms having to experience both the steric effect from the Ce³⁺ cation and the electrostatic interactions from the formation of the vacancy at the same time.

The rest of the structures shown in Figure 4.3 are some of the lowest energy among the structures which has two Ce³⁺ on the surface (a-i), one surface Ce³⁺ and

one sub-surface Ce³⁺ (j,k), and two sub-surface Ce³⁺ (l). Figure 4.6 shows the population of structures with different Ce³⁺ sites at different ranges of E_{vac} for the surface and sub-surface oxygen systems. In both the systems, the lower E_{vac} ranges consist mostly of structures with two Ce³⁺ cations on the surface (blue bars) while the mixture of one surface Ce³⁺ and one sub-surface Ce³⁺ structures (red bars) populate mainly the middle E_{vac} ranges. The highest E_{vac} ranges consist mostly of structures with two sub-surface Ce³⁺ (green bars).

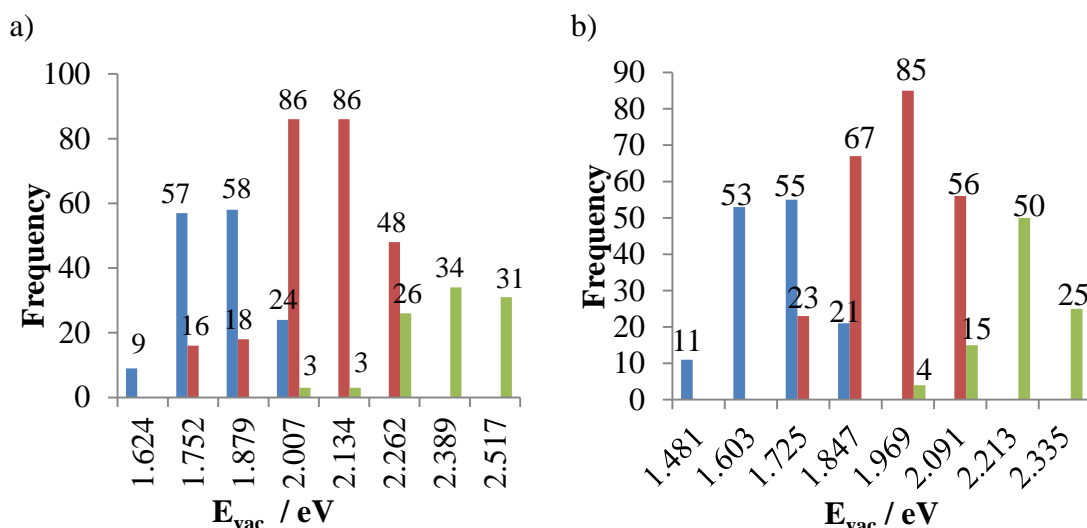


Figure 4.6 Population of structures with different Ce³⁺ localisation and at different E_{vac} ranges on the a) surface and b) sub-surface oxygen vacancy systems obtained from PW91+U calculations. Blue (two surface Ce³⁺), red (one surface and one sub-surface Ce³⁺), and green (two sub-surface Ce³⁺).

Oxygen defect formation on CeO₂ (110) surface was investigated using the same method applied to the (111) CeO₂ surface. However, only cerium sites on the top layer were considered for electron localisation sites. Thus, a total of 66 permutations were found with 36 of them being unique. Table 4.3 shows the oxygen vacancy formation energies obtained along with the number of structures with similar symmetry environment found. A histogram showing count of all symmetry equivalent structures found in various E_{vac} ranges can be seen in Figure 4.7.

Table 4.3 Oxygen vacancy formation energy (E_{vac}) on CeO₂ (110) surface calculated using PW91+U together with the total number of structures generated with similar symmetry environment. Nearest neighbour (N), next nearest neighbour (NN), third nearest neighbour (3N), fourth nearest neighbour (4N), fifth nearest neighbour (5N), and sixth nearest neighbour (6N).

Structures	Localisation sites	$E_{\text{vac}}/ \text{eV}$	Total number of structures with similar symmetry
110/1	N_4N	0.77	2
110/2	N_NN	0.78	2
110/3	NN_4N	0.78	2
110/4	N_4N	0.79	2
110/5	N_NN	0.79	2
110/6	4N_5N	0.81	2
110/7	N_5N	0.81	2
110/8	4N_5N	0.81	2
110/9	N_5N	0.82	2
110/10	NN_4N	0.83	2
110/11	5N_6N	0.85	2
110/12	3N_4N	0.89	2
110/13	NN_3N	0.89	2
110/14	NN_3N	0.89	2
110/15	3N_4N	0.90	2
110/16	3N_5N	0.93	2
110/17	NN_5N	0.94	2
110/18	NN_NN	0.96	1
110/19	6N_6N	0.96	1
110/20	4N_4N	0.96	1
110/21	NN_6N	0.96	2
110/22	3N_5N	0.96	2
110/23	N_6N	0.97	2
110/24	3N_6N	0.98	2
110/25	5N_6N	0.98	2
110/26	4N_6N	0.98	2
110/27	4N_6N	0.98	2
110/28	NN_6N	0.99	2
110/29	N_6N	1.00	2
110/30	N_3N	1.03	2
110/31	NN_5N	1.07	2
110/32	3N_6N	1.07	2
110/33	5N_5N	1.12	1
110/34	N_3N	1.12	2
110/35	N_N	1.15	1
110/36	3N_3N	1.30	1

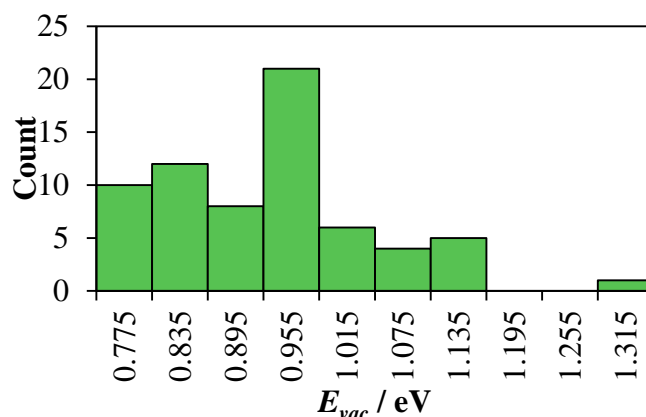


Figure 4.7 Histogram showing the number of (110) CeO₂ surface structures in different ranges of E_{vac} obtained from PW91+U calculations.

The lowest and highest E_{vac} calculated for the (110) surface is 0.77 eV (structure 110/1) and 1.30 eV (structure 100/36), respectively. These values are lower than the corresponding values calculated for the (111) surface. Thus, showing that the (110) surface is more reactive than the (111) surface as oxygen is easily extracted and supplied as a source for oxidation catalysis on the (110) surface.

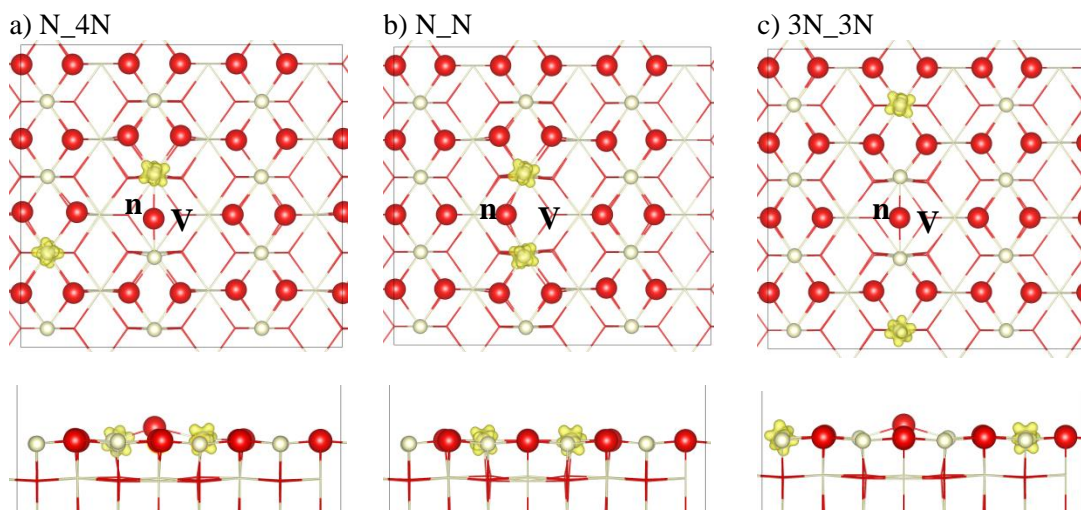


Figure 4.8 Spin densities for optimised defective (110) CeO₂ surface of structure a) 110/1, b) 110/35, and c) 110/36. Top view is shown in images at top row and side view is shown in images at bottom row. Oxygen (red), cerium (cream). Immediate neighbouring oxygen labelled with **n**. **V** indicates vacancy site. Isosurface level is 0.04 electrons \AA^{-3} .

Figure 4.8a shows the spin density for optimised structure with the lowest E_{vac} (structure 110/1). In this structure, the two excess electrons are localised on cerium ions at nearest and fourth nearest neighbour positions (N_4N) with respect to the vacancy site. It is observed that the immediate neighbouring oxygen (O(**n**)) in Figure 4.8) in most structures has moved to between the two nearest cerium ions (Figure 4.8a and c) upon the removal of an oxygen from the surface. However, when two

Ce³⁺ sites are at N_N positions (Figure 4.8b), the O(n) only moved slightly towards the centre of the two Ce ions shortening the Ce-O bond length by about 0.02 Å when compared to the bulk Ce-O bond length of 2.38 Å. The larger ionic radius of Ce³⁺ (1.283 Å)^{52, 53, 221} has hindered the O(n) from moving to the centre position as in most structures. Besides, in the structures where O(n) has moved to the centre of the two neighbouring Ce ions, O(n) has also relaxed upwards away from the surface lattice.

As for the <110>-type step surfaces of CeO₂, only oxygen vacancy formation on the CeO₂-U surface will be discussed. Initially, a total number of 276 permutations can be generated for the structure. However, after eliminating structures with similar symmetry environment and applying stricter cut-off value for maximum Ce-O_v distance of 5 Å, only 13 unique structures are obtained. Only one oxygen vacancy site is studied which is the two coordinated upper layer oxygen at the edge of the step site. This oxygen has only two bonds which in theory should be easier to remove compared to the three or four coordinated oxygen anions. Table 4.4 shows the oxygen vacancy formation energies calculated for the CeO₂-U surface. The lowest energy structure (E_{vac}=0.95 eV) is when the excess electrons are localised on next nearest neighbour cerium on the first and second layer of the surface.

Table 4.4 Oxygen vacancy formation energy (E_{vac}) on <110>-type step surface (CeO₂-U) calculated using PW91+U together with the total number of structures generated with similar symmetry environment. Nearest neighbour (N) and next nearest neighbour (NN). Subscript 1 denotes 1st layer, and 2 denotes 2nd layer.

Structures	Localisation sites	E _{vac} / eV	Total number of structures with similar symmetry
CeO ₂ -U/1	NN ₁ _NN ₂	0.95	1
CeO ₂ -U/2	N ₁ _NN ₁	1.01	1
CeO ₂ -U/3	N ₁ _NN ₁	1.04	1
CeO ₂ -U/4	NN ₁ _NN ₂	1.12	2
CeO ₂ -U/5	N ₁ _NN ₂	1.25	1
CeO ₂ -U/6	N ₁ _NN ₂	1.27	1
CeO ₂ -U/7	N ₁ _N ₁	1.27	1
CeO ₂ -U/8	N ₁ _NN ₂	1.40	1
CeO ₂ -U/9	N ₁ _NN ₂	1.40	1
CeO ₂ -U/10	N ₁ _NN ₂	1.40	1
CeO ₂ -U/11	N ₁ _NN ₂	1.41	1
CeO ₂ -U/12	NN ₂ _NN ₂	1.48	2
CeO ₂ -U/13	NN ₂ _NN ₂	1.76	1

From Figure 4.9a, the oxygen next to the vacancy site is relaxed towards the vacancy. The bond length of the Ce³⁺ on the first layer and the oxygen next to the vacancy has increased from about 2.25 Å to 2.40 Å. The bond length for Ce³⁺ from second layer and the oxygen next to the vacancy has increased from about 2.30 Å to 2.77 Å. This showed that significant relaxation around the vacancy site has occurred in order to form a more stabilised structure. Similarly, relaxation of atoms around the vacancy and Ce³⁺ sites have occurred across all the surfaces with different pairs of Ce³⁺ sites.

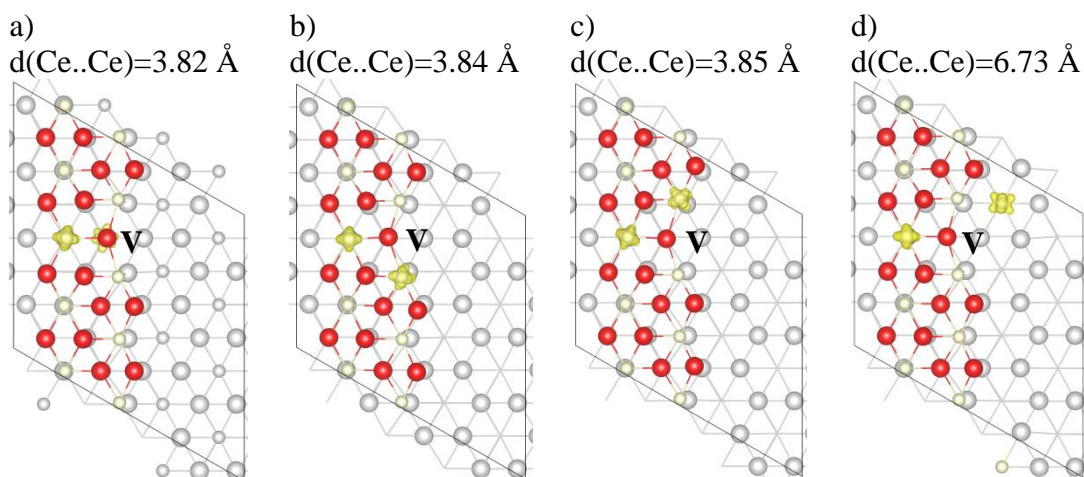
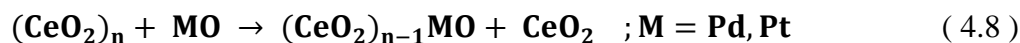


Figure 4.9 Spin densities for four of the O-defective CeO₂-U surface: a) CeO₂-U/1, b) CeO₂-U/2, c) CeO₂-U/3, and CeO₂-U/4. Cerium (cream), oxygen (red), and second CeO₂ layer (silver). Isosurface level is 0.04 electrons Å⁻³.

Overall, oxygen vacancy formation is easier on the (110) surface followed by the CeO₂-U <110>-type step surface and then the (111) CeO₂ surface. Structural relaxation is observed to have influenced the localisation sites for two excess electrons left by the removal of an oxygen from the surface. Besides, significant relaxation is observed among the neighbouring atoms around the vacancy and the Ce³⁺ sites. It is suggested that these relaxations are the key to stabilise the defective surfaces of CeO₂.

4.4 Doping CeO₂ (111) surface with platinum group metals (PGM)

In this section, work on surfaces doped with a single divalent Pd or Pt cation will be presented. Similar methods to doping bulk ceria have been applied for the surfaces. The process of the formation of a divalently doped system can be described as:



The dopants are placed at two different sites in the surface lattice: 1) at square planar position with four neighbouring oxygen atoms, and 2) three coordinated position with three neighbouring oxygen atoms. The optimised structures of Pd/Pt-doped ceria surfaces are shown in Figure 4.10.

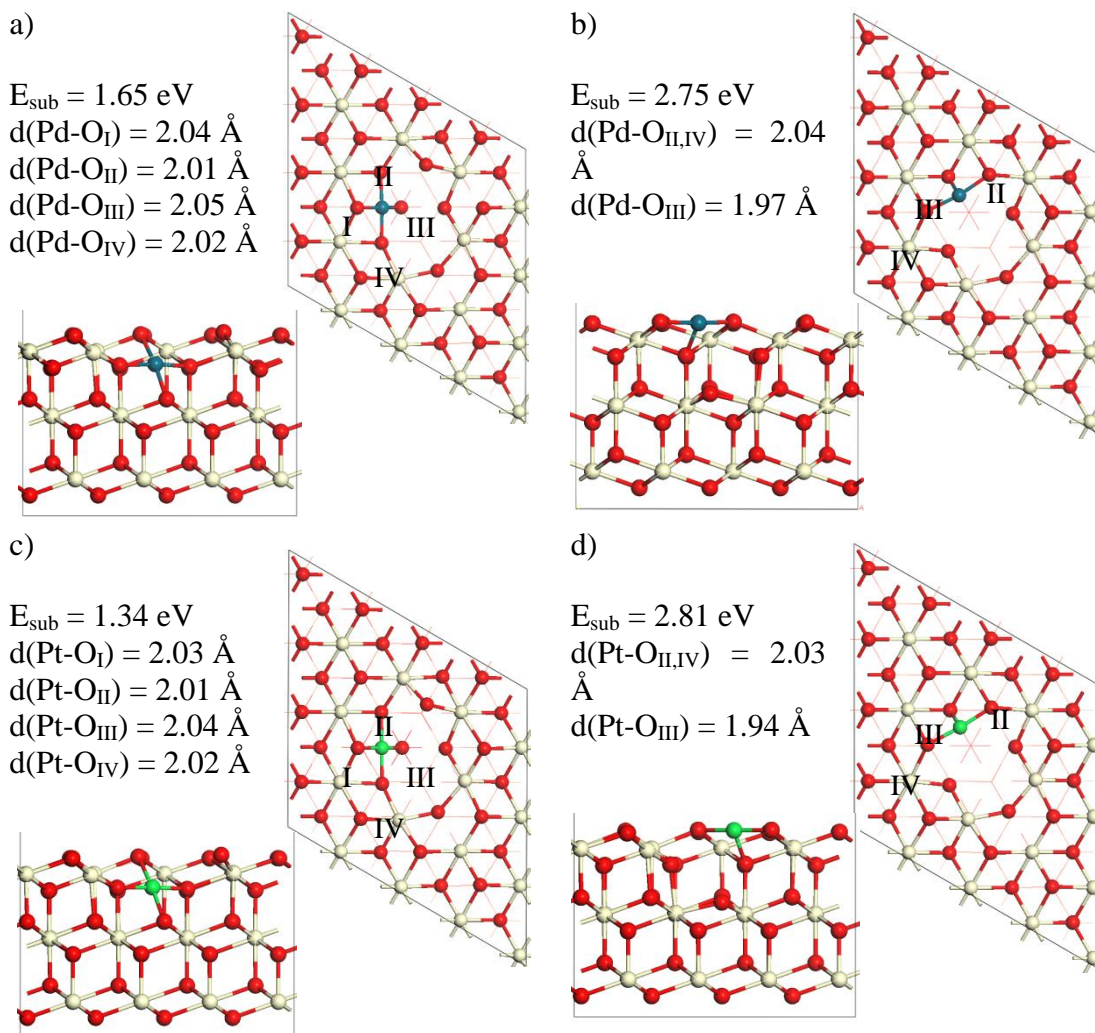


Figure 4.10 Optimised structures of Pd/Pt-doped CeO₂ (111) surface along with E_{sub} and Pd/Pt-O distances at a,c) square planar position with four neighbouring oxygen atoms, and at b,d) three coordinated position with three neighbouring oxygen atoms. Palladium (blue), platinum (green), oxygen (red), and cerium (cream).

When the dopants are at the square planar position with neighbouring oxygen atoms, they are located at the CeO₂ (111) sub-surface level of the top layer (Figure 4.10a and b). The bond lengths of dopants to oxygen atom from the surface (O_I in Figure 4.10) and the oxygen atom from the second layer (O_{III} in Figure 4.10) are longer than those from the side. This gives a distorted square planar geometry. Overall, the distances are similar to those obtained in Pd/Pt-doped bulk CeO₂. Energetically, the Pd/Pt dopants are more like to be at the square planar position compared to the three coordinated position with three neighbouring oxygen atoms. In

the three coordinated position, the Pd/Pt dopant is exposed to the surface. The dopant bonds with two oxygen atoms from the surface, one at each side, and one oxygen atom from the sub-surface. The bond lengths of the Pd/Pt-O_{III} (Figure 4.10b, c) are shorter compared to the Pd/Pt-O_{II} and Pd/Pt-O_{IV}.

Table 4.5 shows the Bader charges for the various atom species in Pd/Pt-doped systems and PdO/PtO (palladium (II) oxide/platinum (II) oxide) bulk structures. The Bader charges confirm that the dopant metals are neither in their metallic state nor in +4 oxidation state. The values are very close to the Bader charges calculated for Pd²⁺/Pt²⁺ in bulk PdO/PtO. Surface cerium and oxygen species have slightly lower Bader charges compared to the bulk species due to the lower coordination number of the cation and anion, respectively. The oxygen atoms bonded to the dopant metals have slightly lower Bader charges compared to the rest of the oxygen species in the slab.

Table 4.5 Bader charges of PdO/PtO and Pd/Pt dopant with its neighbouring oxygen atoms, along with the average Bader charges of cerium and oxygen cations for Pd/Pt-doped CeO₂ (111) surface.

Atom species	Bader charge / <i>e</i>			
	Pd-doped		Pt-doped	
	Square planar	Three coordinated	Square planar	Three coordinated
O_I	-1.03	-1.06	-1.02	-1.06
O_{II}	-1.08	-1.00	-1.08	-0.96
O_{III}	-1.09	-1.06	-1.09	-1.06
O_{IV}	-1.10	-	-1.10	-
Pd/Pt	0.77	0.77	0.78	0.73
O_{surf}	-1.19	-1.19	-1.19	-1.19
O_{bulk}	-1.21	-1.20	-1.21	-1.20
Ce_{surf}	2.37	2.37	2.37	2.37
Ce_{bulk}	2.40	2.40	2.40	2.40
Bulk	PdO*		PtO*	CeO₂
Metal	0.81		0.80	2.44
O	-0.81		-0.80	-1.22

*calculations are performed using standard PW91 functional without on-site Coulomb interaction correction.

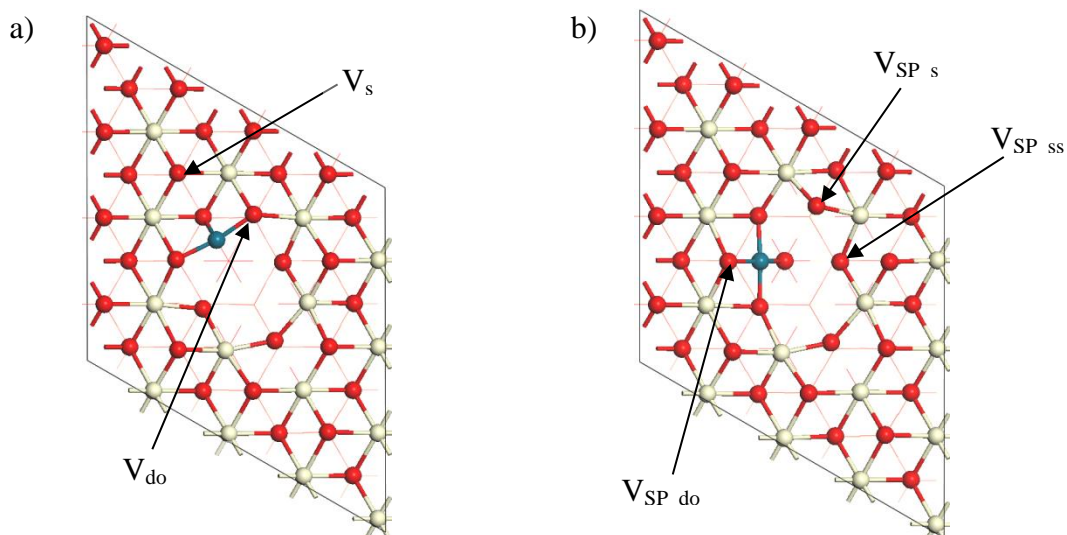


Figure 4.11 Oxygen vacancy sites on the Pd/Pt-doped CeO₂ (111) surface at a) three coordinated site and b) square planar position.

Table 4.6 Oxygen vacancy formation energies (E_{vac}) at various vacancy sites along with Bader charges of Ce³⁺ cations and dopant metals for Pd/Pt-doped systems.

	$E_{\text{vac_doped}} / \text{eV}$	Bader charges / e	
		Ce ³⁺	Pd/Pt
<u>Pd-doped system</u>			
V_{SP_s}	0.68	2.09, 2.14	0.75
$V_{\text{SP}_{ss}}$	1.19	2.10, 2.12	0.75
$V_{\text{SP}_{do}}$	1.49	2.08	0.83
V_s	1.35	2.28, 2.22	0.77
V_{do}	-0.38	2.09, 2.14	0.75
<u>Pt-doped systems</u>			
V_{SP_s}	0.66	2.09, 2.14	0.76
$V_{\text{SP}_{ss}}$	1.16	2.26, 2.17	0.75
$V_{\text{SP}_{do}}$	2.76	2.28, 2.29, 2.22	0.40
V_s	1.39	2.13, 2.13	0.69
V_{do}	-0.80	2.09, 2.14	0.76

The effects of dopant metals to oxygen vacancy formation on CeO₂ (111) surface has also been investigated. Oxygen vacancy has been created on three different sites on the Pd/Pt-doped surface (Figure 4.11) at square planar position: i) surface vacancy (V_{SP_s}), ii) sub-surface vacancy ($V_{\text{SP}_{ss}}$), and iii) dopant bonded oxygen ($V_{\text{SP}_{do}}$). For the Pd/Pt-doped surface at three coordinated site, vacancy sites were created by removing an oxygen atom bonded to the dopant (V_{do}), and from the surface (V_s). Calculated oxygen vacancy formation energies are tabulated in Table 4.6 along with Bader charges of Ce³⁺ cations and dopant metals of respective systems.

The presence of Pd/Pt dopant has reduced the energy required for the formation of a single oxygen vacancy on the surface (refer Figure 4.3, Figure 4.4, and Table 4.6). For the Pd/Pt-doped surface at square planar position, the two coordinated surface oxygen (V_{SP_s}) is the easiest to remove. The required energy is 0.68 eV and 0.66 eV for the Pd- and Pt-doped systems, respectively. The least favourable oxygen vacancy site is where the oxygen is bonded to the dopant metal. It requires an E_{vac_doped} of 1.49 eV and 2.76 eV to remove the oxygen bonded to the Pd and Pt cation on the doped CeO₂ (111) surface, respectively. One possible reason for a higher E_{vac_doped} at V_{SP_do} site on Pt-doped system might be due to the reduction of three Ce⁴⁺ cations rather than one on the Pd-doped system. It is also observed that the Bader charge for Pt at V_{SP_do} is 0.38 e lower than the Pt cation from the stoichiometric Pt²⁺@SPP system. This suggests that there is more covalency in the Pt-O interaction in the final structure. The Pd species at the same site has gained 0.06 e .

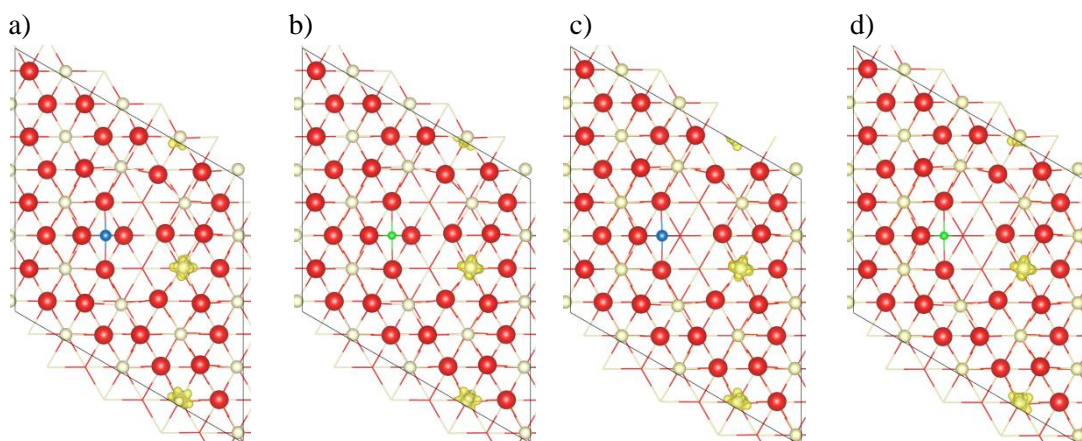


Figure 4.12 Spin densities for optimised structures of a) Pd-, b) Pt-doped CeO₂ (111) surface at square planar position with oxygen vacancy at V_{SP_s} site. c) Pd-, d) Pt-doped CeO₂ (111) surface at three coordinated site with oxygen vacancy at V_s site. Metal dopant in structures c) and d) has undergone repositioning during relaxation producing end structures similar to a) and b). Oxygen (red), cerium (cream), palladium (blue), platinum (green). Refer to Figure 4.11 for vacancy site labels. Isosurface level is 0.04 electrons \AA^{-3} .

In the three coordinated Pd/Pt doped systems, the abstraction of the oxygen bonded to the dopant metal is exothermic. The vacancy formation energies are -0.38 eV and -0.80 eV for Pd- and Pt-doped surface, respectively. The metal dopants were left with a coordination number of 2 upon the removal of an oxygen atom. This caused the arrangement to be less stable. The repositioning of the metal dopant to square planar position during the optimisation process stabilised the system.

Therefore, producing end structures that resemble the optimised structures with a surface oxygen vacancy (V_{SP_s}) (refer to Figure 4.12). The three coordinated sub-surface oxygen requires higher E_{vac} than it is required to remove the oxygen from V_{SP_s} site. This may be due to the coordination number of the oxygen atoms on both systems. The oxygen at V_{SP_s} site is two coordinated while the oxygen at V_s site is three coordinated. Therefore, justifying the higher E_{vac_doped} required to break an extra Ce-O bond at the V_s site. Overall, the PGM dopants are shown to be energetically more stable at square planar coordination on the surface rather than the three coordinated position. The oxygen vacancy formation energy on these doped (111) CeO₂ surfaces are observed to be lower than that on a clean surface except for the oxygen bonded to Pt at square planar position.

4.5 Doping CeO₂ <110>-type step surfaces with platinum group metals (PGM)

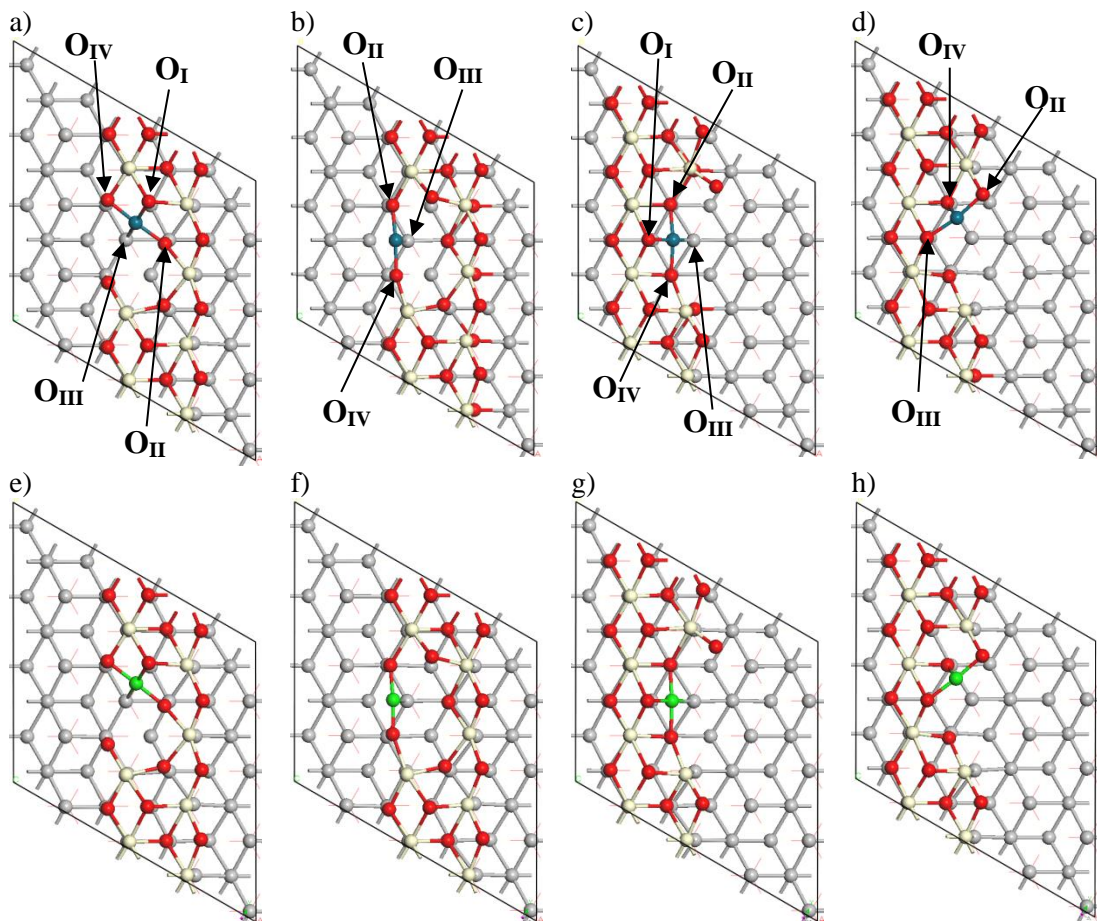


Figure 4.13 Optimised structures for Pd/Pt-doped CeO₂ <110>-type step surfaces. Pd doped systems are a) Pd/CeO₂-D@SPP, b) Pd/CeO₂-D@3C, c) Pd/CeO₂-U@SPP, and d) Pd/CeO₂-U@3C. Pt doped systems are e) Pt/CeO₂-D@SPP, f) Pt/CeO₂-D@3C, g) Pt/CeO₂-U@SPP, and h) Pt/CeO₂-U@3C. Palladium (blue), platinum

(green), cerium (cream), oxygen (red), and second CeO₂ layer (silver). Oxygen labelled O_I, O_{II}, O_{III}, and O_{IV} for Pd/Pt-O distances.

The ⟨110⟩-type step surfaces (CeO₂-U and CeO₂-D) are discussed in this section. The surfaces were doped with divalent Pd or Pt cation at substitution sites similar to those studied for the CeO₂ (111) surface. Figure 4.13 shows the optimised structures for Pd/Pt-doped CeO₂-U and CeO₂-D surfaces. The calculated substitution energies are tabulated in Table 4.7. In general, the calculated substitution energies for the ⟨110⟩-type step surfaces are lower than that of the CeO₂ (111) surface. Similarly, metal dopants substituted at square planar position (SPP) yield lower substitution energies than the three coordinated sites. Pd and Pt substituted at CeO₂-U@SPP have the lowest E_{sub} (1.09 eV and 0.80 eV, respectively) among the other sites.

Table 4.7 PW91+U calculated substitution energies (E_{sub}) and Pd/Pt-O distances for Pd/Pt-doped ⟨110⟩-type step surfaces (CeO₂-U and CeO₂-D). SPP and 3C indicates square planar positions and three coordinated site, respectively. Refer to Figure 4.13 for oxygen labels.

Systems	E _{sub} / eV	Pd/Pt-O distances / Å			
		O _I	O _{II}	O _{III}	O _{IV}
<u>Pd-doped system</u>					
Pd/CeO ₂ -D@SPP	1.36	2.05	2.01	2.03	2.02
Pd/CeO ₂ -D@3C	2.60	-	2.01	1.99	2.03
Pd/CeO ₂ -U@SPP	1.09	2.02	2.02	2.04	2.03
Pd/CeO ₂ -U@3C	1.61	-	1.97	1.99	2.03
<u>Pt-doped system</u>					
Pt/CeO ₂ -D@SPP	1.01	2.05	2.01	2.03	2.02
Pt/CeO ₂ -D@3C	2.69	-	1.94	1.96	1.92
Pt/CeO ₂ -U@SPP	0.80	2.03	2.02	2.03	2.03
Pt/CeO ₂ -U@3C	1.67	-	1.97	1.95	2.03
Experimental Pd/Pt-O distances / Å					
Pd ^a			2.02		
Pt ^b			~2.0		

^ataken from Ref.⁸⁹; ^btaken from Ref.⁸⁸

The Pd/Pt-O distances obtained from system where the metal dopants are at square planar position (SPP) are in agreement with the experimental distances reported in literature.^{88, 89} The Pd-O distances at the three coordinate (3C) site are very close to the SPP structures and the experimental values. As for Pt-doped systems at 3C site, the Pt-O distance are generally smaller than the SPP structures and the experimental values. These show that it is possible that the Pt-doped systems

at 3C site is not in line with experiment while for the Pd case, the doped structures at SPP and 3C site cannot be differentiate.

Table 4.8 Average Bader charges for Pd/Pt and selected oxygen species in each of the stated Pd/Pt doped systems. O_s, O_{ss}, and O_{Pd/Pt} correspond to surface, sub-surface, and Pd/Pt bonded oxygen species, respectively.

Systems	Average Bader atomic charge / <i>e</i>			
	First layer		Second layer	
	O _s	O _{ss}	O _s	O _{ss}
CeO ₂ -D	-1.16	-1.16	-1.20	-1.19
CeO ₂ -U	-1.16	-1.16	-1.19	-1.20
	O _{Pd/Pt}		Pd/Pt	
<u>Pd-doped system</u>				
Pd/CeO ₂ -D@SPP	-1.05		0.75	
Pd/CeO ₂ -D@3C	-1.04		0.80	
Pd/CeO ₂ -U@SPP	-1.08		0.75	
Pd/CeO ₂ -U@3C	-1.01		0.76	
<u>Pt-doped system</u>				
Pt/CeO ₂ -D@SPP	-1.05		0.75	
Pt/CeO ₂ -D@3C	-0.92		0.98	
Pt/CeO ₂ -U@SPP	-1.07		0.76	
Pt/CeO ₂ -U@3C	-0.99		0.74	

Further analysis of the electronic properties of each system was carried out via Bader analysis. Table 4.8 shows the average Bader charges for selected species in the Pd/Pt-doped systems. Overall, all the oxygen bonded to Pd or Pt have higher average Bader charges than the corresponding oxygen from respective layers in the clean stoichiometric surfaces. The Bader charges for Pd/Pt dopant in the surfaces are similar to the values obtained from the metal dopants in CeO₂ (111) doped surfaces. The Pd and Pt species are in +2 oxidation state as an oxygen atom is removed for the systems to have an overall neutral charge and there are no Ce³⁺ species observed in any of the systems. However, the Bader charges for Pd and Pt dopant in CeO₂-D@3C are slightly higher than the rest (0.80 *e* and 0.98 *e* for Pd and Pt, respectively).

4.6 CO adsorption and oxidation on CeO₂ surfaces

CO was used as probe molecule to study adsorption reactions on the CeO₂ surfaces. A CO molecule was adsorbed atop the Ce and atop the metal dopants on

the (111) and $\langle 110 \rangle$ -type steps CeO₂ surfaces. The calculated adsorption energies for CO on CeO₂ (111) and $\langle 110 \rangle$ -type step surfaces are shown in Table 4.9.

Table 4.9 CO adsorption energies, stretching frequencies, and distance of carbon to adsorption site for stoichiometric and reduced CeO₂ (111), and $\langle 110 \rangle$ -type steps surfaces. PW91+U calculated stretching frequency for gas phase CO is 2123 cm⁻¹ with d(C-O) of 1.142 Å.

System and adsorption sites	E _{ads} / eV	$\nu(\text{CO})$ / cm ⁻¹	d(C...Ce) / Å	d(C-O) / Å
<u>Stoichiometric CeO₂ (111) surface</u>				
on Ce ⁴⁺	-0.21	2128	2.897	1.141
<u>Reduced CeO₂ (111) surface</u>				
on Ce ³⁺	-0.24	2140	2.951	1.140
on Ce _{7c} ⁴⁺	-0.24	2126	2.841	1.142
on Ce _{6c} ⁴⁺	-0.30	2133	2.887	1.140
<u>$\langle 110 \rangle$-type steps CeO₂ surface</u>				
on Ce _{6c} ⁴⁺ CeO ₂ -D	-0.26	2153	2.943	1.139
on Ce _{6c} ⁴⁺ CeO ₂ -U	-0.20	2130	2.822	1.141

The interaction between CO and the Ce atom on the (111) surface of ceria is known to be weak.^{270, 271} The PW91+U calculated CO adsorption on a clean stoichiometric CeO₂ (111) surface yielded an adsorption energy of -0.21 eV. For the O-defective surface, we find CO adsorption on an O-defective surface gives E_{ads} of -0.24 eV, -0.30 eV, and -0.24 eV for Ce³⁺, 6-coordinated Ce⁴⁺ (Ce_{6c}⁴⁺), and 7-coordinated Ce_{7c}⁴⁺ (Ce_{7c}⁴⁺) sites, respectively (refer to Figure 4.14 for structures). The calculated adsorption energy on clean stoichiometric surface is in agreement with the experimental data reported.^{272, 273} Zaki and Knözinger have studied CO adsorption at 80 K on a pre-oxidised CeO₂ catalyst by transmission infrared (IR) spectroscopy.²⁷² They have found the adsorption energy to be around -0.24 eV. Yang *et al.* have studied the CO stretch vibration frequency using IR spectroscopy with the aid of DFT calculations on stoichiometric and oxygen defective CeO₂ (111) surfaces at temperature below 100 K.²⁷³ They have reported the estimated activation energies for CO desorption from the stoichiometric and defective surface to be 0.27 eV and 0.31 eV, respectively. On the other hand, Breyse *et al.* did a calorimetric study to measure the heat of adsorption at about 574 K.²⁷⁴ The reported adsorption energy is about -1.08 eV which is about 0.78 eV to 0.82 eV lower than our calculated values. This is due to the catalyst was reduced prior to adsorption of CO so there will be

much more oxygen taken out of the catalyst than in our defect calculations. Besides, there are different facets exposed on the catalyst used.

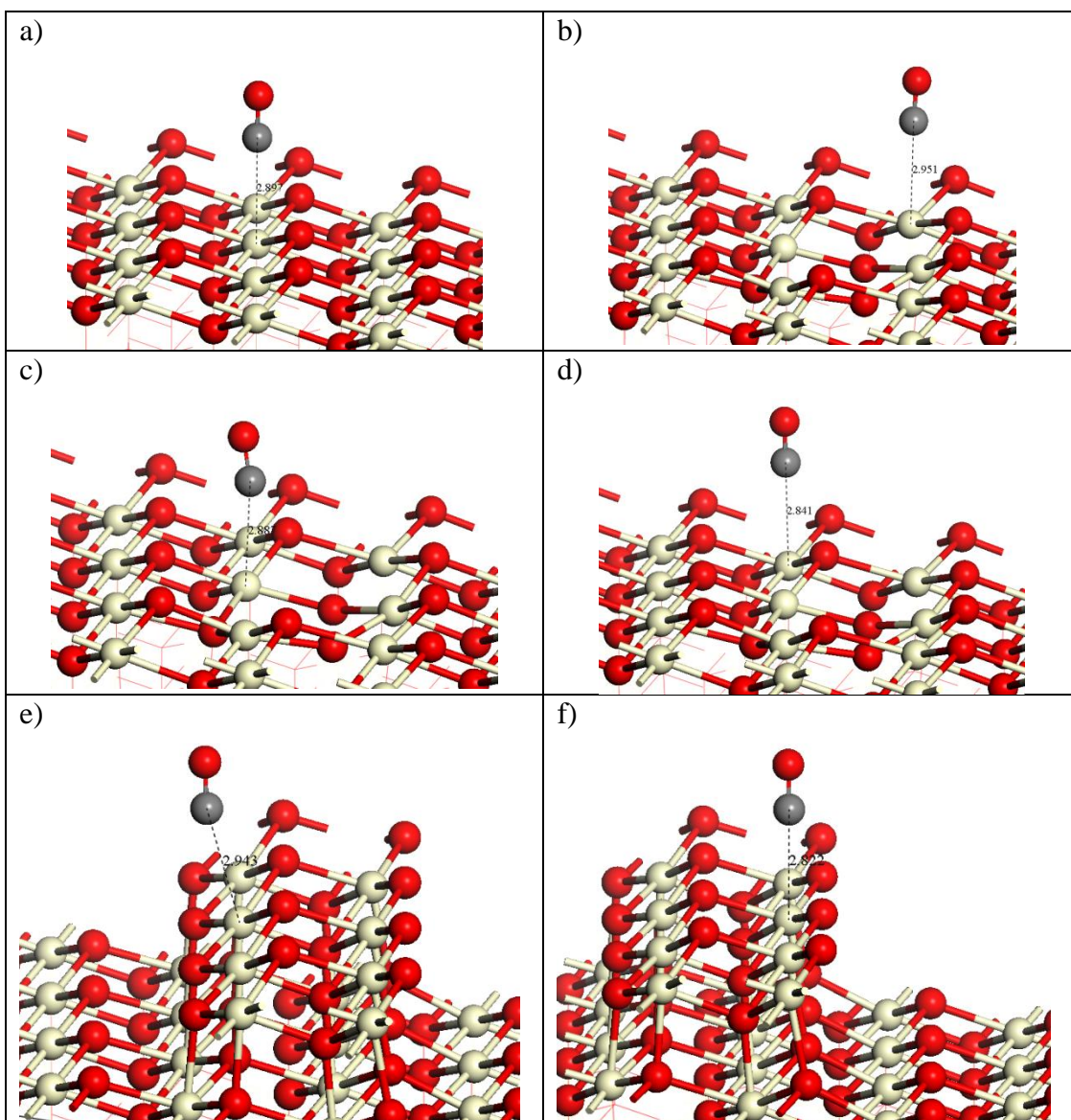


Figure 4.14 Optimised structures of CO adsorbed on (111) and $\langle 110 \rangle$ -type steps CeO₂ surfaces using PW91+U ($U_{\text{eff-Ce}}=5.0$ eV). a) CO adsorbed on Ce⁴⁺ on stoichiometric surface. CO adsorbed on b) Ce³⁺, c) Ce_{6c}⁴⁺, and d) Ce_{7c}⁴⁺ on O-defective surface. CO adsorbed on Ce⁴⁺ on e) CeO₂-D and f) CeO₂-U stoichiometric surfaces. Cerium (cream), oxygen (red), and carbon (grey).

In this work, we have calculated the stretch frequency of CO adsorbed on the stoichiometric surface to be 2128 cm⁻¹. For CO bound to the defective surface, blue shifts are observed with respect to CO bound on the stoichiometric surface except for CO bound to Ce_{7c}⁴⁺ which gave a $\nu(\text{CO})$ value of 2126 cm⁻¹. The CO bound to Ce³⁺ yielded a $\nu(\text{CO})$ of 2140 cm⁻¹ while a slightly lower frequency of 2133 cm⁻¹ is observed for at Ce_{6c}⁴⁺ site. Similar trend is observed by Yang *et al.* in the IR spectroscopy study where they have shown that $\nu(\text{CO})$ for CO bound on the reduced

surface sites exhibits blue shifts when compared to CO bound on the stoichiometric surface.²⁷³

Table 4.10 Bader charges for Pt, Ce, C, and O atoms involve in CO adsorption on various CeO₂ (111) surfaces. SPP=square planar position, 3C=3-coordinated site. Values in brackets are corresponding atomic Bader charges prior to CO adsorption.

System	Bader charges / <i>e</i>			
	Pd/Pt	Ce	C	O
Gas phase CO	-	-	1.08	-1.08
<u>Stoichiometric CeO₂ (111) surface</u>				
on Ce ⁴⁺	-	2.38(2.37)	1.12	-1.13
<u>Reduced CeO₂ (111) surface</u>				
on Ce ³⁺	-	2.14(2.14)	1.11	-1.13
on Ce _{7c} ⁴⁺	-	2.36(2.37)	1.11	-1.14
on Ce _{6c} ⁴⁺	-	2.28(2.32)	1.09	-1.13
<u><110>-type steps CeO₂ surface</u>				
on Ce _{6c} ⁴⁺ CeO ₂ -D	-	2.33(2.33)	1.11	-1.11
on Ce _{6c} ⁴⁺ CeO ₂ -U	-	2.34(2.30)	1.12	-1.13
<u>Pd-doped CeO₂ (111) surface</u>				
on Ce _{7c} ⁴⁺ (Pd@SPP)	0.77(0.77)	2.38(2.38)	1.12	-1.13
on Pd (Pd@SPP)	0.77(0.77)	-	1.09	-1.10
on Ce _{7c} ⁴⁺ (Pd@3C)	0.77(0.77)	2.37(2.36)	1.11	-1.13
on Pd (Pd@3C)	0.81(0.77)	-	1.08	-1.11
<u>Pt-doped CeO₂ (111) surface</u>				
on Ce _{7c} ⁴⁺ (Pt@SPP)	0.78(0.78)	2.39(2.38)	1.12	-1.13
on Pt (Pt@SPP)	0.78(0.78)	-	1.09	-1.10
on Ce _{7c} ⁴⁺ (Pt@3C)	0.74(0.73)	2.36(2.35)	1.11	-1.13
on Pt (Pt@3C)	0.85(0.73)	-	1.03	-1.12
<u>Pd-doped <110>-type steps</u>				
on Pd (Pd/CeO ₂ -U@3C)	0.79(0.76)	-	1.10	-1.11
<u>Pt-doped <110>-type steps</u>				
on Pt (Pt/CeO ₂ -D@SPP)	0.76(0.75)	-	1.15	-1.21
on Pt (Pt/CeO ₂ -U@3C)	0.83(0.74)	-	1.05	-1.11
on Ce _{5c} ⁴⁺ (Pt/CeO ₂ -D@3C)	0.94(0.98)	2.06(2.27)	1.11	-1.11
on Pt (Pt/CeO ₂ -D@3C)	0.87(0.98)	-	1.06	-1.11
on Pt (Pt/CeO ₂ -U@SPP)	0.76(0.76)	-	1.12	-1.15

Calculations were also done for CO adsorption on stoichiometric <110>-type steps of CeO₂(111) surfaces. The E_{ads} on the CeO₂-D and CeO₂-U surface is shown in Table 4.9. CO adsorbed on CeO₂-D surface yield and E_{ads} of -0.26 eV while on CeO₂-U surface, an E_{ads} of -0.20 eV is obtained. The stretching frequency for CO on CeO₂-D is 2153 cm⁻¹ which is higher than the frequencies calculated for the

stoichiometric and reduced CeO₂ (111) surfaces. On the other hand, lower $\nu(\text{CO})$ (2130 cm⁻¹) is observed for CO adsorbed on CeO₂-U.

Bader analysis on CO adsorption on the stoichiometric and reduced CeO₂ (111) surface shows that C and O become slightly more positive and negative, respectively. The difference in the Bader charges for Ce species before and after adsorption is insignificant. The C-O bonds for both the systems were not elongated so showing no signs of activation of CO. Similar observations are seen for the clean stoichiometric <110>-type steps CeO₂ surfaces. These confirm that CO physisorbs on these model surfaces.

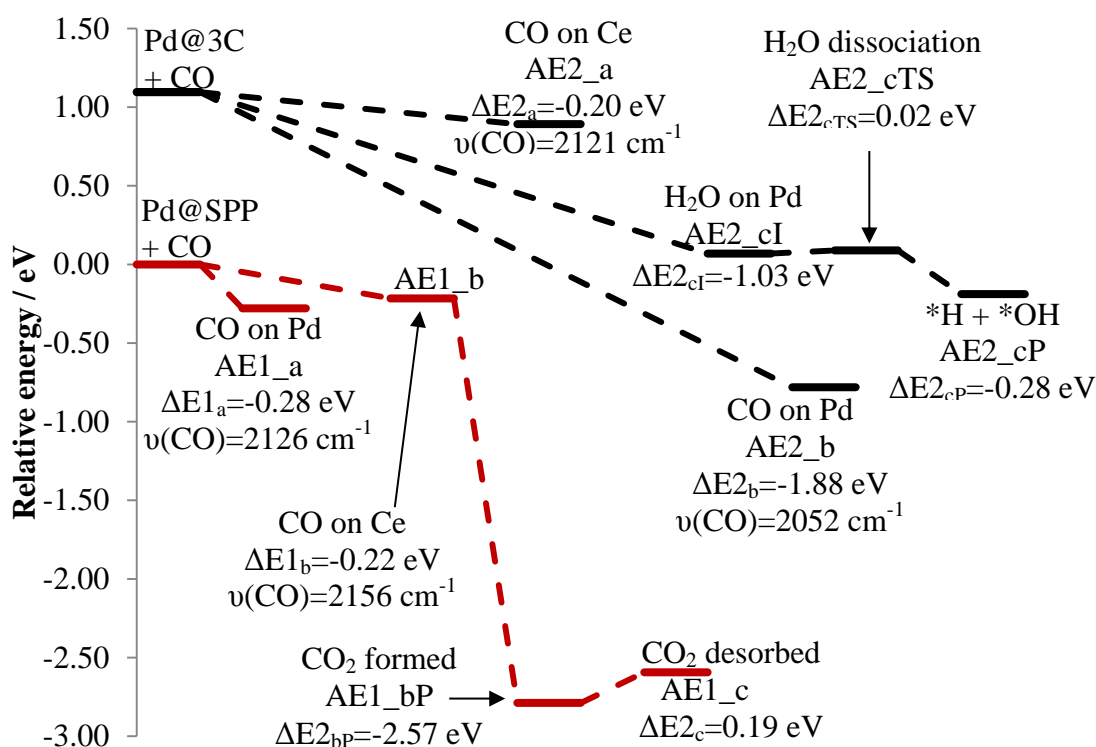


Figure 4.15 Energy diagram of CO and H₂O adsorption, H₂O dissociation, and CO₂ formation on Pd-doped CeO₂ (111) surface. Energies are set in relative to Pd/CeO₂ at SPP with CO. Refer Figure 4.16 and Figure 4.17 for images of optimised structures.

For both the SPP and 3C positions of Pd in the Pd-doped CeO₂ (111) surfaces (Figure 4.15), CO adsorbed on Ce site is iso-energetic as the CO adsorption on the clean stoichiometric surface. CO₂ formation is performed on Pd/CeO₂@SPP by using an oxygen atom from the surface lattice. The most favourable oxygen vacancy site (V_{SP_s}) was considered as the oxygen source. The system with the CO₂ formed is 2.57 eV lower than the overall energy of the system with CO adsorbed on the surface. Desorption of CO₂ from the surface requires 0.19 eV.

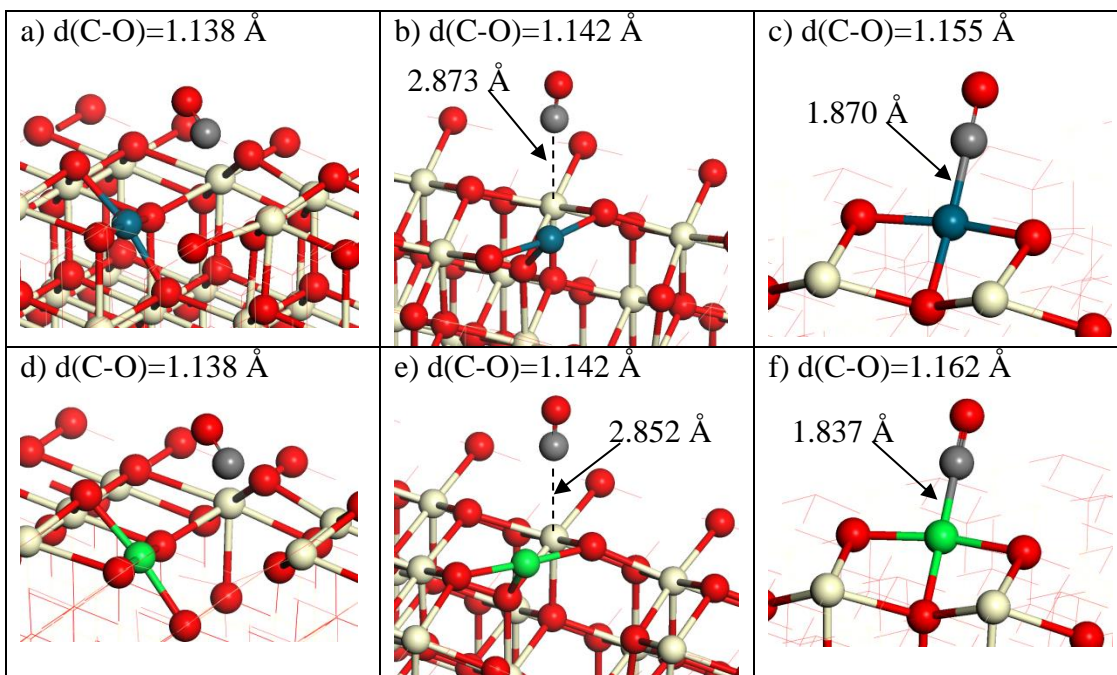


Figure 4.16 Optimised structures for CO adsorbed on doped CeO₂ (111) surface; on a) Pd in Pd@SPP (AE1_a), b) Ce_{7c}⁴⁺ in Pd@3C (AE2_a), c) Pd in Pd@3C (AE2_b), d) Pt in Pt@SPP (BE1_a), d) Ce_{7c}⁴⁺ in Pt@3C (BE2_a), and e) Pt in Pt@3C (BE2_b). CO bond lengths are shown for each structure. Cerium (cream), oxygen (red), carbon (grey), palladium (blue), and platinum (green). PW91+U calculated gas phase d(C-O)=1.142 Å.

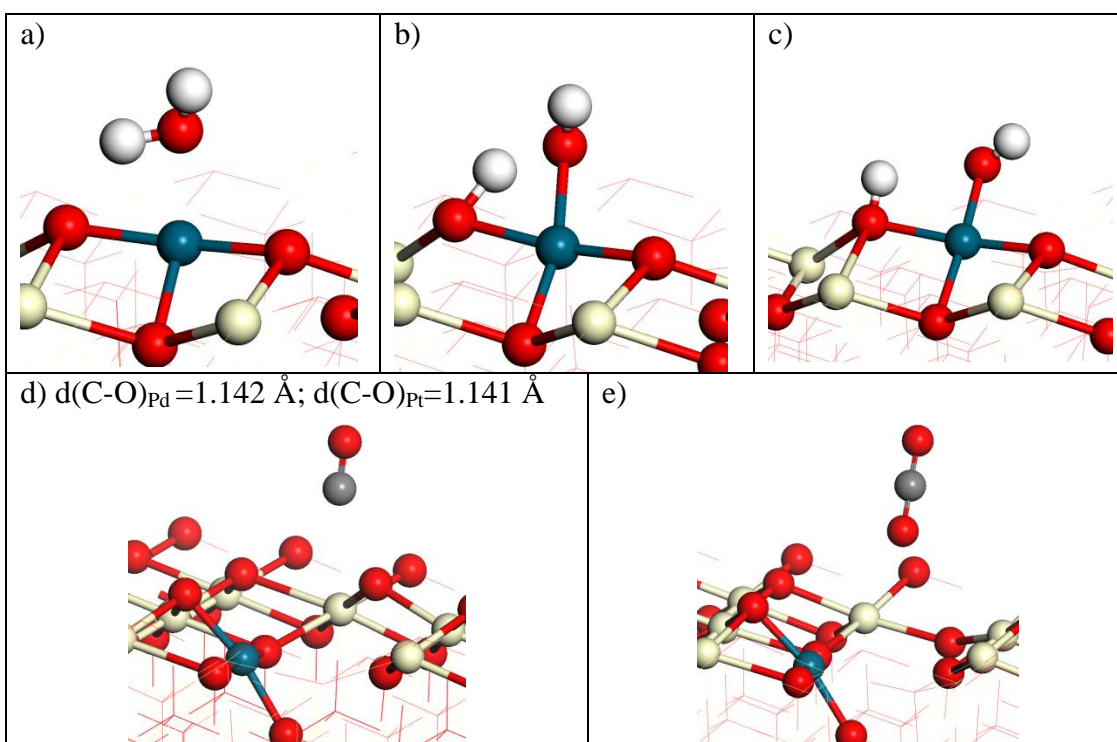


Figure 4.17 Optimised structures for H₂O dissociation and CO oxidation. a) H₂O adsorbed on Pd/Pt@3C site (A/BE2_cI), b) transition state for H₂O dissociation (A/BE2_cTS), and c) dissociated H₂O (A/BE2_cP). d) CO adsorbed on Pd/Pt@SPP site (A/BE1_b) and e) formation of CO₂. Cerium (cream), oxygen (red), hydrogen (white), carbon (grey), palladium/platinum (blue).

CO adsorbed at Pd on the Pd/CeO₂@SPP surface relaxed to a position where carbon is directed towards one of the cerium atoms opposite the Pd (Figure 4.16a). This process yields adsorption energy of -0.28 eV. As for the Pd/CeO₂@3C surface, CO adsorbed strongly on the Pd site ($E_{\text{ads}}=-1.88$ eV). This is due to CO, which can take up the vacant coordination site in the plane at the three coordinated Pd ion. In actual experimental conditions, the catalyst will have water adsorbed from the environment. Thus, we have adsorbed one water molecule at the Pd site which gave adsorption energy of -1.03 eV. Comparing both the adsorption of CO and water, we can observe that CO adsorption is stronger than water ($\Delta E_{\text{ads}}=-0.85$ eV) which enables it to displace water from the Pd site. However, it is also found that the dissociation of water to H⁺ and OH⁻ can be spontaneous giving a surface oxygen protonated and a hydroxyl group taking up the vacant coordination site at three coordinated Pd ion. Using the NEB method, the calculated activation energy for the dissociation of water is 0.02 eV.

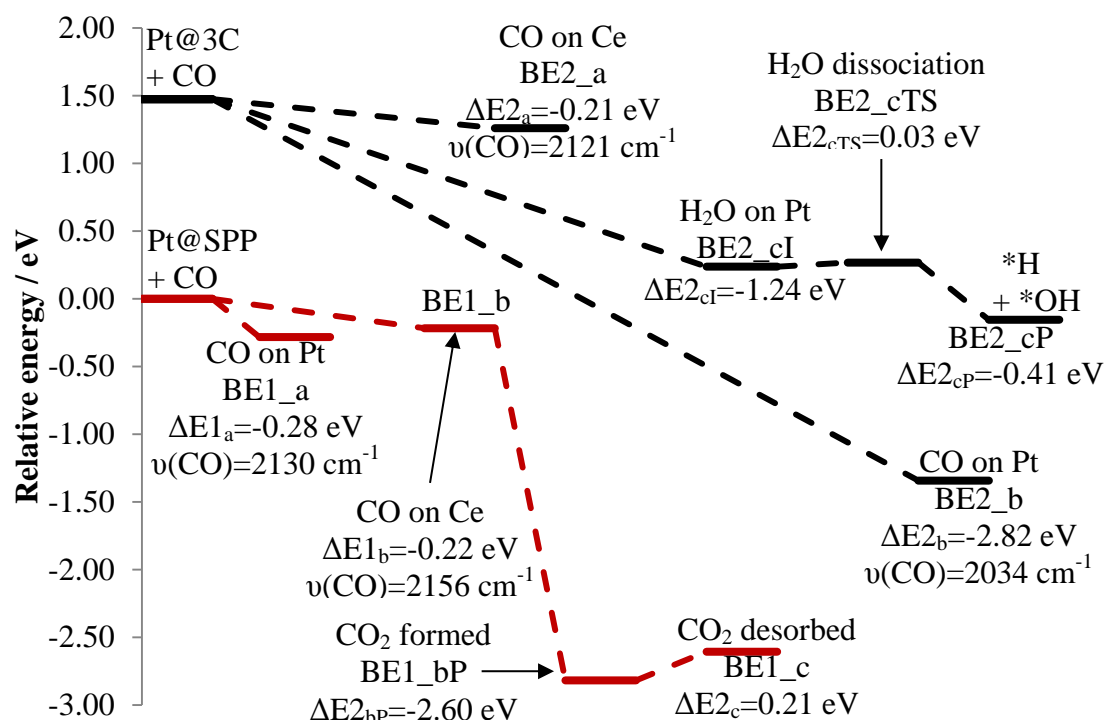


Figure 4.18 Energy diagram of CO and H₂O adsorption, H₂O dissociation, and CO₂ formation on Pt-doped CeO₂ (111) surface. Energies are set in relative to Pt/CeO₂ at SPP with CO. Refer Figure 4.16 and Figure 4.17 for images of optimised structures.

The CO adsorption and oxidation energies on Pt-doped CeO₂(111) surfaces are similar to the energies obtained for the Pd-doped system. In Figure 4.18, it is shown that the CO adsorbed on Ce site for both the Pt-doped CeO₂ (111) surfaces are also iso-energetic as the CO adsorption on the clean stoichiometric surface. The

formation of CO₂ using the oxygen from the V_{SP,S} vacancy site has an overall system energy of 2.60 eV lower than the overall system energy with CO adsorbed on the surface. It requires 0.21 eV for the CO₂ to desorb from the surface.

Similar to Pd/CeO₂@SPP, the adsorbed CO has relaxed with the O-C pointing towards one of the cerium atoms opposite Pt (Figure 4.16d). CO adsorbed at Pt on the Pt/CeO₂@SPP surface with E_{ads} of -0.28 eV. Stronger adsorption is observed when CO adsorbed on Pt on the Pt/CeO₂@3C surface (-2.82 eV) compared to square planar Pt position (-0.28 eV) and Pd/CeO₂@3C surface (-1.88 eV). Similar to Pd-doped system, one water molecule has been adsorbed at this Pt site. A lower adsorption energy is obtained (-1.24 eV) on Pt which is 0.21 eV lower than the adsorption of water on Pd site at the same position. The dissociation of water yields a lower overall system energy with activation energy of 0.03 eV. This also suggests that the dissociation of water to adsorbed H⁺ and OH⁻ species can be spontaneous as has been observed on the Pd/CeO₂@3C system.

Through Bader analysis, it is observed that CO bonded to PGM dopants has overall become more δ⁻. When CO is bonded to PGM dopants, both Pd and Pt cations have lost electrons which resulted in the increase in Bader charges. An elongation in C-O bond lengths for both systems is also observed (Refer to Figure 4.16). These are due to the back donation that occurs from metal highest occupied molecular orbital (HOMO), the filled *d_π* orbital, to the CO lowest unoccupied molecular orbital (LUMO). The electron density at both C and O are increased which in turn elongates the CO bond length. There are no significant changes observed in Bader charges for Ce, C, and O species in CO adsorbed at Ce_{7c}⁴⁺ on Pd- and Pt-doped CeO₂(111) surfaces.

Figure 4.19 shows the optimised structures for CO adsorbed on various sites on <110>-type steps CeO₂ surfaces. Strong interaction is observed when CO is adsorbed at three coordinated (3C) Pd/Pt sites (Figure 4.19a, c, e). However, the Pt-doped systems gave stronger CO adsorption energy; -2.79 eV and -2.76 eV for CO adsorbed on Pt at CeO₂-U@3C and CeO₂-D@3C, respectively. Bader analysis also shows that C becomes less positive and O become more negative upon adsorption on these three sites. This is also accompanied by the elongation of C-O bond length (Figure 4.19a, c, e).

Only weak adsorption of CO is observed on Pt (Pt/CeO₂-D@SPP) and Pt (Pt/CeO₂-U@SPP) systems. The CO adsorbed on Ce (Pt/CeO₂-D@3C) gave an adsorption energy (-0.29 eV) which is 0.03 eV lower than CO adsorbed at Ce site on clean stoichiometric CeO₂-D surface.

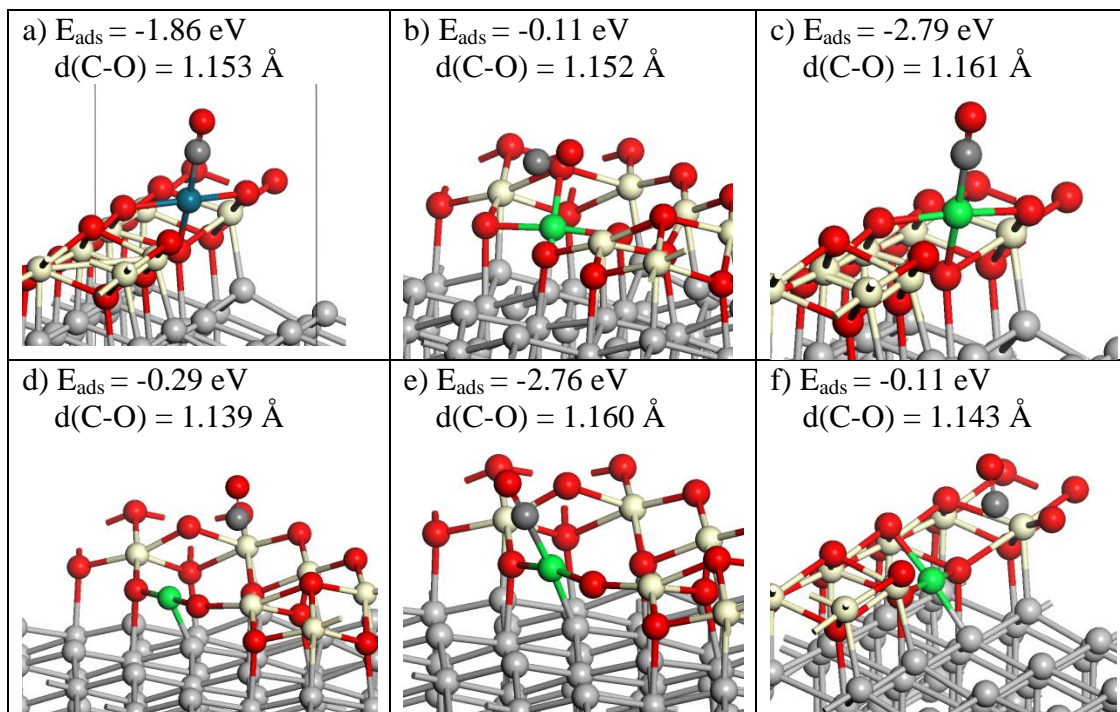


Figure 4.19 Optimised structures of CO adsorbed on a) Pd (Pd/CeO₂-U@3C), b) Pt (Pt/CeO₂-D@SPP), c) Pt (Pt/CeO₂-U@3C), d) Ce_{5c}⁴⁺ (Pt/CeO₂-D@3C), e) Pt (Pt/CeO₂-D@3C), and f) Pt (Pt/CeO₂-U@SPP). Cerium (cream), oxygen (red), carbon (grey), palladium (blue), and platinum (green). Second layer onwards, atoms are coloured silver. PW91+U calculated gas phase $d(\text{C-O})=1.142 \text{ \AA}$.

Overall, it is observed that CO₂ and a surface with an oxygen vacancy is overall energetically more stable system compared to CO adsorbed on Ce site in Pd- and Pt-doped CeO₂ (111) surface. The adsorption of CO is found to be weak on the stoichiometric and reduced CeO₂ (111), and stoichiometric <110>-type steps CeO₂ surfaces. Thus, at temperatures higher than room temperature, it is suggested that the Mars-van Krevelen mechanism for CO oxidation will follow the Eley-Rideal mechanism where the gas phase CO will react with the surface oxygen without pre-adsorption. However, by doping the CeO₂ (111) surfaces, the CO oxidation may proceed following the Langmuir-Hinshelwood mechanism as CO will adsorb strongly on the three coordinate Pd/Pt cation. Water is also found to be easily dissociated upon adsorption at the three coordinated Pd/Pt site. Following this, H and OH species are formed on the surface. This may suggest a water-gas shift reaction where it can follow an associative mechanism or a redox mechanism. CO can react

with the adsorbed hydroxide to form a carboxyl or formate intermediate which then decomposes into CO₂ and the adsorbed H species. The final result will produce CO₂ and H₂.

4.7 Conclusion

From the calculations performed in this work, the ease of abstracting an oxygen atom from the surface lattice increases in the order (111) < ⟨110⟩-type steps CeO₂-U < (110). The lowest energy required to form an oxygen vacancy on the (111), CeO₂-U, and (110) surfaces are 1.56 eV (surface vacancy on (111)), 1.42 eV (sub-surface vacancy on (111)), 0.95 eV, and 0.77 eV, respectively. It is also shown that the different location of Ce³⁺ pairs created affects the vacancy formation energy across the surfaces. The difference in energy on the same system can go up to 1.02 eV. Migani *et al.*²⁷⁵ suggested that oxygen vacancy formation energy can be decomposed into three components:

- 1) the energy to transfer two electrons from the O anion to be depleted to two Ce cations, ($O^{2-} + 2Ce^{4+} \rightarrow O + 2Ce^{3+}$), resulting in atomic O;
- 2) the removal of O atom from the lattice;
- 3) the relaxation process.

The energy needed to transfer two electrons from the O anion to two Ce cations and for relaxation of the lattice atoms do contribute to the vacancy formation energy. Li *et al.*^{81, 182} have also shown that the structural relaxation of the reduced surface made the sub-surface O vacancy have a similar stability to the top surface O vacancy. Besides, structural relaxation is also reported to determine the distribution of localised electrons.^{81, 276} We have shown that the atoms around the Ce³⁺ cation is significantly relaxed to accommodate the increased cation size (1.11 Å to 1.283 Å).^{52, 53, 221} Besides, the oxygen vacancy created caused the neighbouring oxygen to relax towards the site. There are many possibilities for the distribution of the two excess electrons upon the removal of an oxygen atom. As discussed in previous chapter (Chapter 3.4, refer to Figure 3.5), the distribution of electron locations is likely to depend on the system temperature. The increase in temperature will increase the population of defect structures that has higher E_{vac} of different Ce³⁺ sites.

The square planar position for the dopant metals in bulk has been retained. Using this structural configuration, the Pd- and Pt-doped CeO₂ (111) and CeO₂-U surfaces are modelled. There are two possible positions where the metal dopant stays in the similar structural configuration in the CeO₂ (111) surface, which are at the sub-surface layer coordinated to four neighbouring oxygen atoms giving a proper square planar coordination (Figure 4.10a, c) and at top surface coordinated to three oxygen atoms (Figure 4.10b, d). The later gave a higher E_{sub} for both metal dopants used which are 2.75 eV and 2.81 eV for Pd and Pt, respectively. Substitution of Pd and Pt at the square planar position required 1.65 eV and 1.34 eV, respectively.

Investigation of various oxygen vacancy sites were performed on the Pd- and Pt-doped surfaces. It is shown that the abstraction of an oxygen atom from the surface lattice from the doped surfaces is easier than the stoichiometric clean surface. The formation of an oxygen vacancy on the Pd- and Pt-doped surfaces at square planar position yield E_{vac} of 0.68 eV and 0.66 eV, respectively. While on the three coordinated Pd- and Pt-doped surfaces, the oxygen vacancy formed next to the metal dopant itself is exothermic. This is due to the structural relaxation that occurs to reposition the metal dopant to a square planar position upon the removal of the oxygen bonded to the metal.

In general, the substitution of Pd and Pt on CeO₂-D and CeO₂-U surfaces require lower energy than the same process on CeO₂ (111) surface. The lowest substitution energy is obtained on CeO₂-U surface when the metal dopant is at the square planar position (Figure 4.13c, g). The substitution energies are 1.09 eV and 0.80 eV for Pd- and Pt-doped CeO₂-U surface, respectively.

DFT+U calculation on CO adsorption were performed for the different surfaces studied. Weak adsorption is observed on the surfaces as reported in literature.^{270, 271} CO adsorptions at Ce sites on stoichiometric surfaces are fairly iso-energetic with the maximum difference of about 0.08 eV in the values of E_{ads} obtained for the clean stoichiometric CeO₂ (111) surface. These observations suggest that CO oxidation via reaction with the lattice oxygen will occur following the Eley-Rideal mechanism rather than the Langmuir-Hinshelwood mechanism.

However, CO oxidation following the Langmuir-Hinshelwood is still possible because strong adsorption is observed at the PGM site for Pd/CeO₂@3C and Pt/eO₂@3C surfaces (Figure 4.15 and Figure 4.18, respectively) which yield E_{ads} of -

1.88 eV and -2.82 eV, respectively. The adsorption of a water molecule at the PGM site on the Pd/CeO₂@3C and Pt/CeO₂@3C surfaces are less exothermic compared to adsorption of CO. However, through NEB method, activation barriers of 0.02 eV and 0.03 eV are obtained for the dissociation of water on Pd/CeO₂@3C and Pt/CeO₂@3C, respectively. Even when water has dissociated, it is still not as good as putting the CO on the three coordinated metal ion, so CO can still displace water under the right conditions. Nevertheless, we should not rule out the possibility a water-gas shift reaction which follows the dissociation of water to give adsorbed H and OH species.

Chapter 5

Gold nanoparticles supported on α -Fe₂O₃(0001) surface

This chapter consists of theoretical investigations on gold nanoparticles supported on an α -Fe₂O₃(0001) surface which involves the reduction of the surface, CO adsorption and oxidation mechanisms at the periphery of the gold nanoparticle. The chapter begins with a brief introduction followed by computational details and then some results obtained that will be discussed in three different sections: effects of Au₁₀ on oxygen vacancy formation on α -Fe₂O₃(0001) surface, CO adsorption and oxidation on Au₁₀O₆/Fe₂O₃, respectively.

5.1 Introduction

Supported Au catalysts have been applied in indoor air quality control, pollutant abatement, H₂ energy carrier, and chemical processes such as CO oxidation, propylene epoxidation, water gas shift reactions, and hydrogenation of unsaturated hydrocarbons.²⁷⁷ My work involves the modelling and theoretical study of such catalysts, of which the support presented in this work is hematite, α -Fe₂O₃(0001) surface. There has been much interest for supported Au nanoparticles in oxidation catalysis ever since Haruta *et al.* reported about room temperature CO oxidation using such catalyst.¹⁴⁷ Hutchings, Kiely, and co-workers¹⁴⁵ came to a conclusion, using the aberration-correction transition electron microscopy (TEM) data obtained, that active catalysts contain bi-layer particles of about 10 Au atoms which are not present in the inactive material. The model is built based on the findings by Hutchings, Kiely, and co-workers.¹⁴⁵ There is also much debate as to whether Au⁰ or Au ^{δ +} species is responsible for the catalytic activity.¹³⁸

Experimental work reported by Schubert *et al.* showed that CO oxidation rates are enhanced by using gold catalysts supported on “active” support materials (Fe₂O₃, TiO₂, NiO_x, CoO_x).¹³⁷ The oxide support can provide reactive oxygen for the CO oxidation reaction. Thus, the dependence of the turnover frequency on the size of the gold particle is reduced. They suggested that the dissociation of molecularly adsorbed oxygen to occur at the metal-support interface. There is also possibility of subsequent spillover process of atomic oxygen on the gold particles before the

adsorbed CO reacts with the oxygen at gold and/or at the interface. Through isotope studies, they have ruled out a direct reaction of adsorbed CO with molecular oxygen species involving a carbonate-like intermediate or transition state. However, the reaction scheme including molecular oxygen should not be generally excluded

Boronat and Corma²⁷⁸ have investigated the influence of particle size, particle shape, and support interaction on oxygen activation on gold nanoparticles by means of density functional theory (DFT) calculations. Adsorption energies and the degree of molecular activation were reported to depend on particle size. They have also found that the O₂ adsorbed on gold stably in two conformations: i) top-bridge-top conformation with each oxygen atom in O₂ directly bonded to a gold atom, and ii) bridge-bridge conformation in which each oxygen atom forms a bridge with two different gold atoms.²⁷⁸ The bridge-bridge conformation is found to have the highest degree of molecular activation and the lowest activation barrier for O₂ dissociation. The O₂ adsorbed on a bridge-bridge conformation on isolated Au₁₃ and Au₃₈ nanoparticles yield exothermic adsorption energies (-0.98 eV for both systems). O₂ dissociates more easily on Au₁₃ with the activation energy barrier of 0.18 eV rather than .36 eV on the Au₃₈ nanoparticle. When the gold nanoparticles are supported on TiO₂, O₂ adsorbed and dissociated better at the metal-support interface than on the gold particle.

Howard and Willock¹⁵⁹ have shown the dissociation of molecular O₂ at the interfacial sites between Au and the Fe₂O₃ support is more favourable than desorption of its molecular species. Recently, Carley *et al.* have reported that in their XPS experiments at 25 °C, CO cleavage only occurs when O₂ is co-adsorbed.²⁷⁹ In the same work, they also performed DFT calculations with the inclusion of Hubbard *U* parameter (DFT+*U*) on the model system and found that under the conditions where O₂ has dissociated to form a stable O-Au-O structure at the periphery of the cluster, the co-adsorbed CO can dissociate along with the oxidation of Au atoms exposed at the cluster edge.²⁷⁹

The theoretical work reported by Bruix *et al.*²⁵⁵ provide insight regarding deposited metal particles on the reducibility of oxide surface. They have studied the effects of Pt₈ cluster on the reducibility of CeO₂(111) surface by means of DFT+*U* calculations. Spontaneous oxidation of the Pt₈ cluster together with the reduction of up to two Ce⁴⁺ cations to Ce³⁺ are observed upon its deposition over the ceria

surface. However, only three Ce³⁺ cations were formed rather than four when an oxygen vacancy is created on the surface with the presence of the Pt particle. Besides, their calculations suggest that the presence of Pt₈ particle has only affected the O vacancy formation energy by a little. They also suggest that the formation of oxygen vacancies can be substantially facilitated by the so-called reverse spillover of atomic oxygen from the CeO₂(111) support to the metal particle. This process requires only 1.00 eV which is significantly smaller than the energy to form an oxygen vacancy on the clean CeO₂(111) surface (2.25 eV).

In this work, we consider the supply of oxygen from the support lattice as a possible source in the mechanism for CO oxidation. We present here the DFT+U calculated oxygen vacancy formation energies at various positions on the surface. The presence of Au₁₀ nanoparticle have shown to facilitate oxygen vacancy formation. This is more evident when the periphery of the Au₁₀ nanoparticle interface with the oxide support is oxidised with oxygen molecules, resulting in the oxygen vacancy formation energy on the surface to be less endothermic. Subsequently, CO oxidation at various sites on the partially oxidised Au₁₀/Fe₂O₃ system is also investigated. We also show that the ease of releasing oxygen by the metal oxide support acts as an oxygen buffer for catalytic reactions.

5.2 Computational details

Calculations were performed using the ab-initio plane wave basis set code, VASP.¹⁰⁻¹³ The projector augmented wave method was used in representing the core states.^{215, 216} The iron atom's $3d$, $4s$, oxygen's $2s$, $2p$, and gold atom's $5d$, $6s$ electrons were treated explicitly as valence electrons with a plane wave cut-off of 500 eV. We have used generalized gradient approximation method applying the Perdew-Burke-Ernzerhof (PBE) functional in this work.^{199, 200} An on-site Coulomb interaction correction following Dudarev's approach ($U_{eff}=U - J$)²⁰¹ was applied to properly describe the strongly correlated d -states of iron. Similar to our previous work¹⁵⁹, I have applied a U_{eff} of 4.0 eV. This has shown to give reasonable results regarding lattice parameters, bulk moduli, density of states, band gap, and magnetic moment for the Fe₂O₃ system.^{158, 159} The Au₁₀/ α -Fe₂O₃ system was modelled by placing the Au₁₀ nanoparticle on top of a 4 layered slab (Fe–O₃–Fe) built of the $p(3\times 3)$ supercell of the (0001) surface. The bottom 3 layers were fixed during optimization.

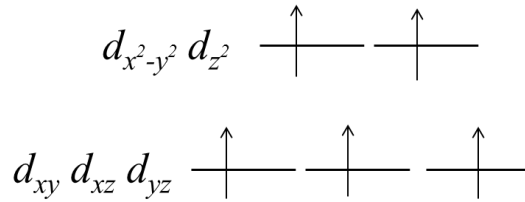


Figure 5.1 Fe³⁺ ions in high spin state.

The Fe³⁺ ions are d5 metal ions in a low field environment. These Fe³⁺ ions have a high spin state (Figure 5.1). The initial magnetic moment ordering were set to ± 5 in the sequence $+--++--+$ for each iron layer in order to ensure that we obtain an optimised structure with the desirable magnetic ordering. To accommodate the gold nanoparticle, the vacuum gap of the Fe₂O₃ slab is set to 25 Å. The system was sampled at Γ -point using the Monkhorst-Pack scheme. A dipole correction along the z -direction of the slab is applied in all calculations since we have the bottom 3 layers fixed.

I have investigated different positions of surface oxygen vacancy of the systems. For both the Au₁₀/ α -Fe₂O₃ and Au₁₀O₆/ α -Fe₂O₃, a surface oxygen next to the nanoparticle, second nearest, and furthest from the Au₁₀ nanoparticle has been removed and the whole system was optimised separately. The single oxygen vacancy formation energy was calculated as follows:

$$E_{\text{vac}} = E(\text{Au}_{10}/\text{Fe}_{72}\text{O}_{107}) - E(\text{Au}_{10}/\text{Fe}_{72}\text{O}_{108}) - \frac{1}{2} E(\text{O}_2) \quad (5.1)$$

where (Au₁₀/Fe₇₂O₁₀₇) is oxygen defect system, (Au₁₀/Fe₇₁O₁₀₈) is the stoichiometric system, and (O₂) is the gas phase oxygen in the triplet ground state. From Equation (5.1), a more positive value signifies the process to be more endothermic.

Adsorption energies are calculated following:

$$E_{\text{ads}} = E(\text{CO}_{\text{ads}}) - E(\text{CO}_{\text{gas}}) - E(\text{surface}) \quad (5.2)$$

where CO_{ads} and CO_{gas} are the adsorbed and gas phases CO species, respectively. Energy of the clean slab is denoted as E(surface). Gibbs free energies for the adsorption of a CO molecule at various sites studied in 1 and 100 atmospheric pressure have been calculated using

$$\Delta G = E_{\text{ads}} - \Delta\mu_{\text{CO}}(T, P^\circ) - kT \ln\left(\frac{P}{P^\circ}\right) \quad (5.3)$$

where E_{ads} is calculated following equation (5.2). The chemical potential ($\mu_{\text{CO}}(T, P^\circ)$) as a function of CO pressure and temperature are calculated from the vibrational, rotational, and translational partition functions of the gas molecule (equation (5.4)).

$$\mu = -kT \ln\left(\frac{q}{N}\right) ; q = q_{\text{vib}}q_{\text{rot}}q_{\text{tr}} \quad (5.4)$$

where N is the Avogadro's constant. The third term in equation (5.3) is the multiplication of Boltzmann constant (k), temperature in Kelvin (T), and natural logarithm of the ratio of pressure of CO to the absolute pressure of 1 atm. The vibrational (q_{vib}), rotational (q_{rot}), and translational (q_{tr}) partition function are calculated following:

$$q_{\text{vib}} = \frac{1}{1 - e^{-\frac{h\nu}{kT}}} \quad (5.5)$$

$$q_{\text{rot}} = \frac{1}{\sigma} \left(\frac{kT}{hcB} \right) \quad (5.6)$$

$$q_{\text{tr}} = \frac{V}{\Lambda^3} ; \Lambda = \left(\frac{h^2\beta}{2\pi m} \right)^{\frac{1}{2}} \quad (5.7)$$

where $h\nu$ is the vibrational energy for gas phase CO obtained using the PBE calculated vibrational frequency of gas phase CO of 2125 cm⁻¹. The rotational

constant (B) obtained from the NIST-JANAF thermochemical tables, is 1.9302 cm^{-1} .²⁸⁰ The vibrational partition function has been neglected in the adsorbed species in order to avoid large errors associated with neglecting entropy contributions of adsorbed species. This has been shown by Ammal and Heyden in their *ab-initio* thermodynamics study of the nature of Pt_n/TiO₂(110) interface under water gas shift (WGS) conditions that inclusion of vibrational entropy contributions does not alter free energy differences by more than 0.1 eV under relevant conditions.²⁸¹

For the density of states calculation, the systems were sampled with $3 \times 3 \times 1$ k-points following the Monkhorst-Pack scheme. A smearing of 0.20 eV was used on the final density of states plots. The Bader analysis code developed by Henkelman's research group^{12, 233-235} was used to estimate the Bader charges of each ion species in the systems studied. The Bader charges, q , are computed following:

$$q_i = q_i(\text{valance}) - q_i(\text{Bader}) \quad (5.8)$$

where $q_i(\text{valance})$ is the valence charge obtained from POTCAR used and $q_i(\text{Bader})$ is the Bader charge obtained from Bader code for the i -th atom, respectively.

Energy barriers for the CO oxidation process were obtained using the nudged elastic band (NEB) method. The process was modelled using a chain of 9 images that were interpolated linearly between two end points of the optimised adsorbed and oxidised structures. The interpolation was performed using an in-house code for pre- and post-processing of VASP calculations which has also been applied by Willock and co-workers for the deprotonation of H₂O₂.²³⁹ The transition state is determined with a frequency calculation and when only one imaginary mode is present.

5.3 Effects of Au₁₀ nanoparticle on oxygen vacancy formation on α -Fe₂O₃(0001) surface

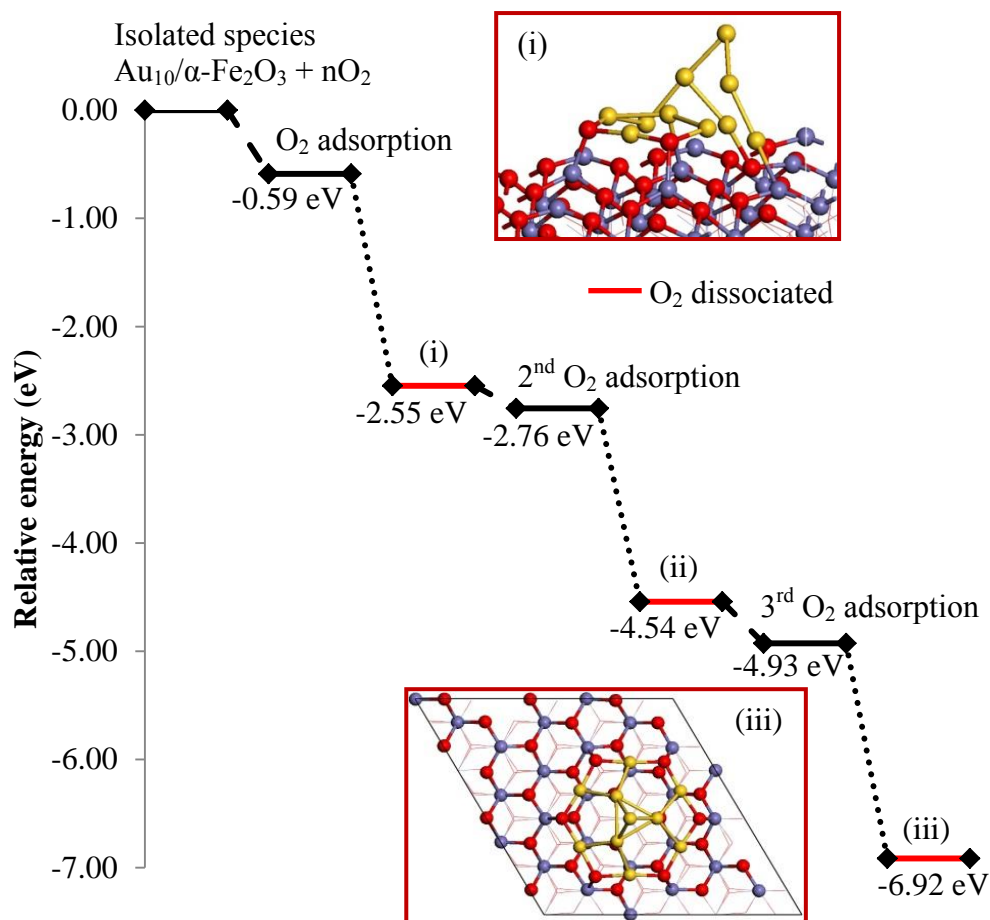


Figure 5.2 PBE+U calculation for the adsorption (dashed lines) and dissociation (dotted lines) of O₂ molecules on α -Fe₂O₃ supported Au₁₀ nanoparticle. Energies are with reference to Au₁₀/Fe₂O₃ + O₂. Oxygen (red), gold (yellow), and iron (blue violet)

From previous work reported by Howard and Willock,¹⁵⁹ the dissociation of a molecule of oxygen on a supported Au₁₀ nanoparticle is energetically more favourable compared to the desorption of the molecular species. Following on from their work, this work has examined the oxidation of Au atoms exposed at the periphery of the Au₁₀ nanoparticle with two extra pairs of O₂ molecules. Figure 5.2 shows the energy profile diagram for the addition and dissociation of O₂ molecules on the supported Au₁₀ nanoparticle. Figure 5.2 shows that subsequent addition and dissociation of O₂ to the base of Au₁₀ is energetically favourable. The adsorption energy for the first O₂ molecule is -0.59 eV. The dissociated O₂ species at the periphery of Au₁₀ nanoparticle is stabilised with stabilisation energy of -2.55 eV. Second and third O₂ molecules adsorbed with energies of 0.21 eV and -0.39 eV,

respectively. The final structure, Figure 5.2 (iii), with three pairs of dissociated O₂ at the exposed Au atoms at the interface between Au and Fe₂O₃ is stabilised by -6.92 eV with respect to the starting structure. The dissociated O₂ at the interface of Au and Fe₂O₃ forms a O–Au–O structure with Au–O bond length of 2.04 Å and O–Au–O angle of 174° (Figure 5.3b). The Au–Au distances between base Au atom and second layer Au atom, between second layer Au atoms, and between second layer Au atom and top layer Au atom are 2.69 Å, 2.73 Å, and 2.71 Å, respectively.

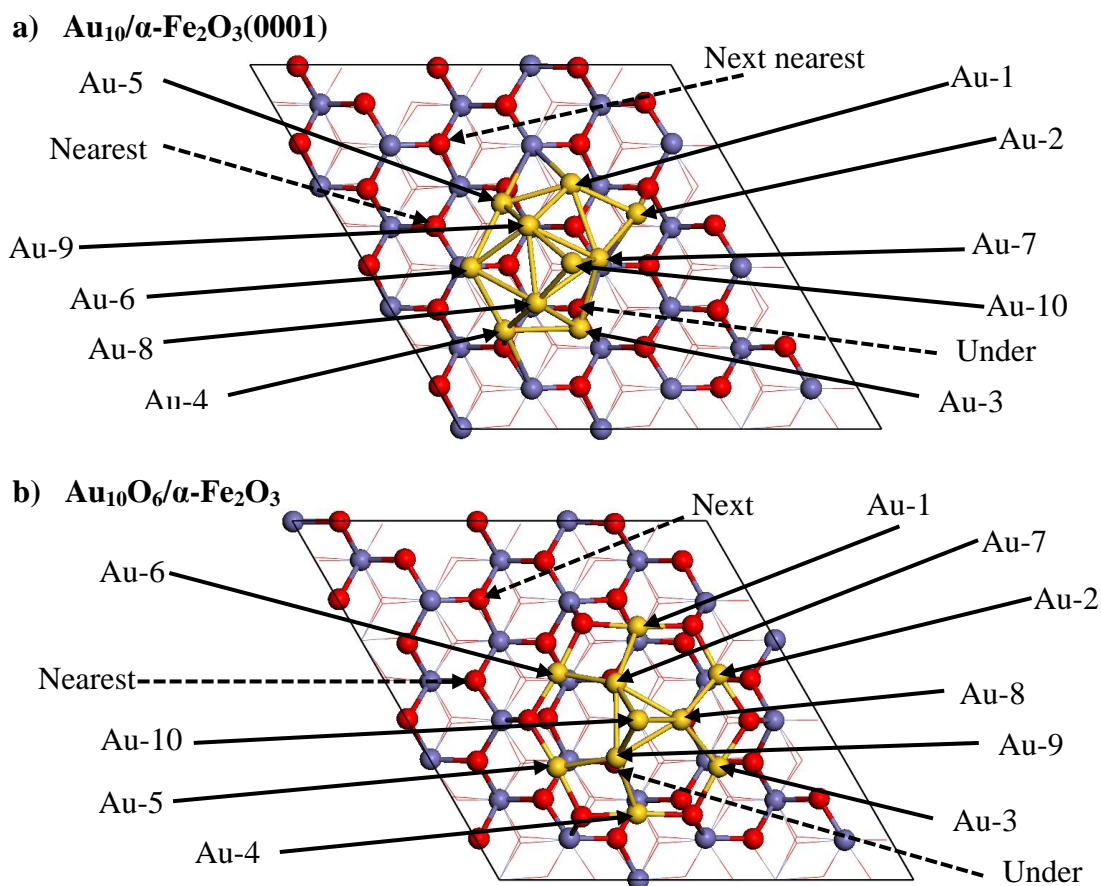


Figure 5.3 Optimised structures of a) Au₁₀/Fe₂O₃ and b) Au₁₀O₆/Fe₂O₃ with the labels of gold atoms and various oxygen vacancy sites studied. Oxygen (red), gold (yellow), and iron (blue violet).

In the Au₁₀O₆/Fe₂O₃ system, all the six gold atoms at the base of the nanoparticle that has direct contact with the support are the oxidised species with Bader charges ranging from 0.53 to 0.57 *e* (refer Table 5.4) which are more positive compared to the three gold atoms at the second layer (0.11 *e*, 0.12 *e*, and 0.07 *e*) and one at the tip (0.03 *e*) of the nanoparticle. The average effective charges obtained for the six O atoms at the O–Au–O structure are -0.57 *e*. By applying the same method, Bader charges for the gold atoms in AuCl and AuCl₃ are 0.30 and 0.73 *e*, which implies that the six Au atoms that formed the O–Au–O structure are oxidised (Au^{δ+}). We

note here that the Bader analysis is a charge partitioning scheme based on the calculated electron density. The calculated charges are usually lower than expected for the formal oxidation state since there will be a degree of covalency in the Au-O or Au-Cl bond.

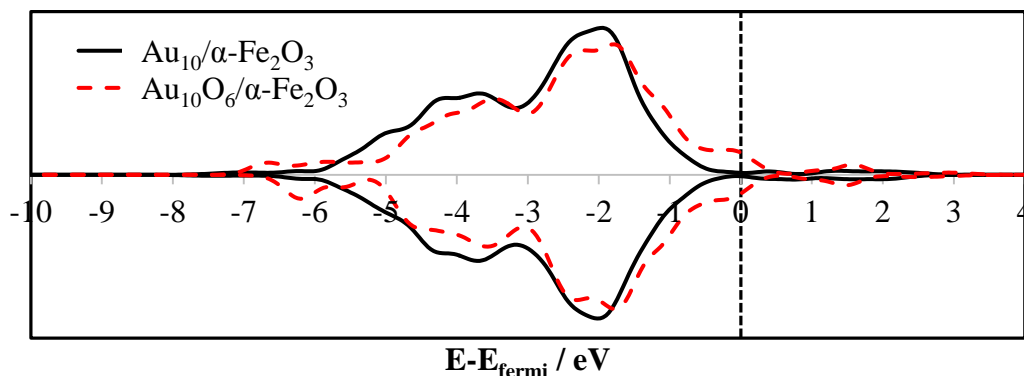


Figure 5.4 PDOS of Au-*d* band states for Au₁₀/Fe₂O₃(0001) (black solid line) and Au₁₀O₆/Fe₂O₃ (red solid line). Energies are corrected to Fermi level and Gaussian smearing width of 0.20 eV is applied.

The partial density of states (PDOS) of Au *d*-band states in Figure 5.4 shows that the Au atom *d*-states range for Au₁₀O₆/Fe₂O₃(0001) system have shifted to higher energies compared to the Au₁₀/Fe₂O₃(0001) data. In Au₁₀O₆/Fe₂O₃, the tail of the main region of Au *d*-band state is extended to above the Fermi level (up to around +0.4 eV) showing that the dissociation of O₂ caused the depletion of occupancy in the Au *d*-band states. This further confirms and supports our conclusion that the six Au atoms are oxidised upon the dissociation of O₂ molecules. Similar results were observed for the dissociation of O₂ on Au₁₀ clusters by Howard and Willock.¹⁵⁹

Table 5.1 Oxygen vacancy formation energies calculated for stoichiometric α -Fe₂O₃, Au₁₀/ α -Fe₂O₃, Au₁₀O₆/ α -Fe₂O₃ systems. Refer Figure 5.3 for label of vacancy sites.

System	$E_{\text{vac}} / \text{eV}$
Fe₂O₃ stoichiometric slab	3.04
Au₁₀/Fe₂O₃	
- under	2.13
- nearest	2.88
- next nearest	3.03
Au₁₀O₆/Fe₂O₃	
- under	0.86
- nearest	0.95
- next nearest	2.00
- Au-O	1.96

The ease of forming an oxygen vacancy on a surface plays a role in oxidation catalysis by providing the oxygen needed in a Mars van Krevelen (M-vK) mechanism. DFT+U calculations were performed of the oxygen defect creation energy based on equation (5.1) for α -Fe₂O₃(0001), Au₁₀/ α -Fe₂O₃(0001), and oxidised supported gold-10 nanoparticle (Au₁₀O₆/ α -Fe₂O₃(0001)) systems. The calculated oxygen vacancy formation energies for the different systems are tabulated in Table 5.1. The vacancy process is always endothermic as it forms the unfavourable step of reducing the catalyst surface. However, this will be compensated by the oxidation of the reactant in an oxidation reaction.

It is observed that the E_{vac} on a stoichiometric (0001) surface is 3.04 eV (293 kJ mol⁻¹) which is highly endothermic. The presence of the Au₁₀ nanoparticle lowers the E_{vac} . However, it only affects the E_{vac} up to certain extent given that the vacancy site formed is still near to the nanoparticle. In Figure 5.3, we define three types of surface oxygen ions. Those oxygen atoms that are covered by the Au cluster are labelled “under”. Sites have an Au atom at similar distance to their neighbours in the oxide in the plan view of Figure 5.3 are taken to be “nearest” to the cluster/oxide interface. Finally, “next nearest” vacancy site have one other surface atom in between the vacancy site and the cluster.

The next nearest vacancy site, furthest from the nanoparticle, yield an E_{vac} value of 3.03 eV which is similar to the E_{vac} obtained from a bare α -Fe₂O₃(0001) surface. Vacancy formation at the nearest site gives an E_{vac} value of 2.88 eV which 0.16 eV lower than the bare α -Fe₂O₃(0001) surface. Further reduction (0.91 eV) is observed for an oxygen vacancy creation under the Au₁₀ cluster. These showed that the vacancy formation energy was not affected when vacancy sites are formed away from the immediate vicinity of the nanoparticle/oxide interface.

However, further decrease in E_{vac} is observed with the presence of oxidised Au₁₀. Vacancy formation at the next nearest site gives vacancy formation energy of 1.04 eV lower than for the clean surface. As for the vacancy formed at nearest neighbouring site and under the cluster, the vacancy formation energies are 2.09 eV and 2.18 eV lower than the bare surface. Vacancy formation energy of 1.96 eV is required to abstract an oxygen atom from the oxidised periphery of the gold cluster. This suggests that the oxidised Au region is more stable against reduction than the nearby surface sites on the support.

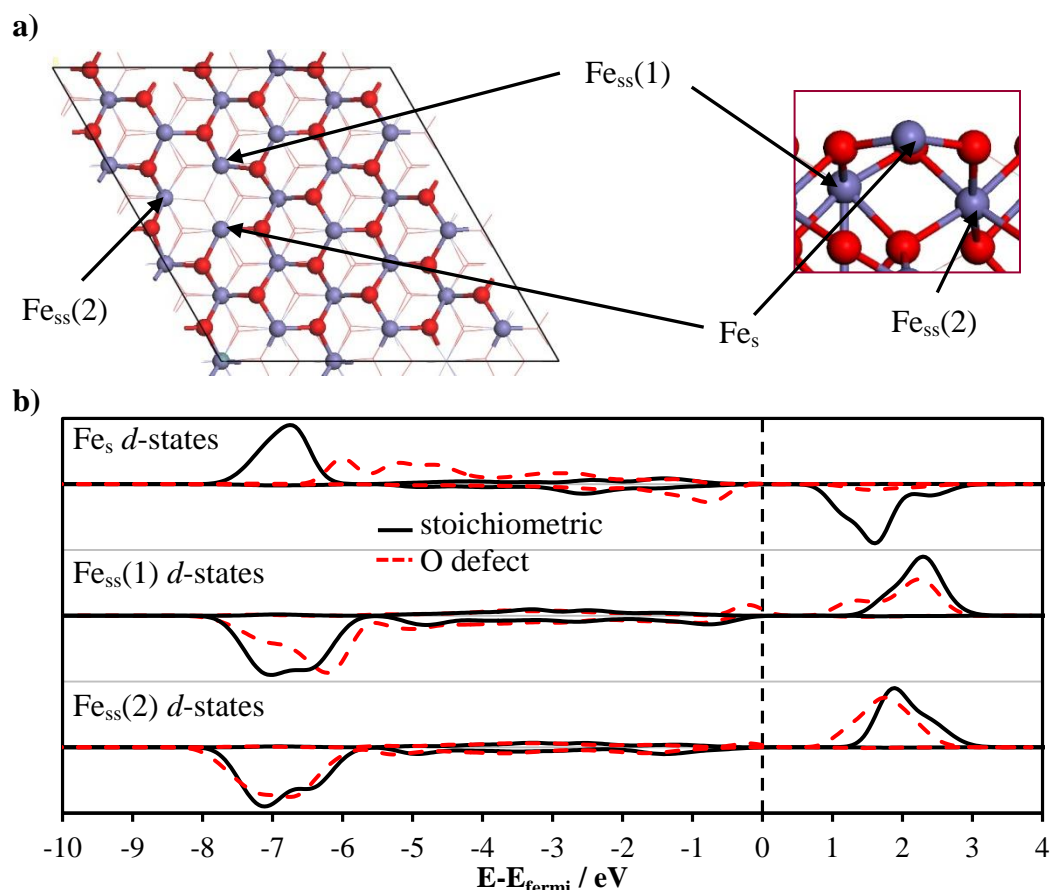


Figure 5.5 a) Optimised structure of an oxygen defective (0001) surface of α -Fe₂O₃ indicating the surface and sub-surface Fe ions that are reduced. Normalise PDOS of b) surface (Fe_s), sub-surface 1 (Fe_{ss}(1)), and sub-surface 2 (Fe_{ss}(2)) Fe atoms *d*-states from stoichiometric (black solid line) and oxygen defective (red dashed line) α -Fe₂O₃(0001) surface calculated using PBE+U. Energies are corrected to Fermi level and Gaussian smearing width of 0.20 eV is applied. Oxygen (red) and iron (blue violet).

We are interested to know where the electrons have gone upon removal of oxygen from the surface. Thus, DOS and Bader analysis were conducted to investigate the electronic properties of optimised defective systems studied. In the surface of α -Fe₂O₃(0001) there are two layers of Fe ions neighbouring surface oxygen anions. These are labelled as surface (Fe_s) and sub-surface (Fe_{ss}) in Figure 5.5a. On the stoichiometric surface Fe_s is three co-ordinate to oxygen and Fe_{ss} is six co-ordinated, as are bulk Fe ions. Figure 5.5b shows the Fe atoms normalised PDOS for a stoichiometric and oxygen defective (0001) surface of α -Fe₂O₃ calculated using PBE+U. Up and down spins are shown above and below the horizontal axis, respectively.

Table 5.2 Bader charges obtained for the Fe_s and Fe_{ss} ions neighbouring the defect site for stoichiometric and reduced $\alpha\text{-Fe}_2\text{O}_3(0001)$, sites as indicated in Figure 5.5a.

Systems	Bader charge / e	
	Stoichiometric	Oxygen defect
$\alpha\text{-Fe}_2\text{O}_3(0001)$		
Fe_s	+1.58	+1.16
$\text{Fe}_{ss}(1)$	+1.70	+1.38
$\text{Fe}_{ss}(2)$	+1.73	+1.55

In Figure 5.5b, the occupied d -states for the stoichiometric surface Fe^{3+} ions (Fe_s) are all up spins and for the sub-surface Fe^{3+} ions (Fe_{ss}) are all down spins. This shows that the Fe_s and Fe_{ss} have an anti-ferromagnetic arrangement as found for the bulk structure.^{158, 159} The opposite spins for the occupied and unoccupied d -states of the Fe^{3+} ions shows the high spin arrangement expected for a d^5 ion in the weak ligand field of the oxygen anions. Figure 5.5b shows that the number of peaks for the Fe_s d -band states for defective $\alpha\text{-Fe}_2\text{O}_3(0001)$ surface has increased compared to the stoichiometric surface and showed a wider spread of energies (-6.0 to -1.0 eV). In addition, the unoccupied states down spin peak at about 1.7 eV is not observed for the defective system. A gap state has appeared at about -0.2 eV below the Fermi level for $\text{Fe}_{ss}(1)$ (Figure 5.5b). The broad down spin peak at about -6.8 eV has shifted to higher energy (-6.2 eV, $\text{Fe}_{ss}(1)$) and become narrower.

With the removal of oxygen from the $\alpha\text{-Fe}_2\text{O}_3(0001)$ surface, two Fe_{ss} and one Fe_s nearest neighbour ions are left with one less neighbour. This does some small geometric changes: In a clean stoichiometric $\text{Fe}_2\text{O}_3(0001)$ structure, the $\text{Fe}_s\text{-O}$ and $\text{Fe}_{ss}\text{-O}$ bond lengths are 1.81 Å and 1.94 Å, respectively. On an oxygen defective surface, the $\text{Fe}_s\text{-O}$ bond length near the vacancy site has increased slightly to 1.85 Å while the $\text{Fe}_{ss}\text{-O}$ bond length near the vacancy site has decreased slightly to 1.92 Å. The surface and sub-surface Fe cations are also reduced by 0.42 e for Fe_s and 0.32 e / 0.19 e for the two Fe_{ss} neighbours (Table 5.2). Fe cations further from the vacancy site show no change of calculated Bader charge. The PDOS data indicates that the d -states of the Fe neighbours to the defect site have been strongly affected by creation of the defect. The Bader analysis shows an increase in electron population for these sites. This suggests that the electrons remaining on the surface after removal of oxygen cause reduction of just the Fe sites neighbouring the vacancy.

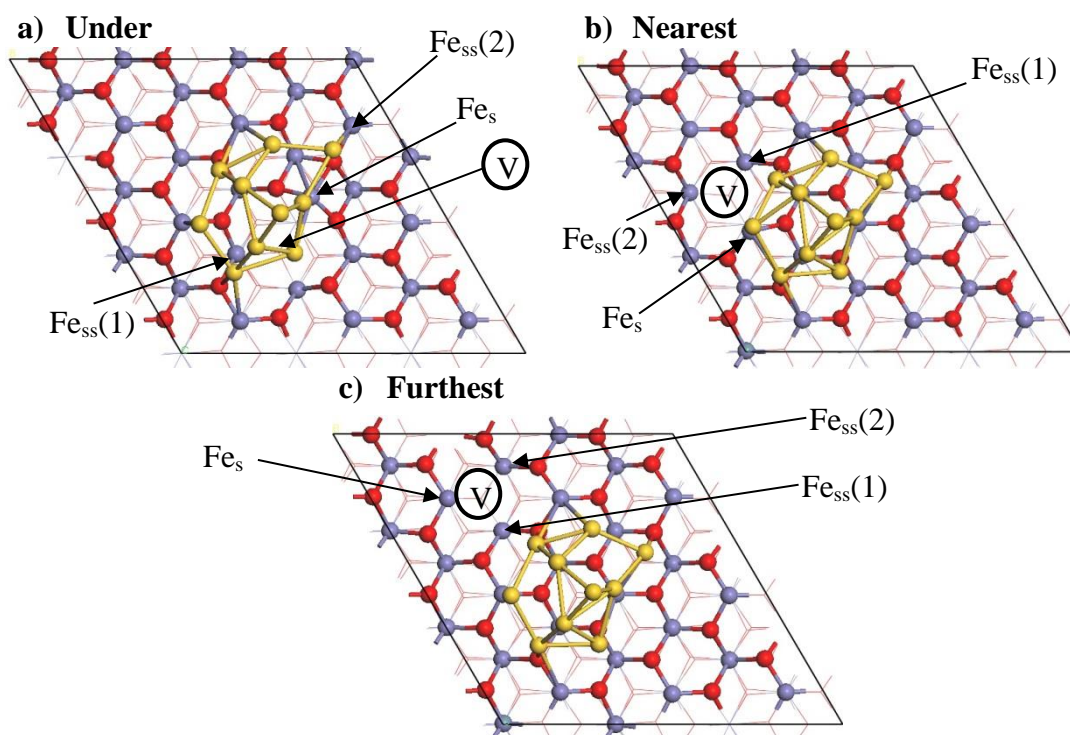


Figure 5.6 DFT+U optimised structures for Au₁₀/Fe₂O₃(0001) systems with single oxygen vacancy at a) under, b) nearest neighbour to cluster, and c) next nearest neighbour to cluster using PBE functional. V in a circle indicates vacancy site. Atoms coloured: Oxygen (red), gold (yellow), and iron (blue violet).

Figure 5.6 shows the optimised structures for Au₁₀/Fe₂O₃(0001) systems with single oxygen defect at three different sites. There are no significant structural changes observed in these structures except for when a vacancy is created under the nanoparticle. It is observed that one of the base Au atom (labelled Au-2 in Figure 5.3a) has moved slightly upwards towards the surface.

Similar results to the single oxygen defect on Fe₂O₃ system were observed for the DOS and Bader analysis when next nearest oxygen from the nanoparticle is removed from the surface lattice in the Au₁₀/Fe₂O₃ system. The electrons have gone to three nearest neighbour Fe atoms. We can see in Table 5.3 the Bader charges show a reduction of 0.42 e for Fe_s atom, 0.31 e for Fe_{ss}(1) atom, and 0.21 e for Fe_{ss}(2) atom. This can also be observed in the PDOS shown in Figure 5.7c, which has similar features as the defective Fe₂O₃ surface shown in Figure 5.5b. The occupied up spin d -band states have shifted to higher energies. No difference was observed for the effective charges of the Au species present.

Similarly, most of the charges have gone to the surface and sub-surface Fe atoms in the case where the oxygen removed is nearest to the nanoparticle as each has been reduced; Fe_s by 0.37 e , Fe_{ss}(1) by 0.33 e , and Fe_{ss}(2) by 0.31 e (Table 5.3). The PDOS

of Fe_s and Fe_{ss} *d*-band states in Figure 5.7b shows that the peak for unoccupied *d*-band states at about 2 eV has diminished upon the removal of an oxygen atom nearest to the gold nanoparticle. A small peak has also appeared right below the Fermi level. All these suggest an increase in occupancy of the Fe_s and Fe_{ss} *d*-band states.

Table 5.3 Bader charges for selected atoms obtained from Bader analysis of different oxygen defect sites in Au₁₀/Fe₂O₃(0001) system. Refer Figure 5.3a for Au atom labels and Figure 5.6 for surface and sub-surface Fe labels.

Systems	Bader charge / <i>e</i>			
	Stoichiometric	Oxygen defect site		
		Under nanoparticle	Nearest	Next nearest
Au₁₀/α-Fe₂O₃(0001)				
Fe _s	+1.51	+1.46	-	-
	+1.51	-	+1.14	-
	+1.58	-	-	+1.16
Fe _{ss} (1)	+1.70	+1.62	-	-
	+1.71	-	+1.38	-
	+1.71	-	-	+1.40
Fe _{ss} (2)	+1.74	+1.67	-	-
	+1.73	-	+1.60	-
	+1.74	-	-	+1.53
Au-1	-0.05	-0.10	-0.10	-0.06
Au-2	+0.10	-0.28	+0.08	+0.10
Au-3	+0.08	-0.01	+0.10	+0.08
Au-4	+0.09	-0.02	+0.04	+0.09
Au-5	+0.12	+0.11	+0.12	+0.12
Au-6	-0.22	-0.24	-0.20	-0.22
Au-7	-0.09	-0.15	-0.09	-0.08
Au-8	-0.03	+0.01	+0.03	+0.03
Au-9	-0.02	+0.04	+0.02	+0.02
Au-10	-0.10	-0.10	-0.10	-0.10
Total Au₁₀	-0.12	-0.74	-0.10	-0.02

Our data indicates that for vacancies on the surface that are not covered by Au atoms, the electrons left by the removal of an O²⁻ anion as ½ O₂ are accommodated by reducing surface and sub-surface Fe cations. On the other hand, when a vacancy is created under the Au nanoparticle, we observed electron transfer to the Au cluster. The Au ions labelled 1 to 7 (refer to Figure 5.3a) are reduced upon the creation of a surface vacancy under the cluster. Slight shifting of the peak and the tail of the Au *d*-

band states to lower energy in the PDOS (Figure 5.8) was also observed indicating that these Au ions have gained some electrons.

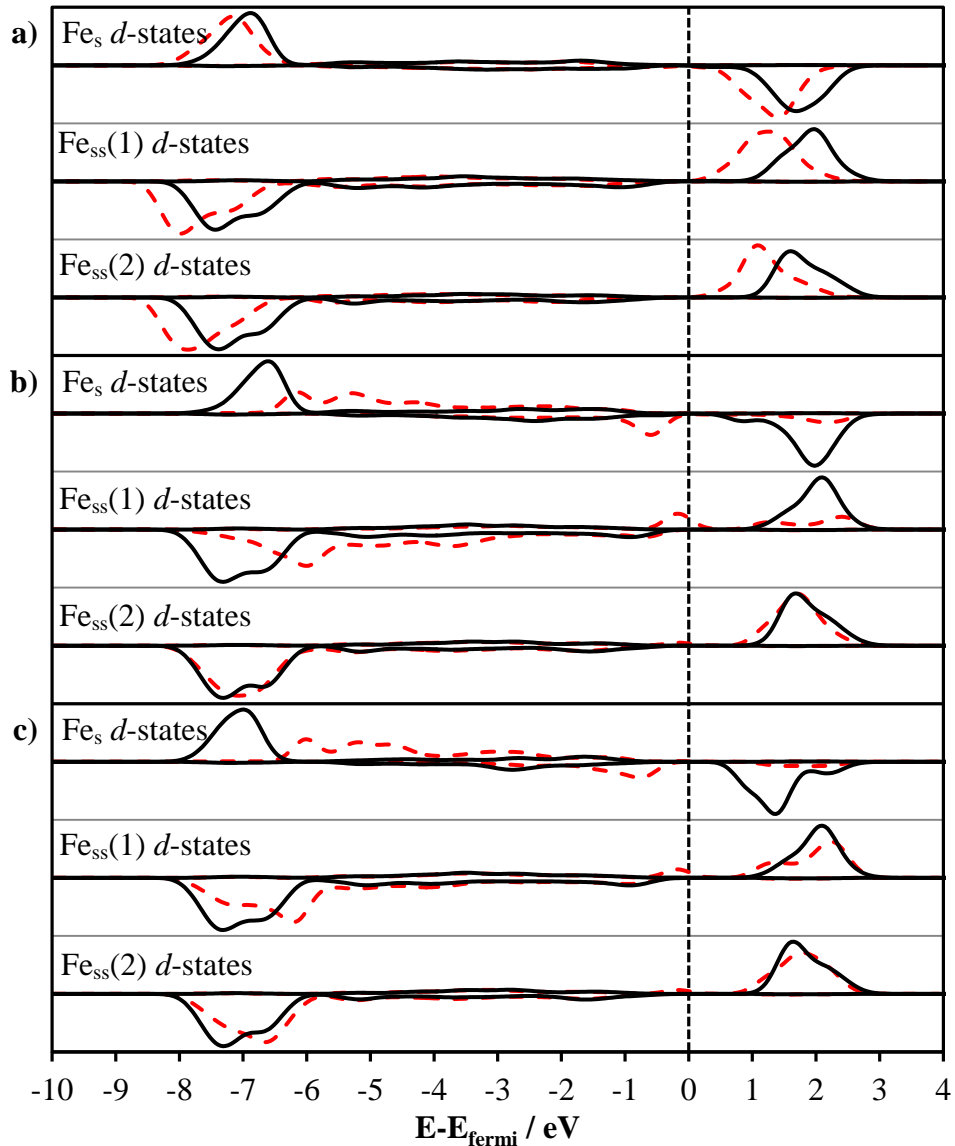


Figure 5.7 PDOS of surface and sub-surface Fe (Fe_s and Fe_{ss} , respectively) d -states for $\text{Au}_{10}/\text{Fe}_2\text{O}_3(0001)$ with oxygen defect site a) under, b) nearest to, and c) next nearest to the Au_{10} nanoparticle. Refer to labels in Figure 5.6a, b, and c for respective systems. Energies are corrected to Fermi level and Gaussian smearing width of 0.20 eV is applied. Stoichiometric (black solid line), oxygen defective (red dashed line).

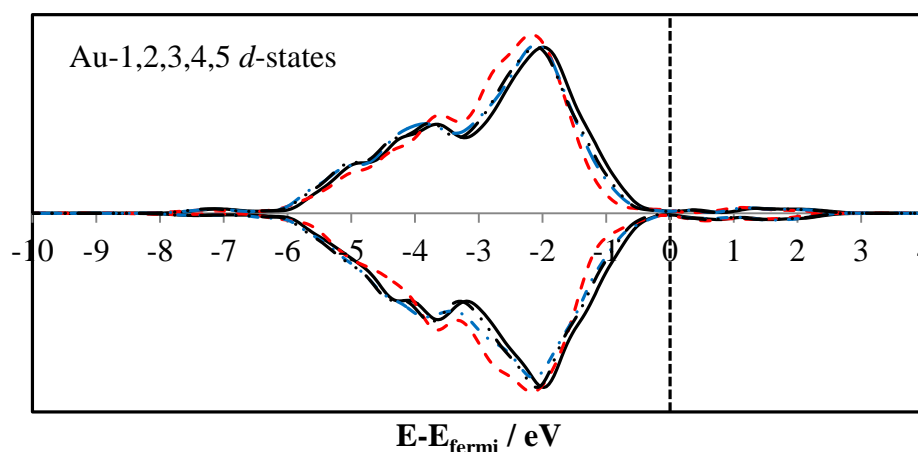


Figure 5.8 PDOS of Au-1 to Au-5 *d*-states for Au₁₀/ α -Fe₂O₃(0001) with oxygen defect site furthest away (next nearest site) from (black dash dot dot line), nearest to (blue dash dot line), and under (red dashed line) the Au₁₀ nanoparticle. Refer labels in Figure 5.3a. Energies are corrected to Fermi level and Gaussian smearing width of 0.20 eV is applied. Stoichiometric system (black solid line).

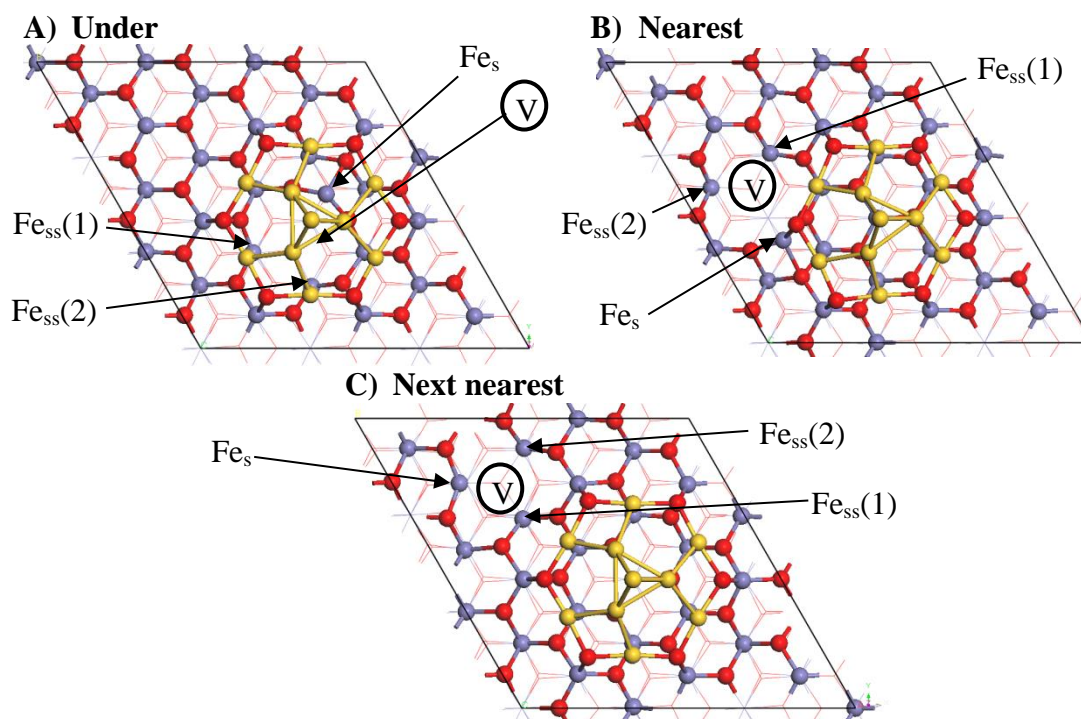


Figure 5.9 PBE+U optimised structures for Au₁₀O₆/ α -Fe₂O₃(0001) systems with single oxygen vacancy at a) under, b) nearest to, and c) furthest away from the Au₁₀O₆ nanoparticle. V in a circle indicates vacancy site. Oxygen (red), gold (yellow), and iron (blue violet).

Figure 5.9 shows the optimised structures for Au₁₀O₆/ α -Fe₂O₃(0001) with single oxygen defect at three different sites. As already discussed, the introduction of oxygen at the periphery of the Au₁₀ cluster leads to oxidation of Au centres, as it can be seen in the calculated Bader charges given in Table 5.4 with six of the Au atoms having charges greater than 0.5 *e* assigned. This result in an overall positive charge for Au atoms of the cluster which is more than balanced by the six oxygen atoms that

have been introduced since the total Bader charge for these species is $-5.21 e$. Three nearest neighbour Fe cations (one surface and two sub-surface ions) were slightly reduced when a single surface oxygen vacancy at three different sites are created on the Au₁₀O₆/ α -Fe₂O₃(0001) system but more prominent when the oxygen vacancy site is next nearest neighbour from the Au nanoparticle.

Table 5.4 Bader charges for selected atoms from Bader analysis of different oxygen defect sites on Au₁₀O₆/Fe₂O₃ system. Refer Figure 5.3b for Au atom labels and Figure 5.9 for surface and sub-surface Fe labels.

Systems	Bader charge / e			
	Stoichiometric	Under nanoparticle	Nearest	Next nearest
Au₁₀O₆/α-Fe₂O₃(0001)				
Fe _s	+1.57	+1.49	-	-
	+1.64	-	+1.59	-
	+1.58	-	-	+1.44
Fe _{ss} (1)	+1.71	+1.62	-	-
	+1.71	-	+1.63	-
	+1.71	-	-	+1.59
Fe _{ss} (2)	+1.74	+1.68	-	-
	+1.74	-	+1.63	-
	+1.74	-	-	+1.64
Au-1	+0.53	+0.43	+0.52	+0.52
Au-2	+0.56	+0.44	+0.55	+0.55
Au-3	+0.54	+0.54	+0.53	+0.54
Au-4	+0.56	+0.53	+0.54	+0.55
Au-5	+0.53	+0.52	+0.41	+0.52
Au-6	+0.57	+0.57	+0.56	+0.55
Au-7	+0.12	+0.08	+0.09	+0.13
Au-8	+0.08	+0.08	+0.10	+0.08
Au-9	+0.11	+0.11	+0.08	+0.08
Au-10	+0.03	+0.03	+0.03	+0.03
Total Au	+3.63	+3.33	+3.41	+3.55

Creating a vacancy nearest to the gold nanoparticle reduced the Bader charges of surface and sub-surface Fe ions only slightly; Fe_s by 0.05 e , Fe_{ss}(1) by 0.08 e , and Fe_{ss}(2) by 0.11 e (Table 5.4). However, a more prominent reduction in the total charge on the Au atoms of the cluster is observed (0.22 e). Similar for a vacancy under the cluster, the charges for surface and sub-surface Fe ions did not alter much, these Bader charges change by 0.09 or less (Table 5.4). The reduction on the total

charge on the Au atoms in this case is more than (a total of $0.30 e$) that is observed on the system with a vacancy at the nearest neighbour position. A vacancy at the next nearest neighbour position caused the Bader charge of the three atoms to alter with a total change of $0.36 e$ accompanied by a much smaller variation ($0.08 e$) in the total charge on Au atoms in relative to the stoichiometric system.

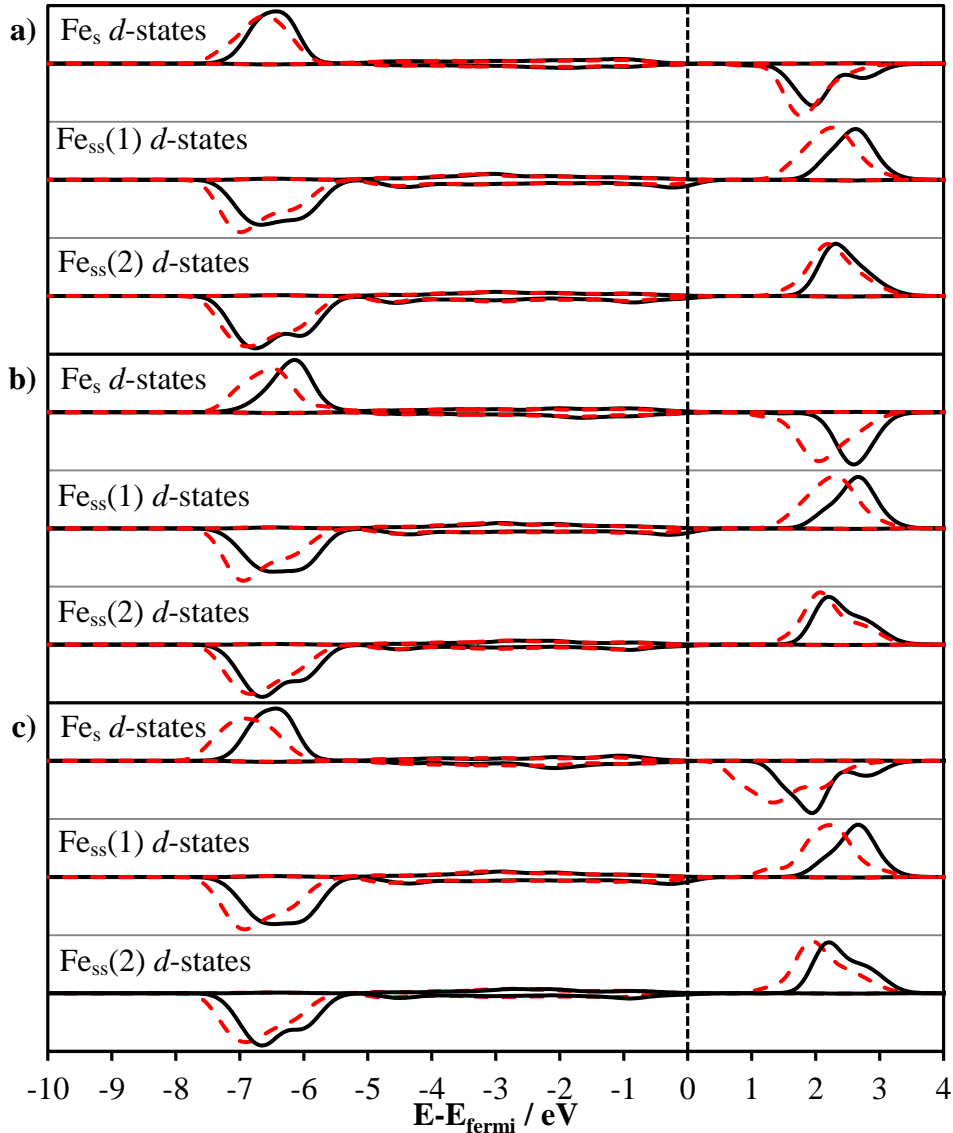


Figure 5.10 PDOS of surface and sub-surface Fe (Fe_s and Fe_{ss} , respectively) d -states for $\text{Au}_{10}\text{O}_6/\alpha\text{-Fe}_2\text{O}_3(0001)$ with oxygen defect site a) under, b) nearest to, and c) next nearest to the Au_{10} nanoparticle. Refer labels in Figure 5.9a, b, and c for respective systems. Energies are corrected to Fermi level and Gaussian smearing width of 0.20 eV is applied. Stoichiometric (black solid line), oxygen defective (red dashed line).

Figure 5.10 shows the PDOS of Fe_s and Fe_{ss} d -band states for the defective systems in comparison to the stoichiometric system. One common observation is that the peaks of the Fe_s and Fe_{ss} d -band states for the defective structure have shifted slightly to lower energy. However, the peaks of the unoccupied d -band states (above

the Fermi level) are still visible and did not shift as drastically as seen in Figure 5.7b and c, which explains the amount of electrons gained by Fe_s and Fe_{ss} in these two vacancy sites are far less than those observed for the oxygen defective systems of Au₁₀/ α -Fe₂O₃(0001). The PDOS of the Au ions *d*-band states for the system where oxygen vacancy is under the nanoparticle are shown in Figure 5.11c. We can see this similar trend in the Au₁₀/Fe₂O₃ system where the Au *d*-band states are shifted to lower energy when an oxygen vacancy is created under the Au₁₀ nanoparticle (Figure 5.8c).

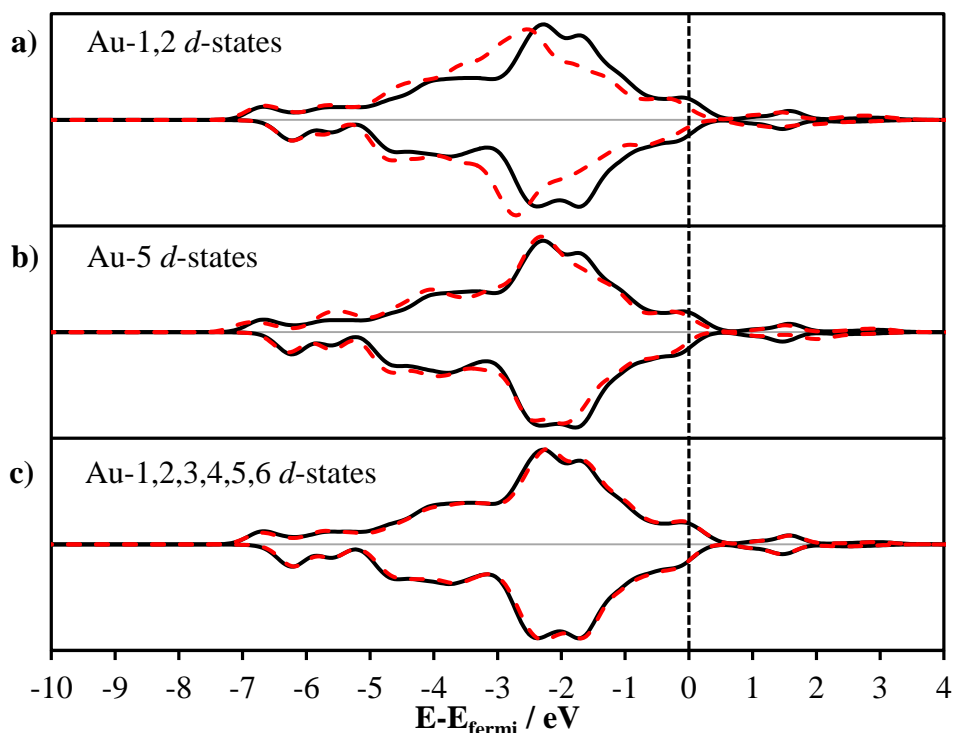


Figure 5.11 PDOS of Au *d*-states for Au₁₀O₆/Fe₂O₃(0001) with oxygen defect site a) under, b) nearest to, and c) next nearest to the Au₁₀ nanoparticle. Refer labels in Figure 5.3b. Energies are corrected to Fermi level and Gaussian smearing width of 0.20 eV is applied. Stoichiometric (black solid line), oxygen defective (red dashed line).

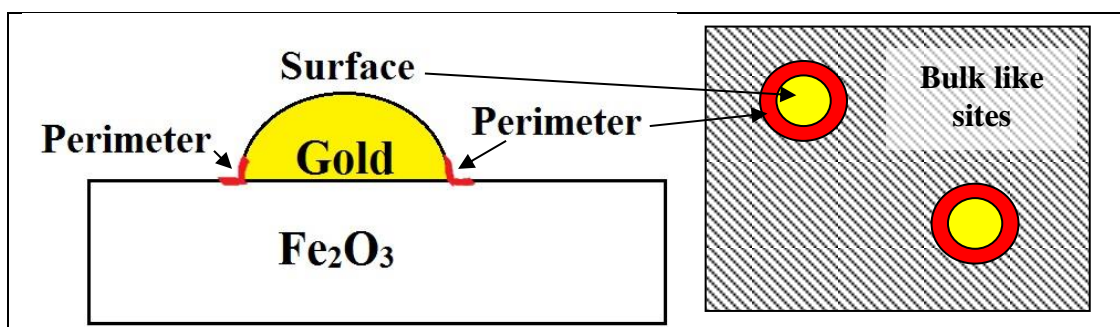


Figure 5.12 Definition of perimeter and surface sites for gold nanoparticle supported on α -Fe₂O₃(0001) surface. The perimeter sites are defined to include the base layer

of Au atoms next to Fe₂O₃ as well as the three-fold Fe (Fe_{3f}) atoms near the Au-Fe₂O₃ interface.

Using an oxygen ion as a point along the largest circumference possible for the perimeter site on Au₁₀O₆/ α -Fe₂O₃ system, the measured radius (r) is 6.797 Å (6.797×10^{-20} m). This gives a surface area (πr^2) of about 1.45×10^{-18} m². The radius of the Au₁₀O₆ cluster is 3.394 Å (3.394×10^{-20} m) which gives a surface area of about 3.62×10^{-19} m² which is in contact with the oxide support. Thus, subtracting this surface area in contact with the oxide support from the perimeter surface area, the accessible perimeter site surface area is about 1.09×10^{-18} m². For the Au₁₀/ α -Fe₂O₃ system, the calculated accessible perimeter site surface area is about 5.52×10^{-19} m². Herzing *et al.* have used 50 mg catalyst samples with a surface area of 190 m² g⁻¹.¹⁴⁵ It is reported that 2.9 % of the mass of the catalyst consists of Au species which gave 0.0015 g of Au in the catalyst used. Following that, the catalyst is calculated to have 4.43×10^{17} Au₁₀ particles per gram. In order to obtain the span of perimeter surface sites on the catalyst used, the accessible perimeter surface area is multiple with the total number of Au₁₀ particles per gram of catalyst. Thus, we suggest that the perimeter surface sites of Au₁₀ cluster spanned only about 0.13% (0.25% for Au₁₀O₆) of the 190 m² g⁻¹ surface of the Au/FeO_x catalyst¹⁴⁵ even if all the gold species on the surface are at this size.

Overall, we have predicted that the influential area of the Au₁₀ nanoparticle to be the perimeter of the interface between the nanoparticle and the surface up to a certain distance as shown in Figure 5.12. We observed that when the oxygen vacancy site is furthest away from the Au₁₀ nanoparticle, the oxygen vacancy formation energy is similar to the one obtained on a clean stoichiometric α -Fe₂O₃ (0001) surface. This clearly shows that the supported Au₁₀ has no effect on the oxygen vacancy formation at sites that have no contact or are away from the interface between the nanoparticle and the surface. The ease of formation of an oxygen vacancy on the oxide surface is observed to be increasing in the order of furthest < nearest < under the Au₁₀ nanoparticle. Similar trend is observed when the Au₁₀ is further oxidised with three molecules of oxygen but produced lower oxygen vacancy formation energies for all three vacancy sites. This shows an increase in the influential area of the nanoparticle. We suggest that the dissociated oxygen species at the base of the gold nanoparticle increases the oxygen saturation in the system thus making it easier to extract oxygen from the support.

5.4 CO adsorption on Au₁₀O₆/Fe₂O₃

Following the study of oxygen vacancy formation on the α -Fe₂O₃(0001) surface with and without the presence of supported Au₁₀ and Au₁₀O₆ nanoparticles, CO adsorption and oxidation mechanism on the α -Fe₂O₃ supported Au₁₀O₆ nanoparticle have also been studied. CO adsorption has been modelled on several sites on the Au₁₀ nanoparticle and on the hematite (0001) surface. The optimised structures of CO adsorbed at various adsorption sites on Au₁₀O₆/ α -Fe₂O₃(0001) are shown in Figure 5.13. Table 5.5 shows the adsorption energies, CO vibrational frequency, CO bond lengths, and M-CO bond lengths for each structure in Figure 5.13.

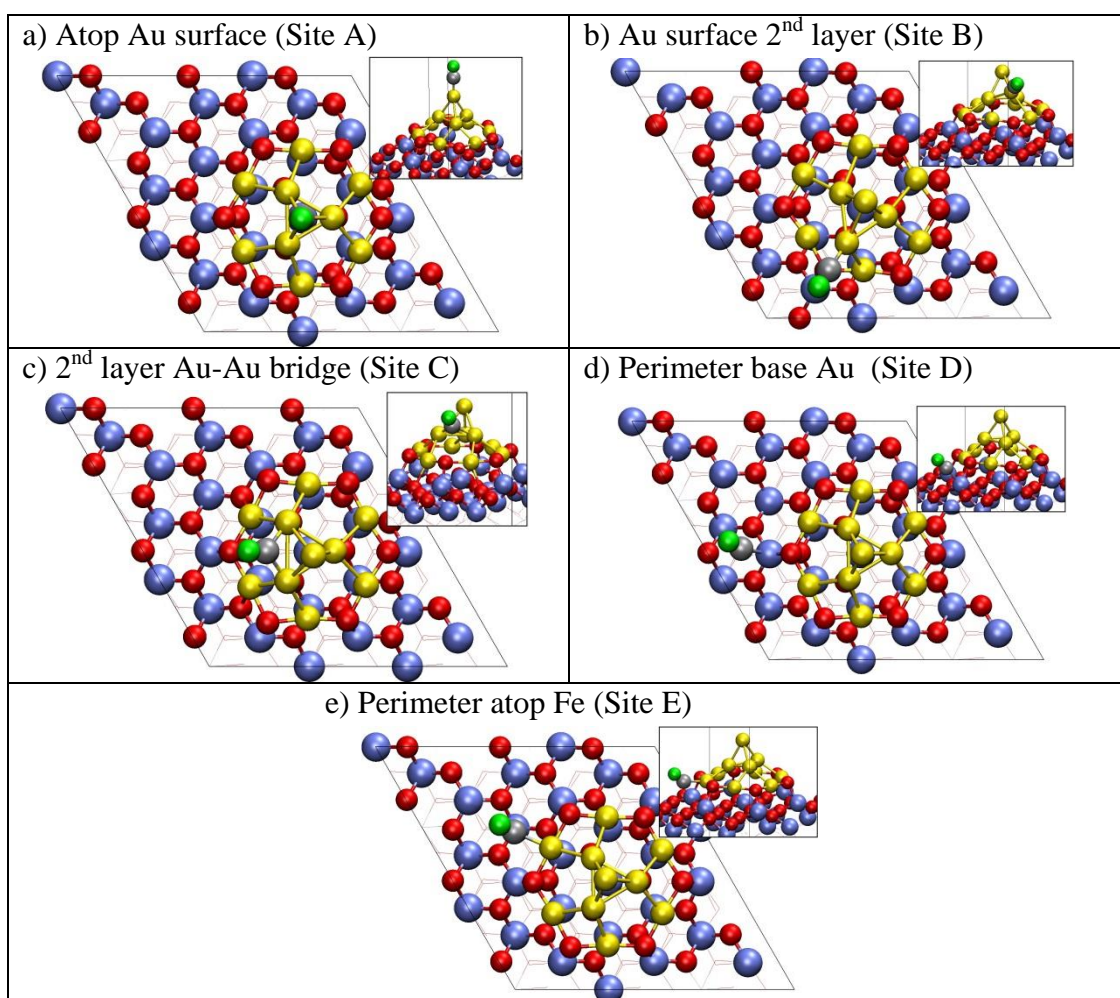


Figure 5.13 Optimised structures of CO adsorbed on Au₁₀O₆/ α -Fe₂O₃(0001) surface at various adsorption sites. Insets are side views of each structure. Oxygen (red), gold (yellow), iron (blue violet), carbon (grey), and oxygen from CO (green).

Table 5.5 PBE+U (Fe $U_{eff} = 4.0$ eV) calculated adsorption energies following and CO vibrational frequencies for various adsorption sites on Au₁₀O₆/ α -Fe₂O₃(0001).

	Site A	Site B	Site C	Site D	Site E
E_{ads} / eV	-1.52	-0.83	-0.14	-0.18	-0.02
$\nu(\text{CO}) / \text{cm}^{-1}$	2077	2081	1858	2122	2044
$d(\text{C-O}) / \text{\AA}$	1.15	1.15	1.18	1.14	1.15
$d(\text{M-CO}) / \text{\AA}$	1.92	1.94	2.08, 2.06	2.38	2.20
$\angle(\text{Au-C-O}) / ^\circ$	179.6	175.3	132.4, 134.8	167.3	142.4
$\Delta q(\text{Au}) / e$	0.20	0.12	0.11, 0.11	0.01	0.07
$\Delta q(\text{C}) / e$	-0.08	0.01	-0.14	0.01	0.01
$\Delta q(\text{O}) / e$	0.08	0.04	0.08	0.01	0.01

A very strong adsorption is observed when CO adsorbed linearly at the top of Au surface (refer Figure 5.13a) of the Au₁₀ nanoparticle ($E_{ads} = -1.52$ eV). This is followed by CO adsorbed diagonally at an Au–C–O angle of 175.3° on Au surface at the second layer of the Au₁₀ nanoparticle (refer Figure 5.13b) ($E_{ads} = -0.83$ eV). CO adsorbed on other sites yielded E_{ads} of -0.18 eV, -0.14 eV, and -0.02 eV for sites C, D, and E, respectively.

The DFT calculated vibrational frequency of a gas phase CO is 2125 cm⁻¹ with a C–O bond length of 1.14 Å. All adsorbed species showed a CO stretching frequency at lower values than the gas phase CO. The frequencies are 2077, 2081, 1858, 2122, and 2044 cm⁻¹ for sites A, B, C, D, and E, respectively. The lower frequencies indicate the extent of metal – carbon (M–C) back bonding and are expected to correspond with an increase in CO bond length. The filled σ orbital on carbon atom overlaps with an empty Au orbital of the correct symmetry and leads an electron density transfer from the CO molecule to the Au metal centre. On the other hand, there is π bonding interaction from the overlapping of filled Au $d \pi$ orbital with the π^* anti-bonding molecular orbital of the CO molecule. Thus, electrons are donated from the metal d -orbital into the anti-bonding orbital of CO, which cause the reduction in CO bond strength. The lowest CO stretching frequency is observed at site C due to the molecule being adsorbed at the Au–Au bridging site. This also explains the longer CO bond length (1.18 Å) measured for the molecule at this site compared to the gas phase $d(\text{CO})$ of 1.14 Å.

In general, when CO is adsorbed on Au (or Fe for the adsorption at site D), the Au cation (Fe cation for site D) should lose electrons which is observed in the

calculated Bader charges shown in Table 5.5. At sites A, B and E, the Au cations involved in CO adsorption are oxidised and the total charge has increased by $0.20 e$, $0.12 e$, and $0.07 e$, respectively. The total charge for both the Au cations at site C are increased by $0.11 e$. A very minor perturbation is observed for the Fe cation at adsorption site D ($0.01 e$) upon the adsorption of CO. As explained earlier in Section 0, the Au atom at site E is an oxidised species and the Au atoms at sites A, B, and C are presumably at 0 oxidation state. Thus, it is more difficult to extract electrons from the oxidised Au species at site E compared to sites A, B, and C.

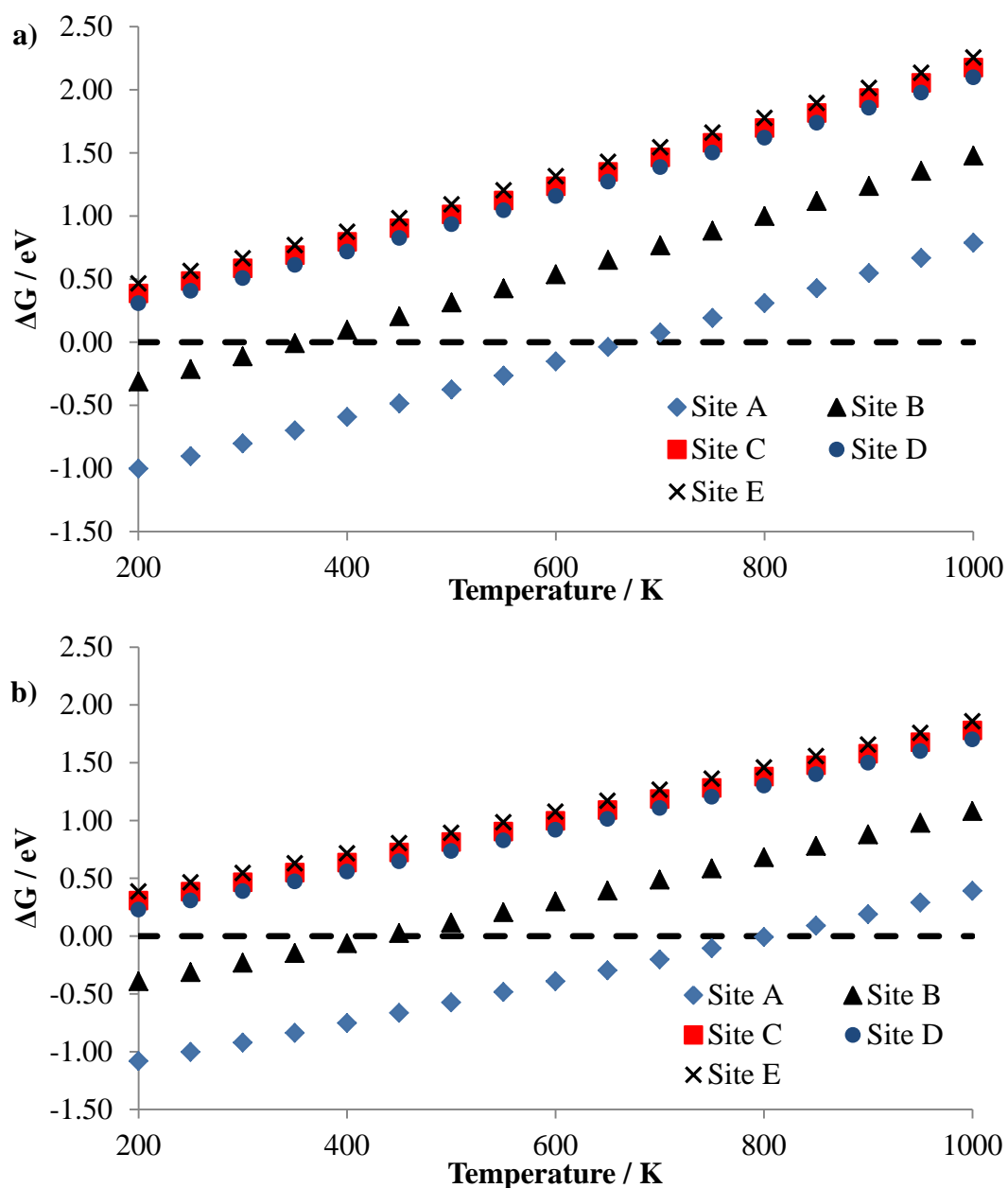


Figure 5.14 Gibbs free energy (ΔG) for the adsorption of a CO molecule at a) 1 atm and b) 100 atm pressure at various sites on $\text{Au}_{10}\text{O}_6/\alpha\text{-Fe}_2\text{O}_3(0001)$ surface ($\text{Au}_{10}\text{O}_6/\alpha\text{-Fe}_2\text{O}_3 + \text{CO} \rightarrow \text{CO-Au}_{10}\text{O}_6/\alpha\text{-Fe}_2\text{O}_3$) against temperature. Refer Figure 5.13 for positions of different adsorption sites.

Figure 5.14 shows calculated Gibbs free energies for the adsorption of CO at pressures 1 atm and 100 atm at adsorption sites illustrated in Figure 5.13 as a function of temperature. The free energy graphs shows that the adsorption of CO gets thermodynamically unfavourable with increasing temperature. Adsorption site B still shows an exothermic reaction up to temperature of 350 K at 1 atm. However, at higher partial pressure of CO, adsorption at sites A and B are favourable up to temperature at 400 K and 750 K, respectively. These thermodynamics data suggest that sites A and B will most likely be occupied at room temperature but not for sites C, D, and E. Thus, in a way these sites are not “poisoned” by CO adsorption. At 300 K and 1 atm, the ΔG for CO adsorption at sites C, D, and E are 0.59 eV, 0.51 eV, and 0.66 eV, respectively. Increasing the pressure to 100 atm lowers the ΔG to 0.47 eV, 0.39 eV, and 0.55 eV for sites C, D, and E, respectively. In the next section, CO oxidation on sites C, D, and E are investigated.

5.5 CO oxidation

A more weakly adsorbed CO increases the rate of CO oxidation with a lower energy barrier compared to a strongly adsorbed CO. Thus, we have performed calculations on CO oxidation by surface lattice oxygen and dissociated oxygen species at the perimeter and Au-Au bridge sites of the system. Activation energy barriers were obtained using NEB method and are tabulated in Table 5.6.

Table 5.6 Activation energy barriers (E_a) for CO oxidation at perimeter sites at base Au and atop Fe by lattice oxygen from oxide surface and base Au. Energies are calculated relative to adsorbed species.

System	Source of oxygen	E_a / eV
Site C	Surface	0.81
Site D	Base Au	1.00
	Surface	0.50
Site E	Base Au	0.86
	Surface	0.28

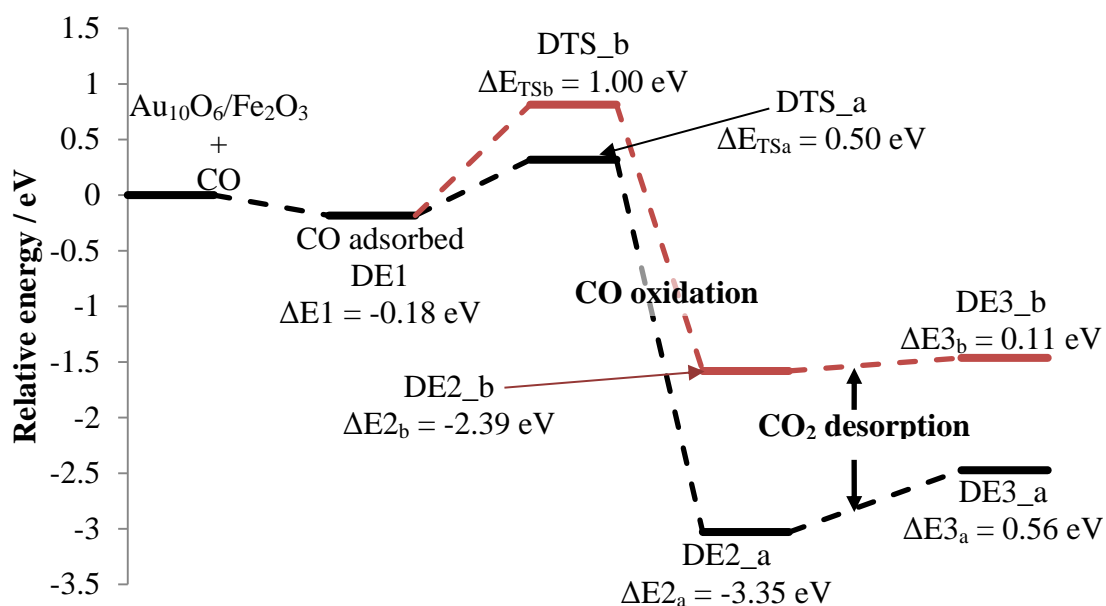


Figure 5.15 CO oxidation by Au_{10} supported on α -Fe₂O₃ (0001) surface at site D using lattice oxygen shown in black lines and using oxygen from Au_{10} cluster shown in red lines. Energies of each stage are presented relative to initial system ($\text{Au}_{10}\text{O}_6/\text{Fe}_2\text{O}_3 + \text{CO}$). ΔE_x or ΔE_{x_i} (where i is a or b) is the difference in energy between x th stage and previous stage, for example ΔE_{2b} is the energy difference between stage DE2_b and DTS_b. ΔE_{TS_i} (where i is a or b) is the energy difference between TS and the previous stage. The structures for each stage are shown in Figure 5.17.

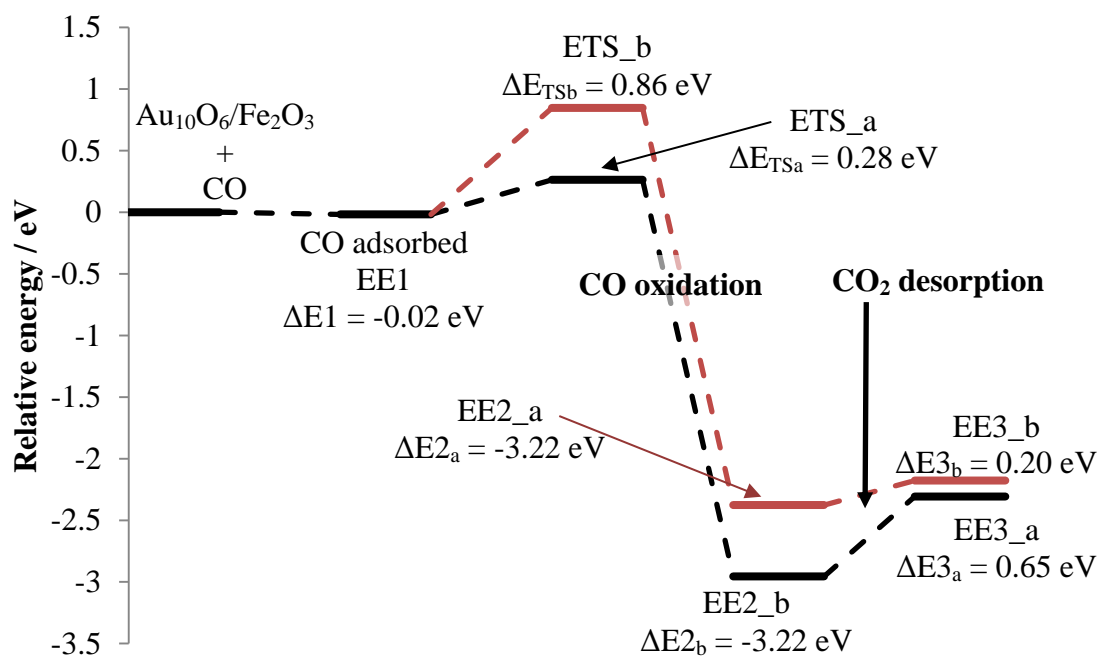
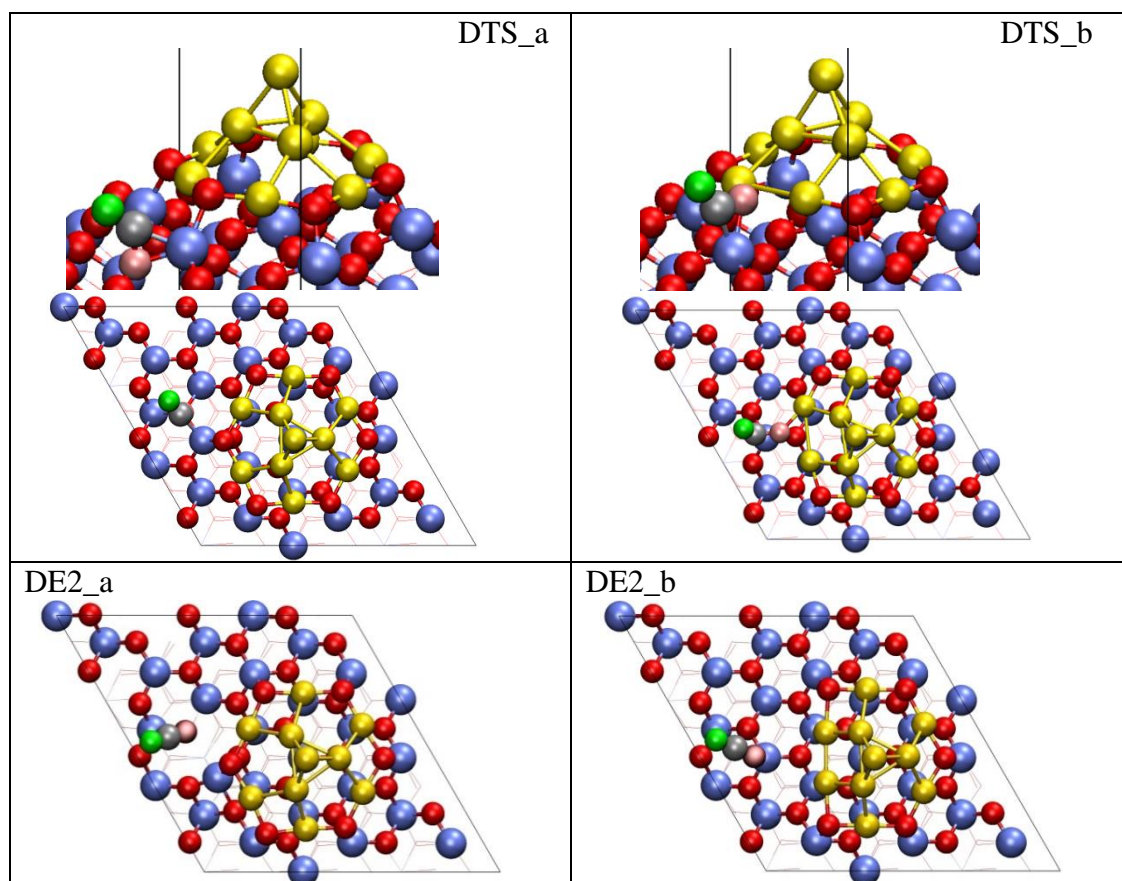


Figure 5.16 CO oxidation by Au_{10} supported on α -Fe₂O₃ (0001) surface at site E using lattice oxygen shown in black lines and using oxygen from Au_{10} cluster shown in red lines. Energies of each stage are presented relative to initial system

(Au₁₀O₆/Fe₂O₃ + CO). ΔE_x or ΔE_{x_i} (where i is a or b) is the difference in energy between x th stage and previous stage, for example ΔE_{2_b} is the energy difference between stage EE2_b and ETS_b. ΔE_{TS_i} (where i is a or b) is the energy difference between TS and the previous stage. The structures for each stage are shown in Figure 5.18.

Figure 5.15 and Figure 5.16 show lower activation energy barriers for CO oxidation by Au₁₀ using lattice oxygen from Fe₂O₃ at perimeter sites. Figure 5.15 shows CO₂ formation proceeds at site D with an activation energy barrier of 0.50 eV when oxygen is taken from the oxide surface lattice; while the activation energy increases to 1.00 eV when oxygen bonded to Au at the perimeter site is used. Similar trend is observed for CO oxidation reaction when CO is adsorbed on the perimeter Au atom at site E (Figure 5.16) where a higher energy barrier (0.86 eV) is observed when oxygen bonded to Au at the perimeter site is used compared to lattice oxygen (0.28 eV). These imply that the perimeter ring of Au oxide will be formed when the Au particle is first exposed to oxygen but then remain stable through the oxidation process and not be reduced by CO. We suggest that the CO oxidation is able to proceed using the lattice oxygen and the oxidised species is energetically favourable compared to the adsorbed CO system. However, the process is more likely to happen when CO is adsorbed at site E.



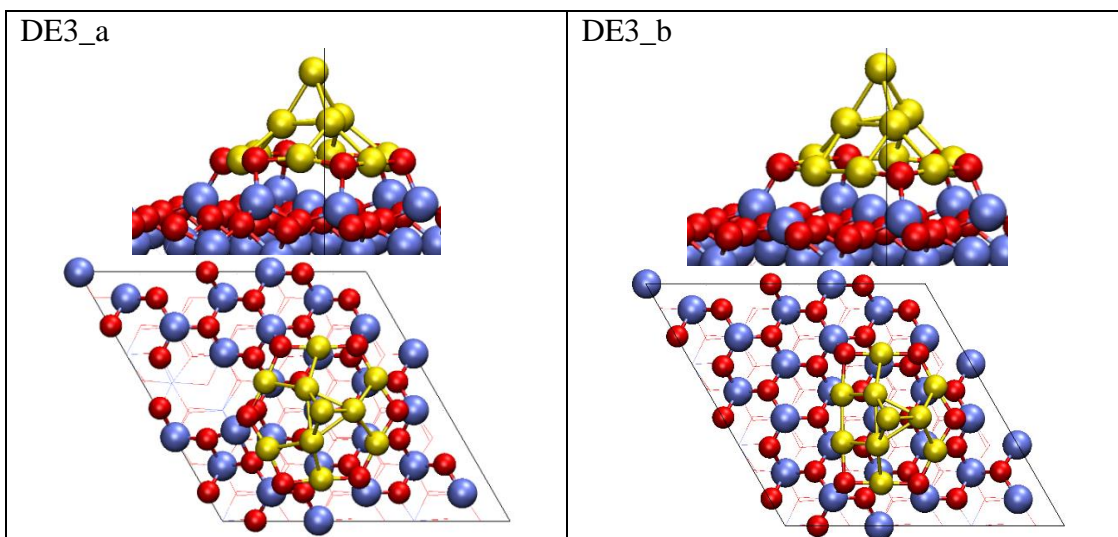


Figure 5.17 Optimised structures for each stages of CO oxidation by Au_{10} supported on $\alpha\text{-Fe}_2\text{O}_3$ (0001) surface at site D using lattice oxygen ($\text{DE}_x\text{_a}$ and DTS_a) and using oxygen from Au_{10} cluster ($\text{DE}_x\text{_b}$ and DTS_b) in reference to Figure 5.15. Oxygen (red), gold (yellow), iron (blue violet), carbon (grey), oxygen from CO (green), and oxygen taken from surface (pink).

The CO_2 desorption process for pathway a (black lines) in both Figure 5.15 and Figure 5.16 requires some energy, which are 0.56 and 0.65 eV for site D and E, respectively. For pathway b (red lines) in both Figure 5.15 and Figure 5.16, the energy needed for CO_2 desorption are 0.11 and 0.20 eV, respectively. We would have expect that both the end structures after the CO_2 desorption process at the same adsorption site will be different. This is true at only at adsorption site D. However, at adsorption site E, it is observed that at the same time when CO_2 is formed using the oxygen bonded to Au, a lattice oxygen from the surface (Figure 5.18, indicated by a black arrow) migrates to replace the oxygen vacancy formed. This resulted in the formation of a structure close in energy (Figure 5.18 $\text{EE}_3\text{_b}$) as the one that has an oxygen abstracted from its lattice surface (Figure 5.18 $\text{EE}_3\text{_a}$) with a total system energy difference of 0.07 eV apart.

For the CO adsorbed at site C, we have modelled the CO oxidation process to take place using an oxygen atom from the Fe_2O_3 surface. We have used the optimised structure (Figure 5.18 $\text{EE}_2\text{_a}$) as the end point for the CO oxidation process. The CO_2 formation for site C using an oxygen atom from the surface proceeds with an activation energy of 0.81 eV (Figure 5.19). The transition state structure (Figure 5.19 (i) and (ii)) forms an O–C–O angle of 128.3° with an OC–O distance of 1.68 Å (a). The calculated CO_2 desorption energy is 0.52 eV.

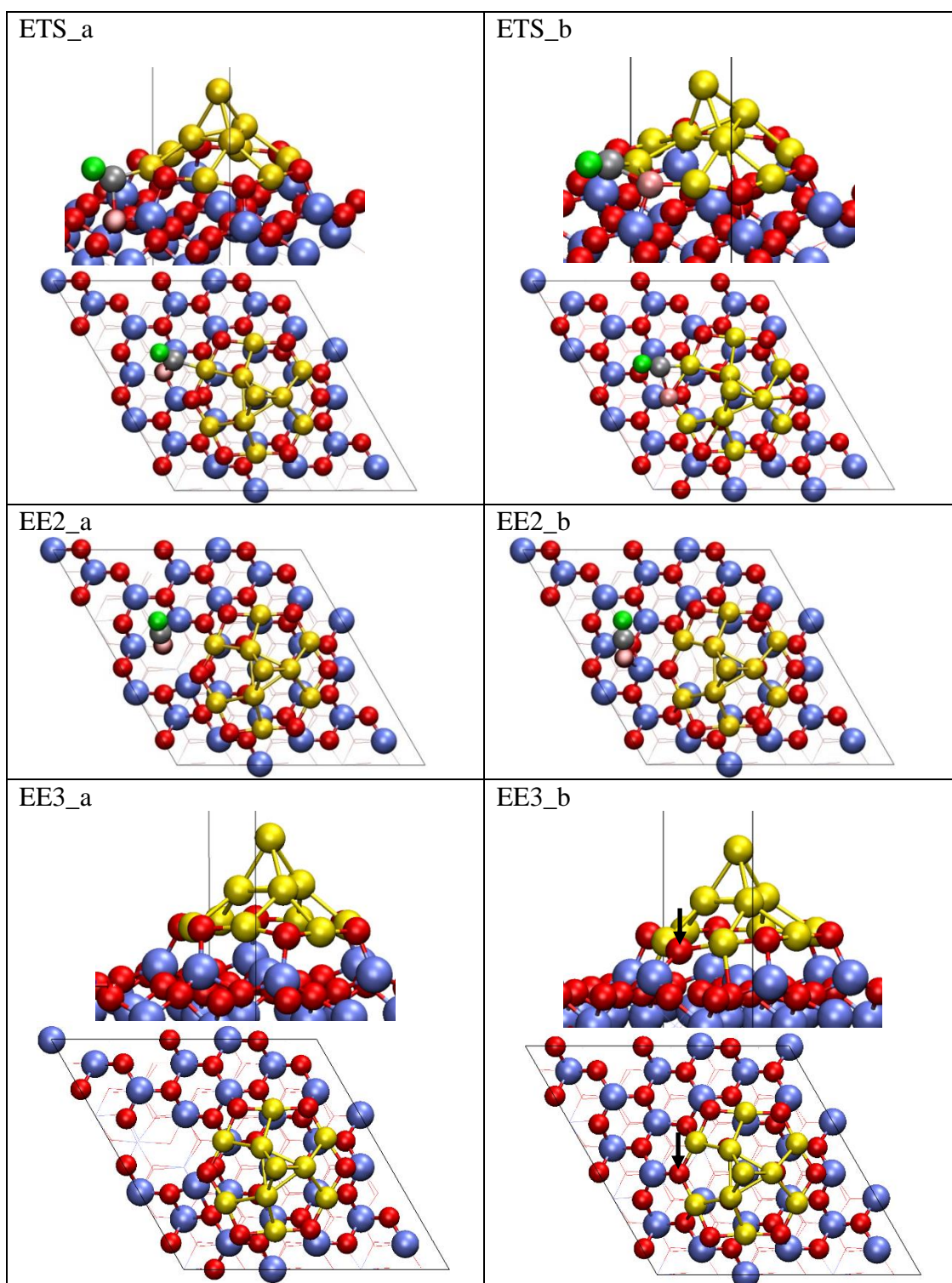


Figure 5.18 Optimised structures for each stages of CO oxidation by Au_{10} supported on $\alpha\text{-Fe}_2\text{O}_3$ (0001) surface at site E using lattice oxygen (EE x _a and ETS_a) and using oxygen from Au_{10} cluster (EE x _b and ETS_b) in reference to Figure 5.16. Oxygen (red), gold (yellow), iron (blue violet), carbon (grey), oxygen from CO (green), and oxygen taken from surface (pink). Black arrow in EE3_b indicates the oxygen that has migrated.

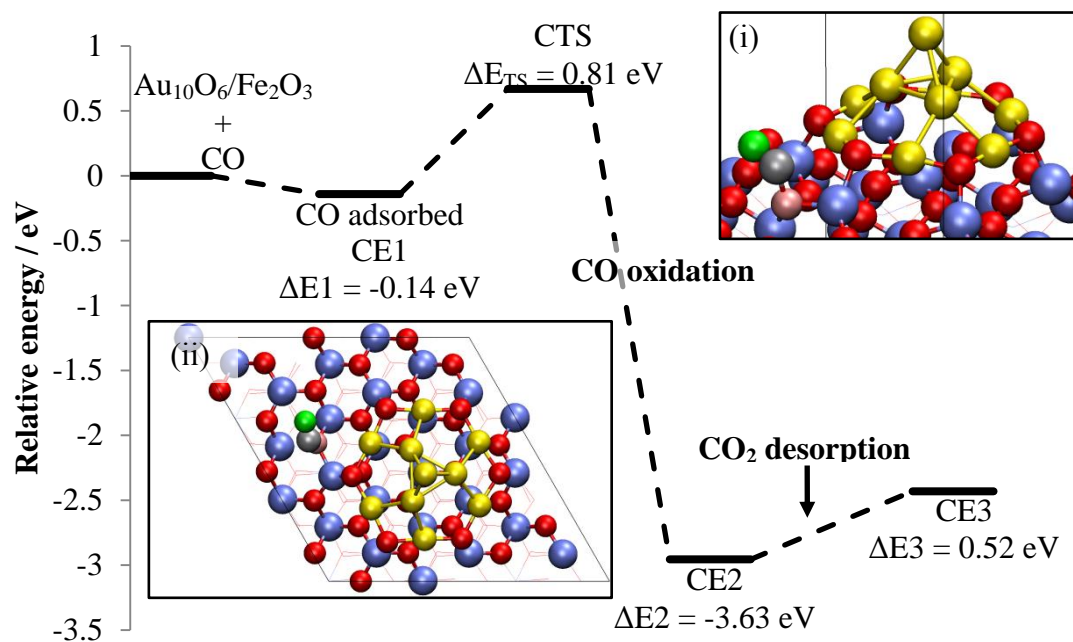


Figure 5.19 CO oxidation by Au₁₀ supported on α -Fe₂O₃ (0001) surface at site C using lattice oxygen. Energies of each stage are presented relative to initial system (Au₁₀O₆/Fe₂O₃ + CO). ΔE_x is the difference in energy between x th stage and previous stage, for example ΔE_2 is the energy difference between stage CE2 and CTS. ΔE_{TS} is the energy difference between TS and the previous stage. Insets are the (i) side and (ii) top views of the transition state structure (CTS).

5.6 Conclusion

In this chapter it is shown that the surface oxygen vacancy formation energy is lowered with presence of the Au₁₀O₆ cluster on α -Fe₂O₃(0001) support. The ease of formation of an oxygen vacancy on the oxide surface is observed to be increasing in the order of furthest < nearest < under the Au₁₀ nanoparticle. Thus, suggesting that the cluster has a limited influential area on the formation of an oxygen vacancy. Vacancy sites at nearest neighbour to the cluster are within the influential area which we termed as perimeter sites. Combining both the optimised structural information obtained from DFT calculations and the experimental data¹⁴⁵, the perimeter surface sites of Au₁₀ cluster spanned only about 3% (5% for Au₁₀O₆) of the 190 m² g⁻¹ surface of the Au/FeO_x catalyst¹⁴⁵ only if all the gold species on the surface are at the size calculated. The percentage of perimeter surface area on the catalyst gives a statistical idea on the chance of an adsorbate to react at that site.

CO adsorption is found to be particularly strong at the top of Au surface (Figure 5.13a). On the other hand, weak adsorptions are observed at the perimeter sites; sites C, D, and E in Figure 5.13. From the calculated Gibbs free energy for the adsorption

of CO at various adsorption sites, we observed that adsorption became unfavourable at sites C, D, and E with increasing temperature (Figure 5.14). At 1 atm, adsorption sites are favourable up to 350 K and 600 K for sites A and B, respectively. The increase in pressure to 100 atm have just increased the temperature by 50 K for site A (100 K for site B) for which the adsorption will still be favourable. The Gibbs free energies graphs (Figure 5.14) suggest that sites A and B will always be occupied by adsorbed molecules. The weak adsorption of CO at sites C, D, and E suggests that the Mars van Krevelen mechanism for CO oxidation on Au₁₀O₆/ α -Fe₂O₃(0001) can occur through the Eley-Rideal mechanism. The CO molecule can be oxidised by the lattice oxygen without adsorbing on the surface.

DFT calculations yield an activation energy barrier of 0.50 eV and 0.28 eV for the CO oxidation at sites D and E, respectively using the lattice oxygen from the oxide support. The activation energy barrier is increased by 0.50 eV for site D (0.58 eV for site E) when oxygen bonded to Au at the perimeter site is used for oxidation.

Chapter 6

General conclusions

Precious metals supported on metal oxides are shown to be effective catalysts for oxidation reactions.^{5, 6, 282, 283} In particular on reducible metal oxides as they have shown to act as an oxygen reservoir.^{62, 137, 168, 255, 284-286} CeO₂ and Fe₂O₃ are two examples of reducible metal oxides that were used in this work. Upon the removal of an oxygen atom from the lattice, the two excess electrons left behind are localised on the metal cations and so reducing the cations; for example Ce⁴⁺ to Ce³⁺ in CeO₂ systems. The reduced metal cations are readily re-oxidised to the initial oxidation state under oxidising environment. This makes the metal oxide a good oxygen storage material for oxidation and reduction reactions. Thus, these reducible oxides are widely used as support for metal catalysts.

In this work, computational techniques employing periodic density functional theory (DFT) through plane wave basis codes such as VASP or local basis set codes such as CRYSTAL09, have been used to study the physical and electronic properties of underlying chemistry problems. Density functional theory with the inclusion of on-site Coulomb interaction (Hubbard U), and hybrid functionals have been shown to produce results in agreement with experimental data.

Various generalised gradient approximation and hybrid functionals applying the plane waves with pseudopotentials and Gaussian-type basis set methods as implemented in VASP and CRYSTAL09, respectively were used to investigate the CeO₂ bulk structure. Overall, the computed lattice parameters for ceria are higher than the reported experimental lattice constant (5.411 Å) by between 0.35 % and 2.14 %. The HSE06 hybrid functional approach yielded a lattice parameter of 5.472 Å while the DFT+U ($U_{\text{eff}}^{\text{Ce } 4f} = 5 \text{ eV}$) method has shown a larger expansion of the bulk cell (5.509 Å (PW91+U) and 5.504 Å (PBE+U)) compared to the other calculated, experimental and reported theoretical values. These DFT+U results are in agreement with the reported work which states that the increase in U value applied to the Ce 4f states will cause an expansion in lattice of the system.¹⁸¹ As for the Gaussian-type basis set approach, the hybrid functional, PBE0, is shown to produce results in best agreement with experimental values. Standard DFT has greatly

underestimated the O $2p$ – Ce $4f$ and O $2p$ – Ce $5d$ band gaps for the CeO₂ bulk structure. However, the use of DFT+U has improved the band gap values. Hybrid functionals such as HSE06 and PBE0 have reproduced O $2p$ – Ce $4f$ band gaps which agrees well with the experimental value of 3 eV^{163, 179} but have overestimated the O $2p$ – Ce $5d$ band gap. The various amount of Hartree-Fock exchange included in hybrid functionals has caused the overestimation of the O $2p$ – Ce $5d$ band gap which has also been reported in literature.^{161, 162}

Using DFT+U method, two Ce⁴⁺ cations are reduced to Ce³⁺ upon the removal of an oxygen atom. These two Ce³⁺ cations are located at next nearest neighbour positions from the vacancy site. The optimised defective structures showed that the lattice relaxes away from the reduced Ce sites. This is due to the Ce³⁺ cations which has larger ionic radius (1.283 Å) than the Ce⁴⁺ cations (1.11 Å).^{52, 53, 221} Other structures with different pairs of Ce³⁺ sites at higher E_{vac} are also present. At higher temperature, it is predicted that the energy gained from thermal heating will allow the defect structure to end up at one of the higher energy structures obtained. Using the canonical partition function in terms of the contribution from different energy levels, the increase in population of defect structures with higher E_{vac} is observed when the temperature is increased from 300 K to 700 K. This shows the increase in temperature causes a greater range of Ce³⁺ arrangements is possible around a defect.

The migration of neighbouring oxygen to the vacancy site is evaluated using the nudged elastic band (NEB) method. The calculated activation energy barriers are not significantly affected even when the electrons have moved from the reduced Ce sites to a different Ce site providing that the end structure is the most stable arrangement with Ce³⁺ cations at NN_NN sites. The calculated activation energy barrier is 0.48 eV when the electrons were localised at the Ce³⁺ sites and did not move during the oxygen migration. In another calculation, the Ce³⁺ sites were shifted to another NN_NN site at the end of the oxygen migration and the activation energy barrier obtained for this process is 0.46 eV. In addition, the electrons were found to move to another next nearest neighbour position from the new vacancy site after the anion has reached the transition state. A slightly higher energy barrier is required ($E_a = 0.57$ eV) when the end structure resulting from the migration of an oxygen atom has Ce³⁺ cations at NN_NN* or NN*_NN positions with respect to the new vacancy site formed; NN and NN* are next nearest neighbours at the distance of 4.57 Å and 6.01 Å away from the vacancy site, respectively. In this case, the two electrons have

remained localised on the same Ce sites but the position of the vacancy site has changed so changing the positions of the Ce sites with respect to the position of the new vacancy site. The defect structures with Ce^{3+} at NN_NN*/NN*_NN positions are at higher E_{vac} range. This also explains that at an increased temperature of 700 K, the oxygen migration energy barrier of 0.57 eV can be overcome and subsequently causes the increase in population of defect structures with higher E_{vac} accompanied by the decrease in defect structures with lower E_{vac} . The energy barrier required for the migration of neighbouring oxygen to a vacancy site will provide insight on ceria as an oxygen reservoir for catalysis reactions. It can suggest the ease of migration of oxygen from bulk sites to replenish vacancy sites on the surface.

On the CeO_2 surface, oxygen vacancy formation is expected to be more facile compared to in the bulk structure because the relaxation around the Ce^{3+} reduced cations centres should be easier. This is due to the cerium cations and oxygen anions on the surfaces are in low coordination state. The ease of abstracting an oxygen atom from the surface lattice increases in the order $(111) < \langle 110 \rangle$ -type steps $\text{CeO}_2\text{-U} < (110)$. For the (111) surface, the formation energy of a sub-surface vacancy is 0.06 eV lower than the surface vacancy. On both the structures, two next nearest Ce^{4+} cations are reduced to Ce^{3+} . Vast majority of the structures with lower vacancy formation energy have two Ce^{3+} on the surface sites, while structures with E_{vac} at mid-range consist of mostly one surface and one sub-surface Ce^{3+} sites. Defective surface at higher E_{vac} are mostly structures with two sub-surface Ce^{3+} sites. As for the (110) surface, the lowest E_{vac} structure is when the Ce^{3+} sites are located one at nearest neighbour and the other at fourth nearest neighbour sites. The oxygen anion nearest to the vacancy site has undergone significant relaxation where it has moved to a bridging position between two nearest neighbour Ce cations. For the $\text{CeO}_2\text{-U}$ surface, the Ce^{3+} sites are both at next nearest position but with one at first layer and the other at second layer.

For both the bulk and surface structures, it is shown in this work that vacancy formation energy and the distribution of localised electrons are affected by the relaxation of the lattice atoms. Atoms around the Ce^{3+} cations are significantly relaxed in order to accommodate the increased cation size (1.11 Å to 1.283 Å).^{52, 53, 221} Besides, the oxygen vacancy created also caused the neighbouring oxygen anions to relax towards the site.

$\text{Pd}^{2+}/\text{Pt}^{2+}$ doped systems yield more favourable substitution energies compare to the $\text{Pd}^{4+}/\text{Pt}^{4+}$ doped system. For bulk ceria, the $\text{Pd}^{2+}/\text{Pt}^{2+}$ at square planar site are the most favourable doped CeO_2 structures due to the Pd and Pt cations are d^8 ions that prefer the square planar coordination over cubic. Density of states and Bader analysis data shows that two Ce^{4+} cations were reduced when Pt dopant metal is substituted at the Ce site. This shows that the Pt dopant metal aided the reduction of two Ce cations in the bulk. It is also observed that the migration of a charge compensation vacancy that accompanies the formation of Pd^{2+} and Pt^{2+} doped systems to further away from the dopant metal require a high energy barrier ($E_{\text{CCVmig_Pd}}=0.61$ eV, $E_{\text{CCVmig_Pt}}=0.60$ eV). Substitution of Pd^{2+} and Pt^{2+} on the (111), CeO_2 -U, and CeO_2 -D surfaces require less energy compared to on the bulk structure, except for the three coordinated substitution site on the (111) surface.

Pd and Pt dopants are found to lower the oxygen vacancy formation energy on bulk and surfaces of ceria. Oxygen vacancy sites formed not adjacent to the existing vacancy site are more favourable. On the bulk structures, the removal of an oxygen atom bonded to the metal dopant is less favourable compared to neighbouring low coordinated oxygen anions. However, the vacancy formation energy can be reduced if there is an adjacent oxygen anion which can migrate to replenish the vacancy created next to the metal dopant. Similarly to the undoped bulk structures, the defective structure with two Ce^{3+} cations at next nearest neighbour positions gave the lowest reduction energy.

On the three coordinated Pd- and Pt-doped surfaces of CeO_2 , the formation of an oxygen vacancy next to the metal dopant is exothermic. This is due to the structural relaxation that occurs to reposition the metal dopant to a square planar position. The study of oxygen vacancy formation on the surfaces provides information which is useful for the prediction of an oxidation reaction on the surface. The easier an oxygen atom can be abstracted from the surface, the more likely an oxidation reaction will take place with low activation energy.

The DFT+U calculations in this work shows that CO is weakly absorbed on the $\text{CeO}_2(111)$ surface. Thus, suggesting that CO oxidation may occur via reaction with the lattice oxygen following the Eley-Rideal mechanism rather than the Langmuir-Hinshelwood mechanism. However, adsorption of CO can be improved by doping the surface with Pd^{2+} or Pt^{2+} ions, provided that the dopant is three coordinated with

a vacant coordination site exposed on the surface. A CO molecule is found to adsorb strongly on the three coordinated dopant site. Water molecule adsorbed at the same site is found to dissociate spontaneously. Even when water has dissociated, it is still not as good as putting the CO on the three coordinated metal ion, so CO can still displace water under the right conditions. Nevertheless, the possibility of a water-gas shift reaction which follows the dissociation of water to give adsorbed H and OH species shall not be ruled out.

Besides studying dopant effects, investigations on Au₁₀ nanoparticles supported on α -Fe₂O₃(0001) surface have also been performed. Supported Au catalysts (Au₁₀ and Au₁₀O₆) are found to affect the oxygen vacancy formation energy on the surface of the support. The Au₁₀ cluster is observed to have a limited influential area on the ease of abstracting an oxygen from the surface. Vacancy sites nearest and under the cluster are greatly influenced so lower oxygen vacancy formation energies are obtained at this sites. Abstracting an oxygen at a site next nearest to the cluster yields similar E_{vac} as from the clean surface. The Au cluster which has the Au atoms at periphery sites oxidised (Au₁₀O₆) is observed to further lower the E_{vac} .

DFT+U calculations showed that CO adsorption is particularly strong at the top of Au surface. On the other hand, weak adsorptions are observed at perimeter sites. In addition, the Gibbs free energies calculated for CO adsorption at these perimeter sites have predicted the adsorption to be unfavourable with increasing temperature. The Au surface sites are found to be occupied up to 350 K and 600 K for sites A and B, respectively (refer to Figure 5.13 in Chapter 5). On the other, weak adsorption of molecules on the perimeter sites suggests that the sites will be free and not “poisoned” by strong adsorption of an adsorbate. Weak adsorptions at the perimeter sites also suggest that the Mars van Krevelen mechanism for CO oxidation on Au₁₀O₆/ α -Fe₂O₃(0001) can occur through the Eley-Rideal mechanism. The CO molecule can be oxidised by the lattice oxygen without adsorbing on the surface.

This work has provided insight into the effects of PGM dopants and nanoparticle on oxygen vacancy formation on the support in the atomistic level. CeO₂ on its own has poor thermal stability and undergoes rapid sintering at high temperatures, thus greatly reducing its oxygen storage capacity.^{287, 288} Doping CeO₂ with transition metals greatly increase the thermal stability and OSC of CeO₂.^{88, 89, 102, 288} Both the CeO₂(111) and α -Fe₂O₃(0001) surfaces are quite inert for surface adsorption of

gaseous species and only weak interactions are possible with the pure material. It is also the most stable oxide surface under ambient conditions. However, both the CeO₂ and α -Fe₂O₃ support were reduced more easily with the presence of transition metal atoms or clusters. This shows that the oxygen from the lattice is more readily available than it is from the pure materials. The ease in oxygen abstraction will enhance the activity in CO oxidation which follows a Mars-van Krevelen type mechanism. The results obtained may aid the design of catalysts for oxidation reactions.

6.1 Future work

Overall, this work will provide insight into more thorough study of the redox reactions on metal oxide supported metal catalyst. Different substitution sites for Pd and Pt cations on the $\langle 110 \rangle$ -type step surfaces has been studied here. Further investigation on the oxidation reaction mechanism on CeO₂ step surfaces can be carried out in the future. It will also be beneficial to the research community if the work can be carried out on model systems such as CeO₂ supported metal clusters (i.e. Pd, Pt, and Au). The influence of different metal catalyst to oxidation reactions. For gold supported on hematite, our group has extended the work by substituting gold for palladium. This study will compare the selectivity and conversion efficiency of palladium and gold clusters supported on hematite.

Appendix

A1. Basis sets and ECPs for CeO₂ in CRYSTAL09

Small core ECP for Ce

M is the number of terms in equation (2.53). M0, M1, M2, M3, and M4 are the number of terms in equation (2.54) for $\ell=0, 1, 2, 3, 4$, respectively.

30. 0 1 1 1 1 1 # $Z_N, M, M0, M1, M2, M3, M4$

20.137829 580.083457 0 # $\alpha_{kl}, C_{kl}, n_{kl}$

15.998482 310.302833 0

14.974187 167.813944 0

23.402455 -49.390229 0

16.570553 -21.331879 0

Large core ECP for Ce

12. 0 2 2 2 1 0

3.902597 119.423291 0

2.090727 -2.511980 0

3.158215 76.607034 0

1.665119 -0.430895 0

2.523621 68.864734 0

2.275701 -4.246970 0

4.645201 -41.694411 0

Valence only basis set for Ce used with small core ECP

The header line for each set of Gaussian Type Functions (GTF) has 5 parameters. In the order from left to right, type of basis set to be used for specified shell (0 for general basis set input), shell type (0,1,2,3,4 for S, SP, P, D, F shell, respectively), number of primitive GTF, formal electron charge attributed to the shell, and scale factor. In each line of primitive GTF input, first parameter is the exponent of the normalised primitive GTF. Second parameter is the relevant function coefficient. If an SP shell is specified, there will be three parameters where the second and third parameter corresponds to the s and p function coefficients, respectively.

0 0 10 2 1

3.89859830000E+03	1.39700000000E-04
5.87562140000E+02	7.25200000000E-04
5.62289570000E+01	7.10783000000E-02
4.01635400000E+01	-3.79178000000E-01
2.86882430000E+01	6.40599400000E-01
1.16721150000E+01	-9.72470200000E-01
3.04133300000E+00	9.69780000000E-01
1.56771300000E+00	4.28922500000E-01
5.95830000000E-01	2.05545000000E-02
2.63553000000E-01	-2.23240000000E-03

0 0 3 2 1

6.49817320000E+00	-1.64521470000E-01
4.33211550000E+00	7.12041140000E-01
2.45411440000E+00	-1.12062200000E+00

0 0 2 2 1

5.28409004897E-01	9.82402630000E-01
2.51142428651E-01	3.64449440000E-01

0 0 1 0 1

1.50000000000E-01	1.00000000000E+00
-------------------	-------------------

0 2 8 6 1

2.28145440000E+02	-7.74300000000E-04
2.87764530000E+01	6.84900000000E-03
2.03808040000E+01	-1.95845400000E-01
1.45577170000E+01	4.16909900000E-01
4.13703400000E+00	-5.39568300000E-01
2.15984800000E+00	-5.23772500000E-01
1.01808300000E+00	-1.15453800000E-01
5.54170000000E-01	3.87960000000E-03

0 2 4 6 1

3.65644320000E+00	1.55546690000E-01
2.43762880000E+00	-4.11357130000E-01

8.04965750000E-01	3.69655630000E-01
4.20218500000E-01	5.81142840000E-01
0 2 1 0 1	
2.18941286572E-01	1.00000000000E+00
0 3 6 10 1	
5.59994580000E+01	4.64120000000E-03
1.18300230000E+01	-1.32503500000E-01
8.35871600000E+00	2.38309600000E-01
3.93891300000E+00	4.53699900000E-01
2.00383900000E+00	3.85806900000E-01
1.00457700000E+00	1.44397400000E-01
0 3 3 1 1	
1.42931367700E+00	-2.09427350000E-01
9.46546216853E-01	2.97463440000E-01
3.43739796704E-01	4.85714240000E-01
0 3 1 0 1	
1.50344238998E-01	1.00000000000E+00
0 4 6 1 1	
6.54967110000E+01	-8.41580000000E-03
2.47369070000E+01	-5.82477000000E-02
1.04430730000E+01	-1.61418700000E-01
4.65883200000E+00	-2.85725000000E-01
2.09130400000E+00	-3.49945700000E-01
9.19321000000E-01	-3.13624800000E-01
0 4 1 0 1	
5.05560979331E-01	1.00000000000E+00

Valence basis set for Ce used with large core ECP

0 0 3 2 1	
6.4981732E+00	-1.6452147E-01
4.3321155E+00	7.1204114E-01
2.4541144E+00	-1.1206220E+00
0 0 1 2 1	

5.2101881E-01	1.0000000E+00
0 0 1 0 1	
2.4829957E-01	1.0000000E+00
0 0 1 0 1	
6.4111845E-02	1.0000000E+00
0 2 2 6 1	
3.6564432E+00	1.5554669E-01
2.4376288E+00	-4.1135713E-01
0 2 2 0 1	
8.0496575E-01	3.6965563E-01
4.2021850E-01	5.8114284E-01
0 2 1 0 1	
2.0408239E-01	1.0000000E+00
0 2 1 0 1	
8.3899778E-02	1.0000000E+00
0 3 2 2 1	
1.4542098E+00	-2.0942735E-01
9.6947319E-01	2.9746344E-01
0 3 1 0 1	
3.5835913E-01	1.0000000E+00
0 3 1 0 1	
1.5000000E-01	1.0000000E+00
0 4 1 0 1	
9.9160065E-01	1.0000000E+00
0 4 1 0 1	
3.2392317E-01	1.0000000E+00

8-411G* basis set for O

0 0 8 2 1	
8020.000000000000	0.001080000000
1338.000000000000	0.008040000000
255.400000000000	0.053240000000
69.220000000000	0.168100000000

23.900000000000	0.358100000000	
9.264000000000	0.385500000000	
3.851000000000	0.146800000000	
1.212000000000	0.072800000000	
0 1 4 6 1		
49.430000000000	-0.008830000000	0.009580000000
10.470000000000	-0.091500000000	0.069600000000
3.235000000000	-0.040200000000	0.206500000000
1.217000000000	0.379000000000	0.347000000000
0 1 1 0 1		
0.431507251354	1.000000000000	1.000000000000
0 1 1 0 1		
0.155213766714	1.000000000000	1.000000000000
0 3 1 0 1		
0.712949870118	1.000000000000	

A2. Structural and electronic properties of defective bulk ceria

Figure A1 shows the isosurface of spin density for structure **Q** (refer Table 3.3 in Chapter 3). Referring Figure 3.6c in Chapter 3, the two Ce^{3+} peaks correspond to the electron that occupied different f -orbitals at two different Ce^{3+} cations. The occupied $4f$ peak at lower energy nearer to the valence band indicates the Ce^{3+} cation where the excess electron has occupied the $4f_{xyz}$ orbital. The other occupied $4f$ peak at higher energy corresponds to the Ce^{3+} cations with the excess electron occupying the $4f_{x^3}$ orbital.

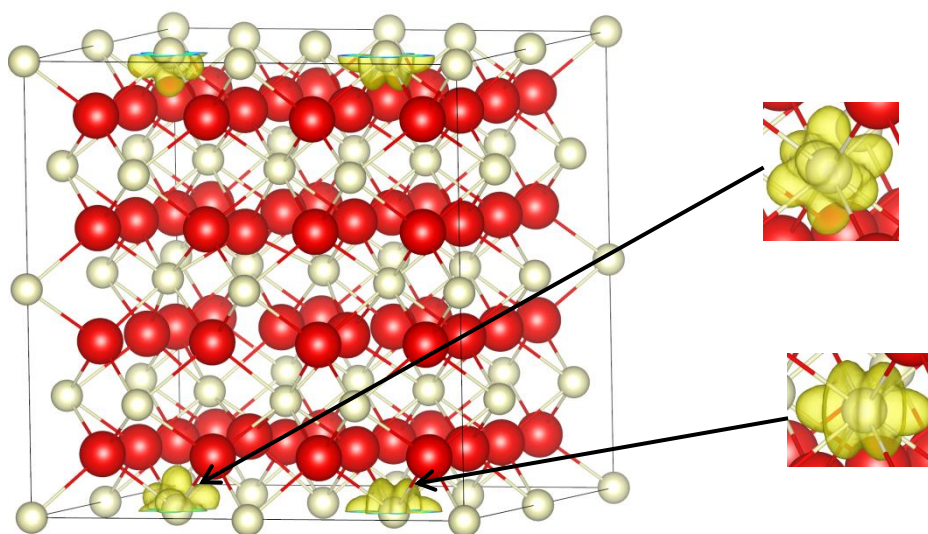


Figure A1. Isosurface of spin density for structure **Q** (refer Table 3.3 in Chapter 3) showing the two Ce^{3+} cations with different f -orbitals. Isosurface level is 0.04 electrons \AA^{-3} .

A3. Effects of platinum group metal (PGM) dopants on oxygen vacancy formation in bulk ceria

Figure A2 shows the start and end structures used for NEB calculation for the migration of oxygen to neighbouring vacancy site in defective bulk CeO_2 .

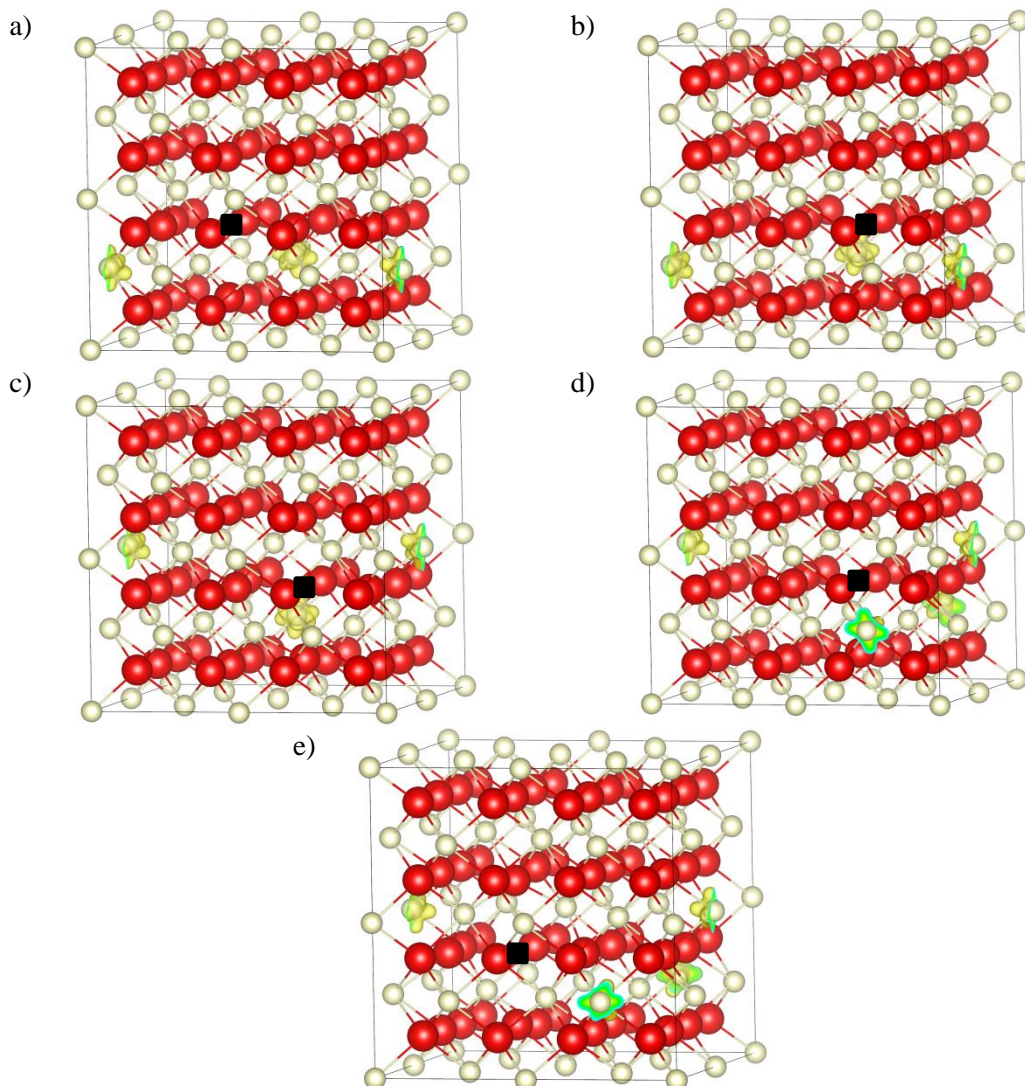
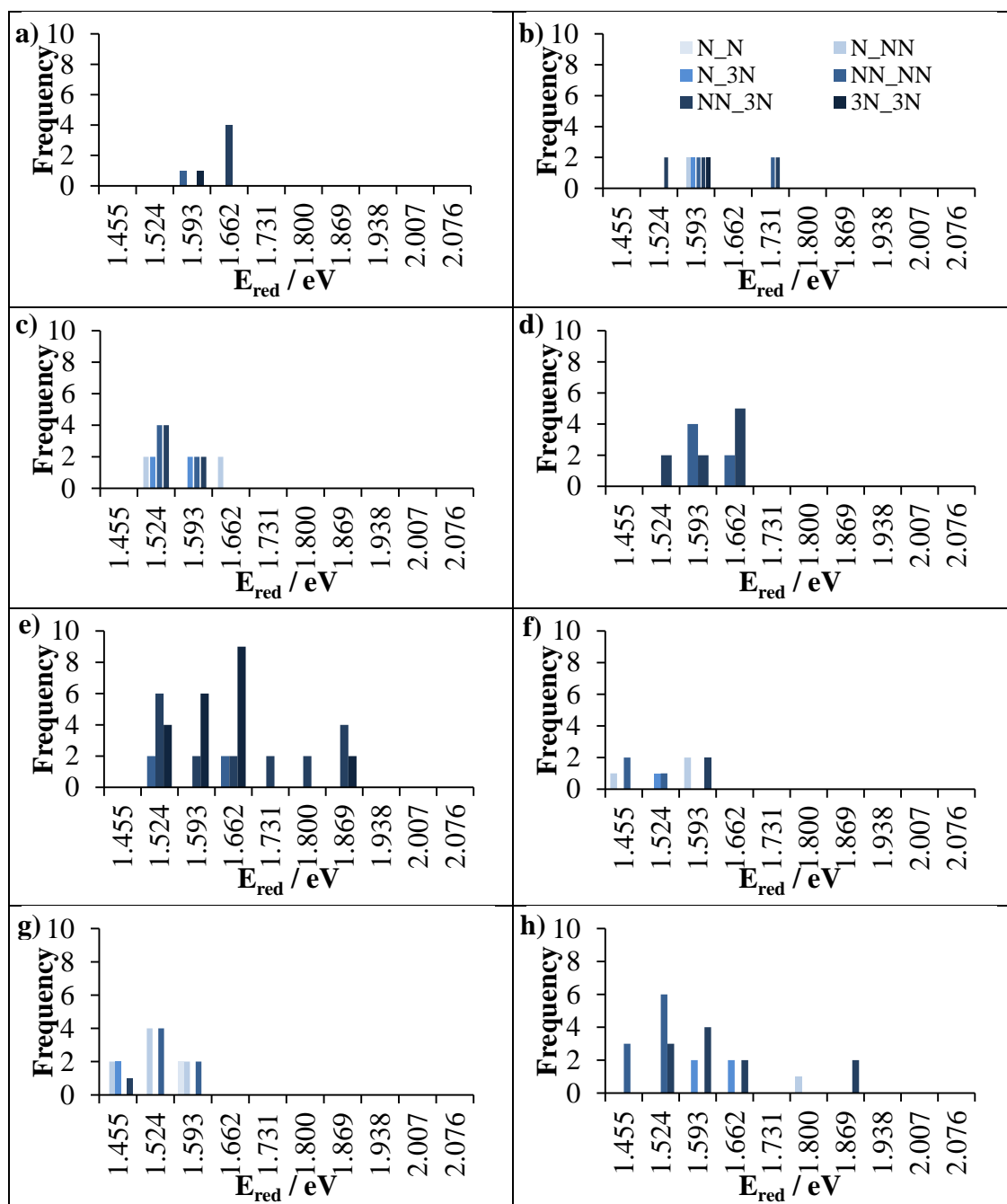


Figure A2. Spin densities showing Ce^{3+} sites of optimised structures used for NEB calculations for the oxygen migration to neighbouring vacancy site. The structures are denote as a) A, b) A*, c) B*, d) H', and e) H according to the legend in Figure 3.7 in Chapter 3. Cerium (white), oxygen (red), vacancy site (black box). Isosurface level is 0.04 electrons \AA^{-3} .

A4. Effects of platinum group metal (PGM) dopants on oxygen vacancy formation in bulk ceria

Figure A3 shows histograms of structures with different Ce^{3+} pairs from the oxygen vacancy site IV (refer Figure 3.14) at various E_{red} ranges. There are a total of Within each histogram plot, the frequency of structures of different Ce^{3+} pairs with respect to oxygen vacancy site (colour code shown in Figure A2a) are populated at various E_{red} range. Each histogram corresponds to different Ce^{3+} distances from Pd^{2+} .



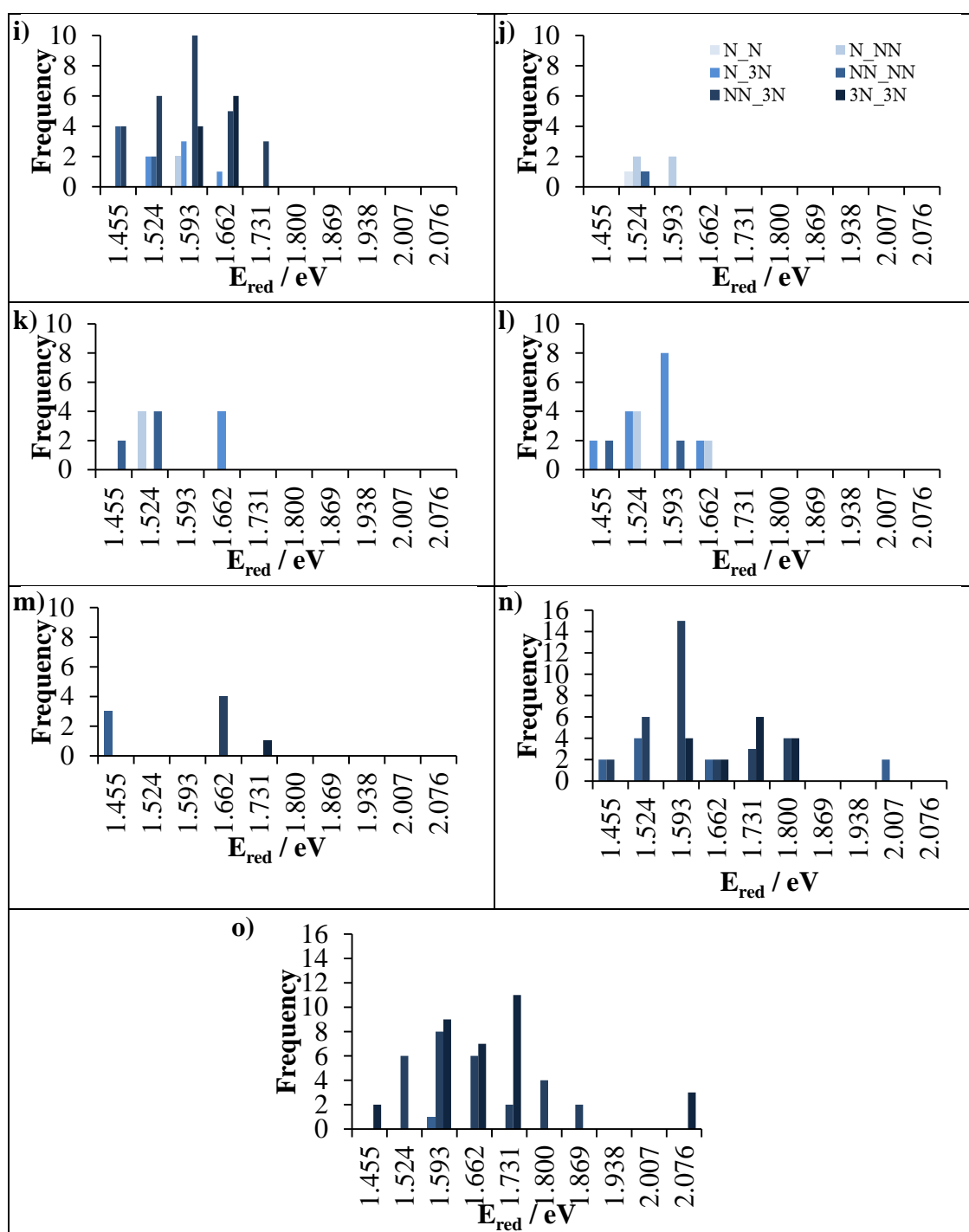


Figure A3. Histograms shows structures with different locations of Ce^{3+} pairs with respect to oxygen vacancy site IV; N_N, N_NN, N_3N, NN_NN, NN_3N, 3N_3N, colour coded from various shades of blue (pale blue to navy blue). Each histogram corresponds to Ce^{3+} distances to Pd^{2+} ; a) N_N, b) N_2N, c) N_3N, d) N_4N, e) N_5N, f) 2N_2N, g) 2N_3N, h) 2N_4N, i) 2N_5N, j) 3N_3N, k) 3N_4N, l) 3N_5N, m) 4N_4N, n) 4N_5N, and o) 5N_5N.

Bibliography

1. P. Bera, K. C. Patil, V. Jayaram, G. N. Subbanna and M. S. Hegde, *Journal of Catalysis*, 2000, 196, 293-301.
2. P. Bera and M. S. Hegde, *Catalysis Letters*, 2002, 79, 75-81.
3. S. Roy, A. Marimuthu, M. S. Hegde and G. Madras, *Applied Catalysis B: Environmental*, 2007, 73, 300-310.
4. S. Roy, A. Marimuthu, M. S. Hegde and G. Madras, *Applied Catalysis B: Environmental*, 2007, 71, 23-31.
5. T. Wakabayashi, S. Kato, Y. Nakahara, R. Oshima, M. Ogasawara and S. Nakata, *Catalysis Letters*, 2013, 143, 687-696.
6. Y. Zuo, X. S. Huang, L. P. Li and G. S. Li, *Journal of Materials Chemistry A*, 2013, 1, 374-380.
7. B. Harrison, B. J. Cooper and A. J. J. Wilkins, *Platinum Metals Review*, 1981, 25, 14-22.
8. S. Roy, N. van Vegten, N. Maeda and A. Baiker, *Applied Catalysis B: Environmental*, 2012, 119, 279-286.
9. M. Karthik and H. L. Bai, *Applied Catalysis B: Environmental*, 2014, 144, 809-815.
10. G. Kresse and J. Hafner, *Physical Review B*, 1993, **47**, 558-561.
11. G. Kresse and J. Hafner, *Physical Review B*, 1994, 49, 14251-14269.
12. G. Kresse and J. Furthmüller, *Computational Materials Science*, 1996, **6**, 15-50.
13. G. Kresse and J. Furthmüller, *Physical Review B*, 1996, **54**, 11169-11186.
14. R. Dovesi, R. Orlando, B. Civalleri, C. Roetti, V. R. Saunders and C. M. Zicovich-Wilson, *Zeitschrift für Kristallographie - Crystalline Materials*, 2005, 220, 571-573.
15. R. Dovesi, V. R. Saunders, C. Roetti, R. Orlando, C. M. Zicovich-Wilson, F. Pascale, B. Civalleri, K. Doll, N. M. Harrison, I. J. Bush, P. D'Arco and M. Llunell, *CRYSTAL09 User's Manual*, University Torino, Torino, 2009.
16. Met Office Education, The Great Smog 1952, <http://www.metoffice.gov.uk/education/teens/case-studies/great-smog>, Accessed 20 December, 2013.
17. news.bbc.co.uk, The Great Smog of London, <http://news.bbc.co.uk/1/hi/england/2545759.stm>, Accessed 20 December, 2013.
18. U.S. Environmental Protection Agency, Understanding the Clean Air Act, http://www.epa.gov/airquality/peg_caa/understand.html, Accessed 20 December, 2013.
19. in 42 U.S.C. 7404-7405, Clean Air Act 1963, §4, 17 December 1963.
20. in 42 U.S.C. 7521, Clean Air Act Amendment 1970, §202 (b), 31 December 1970.
21. U.S. Environmental Protection Agency, Six common air pollutants, <http://www.epa.gov/air/urbanair/>, Accessed 1 January, 2014.
22. in *Council Directive 70/220/EEC*, OJ L 76, 6 April 1970, p. 1.
23. in *Regulation (EC) No. 715/2007*, OJ L 171, 20 June 2007, pp. 1-16.
24. in *Commission Regulation (EU) No. 582/2011*, OJ L 167, 25 May 2011, pp. 1-168.
25. G. J. K. Acres, *Platinum Metals Review*, 1970, 14, 2-10.
26. G. J. K. Acres, *Platinum Metals Review*, 1970, 14, 78-85.

27. G. J. K. Acres and B. J. Cooper, *Platinum Metals Review*, 1972, 16, 74-86.
28. M. V. Twigg., *Platinum Metals Review*, 1999, 43, 168-171.
29. www.matthey.com, Autocatalysts - A Major Contribution to Clean Air, http://www.matthey.com/innovation/history/autocatalysts_a_major_contribution_clean_air, Accessed 20 December, 2013.
30. G. Kim, *Industrial & Engineering Chemistry Product Research and Development*, 1982, 21, 267-274.
31. L. Gerward and J. S. Olsen, *Powder Diffraction*, 1993, 8, 127-129.
32. L. Gerward, J. S. Olsen, L. Petit, G. Vaitheeswaran, V. Kanchana and A. Svane, *J. Alloy. Compd.*, 2005, 400, 56-61.
33. N. Guillen-Hurtado, V. Rico-Perez, A. Garcia-Garcia, D. Lozano-Castello and A. Bueno-Lopez, *Dyna-Colombia*, 2012, 79, 114-121.
34. S. J. Duclos, Y. K. Vohra, A. L. Ruoff, A. Jayaraman and G. P. Espinosa, *Phys. Rev. B*, 1988, 38, 7755.
35. A. Nakajima, A. Yoshihara and M. Ishigame, *Phys. Rev. B*, 1994, 50, 13297-13307.
36. A. Trovarelli, *Catalysis Today*, 1999, 50, 353-367.
37. S. Bernal, G. Blanco, J. J. Calvino, J. M. Gatica, J. A. P. Omil and J. M. Pintado, *Topics in Catalysis*, 2004, 28, 31-45.
38. S. M. Hirst, A. S. Karakoti, R. D. Tyler, N. Sriranganathan, S. Seal and C. M. Reilly, *Small*, 2009, 5, 2848-2856.
39. I. Celardo, J. Z. Pedersen, E. Traversa and L. Ghibelli, *Nanoscale*, 2011, 3, 1411-1420.
40. E. Aneggi, M. Boaro, C. d. Leitenburg, G. Dolcetti and A. Trovarelli, *J. Alloy. Compd.*, 2006, 408-412, 1096-1102.
41. A. Bueno-Lopez, *Applied Catalysis B: Environmental*, 2014, 146, 1-11.
42. A. F. Rossi, N. Amaral-Silva, R. C. Martins and R. M. Quinta-Ferreira, *Applied Catalysis B: Environmental*, 2012, 111, 254-263.
43. S. Karmakar, N. Wang, S. Acharya and K. M. Dooley, *Combustion and Flame*, 2013, 160, 3004-3014.
44. G. E. Batley, B. Halliburton, J. K. Kirby, C. L. Doolette, D. Navarro, M. J. McLaughlin and C. Veitch, *Environmental Toxicology and Chemistry*, 2013, 32, 1896-1905.
45. Z. Fan, C.-C. Chao, F. Hossein-Babaei and F. B. Prinz, *J. Mater. Chem.*, 2011, 21, 10903-10906.
46. E. C. C. Souza, *Journal of Electroceramics*, 2013, 31, 245-253.
47. A. Laachir, V. Perrichon, A. Badri, J. Lamotte, E. Catherine, J. C. Lavalley, J. El Fallah, L. Hilaire, F. Le Normand, E. Quemere, G. N. Sauvion and O. Touret, *J. Chem. Soc., Faraday Trans.*, 1991, 87, 1601-1609.
48. V. Perrichon, A. Laachir, G. Bergeret, R. Frety, L. Tournayan and O. Touret, *J. Chem. Soc., Faraday Trans.*, 1994, 90, 773-781.
49. C. Lamonier, G. Wrobel and J. P. Bonnelle, *J. Mater. Chem.*, 1994, 4, 1927-1928.
50. N. V. Skorodumova, S. Simak, B. Lundqvist, I. Abrikosov and B. Johansson, *Physical Review Letters*, 2002, 89, 14-17.
51. S. Fabris, S. de Gironcoli, S. Baroni, G. Vicario and G. Balducci, *Physical Review B*, 2005, 71, 041102.
52. R. D. Shannon, *Acta Crystallographica Section A*, 1976, 32, 751-767.
53. J. D. van Horn, Electronic table of Shannon Ionic Radii, Accessed 14 January, 2014.
54. J. Paier, C. Penschke and J. Sauer, *Chemical Reviews*, 2013, 113, 3949-3985.

55. *CRC Handbook of Chemistry : a ready-reference book of chemical and physical data*, Boca Raton, FL : CRC Press, 2005, 86th ed. edn., 2005-2006.
56. E. J. Huber and C. E. Holley, *J. Am. Chem. Soc.*, 1953, 75, 5645-5647.
57. F. B. Baker and C. E. Holley, *Journal of Chemical & Engineering Data*, 1968, 13, 405-407.
58. M. Zinkevich, D. Djurovic and F. Aldinger, *Solid State Ionics*, 2006, 177, 989-1001.
59. B. C. H. Steele and J. M. Floyd, *Proc. Br. Ceram. Soc.*, 1971, 19, 55.
60. M. A. Panhans and R. N. Blumenthal, *Solid State Ionics*, 1993, 60, 279-298.
61. R. J. Gorte, *AIChE Journal*, 2010, 56, 1126-1135.
62. G. Balducci, J. Kašpar, P. Fornasiero, M. Graziani, M. S. Islam and J. D. Gale, *The Journal of Physical Chemistry B*, 1997, 101, 1750-1753.
63. C. Frayret, A. Villesuzanne, M. Pouchard and S. Matar, *International Journal of Quantum Chemistry*, 2005, 101, 826-839.
64. M. Nolan, J. E. Fearon and G. W. Watson, *Solid State Ionics*, 2006, 177, 3069-3074.
65. A. Gotte, D. Spångberg, K. Hermansson and M. Baudin, *Solid State Ionics*, 2007, 178, 1421-1427.
66. H. L. Tuller and A. S. Nowick, *Journal of Physics and Chemistry of Solids*, 1977, 38, 859-867.
67. T. X. T. Sayle, S. C. Parker and C. R. A. Catlow, *J. Chem. Soc., Chem. Commun.*, 1992, 977-978.
68. J. Conesa, *Surface Science*, 1995, 339, 337-352.
69. H. L. Tuller and A. S. Nowick, *Journal of the Electrochemical Society*, 1979, 126, 209-217.
70. J. J. Plata, A. M. Márquez and J. F. Sanz, *J. Phys. Chem. C*, 2013, 117, 14502-14509.
71. M. Romeo, K. Bak, J. El Fallah, F. Le Normand and L. Hilaire, *Surface and Interface Analysis*, 1993, 20, 508-512.
72. A. Pfau and K. D. Schierbaum, *Surface Science*, 1994, 321, 71-80.
73. C. Binet, A. Badri and J.-C. Lavalley, *J. Phys. Chem.*, 1994, 98, 6392-6398.
74. H. Nörenberg and G. A. D. Briggs, *Surface Science*, 1999, 424, L352-L355.
75. F. Esch, S. Fabris, L. Zhou, T. Montini, C. Africh, P. Fornasiero, G. Comelli and R. Rosei, *Science*, 2005, 309, 752-755.
76. J. F. Jerratsch, X. Shao, N. Nilius, H. J. Freund, C. Popa, M. V. Ganduglia-Pirovano, A. M. Burow and J. Sauer, *Physical Review Letters*, 2011, 106, 246801.
77. K.-i. Fukui, Y. Namai and Y. Iwasawa, *Applied Surface Science*, 2002, 188, 252-256.
78. Y. Namai, K.-I. Fukui and Y. Iwasawa, *Metallic Oxides: Filling the Gap between Catalysis and Surface Science*, 2003, 85, 79-91.
79. Y. Namai, K.-i. Fukui and Y. Iwasawa, *The Journal of Physical Chemistry B*, 2003, 107, 11666-11673.
80. S. Torbrügge, M. Reichling, A. Ishiyama, S. Morita and Ó. Custance, *Physical Review Letters*, 2007, 99, 056101.
81. H.-Y. Li, H.-F. Wang, X.-Q. Gong, Y.-L. Guo, Y. Guo, G. Lu and P. Hu, *Physical Review B*, 2009, 79, 193401.
82. M. V. Ganduglia-Pirovano, J. L. F. Da Silva and J. Sauer, *Physical Review Letters*, 2009, 102, 026101(026101-026104).
83. S. J. Schmieg and D. N. Belton, *Applied Catalysis B: Environmental*, 1995, 6, 127-144.

84. V. Perrichon, A. Laachir, S. Abouarnadasse, O. Touret and G. Blanchard, *Applied Catalysis A: General*, 1995, 129, 69-82.
85. D. Terribile, A. Trovarelli, J. Llorca, C. de Leitenburg and G. Dolcetti, *Journal of Catalysis*, 1998, 178, 299-308.
86. C. Binet, A. Jadi, J.-C. Lavalley and M. Boutonnet-Kizling, *J. Chem. Soc., Faraday Trans.*, 1992, 88, 2079-2084.
87. M. Mogensen, N. M. Sammes and G. A. Tompsett, *Solid State Ionics*, 2000, 129, 63-94.
88. P. Bera, K. R. Priolkar, A. Gayen, P. R. Sarode, M. S. Hegde, S. Emura, R. Kumashiro, V. Jayaram and G. N. Subbanna, *Chem. Mater.*, 2003, 15, 2049-2060.
89. K. R. Priolkar, P. Bera, P. R. Sarode, M. S. Hegde, S. Emura, R. Kumashiro and N. P. Lalla, *Chem. Mater.*, 2002, 14, 2120-2128.
90. S. Roy and M. S. Hegde, *Catalysis Communications*, 2008, 9, 811-815.
91. S. Roy, A. Marimuthu, P. A. Deshpande, M. S. Hegde and G. Madras, *Industrial & Engineering Chemistry Research*, 2008, 47, 9240-9247.
92. V. A. Sadykov, N. N. Sazonova, A. S. Bobin, V. S. Muzykantov, E. L. Gubanova, G. M. Alikina, A. I. Lukashevich, V. A. Rogov, E. N. Ermakova, E. M. Sadovskaya, N. V. Mezentseva, E. G. Zevak, S. A. Veniaminov, M. Muhler, C. Mirodatos, Y. Schuurman and A. C. V. Veen, *Catalysis Today*, 2011, 169, 125-137.
93. A. Trovarelli, G. Dolcetti, C. de Leitenburg, J. Kaspar, P. Finetti and A. Santoni, *J. Chem. Soc., Faraday Trans.*, 1992, 88, 1311-1319.
94. F. Zamar, A. Trovarelli, C. de Leitenburg and G. Dolcetti, *J. Chem. Soc., Chem. Commun.*, 1995, 965-966.
95. P. Vidmar, P. Fornasiero, J. Kaspar, G. Gubitosa and M. Graziani, *Journal of Catalysis*, 1997, 171, 160-168.
96. A. Bensalem, J.-C. Muller, D. Tessier and F. Bozon-Verduraz, *J. Chem. Soc., Faraday Trans.*, 1996, 92, 3233-3237.
97. D. R. Mullins and S. H. Overbury, *Journal of Catalysis*, 1999, 188, 340-345.
98. S. Bernal, *Catalysis Today*, 1999, 50, 175-206.
99. M. D. Salazar-Villalpando, D. A. Berry and T. H. Gardner, *International Journal of Hydrogen Energy*, 2008, 33, 2695-2703.
100. H. W. Jen, G. W. Graham, W. Chun, R. W. McCabe, J. P. Cuif, S. E. Deutsch and O. Touret, *Catalysis Today*, 1999, 50, 309-328.
101. G. Balducci, P. Fornasiero, R. Monte, J. Kaspar, S. Meriani and M. Graziani, *Catalysis Letters*, 1995, 33, 193-200.
102. P. Fornasiero, E. Fonda, R. D. Monte, G. Vlaic, J. Kaspar and M. Graziani, *Journal of Catalysis*, 1999, 187, 177-185.
103. J. Kašpar, P. Fornasiero and M. Graziani, *Catalysis Today*, 1999, 50, 285-298.
104. J. Kaspar, P. Fornasiero, G. Balducci, R. Di Monte, N. Hickey and V. Sergo, *Inorganica Chimica Acta*, 2003, 349, 217-226.
105. C. Bozo, N. Guilhaume, E. Garbowski and M. Primet, *Catalysis Today*, 2000, 59, 33-45.
106. C. Bozo, N. Guilhaume and J.-M. Herrmann, *Journal of Catalysis*, 2001, 203, 393-406.
107. M. Valden, X. Lai and D. W. Goodman, *Science*, 1998, 281, 1647-1650.
108. P. A. Carlsson and M. Skoglundh, *Applied Catalysis B: Environmental*, 2011, 101, 669-675.

109. R. A. van Santen and M. Nuerock, *Molecular Heterogenous Catalysis*, Wiley-VCH, 2006.
110. J. Z. Shyu, K. Otto, W. L. H. Watkins, G. W. Graham, R. K. Belitz and H. S. Gandhi, *Journal of Catalysis*, 1988, 114, 23-33.
111. M. S. Brogan, T. J. Dines and J. A. Cairns, *J. Chem. Soc., Faraday Trans.*, 1994, 90, 1461-1466.
112. A. Caballero, J. P. Holgado, V. M. Gonzalez-delaCruz, S. E. Habas, T. Herranz and M. Salmeron, *Chem. Commun.*, 2010, 46, 1097-1099.
113. D. W. Daniel, *J. Phys. Chem.*, 1988, 92, 3891-3899.
114. S. Roy, A. Marimuthu, M. S. Hegde and G. Madras, *Catalysis Communications*, 2008, 9, 101-105.
115. T. Baidya, P. Bera, B. D. Mukri, S. K. Panda, O. Krocher, M. Elsener and M. S. Hegde, *Journal of Catalysis*, 2013, 303, 117-129.
116. X. N. Chen, J. Y. Chen, Y. Zhao, M. S. Chen and H. L. Wan, *Chinese Journal of Catalysis*, 2012, 33, 1901-1905.
117. M. S. Chen, Y. Cai, Z. Yan, K. K. Gath, S. Axnanda and D. W. Goodman, *Surface Science*, 2007, 601, 5326-5331.
118. B. Hammer and J. K. Norskov, *Nature*, 1995, 376, 238-240.
119. M. Haruta, *CATTECH*, 2002, 6, 102-115.
120. W. A. Bone and G. W. Andrew, *Proceedings of the Royal Society of London. Series A*, 1925, 109, 459-476.
121. G. C. Bond, P. A. Sermon, G. Webb, D. A. Buchanan and P. B. Wells, *J. Chem. Soc., Chem. Commun.*, 1973, 444b-445.
122. M. Haruta, T. Kobayashi, H. Sano and N. Yamada, *Chemistry Letters*, 1987, 16, 405-408.
123. G. J. Hutchings, *Journal of Catalysis*, 1985, 96, 292-295.
124. J. R. Mellor, A. N. Palazov, B. S. Grigorova, J. F. Greyling, K. Reddy, M. P. Letsoalo and J. H. Marsh, *Catalysis Today*, 2002, 72, 145-156.
125. L. Ilieva, G. Pantaleo, I. Ivanov, A. M. Venezia and D. Andreeva, *Applied Catalysis B: Environmental*, 2006, 65, 101-109.
126. D. Andreeva, V. Idakiev, T. Tabakova, L. Ilieva, P. Falaras, A. Bourlinos, A. Travlos and J. Andrés, *Chemical Physics Letters*, 2002, 72, 51-57.
127. D. Mendes, H. Garcia, V. B. Silva, A. Mendes and L. M. Madeira, *Industrial & Engineering Chemistry Research*, 2009, 48, 430-439.
128. J. K. Edwards, E. Ntainjua N, A. F. Carley, A. A. Herzing, C. J. Kiely and G. J. Hutchings, *Angewandte Chemie International Edition*, 2009, 48, 8512-8515.
129. A. Corma and H. Garcia, *Chem. Soc. Rev.*, 2008, 37, 2096-2126.
130. M. Haruta, *Journal of New Materials for Electrochemical Systems*, 2004, 7, 163-172.
131. M. Haruta, *Catalysis Today*, 1997, 36, 153-166.
132. A. S. K. Hashmi and G. J. Hutchings, *Angewandte Chemie - International Edition*, 2006, 45, 7896-7936.
133. D. T. Thompson, *Nano Today*, 2007, 2, 40-43.
134. T. W. Janssens, B. Clausen, B. Hvolbæk, H. Falsig, C. Christensen, T. Bligaard and J. Nørskov, *Topics in Catalysis*, 2007, 44, 15-26.
135. S. C. Carabineiro, N. Bogdanchikova, M. Avalos-Borja, A. Pestryakov, P. Tavares and J. Figueiredo, *Nano Research*, 2011, 4, 180-193.
136. Y. Y. Wu, N. A. Mashayekhi and H. H. Kung, *Catal. Sci. Technol.*, 2013, 3, 2881-2891.

137. M. M. Schubert, S. Hackenberg, A. C. van Veen, M. Muhler, V. Plzak and R. J. Behm, *Journal of Catalysis*, 2001, 197, 113-122.
138. G. C. Bond and D. T. Thompson, *Gold Bulletin*, 2000, 33, 41-51.
139. M. A. P. Dekkers, M. J. Lippits and B. E. Nieuwenhuys, *Catalysis Letters*, 1998, 56, 195-197.
140. M. A. P. Dekkers, M. J. Lippits and B. E. Nieuwenhuys, *Catalysis Today*, 1999, 54, 381-390.
141. J.-D. Grunwaldt, M. Maciejewski, O. S. Becker, P. Fabrizioli and A. Baiker, *Journal of Catalysis*, 1999, 186, 458-469.
142. G. C. Bond and D. T. Thompson, *Catalysis Reviews*, 1999, 41, 319-388.
143. N. Lopez, T. V. W. Janssens, B. S. Clausen, Y. Xu, M. Mavrikakis, T. Bligaard and J. K. Nørskov, *Journal of Catalysis*, 2004, 223, 232-235.
144. G. Bond and D. Thompson, *Gold Bulletin*, 2009, 42, 247-259.
145. A. A. Herzing, C. J. Kiely, A. F. Carley, P. Landon and G. J. Hutchings, *Science*, 2008, **321**, 1331-1335.
146. M. Chen and D. W. Goodman, *Chem. Soc. Rev.*, 2008, 37, 1860-1870.
147. M. Haruta, N. Yamada, T. Kobayashi and S. Iijima, *Journal of Catalysis*, 1989, 115, 301-309.
148. M. Haruta, S. Tsubota, T. Kobayashi, H. Kageyama, M. J. Genet and B. Delmon, *Journal of Catalysis*, 1993, 144, 175-192.
149. G. R. Bamwenda, S. Tsubota, T. Nakamura and M. Haruta, *Catalysis Letters*, 1997, 44, 83-87.
150. G. Dräger, W. Czolbe and J. A. Leiro, *Physical Review B*, 1992, 45, 8283-8287.
151. M. Catti, G. Valerio and R. Dovesi, *Physical Review B*, 1995, 51, 7441-7450.
152. E. Krén, P. Szabó and G. Konczos, *Physics Letters*, 1965, 19, 103-104.
153. L. M. Sandratskii, M. Uhl and J. Kübler, *Journal of Physics: Condensed Matter*, 1996, 8, 983.
154. S. Mochizuki, *Physica Status Solidi (a)*, 1977, 41, 591-594.
155. M. P. J. Punkkinen, K. Kokko, W. Hergert and I. J. Väyrynen, *Journal of Physics: Condensed Matter*, 1999, 11, 2341.
156. R. J. Lad and V. E. Henrich, *Physical Review B*, 1989, 39, 13478-13485.
157. G. Rollmann, A. Rohrbach, P. Entel and J. Hafner, *Physical Review B*, 2004, 69, 165107.
158. A. Rohrbach, J. Hafner and G. Kresse, *Physical Review B*, 2004, 70, 125426.
159. K. L. Howard and D. J. Willock, *Faraday Discussions*, 2011, **152**, 135-151.
160. L. W. Finger and R. M. Hazen, *Journal of Applied Physics*, 1980, 51, 5362-5367.
161. S. Hill and C. Catlow, *Journal of Physics and Chemistry of Solids*, 1993, 54, 411-419.
162. S. Gennard, F. Corà and C. R. A. Catlow, *The Journal of Physical Chemistry B*, 1999, 103, 10158-10170.
163. E. Wuilloud, B. Delley, W. D. Schneider and Y. Baer, *Phys. Rev. Lett.*, 1984, 53, 202.
164. C. Sevik and T. Cagin, *Physical Review B*, 2009, 80, 7.
165. A. Peles, *Journal of Materials Science*, 2012, 47, 7542-7548.
166. C. Loschen, J. Carrasco, K. M. Neyman and F. Illas, *Physical Review B*, 2007, 75, 8.
167. J. J. Plata, A. M. Marquez and J. F. Sanz, *The Journal of Chemical Physics*, 2012, 136, 041101.

168. D. O. Scanlon, B. J. Morgan and G. W. Watson, *Phys. Chem. Chem. Phys.*, 2011, 13, 4279-4284.
169. S. Fabris, G. Vicario, G. Balducci, S. de Gironcoli and S. Baroni, *The Journal of Physical Chemistry B*, 2005, 109, 22860-22867.
170. M. Nolan, S. Grigoleit, D. C. Sayle, S. C. Parker and G. W. Watson, *Surface Science*, 2005, 576, 217-229.
171. M. Nolan, *J. Mater. Chem.*, 2011, 21, 9160-9168.
172. M. Nolan, S. C. Parker and G. W. Watson, *The Journal of Physical Chemistry B*, 2006, 110, 2256-2262.
173. M. Huang and S. Fabris, *J. Phys. Chem. C*, 2008, 112, 8643-8648.
174. M. Nolan and G. W. Watson, *The Journal of Physical Chemistry B*, 2006, 110, 16600-16606.
175. M. Nolan, S. C. Parker and G. W. Watson, *Phys. Chem. Chem. Phys.*, 2006, 8, 216-218.
176. T. Desautay, A. Ringuede, M. Cassir, F. Labat and C. Adamo, *Surface Science*, 2012, 606, 305-311.
177. J. Graciani, A. M. Márquez, J. J. Plata, Y. Ortega, N. C. Hernández, A. Meyer, C. M. Zicovich-Wilson and J. F. Sanz, *Journal of Chemical Theory and Computation*, 2011, 7, 56-65.
178. J. L. F. Da Silva, M. V. Ganduglia-Pirovano, J. Sauer, V. Bayer and G. Kresse, *Physical Review B*, 2007, 75, 045121.
179. F. Marabelli and P. Wachter, *Phys. Rev. B*, 1987, 36, 1238.
180. C. W. M. Castleton, J. Kullgren and K. Hermansson, *Journal of Chemical Physics*, 2007, 127, 11.
181. D. A. Andersson, S. I. Simak, B. Johansson, I. A. Abrikosov and N. V. Skorodumova, *Phys. Rev. B*, 2007, 75, 035109.
182. H. Y. Li, H. F. Wang, Y. L. Guo, G. Z. Lu and P. Hu, *Chem. Commun.*, 2011, 47, 6105-6107.
183. B. Li, O. K. Ezekoye, Q. Zhang, L. Chen, P. Cui, G. Graham and X. Pan, *Physical Review B*, 2010, 82.
184. D. Marrocchelli, S. R. Bishop, H. L. Tuller, G. W. Watson and B. Yildiz, *Phys. Chem. Chem. Phys.*, 2012, 14, 12070-12074.
185. D. Marrocchelli, S. R. Bishop, H. L. Tuller and B. Yildiz, *Advanced Functional Materials*, 2012, 22, 1958-1965.
186. H. Y. Kim and G. Henkelman, *J. Phys. Chem. Lett.*, 2012, 3, 2194-2199.
187. F. Jensen, *Introduction to Computational Chemistry*, John Wiley & Sons Ltd, England, 1999.
188. R. M. Martin, *Electronic Structure: Basic Theory and Practical Methods*, Cambridge University Press, Cambridge, 2005.
189. R. Dronskowski, *Computational Chemistry of Solid State Materials*, Wiley-VCH Verlag GmbH & Co. KGaA, Weinheim, 2005.
190. S. M. Lindsay, *Introduction to Nanoscience*, Oxford University Press, 2010.
191. T. J. Giese and D. M. York, *The Journal of Chemical Physics*, 2010, 133, 244107.
192. L. H. Thomas, *Proceedings of the Cambridge Philosophical Society*, 1927, 23, 542-548.
193. E. Fermi, *Zeitschrift Fur Physik*, 1928, 48, 73-79.
194. P. Hohenberg and W. Kohn, *Physical Review*, 1964, 136, B864-B871.
195. W. Kohn and L. J. Sham, *Physical Review*, 1965, 140, 1133-&.
196. J. P. Perdew and Y. Wang, *Physical Review B*, 1992, 45, 13244-13249.

197. J. P. Perdew, J. A. Chevary, S. H. Vosko, K. A. Jackson, M. R. Pederson, D. J. Singh and C. Fiolhais, *Physical Review B*, 1992, 46, 6671-6687.
198. J. P. Perdew, J. A. Chevary, S. H. Vosko, K. A. Jackson, M. R. Pederson, D. J. Singh and C. Fiolhais, *Physical Review B*, 1993, 48, 4978-4978.
199. J. P. Perdew, K. Burke and M. Ernzerhof, *Physical Review Letters*, 1996, 77, 3865.
200. J. P. Perdew, K. Burke and M. Ernzerhof, *Physical Review Letters*, 1997, 78, 1396-1396.
201. S. L. Dudarev, G. A. Botton, S. Y. Savrasov, C. J. Humphreys and A. P. Sutton, *Physical Review B*, 1998, 57, 1505-1509.
202. A. D. Mayernick and M. J. Janik, *J. Phys. Chem. C*, 2008, 112, 14955-14964.
203. Y.-L. Song, L.-L. Yin, J. Zhang, P. Hu, X.-Q. Gong and G. Lu, *Surface Science*, 2013, 618, 140-147.
204. V. Fock, *Zeitschrift Fur Physik*, 1930, 61, 126-148.
205. J. C. Slater, *Physical Review*, 1951, 81, 385-390.
206. S. H. Vosko, L. Wilk and M. Nusair, *Canadian Journal of Physics*, 1980, 58, 1200-1211.
207. J. P. Perdew and W. Yue, *Physical Review B*, 1986, 33, 8800-8802.
208. J. P. Perdew and W. Yue, *Physical Review B*, 1989, 40, 3399-3399.
209. R. Dovesi, V. R. Saunders, C. Roetti, R. Orlando, C. M. Zicovich-Wilson, F. Pascale, B. Civalieri, K. Doll, N. M. Harrison, I. J. Bush, P. D'Arco and M. Llunell, University Torino, Torino, 2009.
210. M. Ernzerhof and G. E. Scuseria, *Journal of Chemical Physics*, 1999, 110, 5029-5036.
211. C. Adamo and V. Barone, *The Journal of Chemical Physics*, 1999, 110, 6158-6170.
212. J. Heyd, G. E. Scuseria and M. Ernzerhof, *The Journal of Chemical Physics*, 2003, 118, 8207-8207.
213. J. Heyd and G. E. Scuseria, *The Journal of Chemical Physics*, 2004, 121, 1187-1192.
214. J. Heyd, G. E. Scuseria and M. Ernzerhof, *The Journal of Chemical Physics*, 2006, 124, 219906-219901.
215. P. E. Blochl, *Physical Review B*, 1994, **50**, 17953-17979.
216. G. Kresse and D. Joubert, *Physical Review B*, 1999, 59, 1758-1775.
217. G. Kresse, M. Marsman and J. Furthmüller, 2013.
218. H. J. Monkhorst and J. D. Pack, *Physical Review B*, 1976, 13, 5188-5192.
219. J. D. Pack and H. J. Monkhorst, *Physical Review B*, 1977, 16, 1748-1749.
220. F. D. Murnaghan, *Proceedings of the National Academy of Sciences*, 1944, 30, 244-247.
221. M. J. Winter, WebElements: the periodic table on the WWW, <http://www.webelements.com>, Accessed 22 April, 2014.
222. J. C. Slater, *Physical Review*, 1930, 36, 57-64.
223. S. F. Boys, *Proceedings of the Royal Society of London. Series A. Mathematical and Physical Sciences*, 1950, 200, 542-554.
224. M. Hulsen, A. Weigand and M. Dolg, *Theor. Chem. Acc.*, 2009, 122, 23-29.
225. D. Feller, *J. Comput. Chem.*, 1996, 17, 1571-1586.
226. K. L. Schuchardt, B. T. Didier, T. Elsethagen, L. S. Sun, V. Gurumoorthi, J. Chase, J. Li and T. L. Windus, *J. Chem Inf. Model.*, 2007, 47, 1045-1052.
227. G. Frenking, I. Antes, M. Böhme, S. Dapprich, A. W. Ehlers, V. Jonas, A. Neuhaus, M. Otto, R. Stegmann, A. Veldkamp and S. F. Vyboishchikov, in

- Reviews in Computational Chemistry*, John Wiley & Sons, Inc., 1996, pp. 63-144.
228. T. R. Cundari, M. T. Benson, M. L. Lutz and S. O. Sommerer, in *Reviews in Computational Chemistry*, John Wiley & Sons, Inc., 1996, pp. 145-202.
229. M. Dolg, H. Stoll and H. Preuss, *Journal of Chemical Physics*, 1989, 90, 1730-1734.
230. H. Jónsson, G. Mills and K. W. Jacobsen in *Classical and Quantum Dynamics in Condensed Phase Simulations*, World Scientific, 1998, p. 385.
231. G. Henkelman and H. Jonsson, *Journal of Chemical Physics*, 2000, 113, 9978-9985.
232. R. F. W. Bader, *Chemical Reviews*, 1991, 91, 893-928.
233. G. Henkelman, A. Arnaldsson and H. Jónsson, *Computational Materials Science*, 2006, 36, 354-360.
234. E. Sanville, S. D. Kenny, R. Smith and G. Henkelman, *J. Comput. Chem.*, 2007, 28, 899-908.
235. W. Tang, E. Sanville and G. Henkelman, *Journal of Physics: Condensed Matter*, 2009, 21, 084204.
236. Bader Charge Analysis, <http://theory.cm.utexas.edu/henkelman/research/bader/>, 2014.
237. A. Beste, D. R. Mullins, S. H. Overbury and R. J. Harrison, *Surface Science*, 2008, 602, 162-175.
238. P. R. L. Keating, D. O. Scanlon and G. W. Watson, *Journal of Physics: Condensed Matter*, 2009, 21, 405502.
239. A. Thetford, G. J. Hutchings, S. H. Taylor and D. J. Willock, *Proceedings of the Royal Society of London. Series A. Mathematical and Physical Sciences*, 2011, 467, 1885-1899.
240. A. D. Becke, *The Journal of Chemical Physics*, 1993, 98, 5648-5652.
241. C. Lee, W. Yang and R. G. Parr, *Physical Review B*, 1988, 37, 785.
242. N. V. Skorodumova, R. Ahuja, S. I. Simak, I. A. Abrikosov, B. Johansson and B. I. Lundqvist, *Physical Review B*, 2001, 64, 115108.
243. G. Gilat and L. J. Raubenheimer, *Physical Review*, 1966, 144, 390-395.
244. G. Gilat, *Journal of Computational Physics*, 1972, 10, 432-465.
245. R. S. Mulliken, *Journal of Chemical Physics*, 1955, 23, 1833-1840.
246. C. Chai, S. Yang, Z. Liu, M. Liao and N. Chen, *Chinese Science Bulletin*, 2003, 48, 1198-1200.
247. Z. Yang, G. Luo, Z. Lu, T. K. Woo and K. Hermansson, *Journal of Physics: Condensed Matter*, 2008, 20, 035210.
248. Z. Yang, G. Luo, Z. Lu and K. Hermansson, *The Journal of Chemical Physics*, 2007, 127, 074704(074701-074705).
249. A. Gayen, T. Baidya, A. S. Prakash, N. Ravishankar and M. S. Hegde, *Indian Journal of Chemistry*, 2005, 44A, 34-48.
250. Z. Yang, T. Woo and K. Hermansson, *Surface Science*, 2006, 600, 4953-4960.
251. H.-L. Chen, W.-T. Peng, J.-J. Ho, H.-M. Hsieh, Q.-b. Chen, L.-t. Luo, X. Yang, Y. Chen, H. Wang, R. Burch, C. Hardacre and P. Hu, *Chemical Physics*, 2008, 348, 161-168.
252. M. F. Camellone and S. Fabris, *J. Am. Chem. Soc.*, 2009, 131, 10473-10483.
253. A. D. Mayernick and M. J. Janik, *The Journal of Chemical Physics*, 2009, 131, -.
254. A. Bruix, K. M. Neyman and F. Illas, *J. Phys. Chem. C*, 2010, 114, 14202-14207.

255. A. Bruix, A. Migani, G. N. Vayssilov, K. M. Neyman, J. Libuda and F. Illas, *Phys. Chem. Chem. Phys.*, 2011, **13**, 11384-11392.
256. H. Y. Kim and G. Henkelman, *J. Phys. Chem. Lett.*, 2013, **4**, 216-221.
257. M. D. Krcha and M. J. Janik, *International Journal of Quantum Chemistry*, 2014, 114, 8-13.
258. N. V. Skorodumova, M. Baudin and K. Hermansson, *Phys. Rev. B*, 2004, 69, 075401.
259. Z. Yang, T. K. Woo, M. Baudin and K. Hermansson, *The Journal of Chemical Physics*, 2004, 120, 7741-7749.
260. M. Nolan, S. C. Parker and G. W. Watson, *Surface Science*, 2005, 595, 223-232.
261. N. Nilius, S. M. Kozlov, J.-F. Jerratsch, M. Baron, X. Shao, F. Viñes, S. Shaikhutdinov, K. M. Neyman and H.-J. Freund, *ACS Nano*, 2011, 6, 1126-1133.
262. L. J. Bennett and G. Jones, *Phys. Chem. Chem. Phys.*, 2014.
263. I. Yeriskin and M. Nolan, *The Journal of Chemical Physics*, 2009, 131, -.
264. N. C. Hernandez, R. Grau-Crespo, N. H. de Leeuw and J. F. Sanz, *Phys. Chem. Chem. Phys.*, 2009, 11, 5246-5252.
265. Z. Lu and Z. Yang, *Journal of Physics: Condensed Matter*, 2010, 22, 475003-475013.
266. A. D. Mayernick and M. J. Janik, *Journal of Catalysis*, 2011, 278, 16-25.
267. M. D. Krcha, A. D. Mayernick and M. J. Janik, *Journal of Catalysis*, 2012, 293, 103-115.
268. W.-C. Ding, X.-K. Gu, H.-Y. Su and W.-X. Li, *J. Phys. Chem. C*, 2014, 118, 12216-12223.
269. P. Bera and M. S. Hegde, *Catalysis Surveys from Asia*, 2011, 15, 181-199.
270. C. Li, Y. Sakata, T. Arai, K. Domen, K.-i. Maruya and T. Onishi, *J. Chem. Soc., Faraday Trans. 1*, 1989, 85, 1451-1461.
271. C. Li, Y. Sakata, T. Arai, K. Domen, K.-i. Maruya and T. Onishi, *J. Chem. Soc., Faraday Trans. 1*, 1989, 85, 929-943.
272. M. I. Zaki and H. Knözinger, *Materials Chemistry and Physics*, 1987, 17, 201-215.
273. C. Yang, L.-L. Yin, F. Bebensee, M. Buchholz, H. Sezen, S. Heissler, J. Chen, A. Nefedov, H. Idriss, X.-Q. Gong and C. Woll, *Phys. Chem. Chem. Phys.*, 2014.
274. M. Breysse, M. Guenin, B. Claudel and J. Veron, *Journal of Catalysis*, 1973, 28, 54-62.
275. A. Migani, G. N. Vayssilov, S. T. Bromley, F. Illas and K. M. Neyman, *Chem. Commun.*, 2010, 46, 5936-5938.
276. W.-J. Zhu, J. Zhang, X.-Q. Gong and G. Lu, *Catalysis Today*, 2011, 165, 19-24.
277. M. Haruta, *Gold Bulletin*, 2004, 37, 27-36.
278. M. Boronat and A. Corma, *Dalton Trans.*, 2010, 39, 8538-8546.
279. A. F. Carley, D. J. Morgan, N. Song, M. W. Roberts, S. H. Taylor, J. K. Bartley, D. J. Willock, K. L. Howard and G. J. Hutchings, *Phys. Chem. Chem. Phys.*, 2011, **13**, 2528-2538.
280. M. W. Chase, American Institute of Physics, 4th edn., 1998.
281. S. C. Ammal and A. Heyden, *J. Phys. Chem. C*, 2011, 115, 19246-19259.
282. S. Malwadkar, P. Bera, M. S. Hegde and C. V. V. Satyanarayana, *Reaction Kinetics Mechanisms and Catalysis*, 2012, 107, 405-419.

-
283. C. W. Tang, L. C. Hsu, S. W. Yu, C. B. Wang and S. H. Chien, *Vibrational Spectroscopy*, 2013, 65, 110-115.
 284. G. Balducci, M. S. Islam, J. Kašpar, P. Fornasiero and M. Graziani, *Chem. Mater.*, 2000, 12, 677-681.
 285. U. Diebold, *Surface Science Reports*, 2003, 48, 53-229.
 286. T. Baidya, A. Marimuthu, M. S. Hegde, N. Ravishankar and G. Madras, *J. Phys. Chem. C*, 2006, 111, 830-839.
 287. A. Trovarelli, *Catalysis Reviews*, 1996, 38, 439-520.
 288. A. Trovarelli, *Comments on Inorganic Chemistry*, 1999, 20, 263-284.